Epitaxial growth of InN and $In_xGa_{1-x}N$ nanostructured films on structurally modified substrates using MBE

A Thesis

Submitted For The Degree of

Doctor of Philosophy

in The Faculty of Science

by

Arpan De

Under The Guidance of

Prof. S. M. Shivaprasad

Chemistry and Physics of Materials Unit

Jawaharlal Nehru Centre for Advanced Scientific Research

Bangalore - 560 064, India

May 2017

Dedicated to my supervisor
Prof. S. M. Shivaprasad

DECLARATION

I hereby declare that the matter embodied in the thesis entitled "**Epitaxial growth of InN and $In_xGa_{1-x}N$ nanostructured films on structurally modified substrates using MBE**" is the result of investigations carried out by me at the Chemistry and Physics of Materials Unit, Jawaharlal Nehru Centre for Advanced Scientific Research, Bangalore, India under the supervision of **Prof. S. M. Shivaprasad** and that it has not been submitted elsewhere for the award of any degree or diploma.

In keeping with the general practice in reporting scientific observations, due acknowledgement has been made whenever the work described is based on the findings of other investigators. Any omission that might have occurred by oversight or error of judgement is regretted.

Arpan De

Date:

Place: Bangalore, India

CERTIFICATE

I hereby certify that the matter embodied in this thesis entitled "**Epitaxial growth of InN and $\mathbf{In_xGa_{1-x}N}$ nanostructured films on structurally modified substrates using MBE**" has been carried out by Mr. **Arpan De** at the Chemistry and Physics of Materials Unit, Jawaharlal Nehru Centre for Advanced Scientific Research, Bangalore, India under my supervision and that it has not been submitted elsewhere for the award of any degree or diploma.

Prof. S. M. Shivaprasad

(Research Supervisor)

Date:

Place: Bangalore, India

Acknowledgements

This part of the thesis gives me the opportunity to express my thanks to many people that I have met during my long journey in the research world, until I finished writing my PhD thesis.

I am deeply grateful to my supervisor, Prof. S. M. Shivaprasad, for his invaluable academic guidance, constant enthusiasm towards the topic, valuable insights and keen support. It is an honour and a great experience to be working with him. His leadership and tenacity helped me produce this thesis. I am fully grateful for all that he has taught me. It has been a great privilege for me to have been educated by him. I appreciate the efforts that he has made in my personal development as a researcher and in numerous discussions required by this study and thus, the thesis has been dedicated to him.

I would like to express my gratitude to Bharat Ratna Prof. C. N. R. Rao for his endless support and motivation.

I would also like to acknowledge the present and past Chairman of CPMU, Prof. Chandrabhas Narayana, Prof. S. Balasubramanian, and Prof. G.U. Kulkarni for all the help and support. I convey my thanks to Prof. Chandrabhas Narayana, Prof. S. M. Shivaprasad, Dr. Ranjan Datta, Prof. S. Balasubramanian, Prof. U. V. Waghmare and Prof. Shobhana Narasimhan for their wonderful course work during first year, which helped me understand different aspects of experimental and theoretical material science.

I would like to thank Srinath Sir, for helping with matters pertaining to electronic circuits, finding leaks in vacuum systems, baking and maintaining MBE system, fixing other vital pieces of apparatus, without which successful experiments would not have been possible. I also thank Mahesh, Prajwal (for FESEM imaging and CL measurements), Jagadeesh (for HRXRD and XPS measurements) and Jay Ghatak (for TEM measurements) for all the technical help. All the help provided by Academic Section, Administrative

Section, Library, Complab and Hostel Authority are also greatly appreciated.

I thank Council of Scientific and Industrial Research (CSIR) for providing me research fellowship.

I am very thankful to all my past and present lab-mates; Dr. Jithesh Kuyyalil, Dr. Praveen Kumar, Dr. Manoj Kesaria, Dr. Saitsh Shetty, Dr. Malleswararao Tangi, Dr. Varun Thakur, Dr. K. K. Nagaraja, Sanjay, Abhijit, Sachin, Shivaram, Rajendra, Dr. Muthuvinayagam, Dr. Shashidhar, Dr. Saraswati, and Vinayak for creating a very friendly working atmosphere in the lab and for all their help and valuable inputs to my work. I thank Dr. Malleswararao Tangi for helping me learning MBE operation and data-analysis in the initial days and also for all the support and discussions later on, during my work. I want to specially thank Sachin B. M. for assisting me in almost all the experiments and other lab related works.

I am also grateful to my friends Somnath, Saikat, Jia, Sisir, Abhijit, Chandan and Subhajit, who, for small reason, kindly helped me to become the person and researcher I am now. I would not be able to reach my goals without them. I thank Sunita for helping me in PL measurements.

Last but certainly not least, I would like to express my love to my family for raising me the right way, for dedicating so much time and effort in my education and for their love and trust all the way supporting me in whatever pursuit I have chosen.

Synopsis

The nitride semiconductors and related alloys have shown great promise for the development of numerous electronic and optoelectronic devices. Their tunable bandgap from IR to deep UV and their chemical robustness under high electrical current and temperature, are best suited for the fabrication of high power, high temperature and high frequency electronic and optoelectronic devices. Among the ternary compounds of Group-III nitride materials, $In_xGa_{1-x}N$ is considered as the indispensable material for the fabrication of light emitters which are active in the entire visible and partly in the near-UV spectral regions. However, it has been reported that there exists a huge miscibility gap between InN and GaN and the calculated solubility of InN in GaN at 800 °C is less than 6%. There is a large difference in bond-length, vapour pressure and formation enthalpy between InN and GaN. All these result in phase-separation, low indium incorporation and indium surface segregation in $In_xGa_{1-x}N$. Moreover, several technical limitations, e.g. the difficulty in growing high-quality $In_xGa_{1-x}N$ alloys, particularly with high indium molar fraction, due to the large difference between growth temperature of InN and GaN, the inaccuracy and uncertainties in determining the indium composition, and the presence of multiple phases within the same structure, exists for the $In_xGa_{1-x}N$ material system. Therefore, the fundamental physics related to the different phases of $In_xGa_{1-x}N$ materials has not been well developed, as some of the physical and chemical properties such as the band gap, lattice parameters, elastic constants, effective electron mass, are still estimated based on the two binary compounds, GaN and InN.

A severe drop of efficiency of $In_xGa_{1-x}N$ LEDs, especially green emitters (emitting wavelength $\approx$ 530 nm and therefore having more than 40% indium content), on increasing injection current through the LEDs, is a long-standing problem for this particular alloy system and popularly known as the "Green Gap". The bandgap of $In_xGa_{1-x}N$ with

indium composition is found to vary nonlinearly and researchers have introduced "bowing parameter" to incorporate the nonlinearity in the linear Vegard's law of bandgap. The value of bowing parameter applicable for the whole composition range of indium is not yet concluded and reported values are in the range from 1.0 eV to 6.0 eV. The origin of luminescence is also observed to be ambiguous. People have observed multiple peaks in PL spectra and nonlinear dependence of PL peak position with temperature, which does not follow Varshni's equation of bandgap. The linear increase of Stoke's shift with the decrease of bandgap of $In_xGa_{1-x}N$ is also reported. All these phenomena have been explained in terms of the presence of high indium content $In_xGa_{1-x}N$ quantum dot like structures within the $In_xGa_{1-x}N$ matrix having lower indium composition. All of these complicate the emission properties in the material, which directly affects the fabrication of high-performance and reliable optoelectronic devices with the desired optical properties.

Recently, the growth of nanostructures has become very popular in the scientific community as low-dimensional structures offer some inherent advantages e.g. reduced defect density, higher light extraction efficiency due to large surface-to-volume ratio, weaker piezoelectric polarization field due to reduced strain distribution, etc., and most importantly change in the density of states with dimension. Thus, looking at the several advantages of nanostructures, we wanted to address the existing issues of $In_xGa_{1-x}N$ by the growth of nanostructures. In order to understand how different growth parameters (e.g. Growth Temperature, indium and gallium flux-rate, Nitrogen Flow-rate etc.) affect the morphology, structure and optical properties of the $In_xGa_{1-x}N$ material system, we have done systematic experiments by varying the growth parameters on *c*-sapphire substrates. The grown films are probed by using several complementary characterization tools to understand the various reasons for the variation of indium composition, epitaxial relationships and bandgap. We have also studied the $In_xGa_{1-x}N$ growth on two other important substrates viz. Si(111) and GaN Nanowall Network template grown on *c*-sapphire, to understand the epitaxy and morphology of the films.

The work in the present thesis is organized in the following chapters:

Chapter 1 gives a brief introduction to the III-nitride material system and discusses the importance and development of their wide range of applications by different researchers. It also includes information regarding crystal structure of III-nitrides along

with different substrates and growth techniques employed to grow thin films of III-nitrides. Some of the commonly observed thin film nucleation and growth modes are also mentioned in this chapter in the context of III-nitride film growth.

Chapter 2 deals with the literature overview of the research performed on $In_xGa_{1-x}N$, which includes the historical background of $In_xGa_{1-x}N$ growth, different growth kinetics, material and optical properties and the problem of indium segregation and piezoelectricity in this alloy system. Difficulty of growth of $In_xGa_{1-x}N$ films and variation of structural and optical properties with different growth parameters are reviewed in detail, which brings out the challenges that confront the growth of the $In_xGa_{1-x}N$ material systems, and provides the motivation to undertake this work.

Chapter 3 provides the details of the various experimental techniques employed in this study. It begins with the basic information of the Plasma Assisted Molecular Beam Epitaxy (SVTA-USA) growth system, which includes Effusion Cells, Nitrogen RF-Plasma Source, Residual Gas Analyzer and Reflection High Energy Electron Diffraction set up. Then the details of various characterization tools such as, Field Emission Scanning Electron Microscope, High Resolution X-ray Diffraction, Ultraviolet-Visible-Near-Infrared Spectroscopy, Photoluminescence and Cathodoluminescence Spectroscopy, X-ray Photoelectron Spectroscopy and Hall Effect Measurements, are also discussed.

Chapter 4 contains the work which discusses the growth of $In_xGa_{1-x}N$ nanostructures on *c*-sapphire using different growth parameters e.g. growth temperature, metal (indium and gallium) and nitrogen fluxes and describes the effects on the morphology, crystal quality, indium incorporation and optical properties of the grown films. The grown morphology is mostly 3D as we have maintained high V/III-ratio in all the growths and it has been observed that the morphology strongly depends on the growth parameters. Low growth temperature, lower gallium flux and higher V/III ratio is found to be suitable for suppression of phase separation and increase of indium incorporation in $In_xGa_{1-x}N$ grown on $Al_2O_3(0001)$. It has also been observed that higher indium incorporation leads to 30° in-plane rotation among the grown crystals. Under high V/III BEP ratio $In_xGa_{1-x}N$ phase with $\approx 60\%$ indium content has been achieved and room temperature emission has been observed. Possible growth mechanism and consequent morphology has been discussed wherever possible and the observed structural and optical properties of the grown

films are explained in accordance with the growth conditions.

Chapter 5 discusses the growth of InN and $In_xGa_{1-x}N$ nanostructures on different modified Si(111) surface while monitoring the consequent effects on the morphology, crystal quality, indium incorporation and optical properties of the grown films. In the first part, indium induced superstructural phases of Si(111) substrate has been utilized to grow good quality and epitaxial InN at lower temperature than conventionally used in MBE. Further, InN films are grown at a slightly higher temperature on those low temperature grown templates and show better crystal quality than the templates themselves. In the next part, growth of $In_xGa_{1-x}N$ on both bare and nitrided Si(111) surface at different growth temperature has been discussed. Surface nitridation of Si(111) surface has been found to increase the indium incorporation and improve the epitaxy of the overgrown $In_xGa_{1-x}N$ films.

Chapter 6 talks about the growth of InN and $In_xGa_{1-x}N$ nanostructures on GaN Nanowall Network (NWN) template, which is grown on *c*-sapphire and describes the effects on the morphology, crystal quality, indium incorporation within the lattice and optical properties of the grown films. In the first part, spontaneous growth of high quality InN nanorods with very high mobility ($\approx$ 4453 cm^2/V-sec) and low carrier concentration ($\approx$ 1.1×10^{17} cm^{-3}) on GaN NWN is shown. In the next part, GaN NWN template is utilized to spontaneously grow $In_xGa_{1-x}N$ NWN, which shows good structural, morphological and optical quality.

Chapter 7 summarizes the contents of the present thesis and draws conclusions from the observed results. Overall, the thesis is a systematic approach to understand the growth of $In_xGa_{1-x}N$ with different morphology as well as to obtain different indium compositions without phase separation. This chapter also provides a brief outlook for the future direction for research as an outcome of the present work.

Highlights of The Thesis

The most important and significant observations made in the present work have been listed below:

- Low growth temperature, low gallium flux and high V/III ratio is found to be suitable for forming $In_xGa_{1-x}N$ on *c*-sapphire with suppression of phase separation and increased indium incorporation. [**Publication**: Materials Research Express **1**, 035019 (2014), Journal of Physics D: Applied Physics **49**, 355304 (2016)]

- Under high V/III BEP ratio, $In_xGa_{1-x}N$ phase with $\approx$ 60% indium content has been achieved, for which room temperature CL emission has been observed.

- *in-situ* Surface modification of Si(111) substrate has been utilized to grow good quality InN on the indium induced Si(111)-1×1 superstructural phase, at lower temperature than conventionally used in MBE, due to the smallest lattice mismatch of 8% between the InN unit cell and 1×1 surface reconstruction, as compared to other observed superlattices. [**Publication**: Physica Status Solidi A **210**, 2409 (2013)]

- Surface nitridation of Si(111) surface is found to increase indium incorporation in $In_xGa_{1-x}N$ films upto 30%. [**Publication**: Journal of Applied Physics **118**, 025301 (2015)]

- Very high mobility and dislocation free InN nanorods have been grown on a GaN Nanowall Network template, that show very high electron mobility ($\approx$ 4453 cm^2/V-sec) and low carrier concentration ($\approx$ 1.1×10^{17} cm^{-3}), which can be a very appropriate material for terahertz emission and detection. [**Publication**: Journal of Applied Physics **119**, 205701 (2016), IEEE Conference Proceedings, 1-5 (2014)]

- Spontaneous growth of $In_xGa_{1-x}N$ Nanowall Network has been demonstrated on GaN Nanowall Network, which shows $\approx 7\%$ indium incorporation in the InGaN NWN film and the epitaxial relationship between the grown films and substrate is $(0001)_{InGaN} \parallel (0001)_{GaN} \parallel (0001)_{Sapphire}$ and the 7% indium content phase is stable in the sample, which emits at 3.02 eV at RT.

Contents

List of Figures

List of Tables

Acronyms

AFM	Atomic Force Microscopy
AP-MOCVD	Atmospheric Pressure Metal Organic Chemical Vapor Deposition
BEP	Beam Equivalent Pressure
CL	Cathodoluminescence
CPS	Counts Per Second
CW	Continuous Wave
DFT	Density Functional Theory
EDS	Energy Dispersive X-ray Spectroscopy
EL	Electroluminescence
ELOG	Epitaxial Lateral Overlayer Growth
EPMA	Electron Probe Microanalysis
EQE	External Quantum Efficiency
FESEM	Field Emission Scanning Electron Microscopy
FIB	Focused Ion Beam
FM	Frank-van der Merwe
FWHM	Full Width at Half Maximum
HCP	Hexagonal Close Packed
HEMT	High Electron Mobility Transistor
HFET	Heterostructure Field Effect Transistor
HRXRD	High Resolution X-ray Diffraction
IC	Integrated Circuits
ICP-RIE	Inductively Coupled Plasma Reactive-Ion Etching
IDT	Interdigital Transducer
IQE	Internal Quantum Efficiency

K-cells	Knudsen effusion cells
LD	Laser Diode
LED	Light Emitting Diode
LEEBI	Low Energy Electron Beam Irradiation
MBE	Molecular Beam Epitaxy
ML	Monolayer
MOCVD	Metal Organic Chemical Vapour Deposition
MQW	Multiple Quantum Well
NR	Nanorod
NW	Nanowire
NWN	Nanowall Network
OT	Optical Transmission
PAMBE	Plasma Assisted Molecular Beam Epitaxy
PBN	Pyrolytic Boron Nitride
PES	Potential Energy Surface
PL	Photoluminescence
PR	Photoreflection
PVD	Physical Vapor Deposition
QCSE	Quantum-Confined Stark Effect
QD	Quantum Dot
QMS	Quadrupole Mass Spectrometer
QW	Quantum Well
RBS	Rutherford Backscattering Spectroscopy
RGA	Residual Gas Analyzer
RHEED	Reflection High Energy Electron Diffraction
RIE	Reactive-Ion Etching
RMS	Root Mean Square
RSM	Reciprocal Space Mapping
RT	Room Temperature
SAED	Selected Area Electron Diffraction
SAG	Selective Area Growth

SAW	Surface Acoustic Wave
SCLC	Space Charge Limited Current
SIMS	Secondary Ion Mass Spectroscopy
SK	Stranski-Krastanov
SQW	Single Quantum Well
TEM	Transmission Electron Microscopy
UHV	Ultra High Vacuum
UV-Vis-NIR	Ultraviolet-Visible-Near-Infrared
VCSEL	Vertical Cavity Surface Emitting Laser
VLS	Vapour-Liquid-Solid
VPE	Vapour Phase Epitaxy
VW	Volmer-Weber
XPS	X-ray Photoelectron Spectroscopy
XRD	X-ray diffraction
YAG	Yttrium Aluminium Garnet
0/1/2/3D	Zero/One/Two/Three Dimensional
2DEG	Two-Dimensional Electron Gas

Chapter 1

Introduction

This chapter describes the importance of Group-III nitrides and their applications. It discusses the crystal structure of Group-III nitrides grown on various substrates. The techniques used to grow semiconductor thin films and the growth mechanisms involved are also discussed.

1.1 A brief introduction to Group-III Nitrides

In the 'Semiconductor Age' in last 50 years, our views, our attitudes and our way of living have been modified by the research and technological advancements made in electronic materials. Tools and gadgets like personal computers, mobile phones and Light Emitting Diodes (LED) based lighting and display gadgets, are just some of the examples among the vast number of electronic devices we use in our day to day life. In this context, the nitride based LED and Laser Diode (LD) are clear examples: the blue LED was the result of a technological breakthrough in 1994 which led to a revolution in optoelectronics, for which the prestigious Nobel prize of 2014 was awarded to Shuji Nakamura, Hiroshi Amano and Isamu Akasaki.

Group-III nitride semiconductors (InN, GaN, AlN and their alloys) represent a unique family of materials for the development and mass production of numerous electronic and optoelectronic devices. The remarkable properties are well studied and several books[1,2] and review articles[3–14] have been published in the literature. The first important property is their direct bandgap spanning from 0.64 eV(InN)[15] to 6.015 eV(AlN)[16] at

room temperature (RT), which should allow absorption, emission and detection of wavelengths ranging from infrared to deep ultraviolet. This is in a contrast to the (Ga,Al)As based LEDs (1.5 - 2.2 eV) or (Al,Ga,In)P based LEDs (1.3 - 2.5 eV) that cover only the IR to yellow region of the electromagnetic spectrum (Figure 1.1).

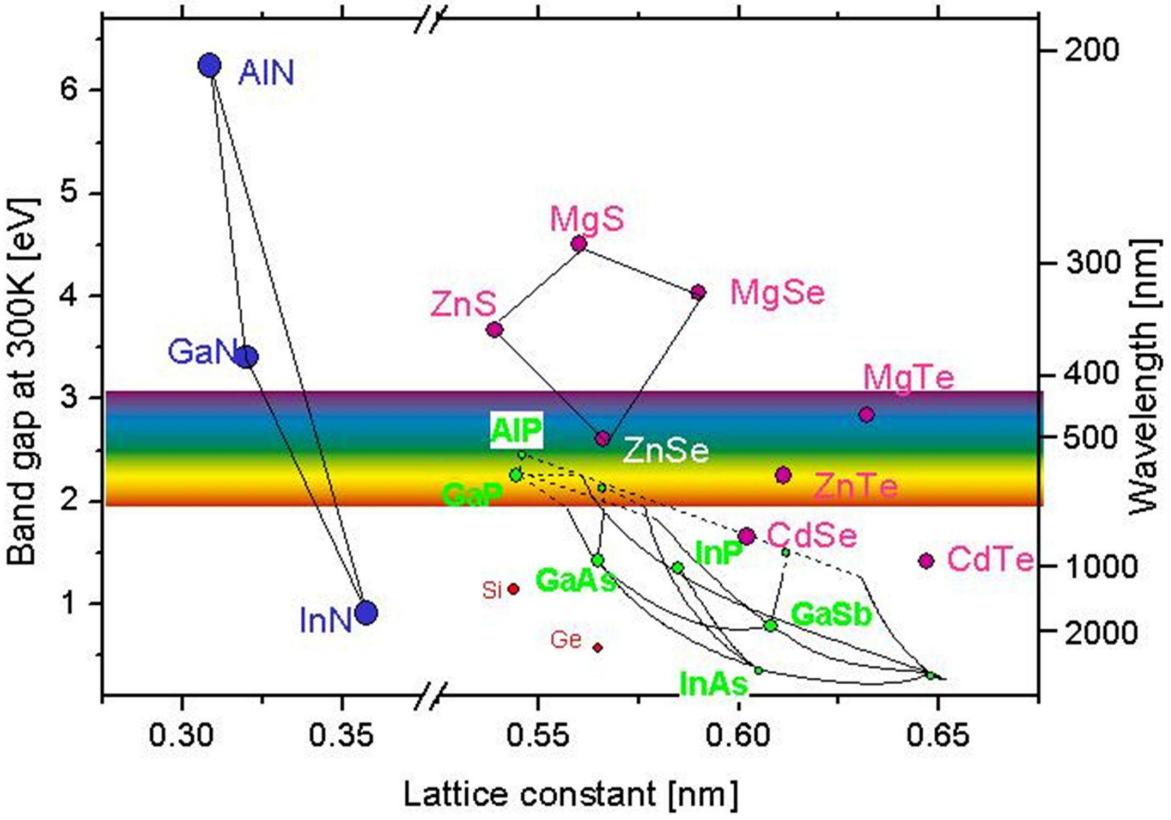

Figure 1.1: shows RT bandgap energy versus lattice constant of III-nitrides and other compound semiconductors.[†]

The other advantage of the III-nitride semiconductors is their strong chemical bond, having a mixture of covalent and ionic nature, which makes them very stable and resistant to degradation under high electric currents and high temperatures. Their high thermal and mechanical stability, large piezoelectric constants, or spontaneous polarization make them good candidates for the fabrication of electronic and optoelectronic devices, able to operate at high temperature, high frequency and high power densities, which open up applications in a wide range of areas including full colour displays, high density optical information storage, solid state lighting, sensors and diagnosis, RF amplifiers and power electronics.[17] As evident from Figure 1.1, the system provides a great opportunity for

[†] http://www-opto.e-technik.uni-ulm.de/lehre/cs/

bandgap engineering by alloying the indium or aluminium into GaN, to yield desired direct bandgap ranging from 0.64 eV to 6.12 eV.

In 1938, Juza *et al.* first reported the synthesis of GaN and InN crystallites.[18] GaN was formed by flowing Ammonia over hot gallium, and the InN from the reduction of $InF_6(NH_4)_3$. This study was focussed to measure lattice parameters of the synthesized materials and little importance was given to their optical properties at that stage. After almost 30 years, Maruska *et al.* first grew GaN layers by vapour phase deposition on sapphire substrates which increased the interest in the nitrides.[19] Following this report, blue LEDs based on GaN:Zn/nGaN structures were produced by Pankove *et al.*[20] on vapour phase grown GaN, where the structures relied on hot carrier injection from avalanche breakdown to generate holes.

Despite subsequent advances in growth, p-type GaN proved elusive and it was not until 1989 when Amano *et al.* succeeded in reliably producing p-type GaN by Mg doping.[21] Research carried out at Nichia Chemical Industries by Nakamura *et al.* utilised Mg doping to form p-n junctions, and produced at the time, the brightest blue LEDs made from any material system.[22–24] Blue and green LEDs were then commercialized by Nichia Chemical Industries and others. Akasaki *et al.* and Nakamura *et al.* subsequently produced the first LDs based on III-nitride material system.[25] Since then, the progress has continued at a remarkable rate, with increasing number of research groups contributing to the science and technology of III-nitrides.

In the early 1990s, it was discovered that the III-nitride materials exhibit strain induced and spontaneous piezoelectric polarization effects. This lead to the demonstration of the 2-Dimensional Electron Gas (2DEG) at an $Al_xGa_{1-x}N$/GaN polar heterostructure and also the demonstration of an $Al_xGa_{1-x}N$/GaN High Electron Mobility Transistors (HEMTs).[26,27] In 2001, use of the ternary InAlN was proposed,[28] in order to replace AlGaN and improve the reliability of HEMTs. Recent efforts have focused on improving the efficiency of nitride based LEDs and LDs by extending the range of wavelengths over which they operate. Added effort has also been applied to HEMTs based on nitride hetero-junctions.[29] In 2002, Nichia announced the development of high power InGaN LEDs for white, blue and green light emission with an expected lifetime of 100000h. Therefore, starting from the hetero-structure LED and LD up to HEMT, all devices are

now investigated using the nitride compounds and their alloys.

The success of the nitride system for light emitting devices has been somewhat of a mystery. Other commercially successful LED and LD technologies incorporate the use of native substrates for epitaxy, which is insufficient in case of the nitrides as it is difficult to make bulk single crystals of nitrides and they are very expensive as well. Native substrates are a distinct advantage as they provide a perfect lattice match for growth of epitaxial layers and thus avoid the problem of misfit dislocations which inevitably form when growing on a lattice mismatched substrate. These dislocations are known to act as non-radiative recombination centres in III-V semiconductors. For example, GaAs and InP devices containing 10^8 - 10^9 dislocations/cm^2 (the common level of dislocations found in nitride based devices) would have luminescence quenched almost entirely by recombination at the dislocations, on the contrary III-nitrides can emit considerably even after containing high density of dislocations.[7] One theory used to describe the tolerance of nitrides for high levels of dislocations has been in terms of compositional fluctuations. indium rich regions within the active quantum well (QW) regions can act as quantum dots (QDs), localizing electrons and holes spatially and enhancing the probability that they will recombine radiatively. Once trapped in the QD, the carriers are also prevented from moving to dislocation sites and recombining non-radiatively.[30,31] Thus, lot needs to be done to exploit the theoretical potential of the III-nitrides to develop high efficiency optoelectronic devices.

1.2 Applications of Group-III Nitrides

1.2.1 LEDs and Displays

Efficient radiative recombination in direct bandgap III-nitride semiconductors has permitted the development of light-emitting devices, and the LED technology has advanced from an exploratory research stage to industrial fabrication and application within a surprisingly short time. Since the LED is a simple, rugged, long-lived and inexpensive device, which efficiently converts electrical energy into light, it has an expanding number of diverse applications in displays, lighting, indicator lights, traffic signs and signals, as light sources for accelerated photosynthesis, and in medicine for diagnosis.

Most of the research has been done to develop high brightness blue-LEDs for use in full colour displays and indicators, and for these purposes, II-VI materials such as ZnSe[32], SiC[33] and III-V nitride semiconductors have been investigated. The lifetime of II-VI based devices is still short and this has hindered commercialization of II-VI optoelectronic devices. The p-type conduction of Mg-doped GaN was realized for the first time by Amano *et al.*[34], by low-energy electron beam irradiation (LEEBI), where the electroluminescence (EL) spectrum of the LED showed a strong near-band-edge UV emission ($\approx$ 370 nm). A blue p-n-LED (Si:GaN/Mg:GaN) was developed by Nakamura and co-workers in 1991,[22] where the peak wavelength and the FWHM of the observed EL were 430 nm and 55 nm, respectively, with the output power of 42 μW and the external quantum efficiency (EQE) of 0.18%.

Further improvement in the blue LED was the growth of a 20 nm thick Si:$In_{0.2}Ga_{0.8}N$ active layer between the n- and p-type GaN films, where the p-GaN/n-InGaN/n-GaN double-hetero-structure LEDs had an output power of 125 μW with an EQE of 0.22% and the EL had a peak wavelength of 440 nm and a FWHM of 180 meV.[35] Then a high-brightness InGaN/AlGaN double-hetero-structure LED with output power of 1500 μW, and an efficiency of 2.7% was also reported.[36] Until 1994 a blue LED with a brightness more than 1 candela (cd) had not been fabricated, and then Nakamura reported highly efficient InGaN/AlGaN double-hetero-structure LEDs with an EQE of 5.4%, fabricated by co-doping Zn and Si into the InGaN active layer.[37] Si and Zn incorporation was used to create donor and acceptor levels, respectively, which enhanced the radiative recombination and reduced the energy difference between the electron and hole states to $\approx$ 2.8 eV, emitting in blue-violet region of the visible spectrum. Later on, green and yellow LEDs were fabricated by increasing the indium fraction of the InGaN active layer, where, without using Zn or Si, the active region of the LEDs was formed by a single quantum well (SQW) structure with a thin InGaN layer, as it was possible to vary the indium content over a wide range by growing very thin InGaN layers, and the doping by Si and Zn was also could be avoided, without a reduction of the efficiency. Nakamura *et al.* also introduced a white LED, consisting of a blue LED, similar to the LEDs already described, and packaged with a yttrium aluminium garnet (YAG) phosphor to convert blue light into white light. That white LED had an EQE of 3.5% and an output of 1 mW.

Recently, InGaN-based MQWs yellow light-emitting LEDs have been grown on Si substrate,[38] where blue MQWs are introduced as strain modulation layers for yellow MQWs, which exhibits much better performance than samples without strain modulation layers. As a result, LEDs based on this structure emit yellow light (566 nm) with 9.4% external quantum efficiency (EQE) and 72 mW light output power at 35 A/cm^2 under RT, and reaches a peak EQE of 22.2% at 0.07 A/cm^2, signifying that long-wavelength emission of InGaN system can be realized if the strain of MQWs is properly modulated. Yellow/amber (570-600 nm) emitting InGaN/AlGaN/GaN MQWs grown on GaN/sapphire template has been reported,[39] where it has been observed that the high compressive strain in InGaN/GaN MQWs can be compensated by the tensile strain of AlGaN layers in the barriers, which also increases the internal electric field and improves the radiative efficiency at RT with a red-shift. N-polar (000$\bar{1}$) InGaN LEDs with emission wavelengths ranging from 444 to 633 nm under a constant current of 20 mA has been achieved by changing the growth temperature of QWs from 880 to 790 °C.[40] InGaN based red LED grown on *c*-sapphire substrates has been demonstrated,[41] where AlGaN interlayer with 90% aluminium content has been embedded within the InGaN MQW active layer to reduce the additional 430 nm emission related to the phase separation of the InGaN QWs. The light output power and external quantum efficiency are 1.1mW and 2.9%, respectively, for 629 nm at a dc current of 20 mA. Semipolar InGaN/GaN MQWs has been grown on low defect (11$\bar{2}$2) GaN templates fabricated on *r*-sapphire,[42] where the emission wavelength is found in the range of 450 – 550 nm. Semipolar InGaN SQW LEDs emitting in the green, yellow-green, yellow and amber spectral range has been grown on semipolar (11$\bar{2}$2) GaN on micro-rod array templates, fabricated on (11$\bar{2}$2) GaN grown on *m*-sapphire.[43] These LEDs show reduction in efficiency droop, injection current induced blue-shift of emission and QCSE in the crystal, compared to commercial *c*-plane LEDs.

Thus, solid state white LEDs (having no filament, therefore, no need for vacuum) are suitable for applications where small light bulbs are used. They are promising because of the longer lifetime and better conversion efficiency of electric power to visible light (reduced power consumption) as compared to incandescent lamps. Right now white LEDs are used in large arrays in displays and back-lighting in television sets, mobile phones etc.

1.2.2 Transistors

HEMTs are a particular type of transistors, made up of Group-III nitride semiconductors which utilizes the hetero-junctions for their operation. The hetero-junctions in these devices are formed between semiconductors of different compositions and bandgaps, in contrast to the conventional Si and GaAs-based field effect and bipolar devices, where junctions between same materials are used, e.g. n- and p-type Si in a bipolar transistor. With hetero-junctions, device makers can design the band structure (and therefore, the electric field) as well as the doping types and levels in specific parts of the device. As a result, these devices offer potential advantages in microwave, millimeter wave and high-speed digital integrated circuit (IC) applications over the homo-junction devices presently in use. Recently, AlGaN/GaN-based field effect transistors have shown great promise as a candidate for microwave power devices.[44] Theoretical simulations have predicted a high peak electron velocity of 2.7×10^5 m/s and a high saturation velocity of 1.5×10^5 m/s at electric fields of about 150 kV/cm in the AlGaN/GaN systems. Moreover, an electron mobility (μ_e) of $\approx$ 2000 cm^2/V-s has been calculated in the GaN channel at RT, at a carrier concentration of 10^{17} cm^{-3}.[45–49]

Gaska *et al.*[50] investigated two-dimensional electron transport in doped AlGaN/GaN hetero-structures and the highest measured Hall mobility of 2D electron gas in GaN at RT was found to be 2019 cm^2/V-s, which is much larger than for comparably doped Silicon ($\approx$ 500 cm^2/V-s) and about half of that for comparably doped GaAs ($\approx$ 4000 cm^2/V-s).[51] These high values of electron mobility are promising to make GaN and GaN-based hetero-structures for applications in microwave and millimeter wave devices, which can operate in a wide temperature range because of the wide energy gap and fairly good thermal conductivity (1.3 W/cm-K[52]). The small electron mobility, compared to GaAs leads to higher source and drain parasitic series resistances, a lower cutoff frequency, and a lower maximum frequency of operation. However, GaN-based transistors have demonstrated outstanding characteristics, such as high maximum current, transconductance, breakdown voltages, and reasonably high cutoff frequencies.[53–57] The large currents and voltages required for high-power applications of transistors lead to self-heating effects and thus, causes power dissipation problems. One commercially available but may not be the best possible solution is the growth of AlGaN/GaN structures on SiC substrates, where the

maximum dissipated DC power is at least three times higher than in similar devices grown on sapphire, due to the effective heat sinking through a SiC substrate, which has a high thermal conductivity.[58]

Analysis of the measured electron concentration profiles, obtained by Yu *et al.*[59], for AlGaN/GaN FETs, reveals the presence of a high sheet carrier density in the GaN channel of a nominally undoped $Al_{0.15}Ga_{0.85}N$/GaN transistors, which may be explained as a consequence of piezoelectrically induced charges present at the AlGaN/GaN interface. Thus, electric field induced by spontaneous and piezoelectric polarization, can lead to an increase or decrease of the electron sheet concentration in the channel of the transistor, depending on the polarity of the hetero-structure. In the case of an increase, it has been estimated that the piezoelectric field and channel doping can result in an electron sheet concentration as high as 10^{13} cm^{-2}, which will confine the carriers more closely to the AlGaN/GaN interface (hence, closer to the gate contact) and in turn will reduce the turn-off voltage of the transistor. Thus, the AlGaN/GaN-based HEMTs show the great potential of the Group-III nitrides to be explored as the desired material for the fabrication of high-temperature and high-power devices.

1.2.3 Lasers

Presently, most of III-V nitride research is focussed on the realization of vertically emitting semiconductor LD by electrical pumping to get shortest wavelenghts. These diodes operates in the blue and near-UV spectral range, and thus, are useful in a variety of applications requiring high resolution, such as high-speed laser printers, scanners, high-density optical data storage devices and also for optical communication. Optically pumped stimulated emission and laser action was observed near 3.45 eV in single-crystal GaN needles with electron concentrations higher than 10^{19} cm^{-3} by Dingle *et al.*[60] for the first time. Optical gain as high as 10^5 cm^{-1} were achieved for the highest pumping powers.

The development of efficient nitride LEDs has motivated many researchers to work towards the optimization of LD structures of GaN on both *a*-face and *c*-face sapphire. Nakamura's very important work was that he obtained cleaved facets while growing on *a*-face sapphire[61], as the *r*-face cleavage facet is perpendicular to this surface. The cleaved facets of the epitaxial layers (LD) and the substrate were mirror-like and was used as laser

cavity mirrors. Nakamura *et al.*[62] also demonstrated continuous wave (CW) operation at 233 K using a MQW structure consisting of three 40 $\AA$ thick undoped $In_{0.2}Ga_{0.8}N$ well layers as the gain medium, which are separated by 80 $\AA$ thick undoped $In_{0.08}Ga_{0.92}N$ barrier layers. A differential quantum efficiency of 8% per facet and an output power of 9.5 mW per facet were obtained at a current of 250 mA and an operating voltage of 14 V. However, these LDs lasted for very short period of times and were getting destroyed within one second of operation at RT due to enormous heat generation, whereas, the lifetime was longer than 30 minutes when operated at 233 K.[62]

The structural quality and the current threshold and lifetime of the laser structures were found to be drastically influenced by the difficulties of growing the thick AlGaN cladding layers required for optical confinement, due to the formation of cracks during growth and the high dislocation density inside the active region of the LDs. Therefore, in order to prevent the formation of cracks and dislocations due to the lattice mismatch between AlGaN and GaN, strained layer super-lattices were grown instead of one thick AlGaN cladding layer.[63] Further reduction of the dislocation density was achieved by growing the LD on top of a lateral epitaxial overgrown substrate.[64] Under RT CW operation and with a constant output intensity of 2 mW per facet, the best laser structure showed a lifetime of more than 3000 h. The commercial success of reliable production of blue LDs with such a long lifetime and high output intensity has enabled their implementation as optical storage devices, optical sensors and scanners and many other products.

1.2.4 Detectors

UV light ($\lambda < 400$ nm) detection has a wide range of commercial applications, such as, flame and heat sensors, UV calibration devices, plasma diagnostics, engine monitoring and secure inter-satellite communications, etc.[65] The main requirement of most of these applications is a solar blind detector, one which detects only in the UV, but does not sense wavelength longer than 280 nm. UV detection is traditionally done using a photomultiplier tube or Silicon p-i-n photodiode, but both of them have some shortcomings. Thus, the next generation of UV detectors should be fabricated using wide direct bandgap semiconductors ($E_g > 3.0$ eV) and one such promising material system being investigated

for this application is GaN and $Al_xGa_{1-x}N$. The first high-quality GaN photoconductive detectors were fabricated by Khan *et al.*[66], where the spectral responsivity of GaN rises quickly at 365 nm and then remains constant down to 200 nm and also the response is linear over five orders of incident radiation power, which is important for sensitive UV light measurements over a great range of intensity.

Hexagonal AlGaN is also considered to be another promising material for UV detectors due to some unique features like, sharp cutoff wavelength, high quantum efficiency, ease of changing the cutoff wavelength of AlGaN by varying Aluminium composition. Therefore, AlGaN-based hetero-structures can be used to fabricate sensitive, tunable and inexpensive detectors working in the near-UV spectral region. One of the critical issues relevant to these detectors is the electrically active defects which traps the charge and causes high dark currents, DC drift and slow response time. However, over the last few years very high quantum efficiencies, low dark currents and high speeds have been achieved for this material system.[67]

Relatively fast photovoltaic UV detection using GaN p-n and p-i-n diodes or Schottky diodes has been demonstrated by many groups.[68–70] Xu *et al.*[70] investigated the spectral response of front-surface illuminated GaN and AlGaN/GaN p-i-n UV photodetectors prepared by MBE on sapphire. The AlGaN/GaN photodiodes had a maximum zero-bias responsivity of 0.12 A/W at 364 nm with extremely fast decay times between 12 and 29 ns were determined, which enable operation for technical applications at sufficient high frequencies. Zhang *et al.*[71] reported a self-filtering photodetector, consists of a 0.5 μm thick n-GaN layer and a 2 μm thick p-GaN layer, which shows very sharp spectral response. Utilizing backside illumination, photons with energy between 3.45 eV and 6.2 eV are absorbed within the first 100 nm of the n-GaN layer, because of the high absorption coefficient of GaN ($\approx 2\times10^5$ cm^{-1} above the bandgap). The minority carriers recombine before reaching the p-n junction depletion region, due to their smaller diffusion length compared to the thickness of the n-GaN region, and thus produce no photocurrent. Light having an energy very close to the bandgap of GaN can penetrate deeper into the device and reach the depletion region, forming electron-hole pairs which in turn produce photocurrent. As a result, the responsivity of this detector is essentially tuned to the bandgap of GaN. Now, by adding indium or Aluminium to the GaN in this detector, it

is possible to shift this response to longer or shorter wavelengths, to obtain blue and UV detectors which are only sensitive in a small wavelength range. Detectors with such a high sensitivity and responsivity can be used as flame and gas sensors.

1.2.5 Surface Acoustic Wave Devices

Due to the availability of greater bandwidths, communication systems, such as portable telephones, mobile telephones and broadcasting satellites, are moving towards higher frequency bands. Traditionally, dielectric ceramic and surface acoustic wave (SAW) devices are used for these frequency applications, such as filters, duplexers and resonators. Recently, piezoelectric SAW devices have become popular on account of their stable characteristics, lack of need for adjustment and compactness.[72] Thin film piezoelectric materials are being used in the field of microwave acoustics for a long time with the earliest application in bulk wave transducers. Such materials, like preferentially oriented layers of ZnO[73], with the c-axis parallel to the direction of wave propagation, were found suitable to efficiently generate bulk acoustic waves. The required characteristics for microwave generation material are: high sound velocity, very smooth surface, large electromechanical coupling factor, small transition loss and high temperature stability. Group-III nitrides, especially AlN, have been considered to be a promising thin film piezoelectric material for the fabrication of on-chip acoustic wave devices.[74] Epitaxial films grown by MOCVD or MBE have shown smooth surface morphology and some promising acoustic properties.[75–77] Inside a SAW device, due to the converse piezoelectric effect, an electric rf signal applied to an interdigital transducer contact (IDT) produces mechanical stress in the film under the IDT, which causes a periodic mechanical displacement accompanied by an electric field, which then travels as a Rayleigh-type wave along the surface. When the propagating SAW reaches the receiving IDT, the piezoelectric effect generates an electrical response that can be detected. A network analyzer can be used to measure the transfer function of this set-up. By using the simple arrangement of two-finger contacts and one Group-III nitride film or crystal, high-quality electrical filters can be created.

By using epitaxial AlGaN films (grown on sapphire), the propagation velocity of the SAW and the frequency f_{max} of the transfer function can be changed by varying the Aluminium content of the piezoelectric film.[78] AlN-based SAW devices[79] in particular

have reached frequencies, electro-mechanical coupling factors, transition losses and high-temperature stabilities which seem to be very useful for technical applications such as cheap electrical filters, sensors (viscosity of fluids, gases) or photorefractive grids.

1.2.6 Photovoltaics

Since the first proposal to use InGaN for solar cell applications[80], significant efforts and progress have been made toward this goal, though great opportunities and grand challenges exist together. InGaN has the following advantages for solar cell applications: (i) bandgap is continuously tunable within the energy range of the solar spectrum; (ii) superior resistance against high-energy particle radiation, especially suitable for space applications; (iii) advantageous band alignment with respect to Si, so that a recombination junction naturally exists for cells using a Si base.

Till date, the maximum solar energy conversion efficiency ($\approx$ 43%) is achieved in triple-junction cells, which is based on three different semiconductors having fixed bandgaps and nearly matched lattice constant, Ge (0.7 eV), GaAs (1.4 eV), and GaInP (1.9 eV). In order to attain more than 50% conversion efficiencies using the multi-junction concept, four or a higher number of junctions are needed and finding materials with the required bandgap becomes a major challenge in this case. For example, from detailed balance modeling, for an ideal four-junction solar cell that can reach $\approx$ 62% theoretical efficiency, a tandem of junctions with bandgaps of 0.6, 1.11, 1.69, and 2.48 eV is required.[81] In this case, the InGaN alloys allow fine tuning in the performance of these cells by offering flexibility in the choice of the bandgaps.[82]

For double-junction cells, the maximum theoretical efficiency is about 39% where the two junctions are composed of two semiconductors with bandgaps of 1.1 and 1.75 eV.[83] Silicon has a bandgap of 1.1 eV, which is ideally suitable for the bottom junction, whereas, $In_{1-x}Ga_xN$ has a bandgap of 1.75 eV when $x \approx 0.5$. Therefore, a tandem structure of p-$In_{0.5}Ga_{0.5}N$/n-$In_{0.5}Ga_{0.5}N$/p-Si/n-Si would form a high-efficiency double-junction cell. An additional benefit of this structure comes from the band alignment between InGaN and Si[84], as the VBM of Si lines up with the CBM of $In_{1-x}Ga_xN$, at $x \approx 0.5$.[80] Therefore, the n-$In_{0.5}Ga_{0.5}N$/p-Si interface would be a low-resistance Ohmic junction, acting as a natural "recombination junction" connecting the top and bottom

cells, and thus, heavy doping of the interface, normally required for multi-junction cells, is not necessary in this case. Hsu and Walukiewicz calculated[84] the theoretical efficiency of such a double-junction cell, using an analytical model developed by Kurtz *et al.*[83], and found that double-junction InGaN/Si solar cells can have energy conversion efficiency of more than 31% when high-quality materials are used. Adding an InGaN junction on top of low quality, polycrytalline Si can increase the efficiency by more than 50%. Adding a second InGaN junction with an appropriate composition can provide further enhancement to the efficiency. A three-junction $In_{1-x}Ga_xN/In_{1-y}Ga_yN$/Si solar cell could offer energy conversion efficiencies exceeding 35%.[84] In addition, graded-bandgap solar cells have been explored with the InGaN system.[85,86]

Fabrication of these multijunction cells faces major challenges, which includes lattice mismatch, p-type doping, phase separation, and surface states. $In_{1-x}Ga_xN$ (0001) has a lattice mismatch with Si(111) between 8% (when $x = 0$) and 16% (when $x = 1$) and therefore, to achieve good film quality, a thin Si_3N_4 or AlN layer is used as a buffer. InN films[87–93] and nanowire (NW) arrays[89,94,95] have been grown epitaxially on Si substrates using MBE or MOCVD.[96–98] However, it is not clear whether these structures currently have materials quality suitable for high-performance photovoltaics. Similar issues exist in case of the $In_{1-x}Ga_xN/In_{1-y}Ga_yN$ cell and graded-bandgap cell. p-type doping of InN and indium-rich InGaN is still in the early stage, and a p-n junction has yet to be demonstrated. However, fabrication of gallium-rich InGaN cells has been attempted by several groups[99–101] but increase in indium composition leads to leaky junctions with poor photovoltaic performance.[100] Phase separation in InGaN is detrimental to the device performance because it reduces the short-circuit current by generating recombination centers, and reduces the open-circuit voltage through bandgap fluctuations. Jani *et al.* reported the fabrication of p-GaN/i-InGaN/n-GaN solar cells which show high open-circuit voltage and high internal quantum efficiency.[102]

Recent numerical simulations of InGaN p-i-n single junction solar cells reveals that band diagram, short circuit current density, open circuit voltage, and conversion efficiency strongly depend on indium content, thickness, and background doping of the unintentionally doped layer for both heterojunction and homojunction structures.[103] Same study also reports that the maximum efficiency of a p-i-n InGaN/GaN heterojunction

solar cell with low indium content is 11.3%, which drastically reduces for high indium content due to polarization effects, whereas, the maximum efficiency of InGaN single homojunction solar cells with optimized parameters is found to be $\approx$ 17%. A monolithic solar-photoelectrochemical cell based on InGaN/GaN MQWs has been fabricated, which directly generates hydrogen gas under zero bias using solar water splitting and shows excellent chemical stability of InGaN in aqueous solution of hydrobromic acid.[104] At zero bias, 1.5% solar-to-fuel conversion efficiency has been reported for the cell, under the irradiation by a simulated sunlight (1-sun with 100 mW/cm^2). Fabrication of InGaN/GaN MQW solar cells, operating at a wavelength of 520 nm and having nanostructures with a periodic nanorod or nanohole array has been reported.[105] Solar cells with periodic nanohole array structure is found to exhibit superior light absorption as compared to the one with a nanorod array structure, which results in a 51% enhancement of solar conversion efficiency over a wide spectral range of 330 – 500 nm. To minimize front surface reflections across a broad spectral range and maximize rear surface reflections only in the spectral range absorbed by the InGaN, InGaN/GaN MQW solar cells with a front-side anti-reflective coating and a back-side dichroic mirror has been fabricated, which makes them suitable for multijunction solar cell integration.[106] 56% enhancement in peak external efficiency and 37.5% enhancement in conversion efficiency has been obtained with that design. A short-circuit current density of 4.6 mA/cm^2 and an open-circuit voltage of 0.22 V with a power conversion efficiency of 0.5% under 1 sun, air-mass 1.5, illumination has been obtained for PAMBE grown InGaN nanorod solar cells.[107] The high current density is attributed to the nanorod configuration as it provides improved crystal quality due to its strain free nature and enhances light concentration. Introduction of a super-thin AlN layer between the active region and p-InGaN is found to act as a barrier to reduce tunneling of electrons, and also prevents the dislocations from threading into the p-InGaN layer.[108] Another study shows significant improvement in the photovoltaic performances of MBE grown GaN pn-junctions and InGaN solar cells, by adopting leak path passivation process using AlO_x,[109] and as a consequence the open circuit voltage under 1 sun illumination increases from 1.46 to 2.26 V for GaN pn junction, and from 0.95 to 1.27 V for InGaN solar cell.

1.2.7 Chemical Sensors

Surface states in InN and indium-rich InGaN tend to accumulate a high density of electrons over the depth of several nanometers from the surface, regardless of the bulk doping type.[110,111] The unusual electron accumulation and resulting band bending near the surface of InN and indium-rich InGaN are being exploited for chemical sensing devices. These electron properties are believed to be related to the particularly low conduction band minimum at Γ-point and the Fermi stabilization energy E_{FS} deep inside the conduction band. Since the location of Fermi level is below E_{FS}, downward surface band bending and electron accumulation in the near surface region can spontaneously occur.[112] For InN, the efforts to eliminate the surface electron accumulation effect by chemical or physical treatments have not been successful. The charged donor-type surface state density was found to be as high as the order of 10^{13} cm^{-2} (the largest native electron accumulation observed in III-V semiconductors).[110–113] Although the surface electron accumulation effect is detrimental to the realization of InN-based devices requiring both n- and p-type doping[114], the high surface charge density and chemically robust surface properties of InN are beneficial for sensor application. In principle, the positively charged surface donor states of InN should allow negatively charged ions in solutions to be selectively attracted to the InN surface.

Soon after the discovery of the narrow bandgap of InN, Lu *et al.*[115] reported a fast response of sheet carrier concentration and mobility to solvent exposures such as methanol and water. Pt-coated InN nanorods were found to change resistance upon exposure to H_2 but not to N_2 and O_2.[116] The InN surface has been functionalized by aminosilane molecules and used to bind negatively charged Au colloids.[117] Anion sensing using InN with remarkable selectivity, stability, response time, and repeatability was shown by Lu *et al.*[118,119] In all these experiments, InN is sensitive to anions but not cations, indicating that the sensing mechanism is based on positively charged surface states of InN attracting negatively charged ions in aqueous solutions.

1.3 Crystal Structure of Group-III Nitrides

The thermodynamically stable phase of InN, GaN and AlN, is the hexagonal wurtzite structure (α-phase), with four atoms per unit cell. The metal atom (Ga, Al or In), or cation, is surrounded by four nitrogen atoms, at the edges of a tetrahedron, this makes two translated compact hexagonal (HCP-hexagonal close packed) structures, which project along the $[11\bar{2}0]$ direction as an ABAB layered structure, where A, and B form III-N pairs (Figure 1.2). The hexagonal crystal structure of Group-III nitrides can be described by the edge length a_0 of the basal hexagon and the height c_0 of the hexagonal prism. Also, in this structure, the bond length along the [0001] direction between N and the metal atoms is larger than the three other bonds of the basic tetrahedron, and so an internal parameter, named as u, is defined as the ratio of anion-cation bond length along the (0001) axis and the lattice constant c_0. Taking an appropriate origin, the atoms inside the unit cell are then located at (1/3, 2/3, 0) and (2/3, 1/3, 1/2) (Group-III atom) and (1/3, 2/3, u) and (2/3, 1/3, 1/2+u) (N atom). The internal parameter (u) is different for each compound, because of the different cations and ionic radii[120] (Al^{3+}: 0.39 Å, Ga^{3+}: 0.47 Å, In^{3+}: 0.79 Å), and as a result InN, GaN and AlN have different lattice constants and bandgaps as

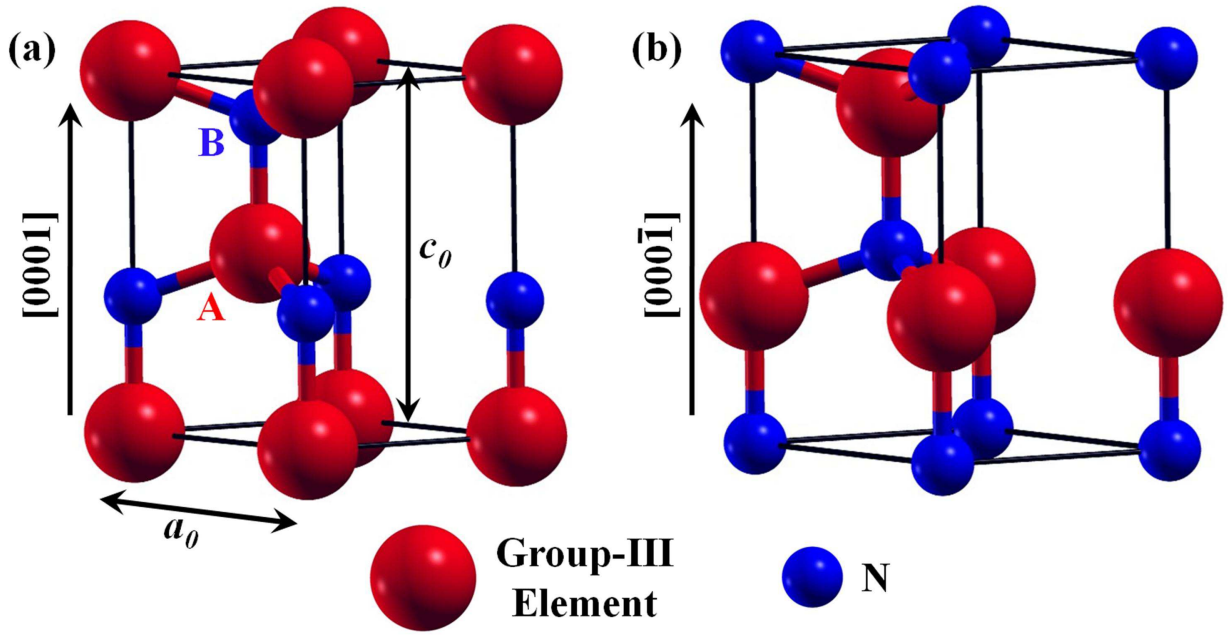

Figure 1.2: shows (a) Metal-polar and (b) N-polar unit cell of wurtzite crystal structure for III-nitrides.

Table 1.1: Lattice constants and bandgaps of hexagonal AlN, GaN and InN.

III-nitride	Lattice Constants (Å)		Bandgap (eV)
	a_0	c_0	at RT
AlN	3.1106[121]	4.9795[121]	6.12[122]
GaN	3.1893[123]	5.1852[123]	3.42[124]
InN	3.5376[125]	5.7064[125]	0.64[15]

shown in Table 1.1. Beside the α-phase, a metastable β-phase with zinc-blende (cubic) structure also exists for Group-III nitride materials. The α- and β-phases of Group-III nitrides only differ in the stacking sequence of nitrogen and metal atoms (polytypes), and therefore, the coexistence of hexagonal and cubic phases is possible in epitaxial layers, due to stacking faults.

Both wurtzite and zincblende structures of III-nitrides have polar axes (lack of inversion symmetry). Particularly, the bonds in the $\langle 0001 \rangle$ direction for wurtzite and $\langle 111 \rangle$ direction for zincblende are all faced by nitrogen in the same direction and by the cation in the opposite direction. Both bulk and surface properties are reported to be significantly dependant on whether the surface is faced by nitrogen or metal atoms.[126,127] The most common growth direction of hexagonal III-nitride is along [0001] direction, which is normal to the $\{0001\}$ basal plane, where the atoms are arranged in bilayers consisting of two closely spaced hexagonal layers, one with cations and the other with anions, so that the bilayers have polar faces. Thus, a III-nitride basal surface should be either metal- or nitrogen-faced. By metal-faced it is meant that the metal atom is on the top position of the $\{0001\}$ bilayer, corresponding to [0001] polarity, and it does not mean metal-terminated; as termination is only used to describe a surface property and not bulk crystal structure. A metal-face surface can be N-terminated if it is covered with nitrogen atoms, but without flipping the crystal it will never become N-faced. Therefore, it is clear that the (0001) and $(000\bar{1})$ surfaces of III-nitrides are inequivalent (by convention, the [0001] direction is given by a vector pointing from a metal atom to a nearest-neighbour N atom). Polar faces are known to have very distinct effects on growth in binary cubic semiconductors. For example, growth along the gallium-faced $\{111\}$ direction of GaAs is found to be slow and has the tendency to produce planar surfaces, whereas growth of the

As-face is fast and rough.[128] Similarly, it is observed that the smooth side of bulk single crystal platelets is gallium-face (0001) whereas the N-face ($000\bar{1}$) is much rougher.[129] It has been reported by several groups, that high-quality epitaxial GaN films deposited by MOCVD on *c*-plane sapphire substrates grow in the [0001] direction with gallium-faced surfaces, while MBE growth of the same commonly occurs in the [$000\bar{1}$] direction, resulting in a N-faced film.[76,129,130] However, due to the recent advancement in the thin film deposition techniques, it is possible to controllably grow Ga-polar or N-Polar films by choosing appropriate growth parameters.

1.4 Substrates used to grow Group-III Nitrides

One particular difficulty in the growth of III-nitride thin films is the limited availability of affordable and sufficiently large single crystals to use as substrates for homoepitaxial growth. Thus, heteroepitaxial growth is the only possible solution, but the choice of substrate becomes critical. This is a long standing problem and a number of studies on the effects of the substrate on the structural, electrical and morphological properties of thin films of these compound semiconductors have been reported.[131–140] Growing heteroepitaxially requires the choice of a substrate with a surface template that matches the crystal symmetry of the desired material. The lattice mismatch between the substrate and the film leads to the generation of misfit dislocations at the interfaces in order to release the mismatch induced strain. Unfortunately, the relaxation is never completely confined to the interface and the dislocations usually propagate along the thickness of the films. During such heteroepitaxial growth, not only the lattice parameter difference plays an important role, but also it is necessary to manage the thermal behaviour of the substrate and the epitaxial layers. Indeed, while cooling down from the growth temperature, the substrate and film will relax in significantly different ways depending on the differences in their thermal expansion coefficients.

Possible substrate materials with low thermal expansion and lattice mismatch for VPE (Vapour Phase Epitaxy) and MOCVD are limited to those unaffected by high concentrations of Ammonia and Hydrogen at temperatures in excess of 1000 °C. Even for PAMBE, in which the growth temperatures are about 250 °C lower than for VPE and

MOCVD, the substrate surfaces have to be stable under the influence of nitrogen plasma at 800 °C. For device production processes, the substrate of choice has to be available in a minimum size of two inches, with atomically flat surfaces, and in large quantities at acceptable prices. Under these presuppositions, sapphire, Silicon carbide and Silicon are the most popular substrate materials. As can be seen in Table 1.2, the lattice parameters, mismatch and thermal expansion coefficients are quite different between the nitrides and the used substrates. Therefore, one expects, if no special care is taken, the generation of large defect densities following heteroepitaxy of nitride layers on these substrates. The main criteria for the substrate choice is that the substrate has a low lattice mismatch this is measured by the misfit parameter (f_m) defined as $f_m = (a_{substrate} - a_{film})/a_{substrate}$, where $a_{substrate}$ and a_{film} are the lattice constant for the substrate and the film, respectively (see Table 1.2).

Among the mentioned substrates sapphire is most extensively used for the epitaxial growth of III-nitrides, and several orientations of sapphire, such as c-(0001), a-$(11\bar{2}0)$, m-$(10\bar{1}0)$ and r-$(10\bar{1}2)$, have been used, although it has large lattice and thermal expansion mismatch with III-nitrides. Due to this large mismatch there is a general tendency of III-nitride unit cells to rotate by 30° around the c-axis with respect to the sapphire unit cell. This rotation reduces the lattice mismatch between sapphire and III-nitrides and also allows the alignment between the Oxygen and III-element sub-lattices of the two materials.[143] In this orientation, the mismatch between sapphire and III-nitride lattice parame-

Table 1.2: Parameters of III-nitride semiconductors and most commonly used substrates.

Material	Crystal Structure	Lattice Constant (Å)		Lattice Mismatch (≈ %) w.r.t.			Thermal Expansion ($10^{-6}K^{-1}$)[2,141]	
		a_0	c_0	AlN	GaN	InN	∥ **a**-axis	∥ **c**-axis
AlN	Wurtzite	3.1106[121]	4.9795[121]	0	2.5	12.1	4.20	5.30
GaN	Wurtzite	3.1893[123]	5.1852[123]	-2.5	0	9.8	3.17	5.59
InN	Wurtzite	3.5376[125]	5.7064[125]	-13.7	-10.9	0	3.09	2.79
Al_2O_3	Hexagonal	4.765[142]	12.982[142]	34.7	33.1	25.7	5.00	9.03
SiC	Wurtzite	3.0806[142]	15.1173[142]	-0.97	-3.5	-14.8	4.30	4.70
Si	Cubic	a = b = c = 5.431[142]		23.4	16.9	8	3.59	

ters is thus calculated using the following relation: $f_m = (a_{substrate} - 2a_{film}cos\theta)/a_{substrate}$, where θ is the angle of rotation of III-nitride unit cell with respect to sapphire. If InN is grown directly on *c*-sapphire, two kinds of in-plane rotated domains can be observed with epitaxial relationships of $[10\bar{1}0]_{InN}\|[11\bar{2}0]_{Sapphire}$ and $[11\bar{2}0]_{InN}\|[11\bar{2}0]_{Sapphire}$ where the magnitude of lattice mismatches are almost equal and thus there is an equal probability for InN to grow in both the epitaxial directions, a tendency which is very common for the growth of InN on sapphire (Table 1.3).

Table 1.3: Lattice mismatch between III-nitrides and *c*-sapphire along $< 11\bar{2}0 >$ and $< 10\bar{1}0 >$ directions.

	$[11\bar{2}0]_{III-nitride}\|[11\bar{2}0]_{Sapphire}$	$[10\bar{1}0]_{InN}\|[11\bar{2}0]_{Sapphire}$
AlN	+34.7%	-13.1%
GaN	+33.1%	-15.9%
InN	+25.7%	-28.6%

On the otherhand, Si(111) is being explored as an alternate substrate for III-nitride growth due to its excellent doping properties, high abundance, low cost, good thermal conductivity, excellent crystal quality, availability of large sized wafers, ease of cleavability, and also for the advantage of integration of III-nitrides with the mature Silicon technology.[144]

1.5 Thin Film Nucleation and Growth

Epitaxial thin film growth is a complex process, especially, producing thin layers for specific applications, on top of completely different substrates. The way the growth takes place depends on various parameters, probably the most critical ones are the energies of the substrate surface, the symmetry of the surface, the lattice mismatch between the substrate and film, the supersaturation (flux) of the crystallizing phase, the growth temperature, and so on. Schematic diagram of different processes involved during thin film nucleation and growth has been shown in Figure 1.3.

After reaching a crystalline surface, the atoms or molecules begin to interact with the surface atoms as well as the Potential Energy Surface (PES) formed by them. Depending on the interaction the incoming atoms are either reflected or they transfer enough energy

to the lattice to be weakly bound to the surface as so-called adatoms. This process also depends on the incoming flux, the trapping probability and the sticking coefficient of the incoming atom on the substrate surface. The adsorbed particles are confined within a two dimensional phase state, and thus, they are not bound to the surface but can rather easily move along the surface due to the energy transfer by lattice vibrations. To perform such movements the adatoms have to cross the saddle ridges present within the PES. An uncorrelated sequence of jumps of an adatom from one PES minimum to another is called as surface diffusion. These adatoms diffuse along the surface until they either desorb again, or a stable nucleus is formed or they gets attached to a already formed stable island. A certain part of the adsorbed atoms forms nuclei, i.e. many body aggregates which are energetically favorable compared to isolated monomers. These aggregates may still decay by the emission of single atoms. Only after a certain nucleus size is exceeded ("critical nucleus") it is energetically more favorable to attach atoms (growth) than to lose them. The surface mobility of adatoms is dependent on the growth temperature, their kinetic energy upon impingement and the strength of interaction between a single atom and the substrate. If this interaction is strong, one obtains a high nucleus density (nuclei per unit area), whereas, a weak interaction results in a low nucleus density. By

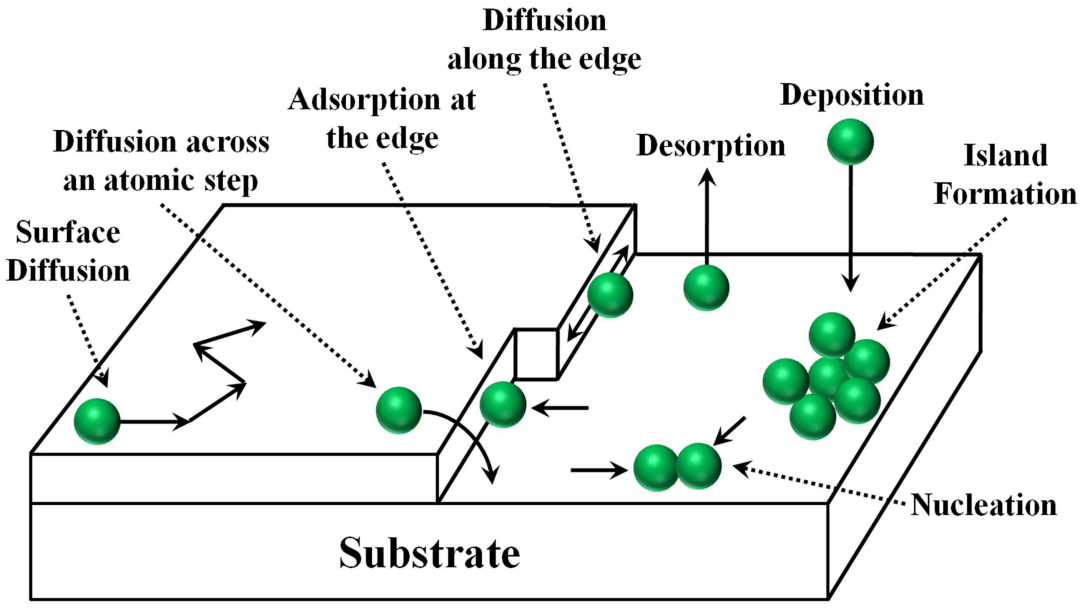

Figure 1.3: shows schematic diagram of different processes involved during thin film nucleation and growth.

the attachment of other adatoms the nuclei grow to islands (at constant nucleus density) which, depending on the given conditions, coalesce to a more or less connected film.

Thus, the stages passed until the formation of a continuous film are as follows:

1. Thermal accommodation
2. Adsorption (physisorption) of atoms/molecules
3. Surface diffusion
4. Formation of molecule-molecule and substrate-molecule bonds (chemisorption)
5. Nucleation: aggregation of single atoms/molecules
6. Growth of islands
7. Structure and microstructure formation (poly-crystalline/single crystalline, defects, roughness, etc.)
8. Changes within the bulk of the film, e.g. diffusion, grain growth etc.

1.5.1 Thin Film Growth Modes

During epitaxial growth of thin films, three basic growth modes have been observed at the nucleation stage, which are illustrated schematically in Figure 1.4 and briefly discussed here.

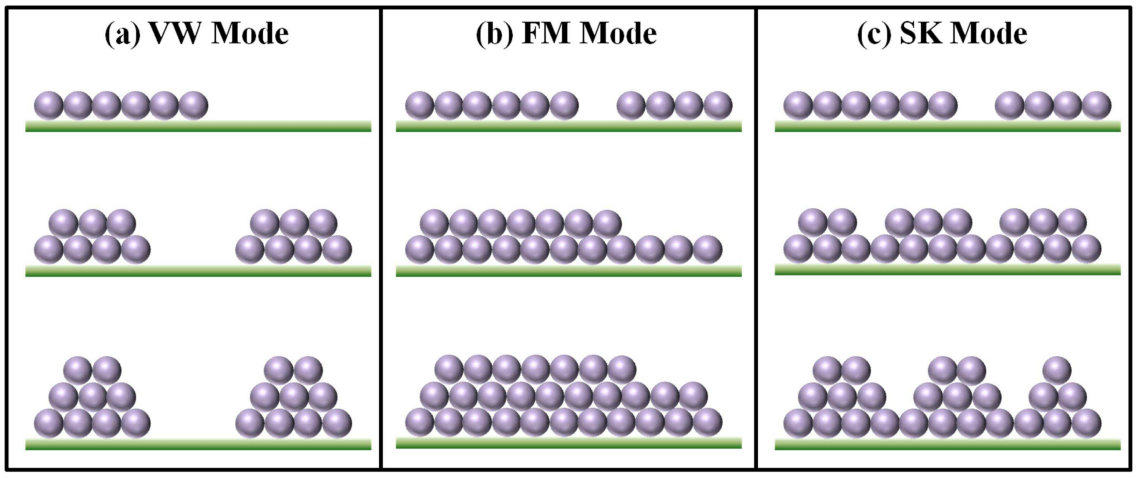

Figure 1.4: shows schematic of different possible growth modes: (a) Volmer-Weber, (b) Frank-van der Merwe and (c) Stranski-Krastanov.

1.5.1.1 Volmer-Weber (VW) mode

This is the island growth, also known as three-dimensional growth mode. In Volmer-Weber mode (Figure 1.4(a)), adatoms form clusters on the substrate which then grow into individual islands. This happens when the adatoms are more strongly bound to each other than to the substrate, which causes slow surface diffusion. Thus, the necessary thermodynamic condition for island growth is

$\gamma_{substrate} < \gamma_{film} + \gamma_{interface}$

where, $\gamma_{substrate}$: surface energy of substrate

γ_{film} : surface energy of film

$\gamma_{interface}$: interface energy between film and substrate

This non-wetting mode will govern the heteroepitaxial growth when the two materials have completely different symmetries, surface energies and large lattice mismatch, e.g. in case of metals growing on insulators and semiconductors, including many metals on alkali halides, graphite and other layer compounds such as mica.

1.5.1.2 Frank-van der Merwe (FM) mode

This is the layer-by-layer growth, also known as two-dimensional growth mode. Frank-van der Merwe mode (Figure 1.4(b)), occurs when the adatoms are more strongly bound to the substrate than to each other, which helps in faster surface diffusion of adatoms. As a result, the first atoms to condense form a complete monolayer on the surface, which becomes covered with slightly less tightly bound second layer and the growth takes place in a smooth, layer-by-layer manner and generally the highest crystalline quality is obtained in this growth mode. Thus, the necessary thermodynamic condition for island growth is

$\gamma_{substrate} \geq \gamma_{film} + \gamma_{interface}$

This wetting growth mode is observed when the two materials have close or highly equal characteristics (symmetry, lattice parameters, surface energies, growth temperatures, etc.) e.g. in the case of adsorbed gases, such as several rare gases on graphite and on several metals, in some metal-metal systems, and in semiconductor growth on semiconductors.

1.5.1.3 Stranski-Krastanov (SK) mode

This is layer-by-layer followed by island growth mode. In Stranski-Krastanov growth mode (Figure 1.4) initially the first monolayer (ML), or a few ML are formed and subsequent layer growth becomes unfavourable and islands starts forming on top of this 'intermediate' layer. There are many possible reasons for this mode to occur, and almost any factor which disturbs the monotonic decrease in binding energy, characteristic of layer growth, may be the cause to initiate consequent 3D growth. For example, the lattice mismatch between film and substrate induces a strain in the film and can explain the transition from 2D layer to 3D islands growth modes. Thus, the necessary thermodynamic condition for island growth is

Initially, $\gamma_{substrate} \geq \gamma_{film} + \gamma_{interface}$

Finally, $\gamma_{substrate} < \gamma_{film} + \gamma_{interface}$ (due to strain effect)

As this growth mode is very common in nature, there are several examples of its occurrence in metal-metal, metal-semiconductor, gas-metal and gas-layer compound systems.

1.6 Thin Film Growth Techniques

The history of the production of Group-III nitrides spans more than 50 years and during that period, different groups have employed several growth techniques. Among them few techniques, which are widely used throughout the world are discussed briefly here.

1.6.1 Vapour Phase Epitaxy (VPE)

VPE has been widely used to grow III-nitrides because of its high growth rates (up to a few hundreds of micrometres per hour) and its lack of carbon incorporation into the film. The high growth rate offers the possibility of preparing very thick films, which can even be removed from a Al_2O_3 substrate by polishing or laser-induced thermal decomposition and can be used as a substrate for homoepitaxy.

In conventional chloride transport VPE of GaN, the gallium source is gallium monochloride (GaCl), which is only stable at temperatures above 600 °C and is produced by the

reaction of liquid gallium with Hydrogen Chloride (HCl) gas. The supply of GaCl is controlled by the gallium cell temperature and the flow rates of the HCl and the carrier gas. The source for nitrogen is generally Ammonia gas, often diluted with a carrier gas like H_2. Thus, for VPE of GaN, an $Ga/HCl/NH_3/H_2$ system is used where reactor is heated by a two-zone resistance furnace. In the first zone, the gallium source is held at a constant temperature between 850 and 900 °C, over which HCl gas is flown to undergo the following reaction:

$$2Ga(l) + 2HCl(g) \rightarrow 2GaCl(g) + H_2(g)$$

In the second zone, substrate (e.g. Al_2O_3) is held at suitable temperature to achieve required growth rate, where GaCl reacts with NH_3 and GaN crystal is formed on the substrate. The deposition of GaN can be described by the overall reaction:

$$GaCl(g) + NH_3(g) \rightarrow GaN(s) + HCl(g) + H_2(g).$$

In some cases, gallium trichloride ($GaCl_3$) has also been used as the gallium source, due to its high vapour pressure. The crystalline $GaCl_3$ is molten and heated in a quartz cell by an electrical heater, resulting in a $GaCl_3$ vapour, which is then transported to the reactor by the nitrogen carrier gas. nitrogen is also used in order to dilute the Ammonia and to increase the total gas flow rate. The $GaCl_3$ supply is controlled by both the cell temperature and the flow rate of the N_2 carrier gas.

Along with high growth rate VPE comes with some major problems. One is high electron concentrations above 10^{17} cm^{-3} in intentionally undoped films, mostly due to Silicon and Oxygen impurities originating from the quartz tubes used in VPE reactors and which can be affected by chlorides at high temperatures. Besides the problem of the high electron concentration, which hinders the growth of p-type material, the high growth temperature in VPE makes it very difficult to grow InGaN alloys. The growth temperature is far above the decomposition temperature of InN, and large over-pressures of NH_3 have to be overcome to prevent InGaN films from decomposing. The lack of p-type GaN and difficulty of growth of InGaN by VPE has so far kept the technique from the fabrication of devices.

1.6.2 Metal Organic Chemical Vapour Deposition (MOCVD)

The growth of Group-III nitrides by MOCVD involves the transport of organometallic precursors in gaseous phase as metal source and hydrides like N_xH_y for the nitrogen source, and transport gases to a heated substrate on which the precursors are pyrolysed in the absence of Oxygen. Pyrolysis leaves the atoms on the substrate surface, which later bond to the surface and a new crystalline layer is grown on the substrate. The underlying chemical mechanism is complex, which involves a combination of gas phase and surface reactions. Required pyrolysis temperature increases with increasing chemical bond strength of the precursor. The more carbon atoms are attached to the central metal atom, the weaker the bond. The diffusion of atoms on the substrate surface is affected by atomic steps on the surface. The vapour pressure of the metal organic source is an important consideration in MOCVD, since it determines the concentration of the source material in the reaction and the deposition rate.

The deposition of epitaxial MN layers (M = In, Ga or Al) by MOCVD has traditionally been carried out using mixtures of trimethylindium, -gallium, or -aluminium (Me_3M), and Ammonia (NH_3). For example, during the growth of AlN, an intermediate gas phase adduct [Me_2AlNH_3] can form initially at RT, from the mixtures of Me_3Al and NH_3 and then AlN deposition occurs via the following reactions:

$2Me_2AlNH_3 \rightarrow MeAl(NH_2)_2AlMe + 2CH_4(g)$

$MeAl(NH_2)_2AlMe \rightarrow Al(NH)_2Al + 2CH_4(g)$

$Al(NH)_2Al \rightarrow 2AlN + 2H_2(g)$.

In MOCVD the injected gases are ultra-pure and can be finely dosed. MOCVD equipment has multi-wafer growth capability and it also enables the deposition of large surface areas with a higher growth rate ($\approx$ few μm/hr.) compared to MBE and is therefore the most cost-effective and significant choice for compound semiconductor manufacturers. With all these remarkable advantages, MOCVD systems come with some shortcomings, e.g. it is very difficult to monitor *in-situ* RHEED as the environment is not kept at UHV; the growth process is not as abrupt as MBE due to gas flow issues and memory effects; optimization of growth parameters is difficult compared to MBE as there are huge set of parameters; there is always a chance of Carbon contamination and unintentional Hydrogen incorporation from the organic byproducts produced during reactions; the used

gases are of toxic nature and harmful for the human users.

1.6.3 Molecular Beam Epitaxy (MBE)

MBE is a very useful thin film growth technique which can rule out almost all of the disadvantages associated with MOCVD growths. MBE was invented in the late 1960s at Bell Telephone Laboratories by J. R. Arthur and Alfred Y. Cho. MBE is a versatile technique which can be used to grow thin epitaxial structures made of semiconductors, metals or insulators. In MBE, the first layer of the thin films crystallizes via reactions between thermal molecular/atomic beams of the constituent elements and a substrate surface which is maintained at an elevated temperature in ultra high vacuum (UHV) (chamber pressure $\approx 10^{-10}$ Torr). Further growth is continued via the reaction between incoming constituent elements and the already formed layer material. The most important feature of MBE is the low deposition rate that allows the films to grow epitaxially. The composition of the grown film and its doping level depend on the arrival rates of the constituent elements and dopants. The absence of carrier gases as well as the UHV environment result in the highest achievable purity of the grown films. MBE growth is carried out under conditions far from the thermodynamic equilibrium, and is governed mainly by the kinetics of the surface processes occurring when the impinging beams of atoms react with the outermost atomic layers of the substrate crystal, which is in contrast to other epitaxial growth techniques, such as Liquid Phase Epitaxy or bulk crystal growth, which take place at conditions near thermodynamic equilibrium and are most frequently controlled by diffusion processes occurring in the crystallizing phase surrounding the substrate.

In solid-source MBE, elements such as gallium and arsenic, in ultra-pure form, are heated in separate Knudsen effusion cells (K-cells) until they begin to slowly sublime. The effusion cells consist of a crucible containing the source material, typically constructed from pyrolytic Boron nitride and a heating source. Heating is then typically performed by one of the two methods, either ohmic heating from a filament wound around the crucible or by electron beam heating. In electron beam heating, thermionic electrons are accelerated toward the source material through a potential of a few kV and deposit tens of watts of power, inducing heating in the source material. The vapour “beam”

of gaseous elements then condense on the wafer, where they interact with each other. This interaction depends on the type of adatoms, the substrate, and the temperature of the substrate, which are responsible for the nucleation and the subsequent growth in the form of thin layers on the substrate. The term "beam" means that the evaporated atoms do not interact with each other or vacuum chamber gases until they reach the substrate, due to the long mean free paths of the atoms, under UHV condition. As each element is delivered in a separately controlled beam, the choice of elements and their relative concentrations can be adjusted for any given layer, thereby defining the precise composition and electrical and optical characteristics of that layer. During the operation, Reflection High Energy Electron Diffraction (RHEED) is often used for monitoring the growth of the crystal layers. A computer programme controls the shutters in front of each effusion cell, allowing precise control of the thickness of each layer, down to a single layer of atoms. Thicker layers are obtained with longer deposition times. Thus, MBE offers tremendous control over layer thickness, composition and purity. Intricate structures of layers of different materials can be fabricated this way. Such control has allowed the development of structures where the electrons can be confined in space, giving QWs or even QDs. Such layers are now a critical part of many modern semiconductor devices, including semiconductor lasers and light-emitting diodes.

For nitride growth, the effusion of the metal atoms (Ga, In, Al) and dopants (Si, Mg) from conventional Knudsen effusion cells has to be combined with a source for nitrogen radicals. Nitrogen at RT is an inert gas and not very reactive, because of the triple bond between the two nitrogen atoms. The dissociation of one molecule into reactive nitrogen atoms requires a relatively high amount of energy. Under the influence of a plasma at reduced pressure, a significant dissociation of the nitrogen molecules takes place. Atomic nitrogen is chemically very active at RT and bonds with many metals (e.g. mercury, zinc, cadmium, magnesium) creating various nitrides. Therefore Group-III nitrides can be grown by plasma-assisted MBE, where the plasma-induced fragmentation of nitrogen molecules is combined with the evaporation of metal atoms from effusion cells. Another approach in case of MBE systems, where ammonia gas is used as the source of nitrogen, is called as reactive MBE, where Ammonia is decomposed only on the surface of the substrate by pyrolysis.

Chapter 2

Literature Overview on InGaN

This chapter begins with the background in literature regarding the growth kinetics, which are associated with different growth parameters, such as growth temperature, V/III ratio, and growth rates which influence the quality of the InGaN films. Afterwards, an overview of the structural and optical characteristics of the InGaN alloys has been discussed. Then, the determination of indium composition by HRXRD using different assumptions and various equations has been demonstrated. Later, the introduction of bowing parameter in Vegard's law, to get an accurate knowledge of the bandgap as a function of alloy composition, has been described. In addition, major factors leading to the uncertainties of the bowing parameter of InGaN have also been addressed. Different emission mechanisms of InGaN, proposed by different research groups are also briefly mentioned. Finally, the importance of nanostructures and different contemporary reports on nanosturctue growth relevant to InN and InGaN material system has been presented. This review served as the motivation to undertake the present work and showed the outstanding issues in the field which needs to be addressed.

2.1 Introduction

As discussed in the Chapter 1, the nitride semiconductors and related alloys have received enormous attention because of their broad range of practical applications. The nitride semiconductors and their suitable alloy combinations in the $In_xGa_{1-x}N$ and $Al_xGa_{1-x}N$ systems, form a continuous alloy system with direct bandgaps, ranging from 0.64 eV(InN)[15]

to 6.015 eV(AlN)[16] including 3.42 eV for GaN[124], at RT.

Among the Group-III nitride materials, InGaN has attracted lot of attention, as it has been considered to be the most important and indispensable materials for the fabrication of light emitters, active in the entire visible and partly in the near-UV spectral regions. However, the fundamental physics related to the InGaN material system has not been well developed, even though significant progress has been achieved recently in InGaN technology. Some of the physical and chemical properties e.g. the bandgap, lattice parameters, elastic constants, effective electron mass and others are still estimated based on GaN and InN. Recently, the bandgap of InN has been experimentally demonstrated to be 0.64 eV[15,145–151], which until 2002 was believed to be 1.9 eV by various research groups[152–154] and these fundamental problems have introduced uncertainties in estimating the optical, structural and electrical parameters of the InGaN, and therefore, resulted in the divergence in the reported values in the literature. At present, the fundamental properties and different aspects of GaN are well studied and several excellent review papers have been published based on that.[3,155–159] On the other hand, even though some of the physical parameters and properties of InN can be obtained from recently published review papers[10,11,151,156,160], most of the fundamental properties of InN are not as well understood as GaN, and thus, it gives rise to complications and ambiguity in the study of InGaN.

To design and fabricate novel optoelectronic device structures, with desired optical emission characteristics, an in-depth understanding of the fundamental properties of the InGaN materials including the accurate knowledge of bandgap as a function of alloy composition is necessary. Several technical limitations, e.g. the difficulty in growing high-quality InGaN alloys, particularly with high indium molar fraction, the inaccuracy and uncertainties in determining the indium composition, and the presence of multiple phases within the same film exist. All of these complicates the emission dynamics in the material and thus different models of emission mechanisms have been proposed by different groups. As a result, the emission mechanism is still ambiguous to the research community, which directly hampers the fabrication of high-performance optoelectronic devices with the desired optical properties.

It is observed that the structural and optical characteristics of InGaN alloys are

significantly affected by the growth conditions and a slight adjustment of the growth parameters leads to a large variation in the quality of the grown InGaN films. Thus, the growth kinetics of InGaN are briefly reviewed in the following section which will eventually help us to grow better quality InGaN films by changing different growth parameters.

2.2 Growth Kinetics of $In_xGa_{1-x}N$

As already mentioned, growth of InGaN is very difficult as it faces several problems, for instance, solid phase miscibility gap caused by the difference in inter-atomic spacing of InN and GaN[161] and low indium incorporation in the InGaN alloy caused by the difference in vapour pressure of InN and GaN.[162] Moreover, the difference in formation enthalpies for InN and GaN also leades to a strong indium surface segregation.[163] Researchers are still encountering all these issues and have tried to minimize those effects by varying different growth parameters.

Piner *et al.*[164] have pointed out that the desorption of indium from the surface is substantially reduced with the reduction of growth temperature for the growth of InGaN on *c*-sapphire by atmospheric pressure metal organic chemical vapor deposition (AP-MOCVD). But they have also observed that the indium incorporation in the film gets reduced at the same time due to reduced growth rate, caused by inefficient cracking of Ammonia at a lower growth temperature. As a result, the density of indium atoms diffusing across the film surface increases, encouraging the formation of indium clusters, which eventually leads to indium droplet formation on the film surface. Thus, the amount of indium droplets increases considerably with the reduction of growth temperature.

Van der Stricht *et al.*[165] have reported that, at growth temperatures below 750 °C, the InGaN films, grown on *c*-sapphire by atmospheric pressure metal organic vapour phase epitaxy (AP-MOVPE), showed metal droplet formation at the suface, which reduces, with increasing Ammonia flow, as the amount of nitrogen radicals as well as availability of nitrogen bonding sites for indium increases.[164] Moreover, the transition from 3D-island nucleation mode to step-flow mode has been reported with the increase of NH_3 flow rate, which could be attributed to the reduction in the energy barrier of adatom incorporation at the step-edges[166] and thus it shows that the morphology of InGaN gets influenced by

the amount of NH_3 on the growth surface.

Along with the growth temperature, growth rate and growth pressure are also found to affect the indium incorporation in bulk InGaN films. Evaporation of indium atoms gets reduced at lower growth temperature and higher growth rate as they gets incorporated by the growing layer, as observed for the growth of InGaN on *c*-sapphire and GaN epilayer by MOCVD.[167,168] By reducing the growth temperature, indium incorporation gets increased, but at the same time the surface mobility of the adatoms gets drastically reduced, which causes problems like formation of indium droplets, phase separation and composition inhomogeneity throughout the film and these lead to poor quality of the grown InGaN material.[169,170] For MOCVD growth, high-quality InGaN could be obtained, at growth temperatures below 760 °C, by reducing the growth rate.[168] This could be due to the reason that lower growth rate permits the surface adatoms longer time to arrive at 2D-step edges of growth front, which eventually enhances optical and crystal quality.[171] Kim *et al.*[172] reported that indium incorporation in the InGaN thin film increases by 7.5% as the growth pressure was decreased from 250 torr to 150 torr; a similar observation is also reported by Oliver *et al.*[166] However, a large red-shift and broadening of the PL spectra was also observed with the decrease of growth pressure, indicating the degradation of the optical properties due to the inhomogeneous distribution of indium in the InGaN films.

MBE also has been used to grow InGaN for a long time and all the difficulties mentioned already, faced during the growth of InGaN using MOCVD are also encountered during MBE growth of InGaN and the characteristics of indium incorporation during InGaN growth using both techniques are found to be quite similar in certain aspects. For instance, with increasing growth temperature, the indium incorporation decreases.[173–175] However, at constant growth temperature and N_2 flux-rate, when both indium and gallium fluxes are increased keeping the In/(In+Ga) ratio constant, the indium incorporation increases at low metal flux, but it decreases at high metal flux. Chen *et al.*[173] explained that when both indium and gallium fluxes are increased, strong indium surface segregation occurs and most of the additional gallium atoms go into the bulk and displace the indium atoms, which eventually decreases the indium incorporation. Several other groups[150,176] have also demonstrated growth of InGaN using MBE, some of which are discussed briefly here.

Yoshida *et al.*[177] have grown InGaN films by gas source MBE on sapphire substrates, where uncracked Ammonia was used as a source of nitrogen and obtained indium concentration was 20%. They have observed that, for growth temperature more than 800 °C, the concentration of indium is very low, whereas for growth temperature lower than 760 °C, gallium droplets are formed on the surface, due to inefficient decomposition of Ammonia and consequent low value of the V/III ratio at the low temperature. The layers grown at ≈ 780 °C are of good quality, but under these conditions films with more than 20% indium content could not be grown. Strong band-edge peak of InGaN layer at 420 nm, and a buffer layer peak at 365 nm were observed in PL, but deep level related emission was not observed.

Grandjean *et al.*[178] have grown $In_xGa_{1-x}N$ layers with high indium concentrations (up to $x \approx 0.46$) by MBE, where the nitrogen precursor was 50 sccm Ammonia. A 2 μm thick GaN layer was first deposited on *c*-sapphire at 500 °C after nitriding the substrate at 850 °C,[179] on top of which $In_xGa_{1-x}N$ layers were grown at temperatures in the range 500 - 600 °C. The indium incorporation rate was smaller at higher growth temperatures and this result is similar to that obtained by Yoshida *et al.*[177] By increasing the indium flux, up to 46% indium could be incorporated in the films, however, increasing the gallium flux had only a small effect on the indium incorporation rate.

Blant *et al.*[180] have studied the MBE growth of InGaN alloys on clean and oxidized Si surfaces, where the growth temperature was in the range of 400 - 750 °C, depending on the composition of the alloys. They showed that alloys of InGaN could be grown on Si substrate, over the entire composition range from InN to GaN. However, films grown on oxidized surfaces of Si were polycrystalline or amorphous. The growth on chemically cleaned Si substrates showed the usual columnar structure common to the growth of Group-III nitrides. XPS studies indicated that there was little tendency for spinodal decomposition, and the composition of the alloys deduced from Electron Probe Microanalysis (EPMA) studies agreed well with those obtained from X-ray measurements.

Singh *et al.*[181] were also able to grow the InGaN alloys over practically almost the entire composition range, but at the growth temperature of GaN (700 - 800 °C) by MBE. These authors found that if the thickness of the films was > 0.3 μm, incorporation of more than 30% indium resulted in phase separation of InN, which was consistent with

spinodal decomposition. However, such phase separation was absent in thin InGaN films (< 600 $\AA$) grown as GaN/InGaN/GaN heterostructures. In such configurations, up to 81% indium could be incorporated.

Growth of $In_xGa_{1-x}N$ with $x > 0.2$ has been attempted by MBE and phase-separated and/or low structural quality films have been reported.[182] Films grown at growth temperatures of 700 - 750 °C with indium concentration higher than 35%, showed phase separation (appearance of separate InN phase), which is in good agreement with thermodynamic predictions for spinodal decomposition.[161,183,184] Films grown at lower growth temperatures (650 - 675 °C) revealed compositional inhomogeneity (broadening of XRD(0002) peak) when the indium content was larger than 25%. These films, upon annealing to 725 °C, underwent phase separation (appearance of separate GaN phase), similar to those grown at the same temperature.

In addition to phase separation, ordering has also been observed in InGaN alloys where the indium and gallium atoms are no longer randomly located on the metal HCP sublattice but each set of Group-III atoms occupy a preferred metal HCP sublattice. Evidence of ordering can be seen by the presence of the (0001) peak in the XRD scan and the appearance of superlattice spot in selected area diffraction (SAD) pattern.[182,185] In a random InGaN alloy, the structure factor of $(000l)$ planes is zero, when l is odd. In an ordered alloy on the other hand, indium atoms preferentially occupy lattice sites in alternating basal planes, resulting in nonzero structure factors for $(000l)$ planes. The $In_{0.09}Ga_{0.91}N$ films[182] exhibited long-range atomic ordering and the ordering parameter was found to increase with the growth rate of the films, from which the authors have deduced that ordering is induced at the growth surface. The ordered phase was found to be stable up to annealing temperatures of 725 °C. A competition between ordering and phase separation has been observed and lattice strain in the alloy has been attributed to be the driving force for both the phenomena.

Thick $In_xGa_{1-x}N$ ($0.20 < x < 0.27$) layers are grown by PAMBE on GaN/Al_2O_3 templates by Naranjo *et al.*[186] The strain and indium content is estimated from HRXRD, which shows that the bulk samples are not fully relaxed. A bandgap bowing parameter of 3.6 eV is obtained from absorption measurements of $In_xGa_{1-x}N$ layers. Strong indium content dependent excitonic localization is observed in these bulk layers, which leads to

an increase in the absorption band edge with the indium content.

Indium-rich $In_xGa_{1-x}N$ ($0.61 \leq x \leq 1.00$) films are grown directly on *c*-sapphire using RF-MBE by Kurouchi *et al.*[187], where the $In_xGa_{1-x}N$ films showed no macroscopic phase separation. The films showed excellent *a*-axis orientation with the in-plane epitaxial relationship of $[10\bar{1}0]_{InGaN,InN} \parallel [11\bar{2}0]_{Sapphire}$, which was attributed to the effect of substrate nitridation before growth. Rocking Curve-FWHM for (0002) $In_xGa_{1-x}N$ diffraction became broader, and grain size of the $In_xGa_{1-x}N$ films became smaller with the increase in gallium-composition of the films. Reciprocal Space Mapping studies revealed that the $In_xGa_{1-x}N$ films were free from strain. PL peak energy of these strain-free $In_xGa_{1-x}N$ films exhibited a monotonic decrease with the increase in the indium-composition, approaching to 0.66 eV of a strain-free InN film, and the absorption edge showed similar indium-composition dependence. However, its energy was approximately 0.2 eV above the PL peak energy independent of the indium-compositions range investigated. The band bowing parameter of $In_xGa_{1-x}N$ was determined to be 1.8 eV at RT.

PAMBE growth of InGaN films on both nitrogen- and gallium-polar GaN buffer layers was carried out by Shen *et al.*[188] Difference in the film quality between InGaN grown on the nitrogen- and gallium-polar GaN was observed and the gallium-polar GaN was found to be superior in structural quality. Based on this outcome, high-quality InGaN films were obtained on the gallium-polar GaN with an indium composition up to 0.36, which showed intense PL emissions. Comparing the PL peak energy and the indium composition determined by XRD, indium composition dependent bandgap bowing parameter of InGaN films have been reported.

The effects of atomic Hydrogen (H) irradiation on the indium incorporation and ordering in InGaN films grown by RF-MBE have been investigated by Okamoto *et al.*[189] The Hydrogen molecule (H_2) and atomic H irradiation were found to enhance the indium incorporation. Under atomic H irradiation, indium incorporation was enhanced with increasing flow rate of the atomic H, whereas, H_2 flow rate did not have any effect on the indium incorporation under H_2 irradiation. These results suggested that modulation of atomic H irradiation flux could be used to control the indium content in InGaN layers.

The progress of developing InGaN LEDs by MBE has been slow compared to the MOCVD technique. This is in part due to the spectacular results achieved by growing

InGaN LEDs using MOCVD and the subsequent commercialization of such devices. The output power of LEDs grown by MBE have yet to match those grown by the MOCVD technique, where the high efficiency of InGaN LEDs has been attributed to compositional inhomogeneity in the InGaN QWs resulting in exciton localization.[190] Thus, it is possible that under the right set of growth condition, such an effect can also be achieved by the MBE process.

InGaN/GaN double heterostructure LEDs, grown by PAMBE, showed EL at 425 nm with thick $In_{0.2}Ga_{0.8}N$ active region.[191] To isolate the effect of nucleation using MBE, the device structure was grown on a template of GaN layer grown using MOCVD. However, the EL intensity of the LED was still a factor of five to ten lower than that of MOCVD-grown LEDs. Another effort to grow InGaN LEDs by PAMBE on HVPE templates resulted in emission at 447 nm with no significant shift in peak wavelength with injected current of 20 to 120 mA.[192] However, the output power was only 20 μW, which was about two orders of magnitude lower than reported commercial InGaN LEDs.

2.3 Material Properties of InGaN

2.3.1 Structural Properties

The efficiency of optoelectronic devices, using InGaN as the active layer, largely depends on the structural properties of that InGaN layer. The performance of the device is affected by the defect formation within the active layer, induced by the stress originated due to the lattice and thermal expansion coefficients mismatches between the overgrown InGaN and underlying GaN epilayers.[193] The microstructural crystalline quality is closely related to the employed growth parameters, and thus they influence the quality of the film significantly. However, the growth of high-quality InGaN films by MOCVD is a very difficult task due to two main reasons; first, InN dissociates at temperatures beyond 500 °C and the cracking efficiency of Ammonia below 1000 °C is very low for any standard MOCVD system. Higher crystalline quality can be obtained by high temperature ($\approx$ 800 °C) growth, but at the same time indium incorporation in the alloy gets lower. On the other hand, higher indium content can be maintained at lower growth temperatures (500 °C), but at the expense of the crystalline quality. Nakamura[194] obtained InGaN films

with ≈ 33% indium composition at temperatures between 720 and 850 °C. As a result, there exists a trade-off between the film quality and the amount of indium incorporation into the alloy as the growth temperature is changed. Therefore, a commonly used growth temperature for MOCVD is in the range of 500-850 °C for InGaN growth.

It has been observed that, low temperature growth leads to poor surface morphology, because of lower surface mobility of the surface adatoms.[170] As lower growth rates are found to minimize the formation of structural defects in the crystal[170,171,195], InGaN films are usually grown at much lower growth rates as compared to GaN epilayers. On the other hand, the growth mechanism and the morphology of InGaN SQWs and bulk films are found to be affected by the dislocations, e.g. the threading dislocations of partial or pure screw character can induce a spiral growth which can lead to the formation of InGaN islands.[195] For a long time, MBE was considered unsuitable to grow InGaN based optoelectronic device fabrication, as compared to widely used MOCVD technique, which changed with the successful demonstration of MBE-grown InGaN LDs[196] and with recent advancements the performance of InGaN-based optoelectronic devices fabricated by MBE are considered to be comparable to those grown by MOCVD. However, it should be noted that these MBE-grown InGaN LDs were fabricated on MOCVD grown GaN epilayers. Shen *et al.*[197–200] have investigated the quality of InGaN films grown by PAMBE on both gallium- and nitrogen-polar GaN epilayers and observed that the use of nitrogen-polar GaN leads to poor crystalline quality of overgrown InGaN with a large FWHM value of the XRD(0002) InGaN diffraction peak and no PL emission in certain cases. On the other hand, gallium-polar GaN can produce high-quality InGaN films. It is a very common observation that GaN films grown by MBE always produce nitrogen-polarity[201,202] and thus, it is difficult to grow high-quality InGaN films using MBE as compared to MOCVD. Prystawko *et al.*[203] showed that the InGaN film, grown on MOCVD grown gallium-polar GaN substrate, exhibits much narrower PL peak than that obtained from the InGaN film grown on nitrogen-polar GaN.

2.3.1.1 Determination of Indium Composition by HRXRD

Presently, very thin layer of InGaN, mostly in a form of QWs, are used as the active layer of most of the optoelectronic devices and due to the thinness of the layer, determina-

tion of indium composition is very difficult. Most commonly used technique to determine indium composition is High Resolution X-ray Diffraction (HRXRD) measurements. However, for phase-segregated indium-rich QDs[204], it is extremely difficult to determine the indium composition, as HRXRD measurements depend on an interpretation of averaged lattice constants. Moreover, HRXRD is a direct technique used to measure the structural parameters, which determine the indium composition indirectly and thus, this technique may lead to erroneous measurements of the composition, in case lattice strain is present in the system.

The growth of InGaN on GaN leads to strain in the overgrown film as there is a lattice mismatch of 10% between InN and GaN. InGaN remains pseudomorphically strained upto a thickness smaller than the critical thickness, in which the in-plane lattice constant of the overgrown InGaN film matches to that of the underlying GaN substrate. Once the critical thickness is exceeded, strain relaxes by the formation of defects in the film.[205] For the growth of InGaN on GaN, with indium composition $< 20\%$, Akasaki *et al.*[206] reported that the critical thicknesses were much larger than those theoretically estimated using the Mathews and Blakeslee (M-B) model[207] and the Fischer model.[208] In contrast to the M-B and Fischer models, the experimental values of the critical thickness were observed to be independent of the indium compositions.

For a hexagonal unit cell, the interplanar spacing, d, of the *(hkil)* plane is given by

$d = \frac{1}{\sqrt{\frac{4}{3}\frac{(h^2+hk+k^2)}{a^2}+\frac{l^2}{c^2}}}$.

where, a and c are the lattice constants. The c lattice constant can be easily obtained experimentally, from the symmetric reflections of the $(000l)$ planes, which are in the growth direction of InGaN. From Bragg's law, for any allowed $(000l)$ reflection, the lattice constant c, can be derived as

$c = l\lambda/2sin\theta$

which now can be used to determine the indium composition by the application of Vegard's law.

Determination of indium composition from HRXRD measurements are usually done based on two different assumptions considered for the state of strain.[209–211] Firstly, it is assumed that the InGaN layer is fully relaxed and thicker than the critical thickness. This is a justified assumption for a relatively thicker layer. Thus, in absence of strain in the

InGaN film, the actual lattice constant of the relaxed InGaN layer corresponds to the measured value, ($c^{In_xGa_{1-x}N} = c_0^{InGaN}$). Secondly, the variation of indium composition is usually assumed to be linear, as in Vegard's law:

$c^{In_xGa_{1-x}N} = xc_0^{InN} + (1-x)c_0^{GaN}$

where, c_0^{InN} and c_0^{GaN} are the relaxed c lattice parameters of InN[125] and GaN[123], respectively. From the relation, x can be determined by

$x = \frac{c_0^{InGaN} - c_0^{GaN}}{c_0^{InN} - c_0^{GaN}}$

However, the inaccuracy of x can occur from errors in the lattice parameter values of GaN and InN, since different values of lattice parameters are reported in the literature.[212]

2.3.2 Optical Properties

The optical properties of InGaN are influenced by several factors, e.g. the growth temperature, indium composition, growth rate, as well as the thickness of the InGaN layer. Prominent band-edge emission is observed for high temperature grown ($T_g \geq$ 750 °C) samples, whereas the dominant emission from samples grown at low temperature ($T_g \leq 700$ °C) is found to be a deep level or impurity transition.[213] The ratio of band-edge to deep level emission increases, with increasing growth temperature.[165] It has also been reported that, with increasing indium composition, the PL band-edge emission intensity decreases along with a increase in the FWHM of the band-edge emission peak.[164,213–215]

It has been found that the growth rate is a crucial factor which determines the optical properties and structural quality of the InGaN films.[167,168,170,171,216] Higher growth rates can lead to higher indium incorporation, but the low-temperature PL spectra of such indium-rich InGaN are found to be mainly dominated by a deep and broad emission band. Such degradation of the optical quality for the indium-rich InGaN films grown at higher growth rates has been attributed to the reduction of the effective lateral mobility of the surface indium adatoms, leading to the formation of compositional fluctuation in the alloy.[217] Moreover, observation of higher PL intensity for lower growth rates is reported by Lee *et al.*[171], which implies that the optical quality can be improved by decreasing indium inhomogeneity in the film, caused by composition fluctuation.

Nakamura *et al.*[24] varied the indium content of the InGaN layer in SQW LEDs from 0.2 to 0.7, to change the peak wavelength from blue to yellow. Reported values of peak

wavelength of electroluminescence (EL) spectra for blue, green and yellow LEDs are 450, 525, and 590 nm, respectively. The FWHM values of the same EL spectra are 20, 45, and 90 nm, respectively. Thus, with longer peak wavelength, FWHM of the EL spectra increases. The output power of green and yellow LEDs is comparatively smaller than that of blue LEDs, caused by the poor crystal quality of the InGaN well layer, as the layer has large lattice mismatch and difference in thermal expansion coefficient with barrier layers. Moreover, the emission quality can also deteriorate due to out-diffusion of the indium into the barrier layer, which is more serious in case of higher indium content.[218] Martin *et al.*[219] has reported similar growth of InGaN SQWs, where by varying the growth temperatures from 860 to 760 °C, PL peak position is shifted continuously from 430 to 670 nm, accompanied by the decrease of integrated peak intensity and increase of peak FWHM, with increasing indium content in the InGaN SQW.

Several reports have shown that the thickness or size of QWs or QDs of InGaN (embedded in GaN or InGaN) can affect the emission wavelengths.[167,168,186,218,220–223] Generally, with decreasing thickness of InGaN, emission peak blue-shifts, which can be attributed to the Quantum-Confined Stark Effect (QCSE) induced by the presence of a huge piezoelectric field within the crystal. For $In_{0.2}Ga_{0.8}N$/GaN QWs, by varying the thickness from 3 to 5.5 nm, the PL emissions are found to cover the whole visible spectral regions.[220] Thus, it is possible to generate white light by combining two or more suitable wavelengths emitted from different thicknesses of these kinds of low-dimensional structures.

2.3.2.1 Vegard's Law and Bandgap Bowing

It is very essential to have precise knowledge of the bandgap as a function of alloy composition to design and fabricate new optoelectronic device structures with desired emission. Vegard's law is commonly used to estimate the composition of ternary materials from extrapolating from the endpoint binaries. Using similar concept, the bandgap of $In_xGa_{1-x}N$ can be approximated by the composition-weighted average of the GaN and InN bandgaps, and can be expressed as

$$E_g^{In_xGa_{1-x}N} = xE_g^{InN} + (1-x)E_g^{GaN}$$

where, the bandgaps of wurtzite GaN and InN at 300 K are $E_g^{GaN} = 3.42$ eV[124], $E_g^{InN} = 0.64$ eV[15], respectively.

However, in reality researchers have found that InGaN bandgap does not follow the linear dependence on the indium composition and thus, to incorporate the non-linear effects of alloying and to measure the deviation from a linear interpolation between InN and GaN bandgaps, a nonlinear term with a "bowing" parameter, b, can be added to the previous linear Vegard's law and can be expressed as

$$E_g^{In_xGa_{1-x}N} = xE_g^{InN} + (1-x)E_g^{GaN} - bx(1-x)$$

In depth experimental and theoretical studies have been carried out to determine the value of the bowing parameter. However, the origin of the bowing parameter has not been concluded yet and values ranging from 1 to 6 eV have been reported in the literature (see Table 2.1). The diversity of the reported values indicates the difficulty of getting an universal bowing parameter which can be used throughout the composition range, since InGaN samples are grown by different techniques at different conditions. Possible factors influencing the band bowing parameter is discussed below.

2.3.2.2 Factors Influencing The Bowing Parameter

Most of the recent optoelectronic devices consist of very thin (2-3 nm) layer of InGaN, and their light emission characteristics are controlled by the indium composition as well as the layer thickness, as these two factors mainly determine the bandgap and strain of the InGaN layer. According to some researchers, for precise determination of the composition-dependent InGaN bandgap, the bandgap should be measured by Photoreflection[230] or Spectroscopic Ellipsometry[231] rather than from PL, as they believe that InGaN PL emission is shifted relative to the band-edge, which leads to an underestimation of the bandgap.[232] Using Photoreflection (PR) Spectroscopy and Optical Transmission (OT) measurements, smaller bowing parameter as compared to PL, has been reported.[225,226] It has also been discussed that the difference in bowing parameter estimation can result from the error in indium composition determination by XRD measurement, as the thin InGaN layer grown on GaN is greatly strained by biaxial compressive stress which causes a blue-shift of the bandgap as compared to the unstrained InGaN. Therefore, the bandgap of unstrained InGaN is expected to be smaller than that determined by a similar technique.[227] Moreover, theoretical studies have shown that the bowing parameter also depends on the indium composition[205], and similar claim has been experimentally

Table 2.1: The bowing parameter (b), reported by different groups.

Growth Technique	Thickness (nm)	Compo -sition Measure -ment	Indium Content (x)	Strain State	Band Gap Measure -ment	Bowing Parameter b, (eV)
MOCVD	15 - 60	SIMS	0.02 - 0.15	Strained	PR	3.2[224]
MOCVD	-	XRD	0.07 - 0.33	-	PL	1.0[25]
				Strained	PR	2.6[225]
MOCVD	40	XRD	$0 < x < 0.2$	Relaxed	PR	3.8[225]
				Strained	PL	3.2[225]
MOCVD	250	RBS	$x \leq 0.12$	Strained	OT	3.5[226]
MOCVD	40	XRD	0 - 0.2	Strained	PL	3.2[227]
MOCVD	30 - 100	XRD	0 - 0.25	Relaxed	PL	4.11[228]
				Strained		3.42[228]
MBE	300	XRD	0.2 - 0.27	Strained	PL	3.6[186]
MBE	400	XRD	$x < 0.10$	Relaxed	PL	6.0[188]
			$x > 0.13$			4.0[188]
MBE	250	XRD	$0.61 < x < 1.0$	Relaxed	PL	1.8[187]
MBE	200 - 7500	-	0 - 0.5	-	OA	1.4[150,176]
-	-	-	$x = (0.0625,$ 0.125, 0.25)	Relaxed	Simulation	$b = (4.8,$ 3.5, 3.0)[205]
-	-	-	0 - 0.375	Relaxed	Simulation	1.21±0.03[229]

Note: PR: Photoreflection Spectroscopy; PL: Photoluminescence Spectroscopy; OT: Optical Transmission Spectroscopy; OA: Optical Absorption Spectroscopy;

demonstrated by Shen *et al.*[188]

Since the sources of erroneous measurements have led to the inaccuracy of the alloy composition, at present no common agreement is established for the use of Vegard's law in determination of the indium content. However, HRXRD is widely used to determine the lattice parameters of the semiconductor thin films, where the chemical composition is calculated by applying Vegard's law. As discussed in the previous section, this

unique relationship between lattice parameters and chemical composition holds only for the relaxed lattice parameters.[233,234] Under biaxial compression, the InGaN unit cell gets distorted and c lattice constant gets elongated, causing a systematic overestimation of the indium composition[205,226], and this contributes to the underestimation of the bowing parameter. Therefore, it is sometimes suggested that the composition of InGaN alloy should be determined not only by HRXRD, but also by some complementary chemical analysis to minimize the error in the composition value. Presence of strain complicates the determination of the composition by HRXRD, as it requires the use of the correct elastic parameters of InGaN.[224] Chemical techniques such as Rutherford Backscattering Spectroscopy (RBS), Secondary Ion Mass Spectroscopy (SIMS) and EPMA, which are insensitive to the strain state of the samples, are suggested to be used alternatively to analyze the chemical composition[209], but these techniques give better results only if the samples are relatively thick.

It has come to a consensus recently, that the bandgap of InN is smaller than 1.0 eV[145–151], rather than the previously accepted value of 1.9 eV.[235] It has been understood that Burstein-Moss shift in the optical absorption edge, caused by high electron concentration in degenerately doped InN films[150], is responsible for the 1.9 eV bandgap. Although the presently accepted InN bandgap is about 0.64 eV[15], some members of the research community still believe the "classical" 1.9 eV InN bandgap value, as it was strongly supported experimentally by several groups.[152–154,236] This kind of disagreement about the InN bandgap has lead to the large scatter of the reported band bowing parameter values of InGaN.

Therefore, it can be understood that the bowing parameter is strongly influenced by the optical technique used to determine the bandgap, the quality of the materials (e.g. presence of strain, phase separation, compositional inhomogeneity etc.), the measurement of the exact indium content of the alloy, and the correct bandgap value of the constituent binary materials.

2.3.2.3 Emission Mechanism: Indium Segregation and Piezoelectricity

From literature it can be observed that there is a long standing debate on the emission mechanism in the InGaN alloys. Some researchers have claimed that responsible

mechanism is exciton localization caused by spatial indium content fluctuations or phase separation in InGaN due to the formation of self-organized QDs and in support they have reported a large Stoke's shift between optical absorption and emission.[190,232,237–240] Other groups[227,241–243] believe that the radiative recombination occurs due to the Quantum-Confined Stark Effect (QCSE) induced by the large internal electric fields of InGaN. However, Kawakami *et al.*[244] commented that the discrepancy could be attributed to the insufficient information available on optical data, the degree of localization, as well as the contribution from internal electric fields, which are different from sample to sample as they are grown using different growth techniques, under different growth conditions.

It has been predicted from InGaN phase diagram that due to the large miscibility gap, phase separation occurs in InGaN films which leads to the inhomogeneity of the indium content, and as a result, at typical MOCVD growth temperatures of 700 - 800 °C, InGaN is thermodynamically unstable to incorporate even moderate indium concentration.[161] Formation of InN nanoclusters or QDs due to phase separation in MOCVD grown InGaN has been reported by few groups.[238,245–247] The exciton localization in the QDs is considered to be responsible for the unique light emission characteristics of the InGaN alloy and the first model of emission mechanism is based on this concept. The exciton localization determines the emission energy in LEDs and contributes to optical gain in laser structures[248] and thus shows many promising effects on the performance of the InGaN-based optoelectronic devices. In the second model, the QCSE recombination mechanism is attributed to the presence of a large piezoelectric field in InGaN. Presence of huge internal electrical fields in III-nitrides QWs has been reported to occur due to their wurtzitic symmetry.[249–251] This internal electrical field separates the carriers along the polar axis (which is the growth axis in most of the cases), and as a consequence, the radiative lifetime increases drastically, and enhances the non-radiative recombination of carriers at dislocations.[220] Presence of an internal electric field in InGaN QWs has been reported to show red-shift in PL as compared to thicker InGaN films, having the same indium content as that of the QW layer.[220,227,252]

Shapiro *et al.*[253] reported that both indium phase separation and piezoelectric field effects are involved in the radiative recombination processes and found that indium phase separation effects are dominant in the structures with high indium content, whereas piezo-

electric effects dominate in relatively low indium content ($x < 0.15$) structures. Ochalski *et al.*[254] compared PL and PR spectra on a series of identically grown InGaN/GaN QWs, except their growth duration, and pointed out that the emission mechanism of the samples can be explained only if both localization effect and QCSE are considered together. Similar conclusion has been reported by Grandjean *et al.*[220] for GaN/AlN QDs and InGaN/GaN QWs.

In their elaborate work, Monemar *et al.*[255,256] has found that the emission occurs due to the recombination of separately localized electron and holes in the distorted QW potential, where the extent of distortion depends on the strength of the piezoelectric field, and ultimately influences the width of the PL peak. They have also concluded that by lowering the InGaN growth temperature, the short-range potential fluctuations related to indium segregation can be minimized.

During investigation on the origin of carrier localization in the highly efficient radiative traps, Arindam Chowdhury *et. al.*[257] have observed the presence of two distinct classes of carrier localization centers within the same QW sample, using spectrally resolved PL microscopy on green light emitting $In_{0.22}Ga_{0.78}N$ QW LEDs. They have also found that the deep traps originate from local compositional fluctuations of indium within the alloy, while the shallow traps arise from nanometer-scale thickness variations of the active layers, presence of which has also been supported by Poisson-Schrodinger self-consistent calculations done by them.

Recently, localization effect in blue-violet light emitting InGaN/GaN MQWs has been studied[258] with varying InGaN growth rate. From temperature-dependent PL measurement it has been observed that for higher-growth-rate samples two emission peaks appear in their PL spectra, due to the coexistence of two different localization luminescence states (i.e., deep and shallow localization states) in the InGaN QWs with higher QW growth rate. It has been also found that, with decreasing InGaN growth rate, the deep localization state remains almost unchanged whereas the shallow localization state becomes weaker. Below a certain value of QW growth rate, the shallow localization state disappears and only the peak induced by deep localization state survives in the PL spectra. Moreover, an intermediate InGaN growth rate is reported to result in a better light emission efficiency of the MQW.

2.4 Importance of Nanostructures

Nanostructures, structures having atleast one dimension between 1-100 nm, have received enormous interest as a result of their fascinating properties, and superior applications than their bulk counterparts[259–261], and thus, such structures have become an essential part of the modern science and technology. The most significant example is microelectronics, where "smaller" structure has shown greater performance in terms of more components per chip, faster operation, lower cost, and less power consumption.[262] There are constant efforts to develop magnetic and optical storage components with critical dimensions as small as tens of nanometers.[263] Examples involving nanostructures in other technologies are size-dependent excitation or emission,[264–266] quantized (or ballistic) conductance,[267,268] Coulomb blockade (or single-electron tunneling, SET),[269] and metal-insulator transition.[270]

Two-dimensional (2D) nanostructures (or QWs) have been extensively studied by the semiconductor community because of the convenience of preparation of such structures using techniques like MBE, and significant progress has been achieved with regard to zero-dimensional (0D) nanostructures (or QDs)[271,272] in the past two decades. Size dependent fundamental properties[273] of QDs have enabled research community to fabricate model devices using QDs as active components, for instance, QD lasers,[274] single-electron transistors,[275] memory units,[276] sensors,[277] optical detectors,[278] and LEDs.[279]

Recently, one-dimensional (1D) nanostructures such as wires, rods, belts, and tubes have shown huge promise in their applications in mesoscopic physics and fabrication of nanoscale devices.[280,281] Due to the presence of quantum confinement effect, 1D nanostructures can be explored for the fabrication of functional units in electronic, optoelectronic, electrochemical, and electromechanical devices with nano dimensions.

2.4.1 Group-III Nitride Nanostructures

Semiconductor nanostructures are being extensively investigated for applications in high performance electronic[282,283] and optical[284] devices, as they offer a distinct way to study electrical, photonic, and thermal transport phenomena as a function of dimensionality, size reduction, and surface-to-volume ratio. As a result, growth and characterization

of InN and InGaN nanostructures have been carried out by several groups and some of them are briefly discussed here.

Growth of InN nanostructures with different geometries, such as NWs,[285,286] NRs,[95] nanocolumns,[88,287–289] and nanotips,[290] has been reported by several groups, where the bandgap of InN has been observed to be near 0.7 eV, in most of the cases.

PAMBE growth of vertically aligned InN NRs on Si(111) has been demonstrated by Shen *et al.*[95], where individual NRs were wurtzite InN single crystals with the growth direction along the *c*-axis. Near-infrared PL from InN NRs was observed at RT, though the PL efficiency was significantly lower as compared to InN films. Moreover, the variable-temperature PL measurements of InN NRs revealed anomalous temperature dependence, which was proposed to be the results of considerable structural disorder and strong surface electron accumulation effects.

The structural evolution of PAMBE grown InN on Si(111), from microsized grains to nanocolumns, and finally to a 2D film, was studied by Hsiao *et al.*[88] Grainy InN was grown at a higher growth temperature, under a higher N/indium BEP ratio, and on a low-temperature InN buffer layer. On the other hand, a high-quality InN 2D film was grown at a lower growth temperature, under a lower N/indium BEP ratio, and on a high-temperature AlN buffer layer, and the 2D InN film showed a RT Hall mobility and a carrier concentration of 860 $cm^2/(V\text{-}sec)$ and 8.9×10^{18} cm^{-3}, respectively. PL showed the emission peak in the infrared region suggesting the bandgap of the InN to be in the range of 0.64 - 0.66 eV.

The growth conditions to obtain Group-III nitride nanocolumns and nanocolumnar heterostructures by PAMBE are studied by Calleja *et al.*[287] The evolution of the nanocolumnar morphology with the growth conditions is determined for (Ga,Al)N and (In,Ga)N nanocolumns, where growth under very high N-rich conditions is concluded to be the main requirement for nanocolumnar growth. The nanostructure geometry was controlled by means of the growth temperature and the III/V ratio, although the achievement of N-rich conditions was not equivalent in terms of growth temperature, metal flux, and RF power. For InN or high indium content (In,Ga)N nanocolumns, growth temperature was controlled carefully to avoid thermal decomposition and/or a too high indium mobility. It has been established by the authors that the growth of Group-III nitride

nanostructures under excess N does not require any surfactant, catalyst, or seeding of the substrate surface, so that the Vapour-Liquid-Solid (VLS) model does not account for this growth regime. They have also mentioned that when nanocolumns are grown on bare Si substrates using MBE, a very thin SiN layer, having random orientation, develops that may lead to the loss of the epitaxial relationship between the nanostructure and the substrate. The unintentional formation of this SiN thin layer can be avoided by depositing a few ML of Al metal prior to the growth or by using high-temperature AlN buffer layers. However, the growth conditions were found to change from a bare Si substrate to an Al-covered one or AlN-buffered one in terms of the excess nitrogen required, as the surface diffusivity of Group-III atoms was not the same in all the cases.

InN nanocolumns were produced under nitrogen rich conditions, to understand the mechanism of self organized growth of nanocolumns on p-Si(111) using PAMBE by Denker *et al.*[288] It has been shown that the morphology strongly depends on the growth temperature and the indium flux and depending on the growth parameters different growth regimes for nanocolumns were identified according to their final shapes (hexagonal, round, tilted-oblong, layer-like etc.). These structures show high crystal quality and have lengths of about 2 μm and diameters of about 20-70 nm.

The effect of growth parameters, especially on the PL spectra has been investigated for InN NWs grown on Si(111) substrates by Stoica *et al.*[285], where the shape analysis of PL spectra was used to obtain bandgap and intrinsic carrier concentration of InN NWs. For different growth conditions, major variations of InN NW properties are found to be occurring due to changes in the equilibrium carrier concentration. The optical bandgap and the electron concentration of unintentionally doped samples were found in the range 0.73 - 0.75 eV and 8×10^{17} to 6×10^{18} cm^{-3}, respectively. A decrease of the intrinsic doping level with increase in indium flux, growth temperature and growth duration, was observed. HRTEM showed that, despite a good crystallinity, some point defects were present within the bottom part of the NWs.

MBE grown high-quality InN nanocolumns on n-type Si(111) have been electrically characterized by AFM[289], where current-voltage characteristics were measured on InN nanocolumns having similar heights but different diameters. It was shown that electrical conduction in GaN nanocolumns proceeds mainly through the volume, whereas in InN

nanocolumns the conduction path is located mainly at their lateral surface. These facts suggested that there is electron accumulation in as-grown nonpolar InN surfaces.

Unidirectional, well-aligned and single crystalline InN nanoemitters were fabricated on the Si(111) substrate via ion etching on MBE grown InN(0002)/AlN(0002)/Si(111) sample by Wang *et al.*[290] These InN nanotips showed excellent field emission properties with 1 μA/cm^2 field emission current density at a threshold field as low as 0.9 V/μm. This superior property is attributed to the enhancement of the geometrical factor of the InN nanostructures as well as to the inherent high carrier concentration of the degenerate InN, having a surface electron accumulation layer, which induces downward band bending effect and significantly reduces the effective electron tunneling barrier even under very low external field.

Magneto-transport properties in PAMBE grown InN NWs have been investigated by Richter *et al.*[286] By performing temperature-dependent transport measurements and current measurements on a large number of NWs of different dimensions, it has been shown that the carrier transport mainly takes place in a tube-like surface electron gas. Measurements carried out on three representative NWs, under an axially oriented magnetic field, showed magneto-conductance oscillations with a periodicity of a single magnetic flux quantum, which is explained by the effect of the magnetic flux penetrating the coherent circular quantum states present in the InN NWs. The occurrence of the single magnetic flux quantum periodicity is attributed to the magnetic flux dependence of phase-coherent circular states having different angular momentum quantum numbers forming the one-dimensional transport channels. The existence of these phase coherent states is correlated with the ideal crystalline properties of the InN NWs.

Currently, the growth of nanostructures of InGaN on sapphire[291–295] as well as on Si[296–301] is being intensely investigated due to several advantages, such as significantly reduced dislocation density, decreased polarization fields due to low lattice strain and increased light extraction efficiency due to large surface-to-volume ratio.[302]

InGaN/GaN NR structures[291] with different indium compositions has been fabricated by Wang *et al.* from InGaN/GaN MQW epitaxial wafers using a self-organized nickel nano-mask and subsequent dry etching techniques. The IQEs of the NRs are found to be significantly improved as compared to the as-grown InGaN/GaN MQWs. For the

green and blue InGaN/GaN NRs, the IQE enhancement factors are 8 and 3.4, respectively. X-ray Reciprocal Space Mapping (RSM) measurements have confirmed that the majority of strain in InGaN/GaN MQWs is relaxed afe the fabrication of NRs. Moreover, the excitation power dependent PL measurements have demonstrated a significant reduction of the strain-induced quantum confined stark effect in the NR structures.

Similar improvement of IQE and reduction of internal electric field due to strain relaxation has been reported by Bai *et al.*[292] They have observed two distinct regions at moderate forward bias in the current-voltage characteristics of NR LEDs, where the first region is found to be dominated by diffusion-recombination process, whereas in case of the later one tunnelling transport dominates, over a wide range of bias. The reverse leakage current of NR LEDs is observed to be one order of magnitude higher as compared to the planar ones.

Detailed optical characterization has been performed on an assembly of InGaN/GaN nanocolumn structure[293] as well as on a single nanocolumn grown by PAMBE. PL detection of single nanocolumn was achieved using a mechanical lift-off technique, and the results indicate that the broad PL spectrum observed in case of the assembly of nanocolumns, is due to the sum of the sharp PL spectrum originating from individual nanocolumns. These observations suggest that carrier localization as well as the internal piezoelectric field is suppressed in InGaN/GaN nanocolumns.

The optical properties of InGaN/GaN QWs, nanopatterned into cylindrical shapes with diameters of 2 μm, 1 μm, or 500 nm by chemically assisted ion beam etching, were investigated by Kawakami *et al.*[294] PL and time-resolved PL measurements suggested inhomogeneous relaxation of the lattice-mismatch induced strain in the InGaN layers, which lead to an enhanced radiative recombination rate by a factor of 4 - 8. By comparing to a strain distribution simulation, it was found that even though strain was relaxed at the free side wall, it remained in the middle of the cylindrical structures.

InGaN/GaN NR LEDs[296] have been fabricated using inductively coupled plasma reactive-ion etching (ICP-RIE) and a photo-enhanced chemical (PEC) wet oxidation process via self-assembled Ni nanomasks. Six times enhancement in PL intensities of NRs made with the PEC process was achieved as compared to that of the as-grown structure. The PL peak position showed a blue shift of 3.8 nm for the NRs made without the PEC

oxidation process and 8.6 nm for the NRs made with the PEC oxidation process with respect to that of the as-grown LED sample. Moreover, EL spectrum suggested that electrically pumped NR LEDs are more efficient, which showed a 10.5 nm blue-shifted peak with respect to the as-grown LED sample.

Single crystalline and single phase InGaN nanopillars were grown spontaneously on Si(111) using PAMBE by Vajpeyi *et al.*[297] indium incorporation in the nanopillars was controlled by changing the growth temperature, for instance, by lowering the growth temperature indium content was increased, which was determined from EDS and PL spectra. The lower value of indium incorporation compared to the applied indium composition was attributed to indium desorption at the growth temperature employed. It was demonstrated that the emission wavelength could be tuned from a blue to green luminescent region depending on the growth temperature, with the help of RT and low temperature PL spectra. The wavelength tuning was attributed to the higher indium incorporation at lower growth temperature which was consistent with the EDS and HRXRD results. The optical quality of the InGaN nanopillars was found to improve at higher growth temperature.

The nanoscale structural properties of RFMBE grown InGaN nanopillars on Si(111) were investigated using electron microscopy techniques.[298] Single phase, single crystalline initial nanostructures were observed to merge in order to form final nanopillars, whereas some of them, which are perfectly aligned along the growth direction, continue to grow individually. Good crystal quality of the nanopillars were identified by HRTEM and the compositional homogeneity along the *c*-axis of the nanopillars was examined and correlated with their luminescence properties. High growth temperature and desorption of indium was attributed to the negligible indium incorporation in the initial stages of growth. indium accumulation at the tip area of nanopillars was interpreted by the formation of a thin indium-adlayer at steps of the top surface of merged nanopillars. The limited mobility of indium atoms along the *c*-axis, in absence of appropriate migration paths, was found to be responsible for 20% indium-content at the tips of nanopillars, which resulted in the emission in the blue region.

To investigate the indium composition distribution of PAMBE grown InGaN NWs on Si(111), without a buffer layer, EDS was carried out by Tabata *et al.*[299] It was found

that the indium composition line profiles are different at each position in the InGaN NWs, and the indium composition at the top of the NWs was higher than that at any other positions, regardless of the NW length. Moreover, the indium composition at the top of the NWs was found to be dependent on the growth temperature and the indium flux ratio. However, the indium compositions at other positions were not dependent on these factors, and remained constant at about 10%. High growth temperature and low indium flux ratio are reported to improve the indium composition uniformity of the InGaN NWs. These observations are attributed to the limited diffusion of indium atoms from the top of the NWs towards the NWs/Si interface.

Vertically well aligned InGaN NR arrays have been grown by MBE on bare as well as high-temperature AlN-buffered Si(111) substrates by Wu *et al.*[300] In case of growth on bare Si, presence of an amorphous SiN_x layer at the interface was observed by HRTEM, and the thickness and flatness of that layer was found to affect the relative alignment of the NRs with the substrate. The interface quality was improved by using the high-temperature AlN buffer layer, and the obtained InGaN NRs were uniform in nature. Finally, n-InGaN NRs/p-Si heterostructure diodes were fabricated, which demonstrated well rectifying behavior with a low turn on voltage of 1.2 eV and an on/off ratio of 7.2 at 2.5 V.

NRs composed of pure GaN and InGaN segment have been grown on Si(111) using MBE by Kim *et al.*[301] The GaN NRs were crystalline with a wurtzite structure and preferentially oriented in the *c*-direction, whereas the InGaN segment had cubic crystal structure. SEM showed that the NRs had several short branches of pure GaN and their growth direction was [0001]. EDS Indicated that indium was included at some specific region of the NR and the observed branches were pure GaN, which grew on the InGaN segment. CL spectrum of the NRs exhibited two peaks at 3.10 and 3.40 eV at RT, which originated from the InGaN segment and the GaN branches, respectively.

Previously, our group has done some remarkable work on InN[303–307] which are briefly discussed below.

The issue of bandgap controversy has been addressed for InN films grown on *c*-sapphire, under nitrogen rich condition at different growth temperatures by PAMBE.[303] Single crystalline wurtzite InN is formed, but their orientation is found to depend on

the growth temperature. The bandgap measured on these unintentionally degenerately n-doped samples (1.78 eV) is explained in terms of Moss-Burstein shift. These results discount the effects of crystal orientation, presence of Oxygen at grain boundaries and In/N stoichiometry as possible factors influencing the measured bandgap values.

Another set of experiments[304], where wurtzite InN films have been simultaneously grown by PAMBE on differently modified *c*-sapphire substrates, discount Mie resonances caused by metallic indium segregation at grain boundaries as the possible reason for low bandgap values (≈ 0.6 eV) and also the formation of indium oxides and oxynitrides as the possible cause for high bandgap value (≈ 2.0 eV). It is also observed that polycrystallinity, arising from azimuthal misorientation of *c*-oriented wurtzite InN crystals, increases the carrier concentration as well as the bandgap values, and has been attributed to the Moss-Burstein shift with a non-parabolic conduction band approximation.

High quality InN films have been grown on Si(111)-7×7, Si(111)-4×1-In and Si(111)-1×1-In reconstructed surfaces.[305] InN grown on Si(111)-1×1-In reconstructed template shows superior film quality with lowest and narrowest band-edge emission, intense and narrow (0002) XRD peak, low surface roughness and intrinsic carrier concentration one order lower than other samples. The high quality of the film formed at 300 °C has been attributed to the in-plane integral matching of InN lattice and 1×1 super lattice dimensions, and therefore, the study demonstrates that the proposed Superlattice Matched Epitaxy is an useful approach to grow good quality InN at much lower growth temperature.

The carrier concentration, strain, and bandgap issue of InN films grown on *c*-sapphire at different nitrogen-flux by PAMBE has been addressed using XRD and XPS.[306] It has been observed that the strain in InN films arises due to point defects like nitrogen interstitials and nitrogen antisites. Observed minimal biaxial strain is found to occur due to relaxed growth morphology, whereas minimal hydrostatic strain arises due to interstitial nitrogen atoms. Nitrogen interstitials and nitrogen antisites act as donors and causes unintentional degenerate doping and variation in absorption edge, which has been attributed to Moss-Burstein shift.

The surface charge accumulation on InN thin films which strongly effects the mobility of charge carriers have been studied[307], on the PAMBE grown InN films having different morphology, crystallinity, and optical properties. The bandgap values obtained from

optical absorption and PL studies are found to depend on the measured Hall carrier concentration and also follow the Moss-Burstein relation. The bulk carrier concentration is found to be related to the crystalline quality of the InN films. The magnitude of the near surface band bending is calculated by determining the surface and bulk Fermi level position with respect to the valence band maximum using XPS and optical absorption measurements, respectively. These studies show that the surface charge accumulation occurs due to the presence of indium adlayer on the film, which causes band-bending upto 1 eV for low bandgap single crystalline films, whereas the absence of the band-bending is seen to occur for the highly degenerate polycrystalline films, where the bulk carrier concentration tends to equate with the surface charge density.

By now it can be assumed that the readers are convinced about the properties, importance and applications of Group-III nitrides; especially nanostructures and are well aware of the difficulty of InN and InGaN growth and respective characterizations. All these fascinating properties as well as the interesting research work carried out previously by our group have motivated us to continue to work on InN as well as on InGaN.

Chapter 3

Experimental Details

To understand the dependence of various properties of InGaN films on different growth parameters, we have used MBE growth technique and several in-situ and ex-situ characterization tools. This chapter provides the basic information of the various experimental methods used in this study and provides the physical principles that form the basis of the functioning of the apparatus used for both the growth and characterization.

It is organized in the following order: first, the thin film growth method, namely the Plasma Assisted Molecular Beam Epitaxy (PAMBE), is discussed in detail. Next, the characterization techniques used throughout the thesis is elaborated. For morphological and structural characterization, the techniques used are Field Emission Scanning Electron Microscopy (FESEM) and High Resolution X-ray Diffraction (HRXRD) and for optical characterization Photoluminescence (PL), Cathodoluminescence (CL) and UV-Vis-NIR Absorption Spectroscopies are used. For analyzing chemical state of the elements, X-ray Photoelectron Spectroscopy (XPS) is used and Hall Effect measurement system is used to determine the type, mobility and concentration of the majority carriers.

3.1 Plasma Assisted Molecular Beam Epitaxy

Figure 3.1 (a) and (b) show a photograph of Plasma Assisted Molecular Beam Epitaxy (PAMBE) growth system at Jawaharlal Nehru Centre for Advanced Scientific Research (JNCASR) and the schematic diagram of the growth chamber of the MBE system, respectively. The system is manufactured by SVTA, USA.

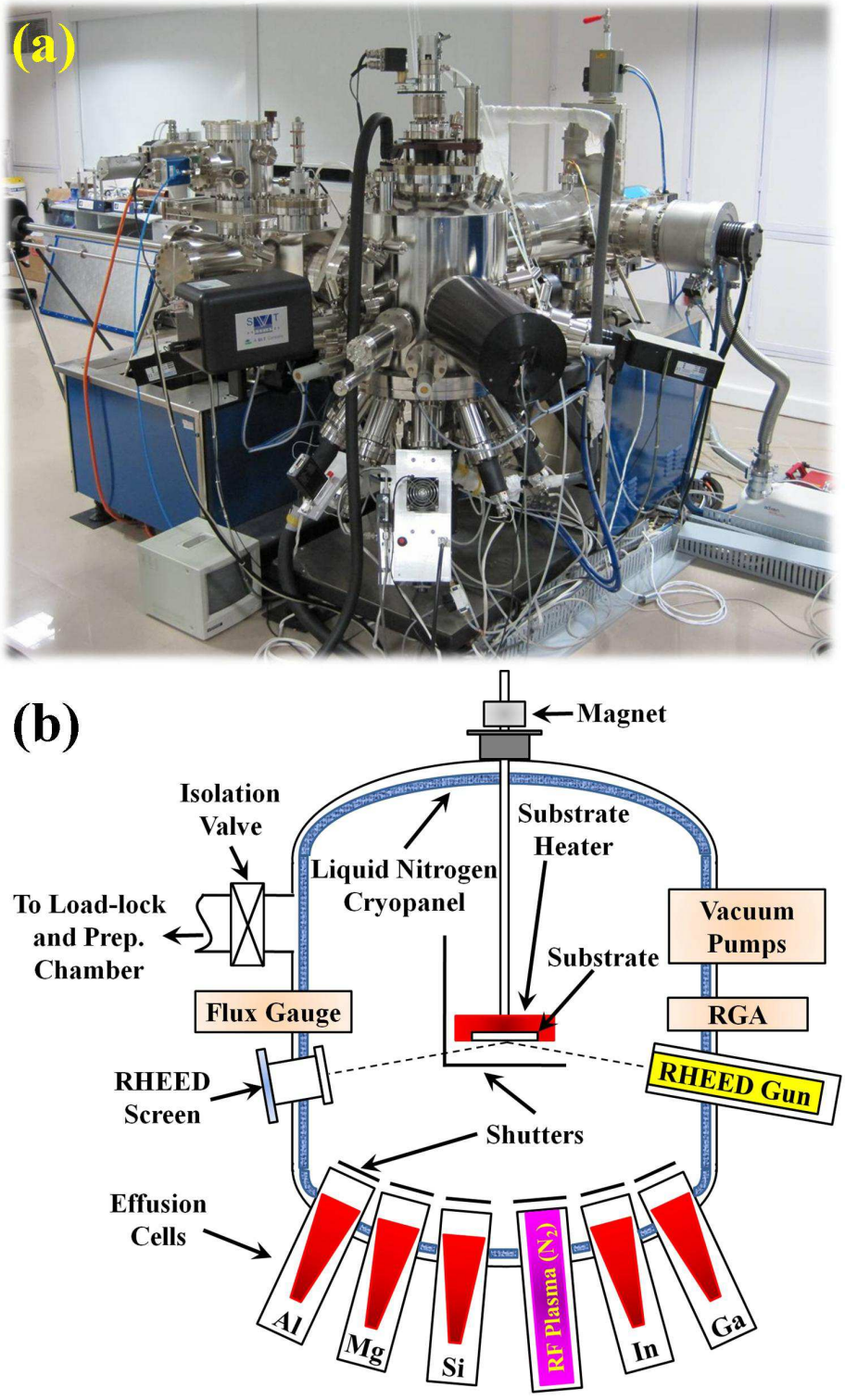

Figure 3.1: (a) shows a photograph of MBE growth system used to grow III-nitride films for this work and (b) shows the schematic diagram of the growth chamber of the MBE system.

Different pumps like turbo, cryo and ion pumps (cryo and trubo pumps exclusively during the growth) are connected with the growth chamber to achieve UHV condition (10^{-11} torr), as measured by ion gauge. Loading and unloading of the samples are carried out through the load-lock chamber, where a turbo pump is connected. All the substrates are chemically pre-cleaned using isopropyl alcohol (IPA) and acetone before being introduced in the load-lock chamber. The preparation chamber has a water cooled sample heating/degassing facility, which can go up to 700 °C. The main chamber consists of a cryo-panel around it, which is cooled by liquid nitrogen to prevent degassing of atoms from the chamber walls, and thus also acts as a cryo pump. The heater, attached with the growth manipulator, can heat the substrate upto 1200 °C, and thus the manipulator is cooled by water during growth. The rotation of the growth manipulator is controlled by the magnet assembly attached to a motor. This motor controller is equipped with an ON/OFF switch and also an option to select clockwise and anticlockwise rotation. Active nitrogen radicals are supplied by a radio frequency inductively coupled plasma source. Group-III metals (In, Ga and Al) and dopants (Si and Mg) are supplied by effusion cells and their fluxes are controlled by the temperature of the cells. Shutters placed in front of the sources permit direct control of the epitaxial growth surface at a monolayer level by changing the incoming beam with the opening and closing of the shutter. Growth can be monitored *in-situ* by a Reflection High Energy Electron Diffraction (RHEED) system. Upto 3-inch substrate can be mounted on the growth stage achieving a growth uniformity of $< 1\%$ over the diameter of 2.8 inch. The growth temperature is monitored by a thermocouple, which is calibrated using a pyrometer. Together the growth temperature, metal flux-rate, plasma power and nitrogen flow-rate determine the morphology and growth rate of the films being grown. The operation of the MBE system can be carried out through the panel control board as well as computer automation. In case, any part of MBE is reassembled for troubleshooting purpose, the system has been baked at 150 °C for at least 48 hrs to remove water and other contamination, before film deposition.

Some of the important components of MBE and *in-situ* techniques attached to MBE are discussed briefly in the following sections:

3.1.1 Effusion Cells

Water cooled standard effusion cells (Knudsen Cells or, most commonly known as K-cells) are used to supply Group-III metal flux. An effusion cell comprises of a crucible containing the solid or liquid evaporant, which is radiatively heated. The electrically insulated heater filaments are wound non-inductively, either spirally or end-to-end, to prevent magnetic interference of electron diffraction facilities in the MBE system. A thermocouple, carefully positioned to ensure intimate contact with the crucible, registers the source material temperature. After flux calibration, the source temperature can thus be used to maintain flux-rate, although frequent recalibration is found to be necessary because of source material depletion, redistribution of charge material, and changes in the thermal environment. Crucibles are made of pyrolitic Boron Nitride (PBN) and high purity (99.9999%) metal ingots are used in the K-cells. Once loaded with metal, all effusion cells were again briefly degassed to approximately 10% above the maximum intended operating temperature. The flux from the effusion cells is calibrated by Flux gauge, where the change in metal BEP is registered with the change of K-cell temperature. A chiller is used to control the temperature of water at 16 °C, and the cold water is flown around the K-cells to take away excess heat during growth.

3.1.2 Nitrogen RF Plasma Source

As nitrogen is inert at achievable growth temperatures, a plasma or ion source is required to activate the N_2 molecule. The primary source used in this work is a radio frequency inductively coupled plasma source (RF-4.5 by SVTA). The basic structure of an RF plasma source is shown in Figure 3.2. An inductively coupled plasma source is essentially a copper coil of several turns, through which cooling water is running in order to dissipate the heat produced in the operation. The coil wraps a confinement tube, a pyrolytic Boron Nitride (PBN) in our case, inside which the induction plasma is generated. One end of the PBN tube is open as the plasma is actually maintained on a continuous gas flow. Ultra high pure (99.9995%) nitrogen gas is controllably leaked into the cavity via the inlet and flow is controlled by a 0 – 10 sccm (standard cubic centimeters per minute) mass flow controller. During induction plasma operation, the generator supplies an alternating current (ac) of radio frequency (r.f.) to the copper coil

and this ac induces an alternating magnetic field inside the coil, according to Ampere's law (for a solenoid coil): $\phi_B = \mu_0 I_C N \pi r_0^2$, where, ϕ_B is the flux of magnetic field, μ_0 is permeability constant ($4\pi \times 10^{-7}$ Wb/A.m), I_C is the coil current, N is the number of coil turns per unit length, and r_0 is the mean radius of the coil turns. The alternating field accelerates charged particles which collide further with other species and a plasma is formed. According to Faraday's Law, a variation in magnetic field flux will induce a voltage, or electromagnetic force: $E = -N(d\phi/dt)$, where, N is the number of coil turns, and the item in parenthesis is the rate at which the flux is changing. The generated plasma is conductive and this electromagnetic force, E, will in turn drive a current in closed loops to resist the change of the magnetic field. The situation is much similar to heating a metal rod in the induction coil and thus the energy transferred to the plasma is dissipated via Joule heating, according to Ohm's Law. In practice, the ignition of plasma under low pressure conditions (< 300 torr) is almost spontaneous, once the r.f. power imposed on the coil achieves a certain threshold value (depending on the source configuration, gas flow rate etc.), a stable induction plasma is created. For the case of atmospheric ambient pressure conditions, ignition is often accomplished with the aid of a Tesla coil, which produces high-frequency, high-voltage electric sparks that induce local

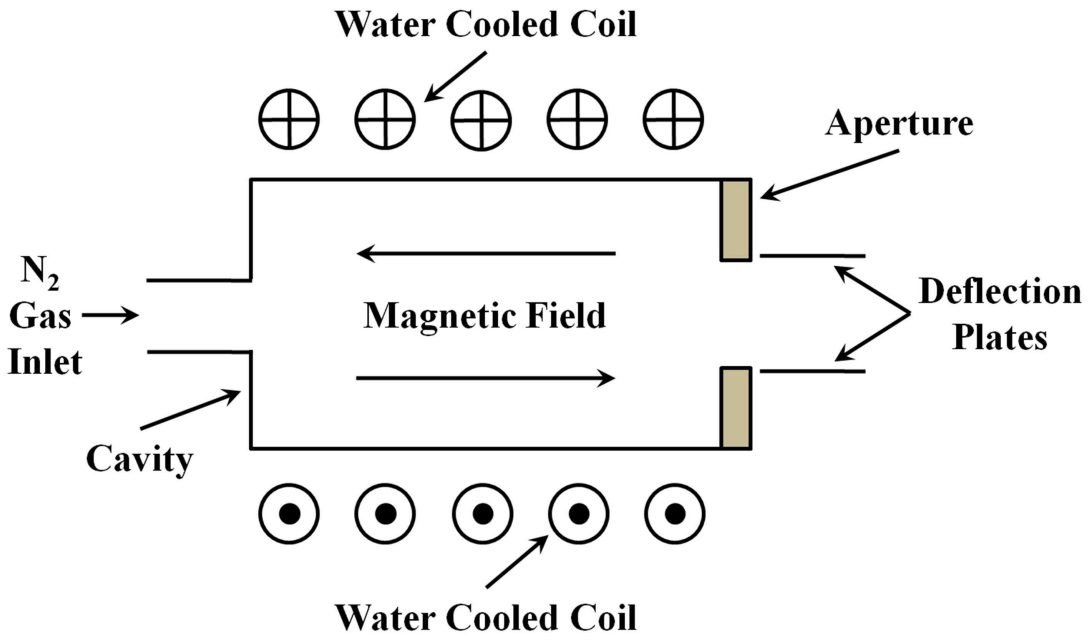

Figure 3.2: shows the schematic diagram of a radio frequency inductively coupled plasma source.

arc-break inside the source and stimulate a cascade of ionization of plasma gas, ultimately resulting in a stable plasma.

Typically the source was operated at RF powers of 300 – 400 W and a flow rate of 2 – 8 sccm for the growth of our films. The species generated by an RF plasma source can vary substantially at different plasma operating conditions and also from different source geometries. The plasma source also contains a deflection plate which is used to deflect the charged species as needed.

3.1.3 Residual Gas Analyzer

A Residual Gas Analyzer (RGA) is a mass spectrometer of small physical dimensions that can be connected directly to a vacuum system and whose function is to analyze the gases inside the vacuum chamber.[308] It uses the difference in mass-to-charge ratio (m/e) of ionized atoms or molecules to separate them from each other. The RGA used here consists of a quadrupole probe, and an Electronics Control Unit (ECU). The quadrupole probe consists of three parts: the ionizer, the quadrupole filter and the ion detector. All of these parts reside in the vacuum space where the gas analysis is carried out.

Ionizer: As can be seen in the inset of Figure 3.3, inside the Ionizer, the filament is resistively heated to emit electrons, which are then accelerated towards the anode grid cage having a wire mesh design. As a result, most electrons do not strike the anode immediately, but pass through the cage where they create ions through electron impact ionization and hence, once the ions formed, tend to stay within the anode grid structure. The focus plate is kept at a negative potential (relative to ground) and its function is to draw the ions out of the anode cage and focus them into the filter section. The repeller, which completely encloses the ionizer, is biased negative relative to the filament and prevents the loss of electrons from the ion source.

Quadrupole mass filter: The general principle of operation of the filter can be visualized (See Figure 3.3) qualitatively in the following terms: One rod pair (X-Z plane) is connected to a positive DC voltage upon which a sinusoidal RF voltage is superimposed. The other rod pair (Y-Z plane) is connected to a negative DC voltage upon which a sinusoidal RF voltage is superimposed, 180 degrees out of phase with the RF voltage of the first set of rods. The potentials are represented by the expression:

$V_{x/y}$ = +/- (U + V_0 cosωt)

where, U is the magnitude of the DC voltage applied to either pair of rods,

V_0 is the amplitude of the RF voltage applied to either set of rods, and

ω is the angular frequency (= 2πf) of the RF.

Light ions (low mass-to-charge ratio) are able to follow the alternating component of the field. For the X direction, those ions will stay in phase with the RF drive, gain energy from the field and oscillate with increasingly large amplitudes until they encounter one of the rods and are discharged. Therefore, the X direction is a high-pass mass filter: Only high masses will be transmitted to the other end of the quadrupole without striking the X electrodes. On the other hand, in the Y direction, heavy ions will be unstable because of the defocusing effect of the DC component, but some lighter ions will be stabilized by the alternating component if its magnitude and amplitude are such as to correct the trajectory whenever its amplitude tends to increase. Thus, the Y direction is a low-pass mass filter: Only low masses will be transmitted to the other end of the quadrupole without striking the Y electrodes.

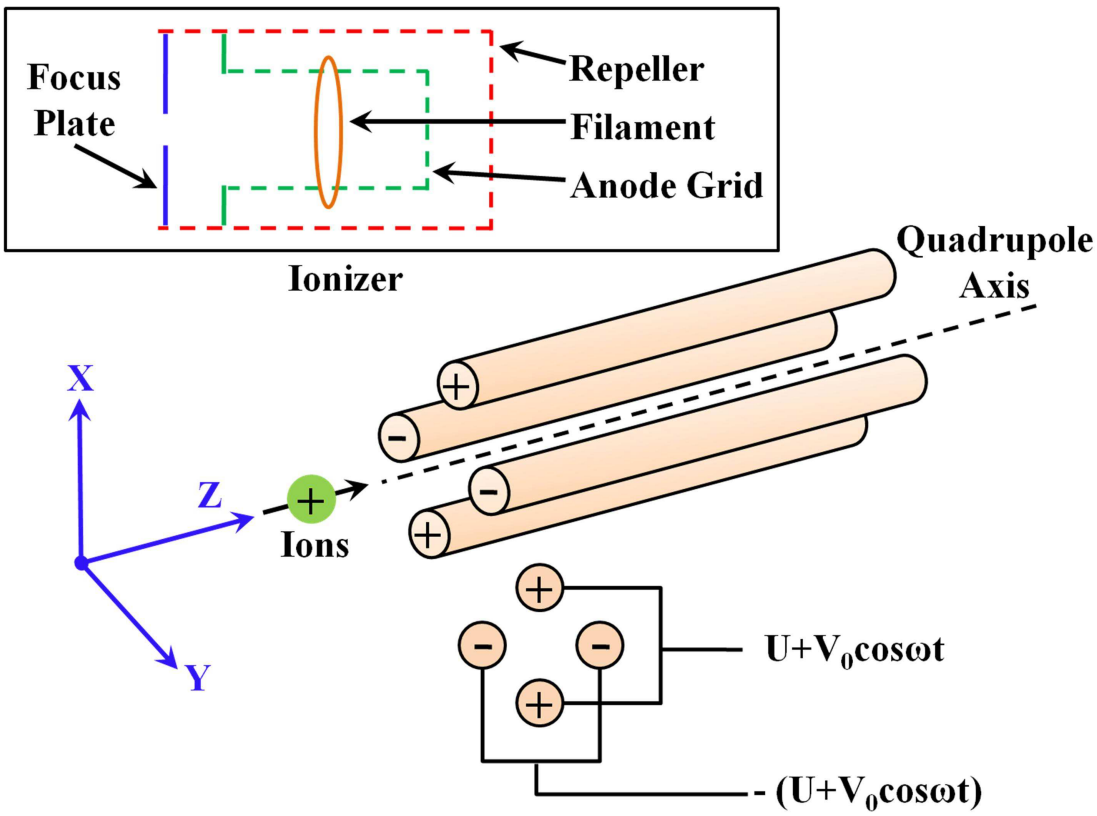

Figure 3.3: shows the schematic diagram of the quadrupole probe of a RGA.

The two directions together give a mass filter suitable for mass analysis: By a suitable choice of RF/DC ratio the filter can be made to discriminate against both high and low mass ions to the desired degree. The RF voltage magnitude and frequency determine the mass of the ions that undergo stable trajectories down the filter. As the RF amplitude increases, heavier ions start to oscillate in phase with the RF and collide with the rods. The DC/RF ratio determines the filter selectivity. As the DC increases (at constant RF) heavier ions are defocused by the negative DC component.

Ion Detector: Positive ions that successfully pass through the quadrupole are focused towards the detector by an exit aperture held at ground potential. The detector measures the ion currents directly (Faraday Cup) or, using an optional electron multiplier detector, measures an electron current proportional to the ion current.

The ECU completely controls the operation of the RGA, handles its data and transmits it to the computer for analysis and display.

Our MBE main chamber is attached with Stanford Research Systems Residual Gas Analyzer (RGA) which can monitor gaseous species of up to 200 a.m.u. This allows outgassing times to be tailored to achieve acceptably low levels of water vapour and also monitor for any residual solvents that may remain after substrate degassing. The dominant gas species remaining at low pressure is H_2, which is the most difficult gas to eliminate in any UHV system since its tiny molecular diameter allows it to enter the chamber even through conflated copper O-ring seals.

3.1.4 Reflection High Energy Electron Diffraction

Reflection High Energy Electron Diffraction (RHEED) is a very powerful *in-situ* real time growth monitoring technique.[309] In our MBE system STAIB RHEED setup is connected. It consists of a high energy electron gun capable of a focused 10 kV beam energy and a phosphor coated screen with recording camera on the opposite side of the chamber to capture the RHEED pattern, as shown in Figure 3.4(a). This technique utilizes the grazing angle (1 - 4°) incidence of the high energy electron beam (Figure 3.4(a)) in which the wavelength of the electron is comparable to typical atomic spacing ($\approx$ 0.1 - 1 nm) and therefore is a surface sensitive tool. The electrons scatter off different atomic planes, within the first few nanometers of the film and interface, constructively and

destructively to form a diffraction pattern on the phosphor screen. From this diffraction pattern (or most commonly known as RHEED pattern) one can monitor the structural and morphological properties of the growing crystal, in real time.

Construction of Ewald's sphere is used to find the crystallographic properties of the sample surface as the spots of a perfect pattern to the Ewald's sphere is related to the reciprocal lattice of the sample surface.[310] The reciprocal lattices of bulk crystals consist of a set of points in 3D space. However, only the first few layers of the material contribute to the diffraction in RHEED, so there are no diffraction conditions in the dimension perpendicular to the sample surface. Due to the lack of a third diffracting condition, the reciprocal lattice of a crystal surface is a series of infinite rods extending perpendicular to the sample's surface. The Ewald's sphere is centered on the sample surface with a radius equal to the reciprocal of the wavelength of the incident electrons. Diffraction conditions are satisfied where the rods of reciprocal lattice intersect the Ewald's sphere (Figure 3.4(b)). Many of the reciprocal lattice rods meet the diffraction condition, however the

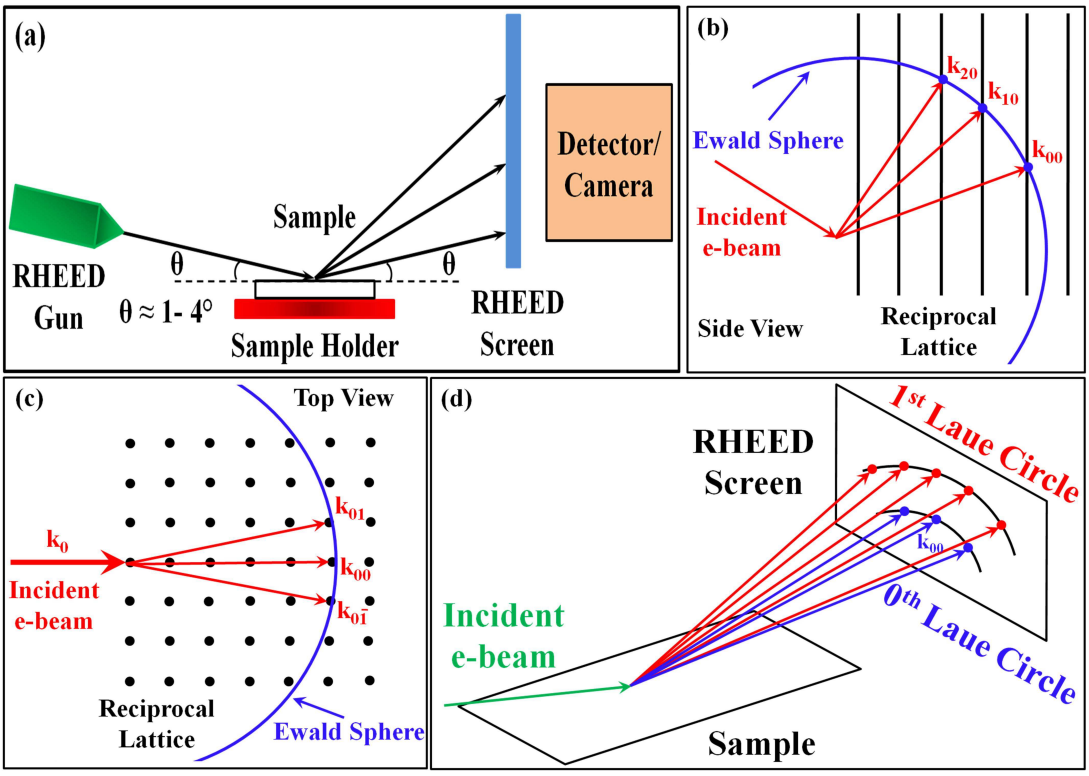

Figure 3.4: (a) shows the setup of a RHEED system. (b) and (c) show the side and top view of RHEED construction of the Ewald's Sphere at the sample surface. (d) shows the Laue pattern formed on the phosphor screen during RHEED experiment.

RHEED system is designed in such a way that only low orders of diffraction are incident on the detector. The pattern are labeled such that the intersections which form the smallest angle with the sample surface and has the highest intensity is called 0^{th} order beam. Each successive intersection of a rod and the sphere further from the sample surface is labeled as a higher order reflection. The radius of the Ewald's sphere is much larger than the spacing between reciprocal lattice rods because the incident beam has a very short wavelength due to its high-energy electrons and as a result rows of reciprocal lattice rods actually intersect the Ewald's sphere as an approximate plane (Figure 3.4(c)). The intersections of these effective planes with the Ewald's sphere forms circles, called Laue circles (Figure 3.4(d)). The RHEED pattern is a collection of points on the perimeters of concentric Laue circles around the center point. However, interference effects between the diffracted electrons still yield strong intensities at single points on each Laue circle.

Typical RHEED pattern of single crystalline surfaces are dominated by a combination of reciprocal lattice streaks and Kikuchi lines. The shadow edge signifies where the beam is blocked by the film/substrate, and the separation of this and the direct beam represent the angle of incidence of the beam impinging on the film. Typical spot size for the electron beam is ≈ 100 μm, and the spacing of the reciprocal lattice streaks is inversely proportional to the spacing of the atomic planes taking part in diffraction. Whether the streaks appear continuous or broken can be used to understand the roughness of the growth front.[311] Streaky RHEED pattern indicate the smoothness of the film on a nm scale and the patterns are solely due to reflection/diffraction. On the other-hand, if the pattern appears spotty then it indicates that there is roughness on the nm scale, in which case some electrons are transmitted through 3D surface features and cause an interference pattern. The growth rate can be determined from RHEED intensity oscillations, for which the period corresponds to one monolayer of growth. In this thesis RHEED is primarily used to determine the crystalline nature of the film surface, e.g. poly or single crystalline and to understand atomically flat or rough surface of the grown film.

3.2 Field Emission Scanning Electron Microscope

Field Emission Scanning Electron Microscope (FESEM) is used for the analysis of surface morphology of the grown films.[312] A schematic diagram of FESEM is shown in Figure 3.5. The typical FESEM system consists of an electron gun as a source of electrons, the column of condenser lenses which regulate the intensity of the electron beam and direct it onto the specimen and finally a detector to detect the secondary electron generated by the bombardment of high energy electron beam and to eventually produce the image.

3.2.1 FESEM Components

In standard electron microscopes, electrons are mostly generated by heating a tungsten filament by passing electrical current to produce a temperature of about 2800 °C. Sometimes electrons are produced by a crystal of lantanum hexaboride (LaB_6) that is mounted on a tungsten filament. This modification results in a higher electron density in the beam and a better resolution than with the conventional device. Particularly in a FESEM, a so-called "cold" source is employed, where an extremely thin and sharp tung-

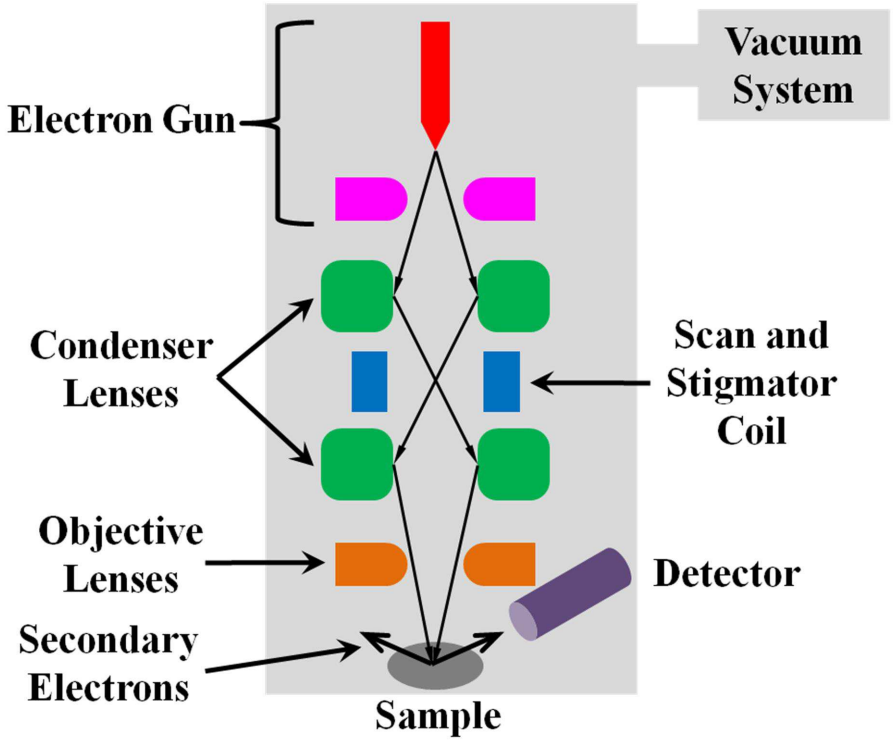

Figure 3.5: shows the schematic diagram of Field Emission Scanning Electron Microscope.

sten needle (tip diameter ≈ 10 - 100 nm) functions as a cathode in front of a primary and secondary anode. The voltage between cathode and anode is of the order of magnitude of 0.5 to 30 kV. Because the electron beam diameter produced by the FE source is about 1000 times smaller than in a standard microscope, the image quality is remarkably better. As field emission (FE) requires an extreme vacuum ($\approx 10^{-8}$ Torr) in the column of the microscope, a device is present that regularly decontaminates the electron source by a current flash. In contrast to a conventional tungsten filament, a FE tip lasts theoretically for a lifetime, provided the vacuum is maintained stable. The microscope (Quanta 3D FEG) used in our study also has FE electron source, which is heated as well and called as Schottky source. The filament of the source is made of tungsten and covered by zirconium oxide (ZrO_2) in order to lower the work function of the cathode material.

The electron beam is focused by the electro-magnetic lenses and the apertures in the column to a tiny sharp spot. The electro-magnetic lens system consists of the following parts:

1. Condenser Lens: The current in the condenser determines the diameter of the beam; a low current results in a small diameter, a higher current in a larger beam. A narrow beam has the advantage of better resolution, but at the same time it has the disadvantage of low signal to noise ratio. The situation is reversed when the beam has a large diameter. The condenser lens generally has two parts, which are distributed before and after the scanning coils.

2. Scan Coils: The scan coils deflect the electron beam over the object according to a zig-zag pattern. The formation of the image on the monitor occurs in synchronization with this scan movement. The scan velocity determines the refreshing rate on the screen and the amount of noise in the image (rapid scan ⇒ rapid refreshing ⇒ low signal ⇒ much noise). The smaller the scanned region on the object, the larger the magnification becomes at a constant window size. Scan coils often consist of upper and lower coils, which prevent the formation of a circular shadow at low magnification.

3. The Objective Lens: The objective lens is the lowest lens in the column. The objective lens focuses the electron beam on the object. At a short working distance (⇒ object in a higher position ⇒ closer to the objective lens) the objective lens needs to apply a greater force to deflect the electron beam. The shortest working distance produces the

smallest beam diameter, the best resolution, but also the poorest depth of field. (The depth of field indicates the range in vertical direction in the object, that can still be visualized sharply).

4. The Stigmator Coils: The stigmator coils are utilized to correct irregularities in the x and y deflection of the beam and thus to obtain a perfectly round-shaped beam. When the beam is not circular, but ellipsoidal, the image looks blurred and stretched.

After the object has been attached with a conductive layer, to avoid the electron accumulation on the samples, which leads to the screening of the sample to new incoming electrons, it is mounted on a holder. The holder along with the mounted sample is placed on a movable stage situated inside the object chamber which is maintained at high vacuum. In the microscope the object can be re-positioned in the chamber by moving the stage using a software controlled by a computer. In addition, the object can also be tilted, rotated and moved in Z direction ($\Rightarrow$ closer or further away to the objective lens), if necessary. The "secondary electron detector" is located at the rear of the object holder in the chamber.

3.2.2 Image Formation

When the finely focused electron beam falls on the object, secondary electrons are emitted from the object surface with a certain velocity that is determined by the levels and angles at the surface of the object. An image is formed by scanning a cathode ray tube to collect the secondary electron signal generated from the beam-sample interaction. An image is build up point by point, which shows the variations in the generation and collection efficiency of the chosen signal at various points over the surface of the specimen. The location and intensity of illumination of the image vary depending on the properties of the secondary electrons. The contrast in the 'real time' image that appears on the screen reflects the structure on the surface of the object, and consequently a digital image is generated which can be further processed.

In this work, all FESEM images are obtained using an Quanta 3D FEG (FEI, Netherlands) FESEM system, which has a CL(Cathodoluminescence) and FIB(Focussed Ion Beam) attachments.

3.3 High Resolution X-ray Diffraction

Almost a century after von Laue's discovery of X-ray diffraction (XRD) by crystals in 1912, XRD is now still widely used to study solid-state physics and material science. X-ray photons with energy in the range of $\sim$ keV has the wavelength in the order of few $\sim \mathring{A}$, which is of the order of the atomic spacing in crystals. This makes XRD a powerful tool to study microscopic properties of solids such as crystal structure, defects, stress and chemical components.[313–315] Compared with some other characterization techniques, X-ray diffraction analysis is nondestructive and the conventional setup is relatively cheap.

When X-rays are diffracted from a crystal lattice, the outcoming X-rays can interfere constructively, which gives rise to the commonly known X-ray diffraction pattern. The constructive interference occurs only when a particular condition is satisfied by the X-rays, popularly known as the Bragg's Law, mathematically expressed as:

$2dsin\theta = n\lambda$

where λ is the wavelength of the X-ray; 2θ is the angle between incident beam and the diffracted beam, also known as diffraction angle; d is the spacing of the reflection planes (not necessarily the planes are parallel to the sample surface) and n is the order of reflection. Bragg's Law allows us to calculate details about the crystal structure. The inter-planar distance (d) is determined by the Miller indices (hkl) of the family of planes. For cubic crystal with lattice constant a, the distance is: $d = \frac{a}{\sqrt{(h^2+k^2+l^2)}}$, and for hexagonal crystal such as wurtzite GaN, the distance is written as: $d = \frac{1}{\sqrt{\frac{4}{3}\frac{(h^2+hk+k^2)}{a^2}+\frac{l^2}{c^2}}}$.

3.3.1 HRXRD Setup

Figure 3.6(a) shows schematically the setup of the HRXRD diffractometer. For the present work we have used a Bruker D8 diffractometer. The diffractometer consists of an X-ray tube with a copper cathode and a four-bounce Ge(220) monochromator, which generates the incident CuK_α X-ray beam ($\lambda = 1.540595(2)\ \mathring{A}$). The angle between the incident X-ray beam and the surface of the crystal is denoted as ω (Figure 3.6(a)). The crystal, that shall be examined, is mounted on the sample holder of a so-called Euler cradle. Therewith, it can be rotated around the three Euler angles ω, ϕ and χ (Figure 3.6(b)). The angle ϕ, ranging from 0 - 360°, measures the azimuthal rotation around the

surface normal of the sample, whereas χ is defined as the angle between sample surface and the plane of interest (in the 0 - 90° range). The scattered beam can be detected by an X-ray detector that encloses an angle 2θ with the incident beam. If the incident ($\mathbf{k_i}$) and diffracted ($\mathbf{k_o}$) beam vectors make appropriate angles with respect to the crystal, the scattering vector ($\mathbf{S} = \mathbf{k_i} - \mathbf{k_r}$) will end at a reciprocal lattice point (as diffraction can also be illustrated in the context of the reciprocal lattice) and thus by varying ω and the position of the detector, the scattering vector ($\mathbf{S}$) can be adjusted (Figure 3.6(b)) and the whole crystal can be probed.

Differentiation of the Bragg's law and subsequent division of the result by the same equation yields the differential Bragg equation: $\frac{\Delta\lambda}{\lambda} = cot\theta.\Delta\theta + \frac{\Delta d_{hkl}}{d_{hkl}}$

From differential Bragg equation, it can be understood that for the accurate determination of the distance d_{hkl} between two adjacent lattice planes it is important to use

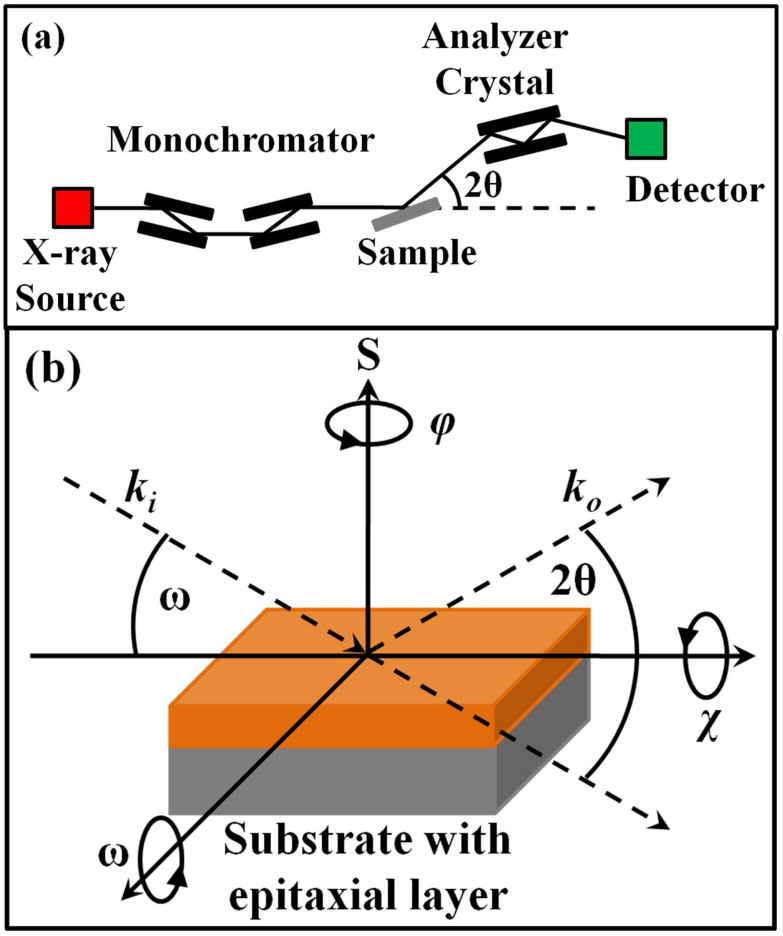

Figure 3.6: (a) shows schematic diagram of HRXRD setup (b) shows the geometry of the goniometer with possible Euler angles of rotation.

a highly monochromatic incident beam and a detector with a very good angular resolution. By means of a Bartels monochromator whose functional principle is based on the Bragg reflection of the primary beam at four germanium crystals with (220) surfaces, the spectral width of the incident CuK_α X-ray beam can be reduced to $\frac{\Delta\lambda}{\lambda} < 1.5 \times 10^{-4}$. In order to enhance the spectral resolution of the diffractometer, diaphragms with aperture angles $\Delta\theta$ ranging from $\frac{1}{32}^\circ$ to 4° or an analyzer with an aperture angle of 12 arcsec can be used. Especially for higher indexed reflexes with low intensities, the use of the analyzer is not always possible and therefore an appropriate diaphragm has to be used instead. Nevertheless, higher indexed reflexes are preferable for the determination of the lattice constants because for $\theta \to 90^\circ$ the influence of $\Delta\theta$ in differential Bragg equation can be significantly suppressed.

3.3.2 HRXRD Scan Types

Different scan types available on high-resolution diffractometers are listed below.

$2\theta - \omega$ scan: The sample (or the X-ray source) is rotated by ω and the detector is rotated by 2θ with an angular ratio of 1:2. In reciprocal space, **S** moves outwards from the origin. The length of **S** changes, but its direction remains the same and depends on the offset. For $2\theta - \omega$ scans, the x-axis is in units of 2θ. When there is no offset and $\omega = \theta$ this is a symmetrical scan $(\theta - 2\theta)$ which is vertical in reciprocal space and same as the standard scan type for powder diffraction. Particularly this scan is useful to check if there are other crystalline phases incorporated in the crystal, which is true if other than the expected reflexes are observed. Moreover, the occurrence of forbidden reflexes hints at structural disorder in the examined crystal.

$\omega - 2\theta$ scan: Simply a $2\theta - \omega$ scan, but with ω on the x-axis, which is same as the standard scan type for reflectivity and high-resolution work. Generally, a combination of $\omega - 2\theta$ scan and ω scan can be used to map a two-dimensional region of the reciprocal space, which is commonly known as reciprocal space map. A reciprocal space map of an asymmetrical reflex allows the determination of both the a and the c lattice constant of the epitaxial layer of interest.

2θ scan: The sample and source remain stationary and the detector is moved. **S** traces an arc along the circumference of the Ewald sphere, where both the length and the

direction of **S** change. This scan is generally used for the preliminary alignment of the epitaxial film under study.

ω **scan:** The detector remains stationary and the sample is rotated about the ω axis. In reciprocal space, **S** traces an arc centered on the origin. The length of **S** stays the same, but its direction changes. The plot of the scattered X-ray intensity as a function of ω is often called rocking curve. The width of the symmetric rocking curve is influenced by a finite crystallite size as well as the tilt of the crystallites with respect to one another. On the other hand, the twist of the crystallites in a mosaic crystal is responsible for the broadening of the asymmetric rocking curve. Therefore the FWHM of the rocking curve is often used as a figure of merit to evaluate the degree of tilt and twist of crystallites within an epitaxial film. The smaller the FWHM, the better the individual crystallites are aligned and the larger their size.

ϕ **scan:** Rotation of the sample about the ϕ axis (usually in the plane of the sample). The length of **S** stays the same, but the sample is moved, bringing the reciprocal lattice spot through **S** so that the direction of **S** changes with respect to the sample. Hence, for asymmetric reflexes of wurtzite III-nitride films, by performing a ϕ-scan of 360°, six peaks can be observed which is in accordance with the sixfold symmetry of the [0001]-axis. By conducting such a 360° ϕ-scan for the substrate and the thin film on top, the in-plane epitaxial relationship between substrate and overgrown film can be established.

χ **scan:** Similar to ϕ scans, except that the sample is rotated about the χ axis (plane of the sample rotated with respect to the incoming beam). This scan also is generally used for the preliminary alignment of the epitaxial film under study.

3.3.3 Diffraction Geometries for $2\theta - \omega$ Scan

Symmetric: In this geometry, planes parallel to the sample surface are investigated. The ω and 2θ of incoming and outgoing beams with respect to the sample surface are simultaneously varied, where $\omega = \theta$.

Asymmetric: An asymmetric $2\theta - \omega$ scan can be performed for the planes having tilt (τ) with respect to the sample surface. As in the case of a symmetrical scan, the detector is placed at an angle of 2θ with respect to the incoming beam. The incoming beam, however makes an angle of ω with respect to the sample surface. Since $\omega = \theta \pm \tau$,

grazing incidence (-) or grazing exit (+) $2\theta - \omega$ scans can be collected in this asymmetric geometry.

Skew-symmetric: An alternative way of getting the asymmetric scan is in the skew-symmetric geometry, where the sample is tilted over a fixed angle around the χ-axis instead of the ω-axis. The rest of the procedure to acquire the $2\theta - \omega$ scan in skew-symmetric geometry is same as symmetric scan.

In this work, HRXRD has been extensively used to extract the following information:

i) The crystalline nature of the film and its epitaxial relation with the substrate.

ii) The c-lattice parameter of the samples to calculate the indium composition of the samples.

3.4 Ultraviolet-Visible-Near-Infrared Absorption Spectroscopy

The bandgap of III-nitride films grown in this study is measured through a simple Ultraviolet-Visible-Near-Infrared (UV-Vis-NIR) spectroscopy.[316] The technique relies on the fact that a photon will travel through a material without getting absorbed as long as there are no available electronic transitions of the same energy as the photon. If there are available transitions for an electron, then there is a finite probability that the photon will get absorbed and the electron will get excited to make the transition to a high energy state. Therefore, by measuring the absorption of photons with different energies, an understanding of the possible electronic levels within the material can be obtained. As we know that ideally all semiconductors have a finite bandgap, then photons with less energy than the bandgap will be transmitted, while the photons with energy greater than the bandgap will be absorbed.

In this technique, a light source with a broad spectrum is normally incident upon a sample. As mentioned already, wavelengths corresponding to allowed energy transitions are absorbed by the sample, and the rest of them, which are not absorbed, pass through the sample (transmitted) and are recorded by the detector. By taking the ratios of the incident and transmitted intensities as a function of wavelength, one can conclude which wavelengths were absorbed to obtain an absorption spectrum of the sample. The intensity

of light transmitted through a film of thickness d is expressed as

$I_t(E) = I_0 exp(-\alpha(E)d)$

which can also be written as $\alpha(E) = \frac{ln(1/T)}{d}$

where, I_0 is the intensity of the incident beam and $\alpha(E)$ is the absorption coefficient and T($= \frac{I_t(E)}{I_0}$) is the transmittance of the given film. Thus, from the absorption measurements, done in transmission geometry, we can calculate the absorption coefficient of the material.

For a semiconductor, absorption coefficient is described by the following relation[317,318],

$\alpha(E) = C(E - E_g)^n$

where, E_g is the bandgap of the semiconductor, C is a constant and the value of the exponent n denotes the nature of the transition; for instance, $n = 1/2$ for direct transitions and $n = 2$ for indirect transitions. Now from these two expression of $\alpha(E)$, it can be understood that by plotting E (the energy of the incident probing light) on the abscissa and the quantity $(\alpha)^n$ on the ordinate, a distinct linear regime can be obtained, which denotes the onset of absorption. Thus, extrapolating this linear region of the plots to $\alpha^n = 0$ yields the energy of the optical bandgap of the material.

In this work RT absorption measurements were carried out in transmission geometry using a Perkin-Elmer Lambda 900 UV-VIS-IR spectrometer, where emission from a Xenon (Xe) lamp is used as a source of incident light.

3.5 Photoluminescence and Cathodoluminescence Spectroscopy

Photoluminescence spectroscopy is a non-contact, nondestructive light-emission based method of probing the electronic structure, impurity and defect levels of semiconductor materials.[319,320] Photoluminescence occurs when light is directed onto a sample, where it is absorbed and photo-excitation takes place, which causes the electrons to jump to a higher electronic state, from where it then releases energy (in the form of photons), so that it can relax and return back to a lower energy level (recombination). The emission of light, or luminescence through this process is called as photoluminescence (PL). A suitable laser or filtered light from Xenon lamp that has a photon energy higher than the

bandgap of the semiconductor is incident on the surface of the sample, which will generate electron-hole pairs. Those electron-hole pairs will recombine, often through a radiative transition back to the ground state. Some of the observed recombination pathways are shown in Figure 3.7. Information about the band structure, donor and acceptor levels, types of defect, impurities, and crystalline quality in the material system can be extracted by measuring the wavelength of the emitted photon.

In cathodoluminescence (CL), energetic electrons are used as excitation source, unlike the photon source in PL.[321] CL is an optical phenomenon where a beam of electrons, is incident on the luminescent material causing the material to emit photons, similar to PL. The electron beam is typically produced in a scanning electron microscope, which can be focused to a sub-nanometer diameter and thus, a key benefit of CL technique over other luminescence characterization techniques is the ability to acquire information with high spatial resolution. Under the right conditions, spatial resolution approaching 1 nm can be achieved, far in excess of other optical techniques. Furthermore, an electron probe is extremely flexible due to the ease of scanning, focusing, and the large depth of field. The interaction volume inside a material for electrons are comparatively larger than that for photons and thus gives the freedom to vary the electron beam energy to change the

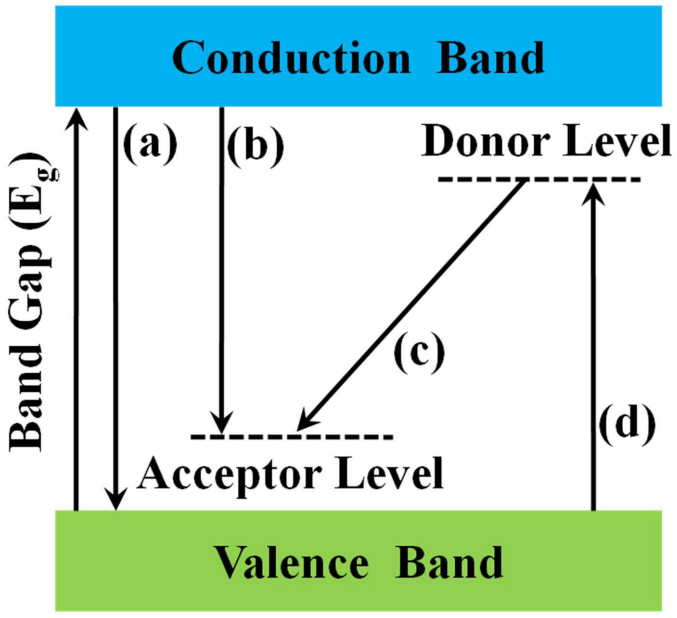

Figure 3.7: shows some basic recombination transitions in semiconductors during photo-luminescence (a) band to band transition, (b) free electron to acceptor level transition, (c) donor-acceptor transition, (d) donor electron and free hole.

penetration depth, in other words the depth resolution can also be achieved efficiently using CL.

For the work carried in the thesis, Horiba Jobin Yvon *i*HR320 PL system with Xenon lamp as the source of light has been used for PL measurements, whereas, a Gatan MonoCL4 detector attached to the Quanta 3D FEG (FEI, Netherlands) FESEM system has been used for CL measurements.

3.6 X-ray Photoelectron Spectroscopy

X-ray Photoelectron Spectroscopy (XPS) also known as Electron Spectroscopy for Chemical Analysis (ESCA) is the most widely used surface analysis technique because it can be applied to a broad range of materials and provides valuable quantitative and chemical state information from the surface of the material being studied.[322–324] XPS spectra are typically obtained by irradiating a solid surface with a beam of mono-energetic Al/Mg-K_α X-rays, having energy of 1253.6/1486.6 eV, while simultaneously measuring the kinetic energy of the electrons that are emitted from the top 1-10 nm of the material being analyzed, using an electron energy analyzer. The reason behind choosing Al/Mg-K_α X-rays is that the core levels of most of the elements lies within 0 - 1000 eV energy range. The source X-rays are generated by bombarding accelerated electrons ($\approx$ 15 keV), obtained by thermionic emission from a proximal tungsten filament, on Al/Mg coated anode. Photo-emitted electrons from the sample are collected using concentric hemispherical analyzer, which acts as a band-pass filter with high resolution (see Figure 3.8(a)). A retarding electrostatic lens-system is placed in front of the hemisphere in order to focus the electrons into the analyzer and to change the angular acceptance. XPS spectrum is recorded by counting ejected electrons over a range of electron kinetic energies. Peaks appear in the spectrum from atoms emitting electrons of a particular characteristic energy. The energies and intensities of the photo-electron peaks enable identification, chemical state and quantification of all surface elements (except Hydrogen and Helium). Spatial distribution information can be obtained by scanning the micro focused X-ray beam across the sample surface. Depth distribution information can be obtained by combining XPS measurements with ion milling (sputtering) to characterize thin film structures.

3.6.1 The Photo-emission Process

X-Ray Photoelectron Spectroscopy (XPS) is based on the photoelectric effect, which was first theorized by Albert Einstein in 1905. The photo-emission process from a solid sample takes place when a highly energetic photon interacts with matter, causing an electron to be removed from an atomic orbital or from a band and to reach the vacuum level. The excitation energy must be large enough for the electrons to overcome the work function of the solid. The initial state of the photo-electron can be either a valence band or a core level state. Thus, the kinetic energy of the photo-electron can be expressed as

K.E. = $h\nu$ - B.E. - Φ

where, $h\nu$ is the incident photon energy, B.E. is the electron binding energy and Φ is the work function of the material (difference between the Fermi level (E_F) and Vacuum level (E_V)) (see Figure 3.8(b)). If $h\nu$ and Φ are known, the measured K.E. would allow us to obtain the B.E. of characteristic core levels in the sample. Since each element has unique set of core levels, B.E. convey information on the chemical composition of the sample. In addition, the chemical environment in which the core electron is found prior to the photo-emission event (the type of bonding, the oxidation state, the possible presence of adsorbates) results in distinctive B.E. shift. A particular kind of chemical shifts are Surface Core Level Shifts, which denote the B.E. shifts between core level electrons originating from the surface and from the bulk. XPS is a quantitative technique because the cross-section for the emission of a photoelectron is not dependent upon the chemical environment of the atom.

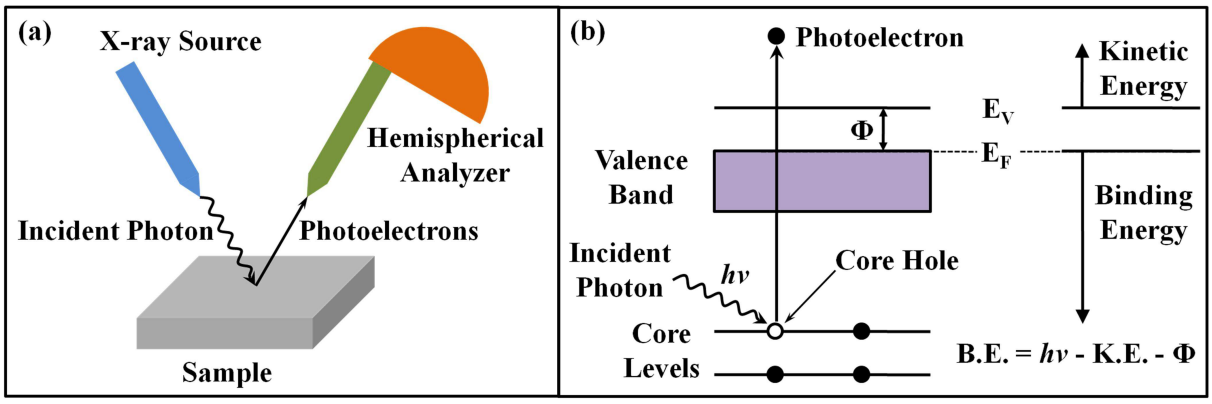

Figure 3.8: shows schematic diagram of (a) XPS system (b) the photo-emission process.

3.6.2 Analytical Information obtained from XPS

Several analytical information which can be obtained form XPS are listed below.[325,326]

Survey Scan: Energy peaks in the survey scan identify the elemental composition of the uppermost layer of the analyzed surface. All elements, except Hydrogen and Helium, are detected. Detection limits are approximately 0.1% for most elements.

High Resolution Core Level Scan: This technique evaluates the chemical state(s) of each element through its core electron binding energies. Precise determinations of binding energies of core levels are made through the use of curve fitting routines applied to the peaks. Shifts in the binding energy can result from the atom's oxidation state, chemical bonds, or crystal structure. A NIST database is available to identify binding energies with specific compounds.

Valence Band Scan: This scan is done generally in the low binding energy region (e.g. 0 - 30 eV) to identify the position of the valence band maixma (VBM) of the sample under study. Position of VBM can give information regarding the electronic structure (metal, semiconductor and insulator) of the sample and also the nature of doping (p- or n-type) in semiconductors. Other minute features in this scan can be used to identify the chemical state of the element of interest.

Quantification: The concentrations of the elements identified in the survey scan are determined by integrating the area under a characteristic peak for each element. Sensitivity factors are applied to the peak area values to determine the elemental concentration. The atomic fraction (relative percentage composition) of any constituent in a sample can be written as:

$X_a = \frac{I_a/S_a}{\sum I_i/S_i} \times 100\%$

where, I_a is the area/intensity of the peak of element A, S_a is the atomic sensitivity factor for the element A and the summation represents over all the constituent elements of the surface.

Depth Profile: The elemental composition is measured as a function of depth into the sample with the help of ion sputtering to remove material from the sample surface.

Elemental Mapping: The relative concentration of one or more elements is determined as a function of lateral position on the sample surface. An image is obtained where brightness indicates the element concentration.

In this work, we have used Omicron XPS system to identify, quantify of different constituent elements and also to analyze the chemical state of the elements of interest. XPS spectral deconvolution is achieved in Fityk open source software, where Shirley-type background subtraction has been done before the deconvolution. The shapes of the peak (height, width, Gaussian/Lorentzian function, etc.) are automatically varied until the best fit to the observed spectrum is achieved, considering physical aspects like peak position and FWHM etc.

3.7 Hall Effect Measurements

Hall effect describes the behavior of free charge carriers in the semiconductor when it is subjected to the electric and magnetic fields.[327] The phenomenon was discovered by Edwin Hall in 1879 and can be considered as an extension of Lorentz force, which describes the force exerted on a charged particle moving through a magnetic field. It is well known that a potential applied across the semiconductor material causes the charge carriers (electrons/holes) within it to move in the opposite/same direction (shown by purple arrows in Figure 3.9) to that of the applied field. Further, it is to be noted that, in this case, the path of the charge carriers will be almost a straight line. Now if the same material is subjected to the transverse magnetic field, the charge carriers start moving along the curved path as shown by green curved arrows in Figure 3.9, due to the force exerted by the

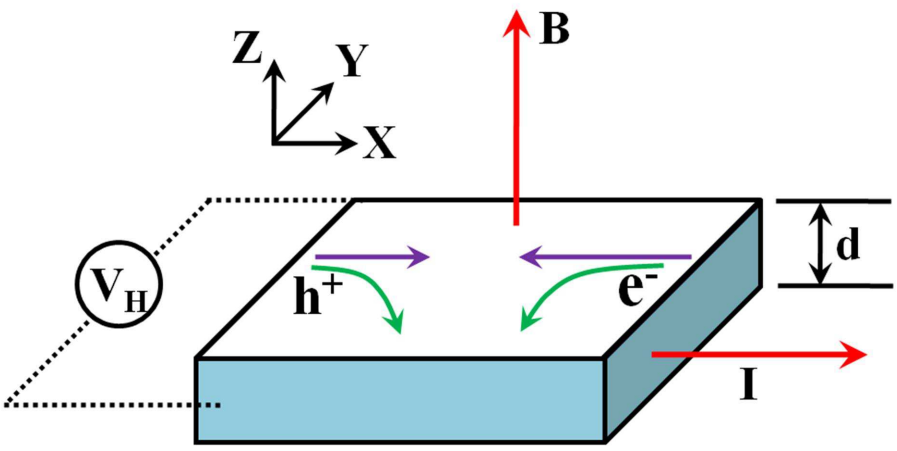

Figure 3.9: shows the schematic diagram explaining the origin of Hall Voltage (V_H) in case of a current carrying semiconductor slab placed under a constant magnetic field.

applied magnetic field on them. This leads to the increase in the number of electrons on one side of the semiconductor while the corresponding opposite side experiences electron deficiency or, hole abundance. As a result, there is a voltage developed across these two sides of the semiconductor material as shown in the Figure 3.9. The voltage so developed is called Hall Voltage (V_H) and the associated phenomenon is referred to as Hall Effect. The direction of the Hall voltage so developed will be perpendicular to both the direction of current flow as well as to the applied magnetic field.

Mathematical expression for the Hall voltage is given by:

$V_H = \frac{IB}{qnd} = R_H \times \frac{IB}{d}$

where, I is the current flowing through the sample, B is the magnetic field strength, q is the charge of charge carrier, n is the charge carrier density, and d is the thickness of the sample. Here the term $\frac{1}{qn}$ is called the Hall Coefficient (R_H) and is negative if the majority charge carriers are electrons, while positive if the majority charge carriers are holes.

3.7.1 Analytical Information obtained from Hall Measurements

Several analytical information which can be obtained form Hall measurements are listed below.

Determination of the Type of Semiconductor: By knowing the direction of the Hall Voltage, one can determine whether the given sample is n-type semiconductor or p-type semiconductor. This is because Hall coefficient is negative for n-type semiconductor while the same is positive in the case of p-type semiconductor.

Calculation of the Carrier Concentration: The expressions for the carrier concentrations of electrons (n) and holes (p) in terms of Hall coefficient are given by,

$n = -\frac{1}{eR_H}$ and $p = \frac{1}{eR_H}$

By knowing the Hall Voltage (V_H), for a known value of applied magnetic field strength, current and the thickness of the given sample, one can obtain the Hall coefficient (R_H), from which carrier concentration can be calculated easily using the above mentioned relationships.

Determination of the Mobility (Hall Mobility): Mobility of the electrons (μ_n) and the holes (μ_p) can be determined from the expression, which involves Hall coefficient

and is given by,

$R_H = \frac{p\mu_h^2 - n\mu_e^2}{e(p\mu_h + n\mu_e)^2}$

Hall effect measurements reported in this work have been performed by using a Ecopia HMS-3000 Hall Effect measurement system. Indium contacts are made to the samples in the Van der Pauw geometry.[328] The system includes a 0.58 T permanent magnet, and the direction of the magnetic field is changed by rotating the magnet by 180°. The system can pass a current up to 20 mA. Hall effect measurements were only made if a linear I-V curve was obtained, indicating the formation of Ohmic contacts with the material under study. During measurements, the sample is placed in a chamber that can be filled with liquid nitrogen, in case low-temperature measurements at 77 K is necessary.

Chapter 4

Growth of InGaN on *c*-Sapphire using different growth parameters

This chapter discusses the growth of InGaN nanostructures on c-sapphire using different growth parameters e.g. growth temperature, metal (indium and gallium) and nitrogen fluxes and describes their effect on the morphology, crystal quality, indium incorporation within the lattice and optical properties of the grown films. The work discussed in this chapter has been published in the following journals: Materials Research Express ***1****, 035019 (2014), Journal of Physics D: Applied Physics* ***49****, 355304 (2016)*

4.1 Effect of Growth Temperature

Effect of growth temperature on the morphology, structural and optical properties of InGaN layers grown under nitrogen-rich conditions, by PAMBE, on *c*-plane sapphire have been studied. By varying the growth temperature we are able to obtain tapered as well as flat-top nanorod and interconnected random network morphology. An increase of indium incorporation, determined by HRXRD, from 1% to 23% with decrease in growth temperature has been obtained. Room temperature PL and absorption measurements on the grown samples follow Vegard's law. A band bowing parameter of 1.54 eV has been determined for the observed composition range. A good quality InGaN film having no phase separation with significant PL emission intensity is obtained at a growth temperature much lower than that conventionally used in MBE for InGaN growth on

sapphire.

4.1.1 Introduction

Since bandgap engineering of InGaN-based semiconductors enables tunability of their absorption and emission properties, in the IR to near UV region of the electromagnetic spectrum, applications such as high efficiency LEDs, LDs and photovoltaic cells are potentially possible.[4,36] While gallium rich InGaN films of high crystalline quality are relatively easy to grow at high temperatures, high quality single phase indium rich InGaN films are difficult to achieve. The low dissociation energy of InN and low miscibility of InN in GaN at high temperatures results in phase separation[161,182,329,330], which in turn have deleterious effects on their electrical and optical properties. Thus, to form single phase crystalline InGaN films at lower temperatures requires maintaining a high non-equilibrium growth condition, which remains a challenge for crystal growers. In addition, the lattice mismatch between InN and GaN leads to strain induced strong piezoelectric polarization[3] and Quantum Confined Stark Effect (QCSE), which reduce the radiative recombination efficiency. The lattice mismatch between InGaN film and the substrate results in a high dislocation density[7], which degrades the device performance. Number of groups have studied the optical properties of InGaN layers[331–333], and they invariably encounter varying degrees of local phase separation into indium rich regions in the InGaN layers.[204,237,334]

Comprehensive studies of the influence of different growth parameters on the incorporation of indium during growth of InGaN are necessary to comprehend the growth kinetics involved. Lin *et al.*[213] reported that, for InGaN films grown by MOCVD on *c*-sapphire, with the decrease in growth temperature the indium incorporation increased. However, the crystallinity of the film is also found to decrease, as manifested by the increase in X-ray diffraction line-widths, decrease in the intensity of near band-edge emission and the dominance of impurity transitions in the PL spectra. Indium composition has also been seen to increase with the increase of RF input power for the growth of InGaN/GaN quantum well by PA-MBE.[174] Growth rate dependent indium incorporation[167] and a reduction of indium segregation by employing a high V/III ratio, resulted in the formation of rough interfaces.[335] Indium/gallium[334,336,337] and N/III ratios[338] were varied to obtain the entire alloy composition of InGaN. AlN[333], GaN[337] and InN[339] buffer layers have

been used to grow good quality indium rich InGaN by MBE on *c*-sapphire. Since the optimum growth temperature of the InGaN at each alloy composition is considered to be greatly related to the large difference in the equilibrium vapor pressure of InN and GaN, the investigation of growth temperature dependence of the properties of InGaN is important. Though thick films reduce some of the previously mentioned negative effects, they come with their own inherent limitations. Thus, of late, formation and characterization of InGaN-based nanostructures are intensely investigated[291–295] due to several advantages, such as significantly reduced dislocation density, decreased polarization fields due to small lattice strain and increased light extraction efficiency due to large surface-to-volume ratio.[302] VLS[340], Flame Transport[341,342] and Plasma assisted techniques[343] have been used to form nanostructures of several semiconducting materials. However, these techniques use external catalysts and involve complex precursor reactions. But to grow epitaxial nanostructures for optoelectronic applications, without external catalysts or precursors and to monitor growth *in-situ*, MBE is the preferred technique.

It is well established by our group and others that under nitrogen rich conditions, nanostructure growth such as self-assembled defect free single-crystalline nanowalls and nanocolumns[344], can be formed. In this section, we discuss our study of the growth temperature dependence of the structural and optical properties of InGaN films grown by PAMBE, directly on *c*-sapphire, under nitrogen rich conditions.

4.1.2 Experimental Details

All the InGaN samples discussed in this section were grown by PAMBE, on *c*-sapphire for 3hrs. For all the growths, indium and gallium K-cells were held at 800 °C (indium BEP = 2.3×10^{-7} Torr) and 1000 °C (gallium BEP = 4.8×10^{-7} Torr), respectively, and N_2 flow rate of 4.5 sccm, with Radio Frequency (RF) plasma forward power of 375 W, was kept constant to maintain a N-rich condition. Chemically pre-cleaned *c*-sapphire substrates were thermally degassed inside the preparation chamber at 600 °C for 60 min, followed by annealing in the growth chamber at 850 °C for 15 min to obtain the characteristic RHEED pattern of atomically clean *c*-sapphire. The InGaN growth was carried out at three different growth temperatures of 330 °C, 430 °C, and 530 °C. All the samples are then probed using different complementary characterization techniques,

which are RHEED (*in-situ*), FESEM, HRXRD, RT PL Spectroscopy and RT Optical Absorption Spectroscopy (UV-VIS-NIR Spectroscopy in transmission geometry).

4.1.3 Results and Discussions

4.1.3.1 FESEM: Morphology

Figure 4.1(a), (b) and (c) shows the plan-view FESEM images of the InGaN samples grown on *c*-sapphire at three different temperatures of 330 °C, 430 °C, and 530 °C. From

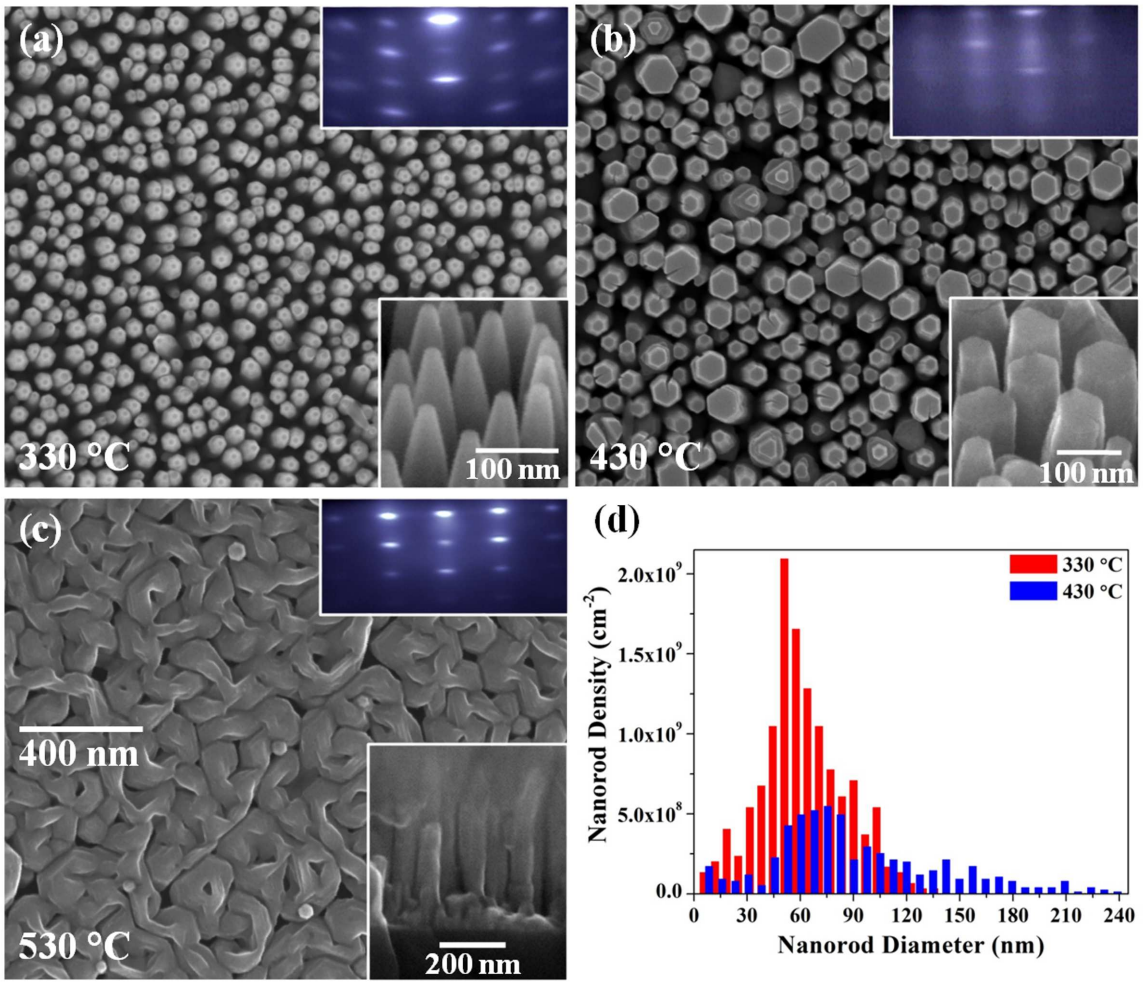

Figure 4.1: (a−c) show the top view FESEM images of the samples (Respective growth temperatures are indicated at the bottom left corner and scale bar for all the top view images is shown in (c)). The bottom right insets of (a) and (b) show the 45° tilted view FESEM image, whereas that of (c) shows the cross-section view FESEM image of the respective samples. The top right inset of (a−c) shows the RHEED pattern for the respective samples, taken after growth with e-beam along<11$\bar{2}$0>. Figure 4.1(d) shows the distribution of NRs as a function of NR diameter for the samples grown at 330 °C and 430 °C.

Figure 4.1(a) and (b) it can be seen that at 330 °C and 430 °C the InGaN samples grow as nanorod (NR) arrays. The 330 °C grown sample has isolated hexagonal shaped NRs and are vertically aligned along the substrate normal (c-oriented) with homogeneous length and diameter distribution. From the tilted view in the bottom right inset of Figure 4.1(a), it can be seen that all the NRs are tapered at the top and have a needle-like morphology. RHEED pattern of the sample is spotty, which is due to the transmission of electrons through the NRs, as shown in the top right inset of Figure 4.1(a). The InGaN sample, grown at 430 °C, shows isolated non-tapering hexagonal NRs with a flat-top morphology as can be seen from Figure 4.1(b). Though there is a variation in the diameter and length for these rods, all of them have a flat-top which is clearly visible in the tilted view in the bottom right inset of Figure 4.1(b). In this case, the RHEED pattern displays, as shown in the top right inset of Figure 4.1(b), both spots and streaks due to both transmission of electrons through the NRs, and scattering from the flat-top c-plane regions of the NRs, respectively. At higher growth temperature of 530 °C, the morphology of the grown film changes to an interconnected 3D random network structure as shown in Figure 4.1(c). From the cross-sectional image in the bottom right inset of Figure 4.1(c), it can be seen that the film has initially grown as well-separated columns up to a height of $\approx$ 400 nm, and then these columnar structures coalesce to yield a random network morphology which is clear from the plan view image. The corresponding RHEED pattern is once again spotty due to the transmission of electrons through the 3D morphology. Figure 4.1(d) shows the relationship between the NR diameter and their density in a bar chart for both the films grown at 330 °C and 430 °C. NR diameter is measured visually from the top view FESEM image using the "Gwyddion" software. For the tapered NRs the diameter is measured at the region from where the tapering starts (as the tapering does not start from the bottom of the NRs). The 330 °C grown InGaN NRs have an average (across the wafer) diameter of $\approx$ 60 nm with a density of $\approx 2.0\times10^{9}$ cm^{-2}, whereas, the 430 °C grown NRs have an average diameter of $\approx$ 75 nm with a density of $\approx 5.5\times10^{8}$ cm^{-2}. It can also be seen from Figure 4.1(d), that due to differences in the growth kinetics, the 330 °C grown NRs have a narrow range of diameter distribution and high density, compared to those grown at 430 °C. The diameter distribution for the sample grown at 430 °C is asymmetric and tails at higher diameter values because of the presence of larger diameter NRs ($\approx$ 150 nm) with

low density.

4.1.3.2 Growth Mechanism

It has been reported that the nitrogen rich condition retards surface diffusion of metal adatoms[345], leading to the formation of small 3D islands or adatom clusters of different sizes, following a Volmer-Weber (VW) growth mode, where adatom-adatom interactions are stronger. Now these adatom clusters react with nitrogen plasma and form nucleation sites to promote further NR growth, and thus the size of the clusters determine the diameter of the formed NRs[346], which grow in the *c*-direction with *m*-faceted sidewalls. The metal adatoms diffusing on the substrate surface reach the rods and migrate along the *m*-faceted sidewalls of the NRs and reach the top of the rod due to lower chemical potential at the *c*-plane.[347,348] In addition, the metal atoms that directly impinge on the top of the NRs also contribute to the growth of the NR along the *c*-direction. The relative rates of sidewall migration and direct impingement determines the tapering or broadening of NR diameters during growth. In addition, since the nucleation process may not occur simultaneously all over the substrate, some NRs start growing earlier than others, resulting in variation in their heights and diameters. Higher growth temperature leads to increased surface diffusion along the sidewalls as well, and so at 530 °C, initially formed NRs tend to grow thicker with length and eventually coalesce with each other at the top[345], to form a 3D interconnected random network structure as can be seen from Figure 4.1(c) and its cross-section image in the bottom right inset. The coalescence effect decreases with the reduction of growth temperature and as a result growth at lower temperatures of 430 °C and 330 °C, yields well separated NRs. Interestingly, the NRs have uniform diameter, with a flat *c*-plane top, since the rate of migration of adatoms along the sidewalls reaching the top and those directly impinging on the *c*-plane top, remain constant throughout the growth duration. When the growth temperature is further reduced to 330 °C, the surface diffusion along the side-walls reduces and results in the tapering of the upper part of each NR.[349] At 430 °C, relatively high surface diffusion of adatoms on *c*-plane compared to those at 330 °C, helped some of the NRs grow thicker at the expense of others and thus have higher diameters and heights, which results in the asymmetric distribution in Figure 4.1(d).

4.1.3.3 HRXRD: Crystal Structure, Indium composition and Epitaxial Relationship

To understand the structural quality, HRXRD measurements are performed on all the thin film samples. Figure 4.2 shows the $2\theta - \omega$ scans (and their corresponding ϕ-scans as insets) acquired on the symmetric (0001) plane for the InGaN samples grown at 330 °C, 430 °C, and 530 °C, respectively, after aligning them with respect to the strong Al_2O_3(0006) reflection observed at 41.68°. As can be seen for all the samples, (Figure 4.2) along with the sharp and strong substrate peaks, a dominant peak appears in the vicinity of 34°, which is assigned to the (0002) reflection of wurtzite InGaN. The absence of any other reflection from InN or GaN confirms the absence of those phases in our samples. InGaN(0002) peak positions are observed at 33.78°, 33.92° and 34.53° for the samples grown at 330 °C, 430 °C, and 530 °C, respectively. Employing the Vegard's law that relates indium composition to its lattice parameter obtained from the InGaN(0002) peak positions and using the reported values of lattice parameters of InN and GaN[123,125], we have calculated the indium content (x) as 0.01, 0.18 and 0.23 for the films formed at growth temperatures of 530 °C, 430 °C and 330 °C, respectively. Absence of metallic indium or gallium related peak in HRXRD confirms the absence of metal clusters of indium or gallium. At 530 °C, the desorption rate of indium is highest among the three samples and it is also well known that Ga-N bond strength is much higher than that of In-N. These two factors together have resulted in the low incorporation of indium in the lattice for the sample grown at 530 °C. It is therefore evident that the indium desorption rate will decrease and indium incorporation in lattice will increase with the reduction of growth temperature. While the sample grown at 330 °C shows a single compositional phase, the films formed at 430 °C and 530 °C, show a shoulder to the InGaN(0002) XRD peak at lower 2θ values. This reflects the presence of another InGaN phase having slightly higher indium content than that calculated for the respective samples grown at 430 °C and 530 °C. In the case of 430 °C grown sample the shoulder is appreciably larger and appears at 2θ value of 32.92° which corresponds to an indium content (x) of ≈ 0.48 while for the 530 °C grown sample the shoulder appears at 34.06° and corresponding indium content (x) is ≈ 0.14, showing evidence for distinct phase separation in these two samples.

To understand the epitaxial relationship, the ϕ-scans of the InGaN(10$\bar{1}$1) plane are

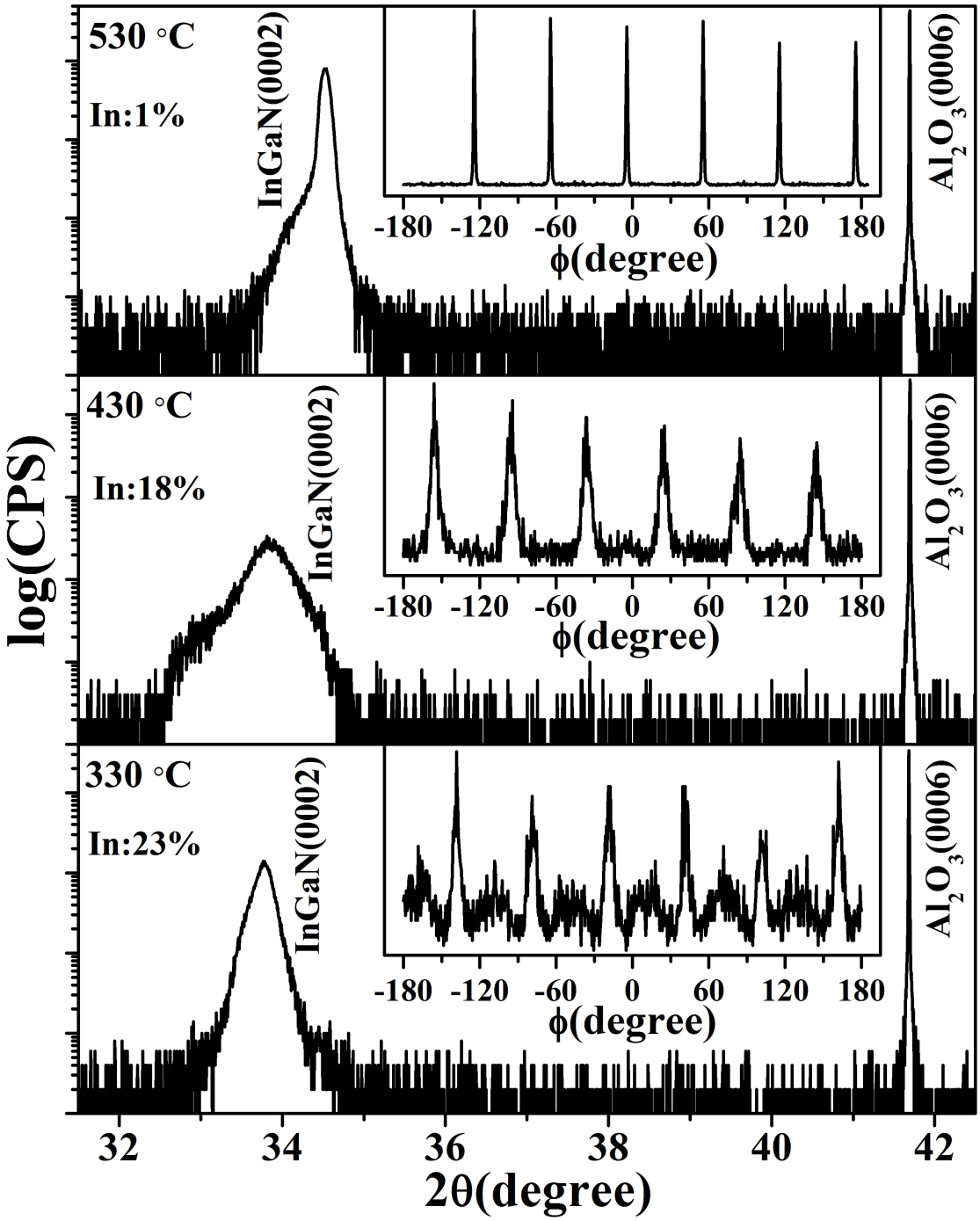

Figure 4.2: shows symmetric $2\theta - \omega$ scans acquired by HRXRD for all the samples (Respective growth temperatures and calculated indium compositions are indicated at the top left corner). Top right inset shows the ϕ-scan acquired on the InGaN($10\bar{1}1$) plane for the respective samples.

shown as the top right insets for the respective samples. For the 530 °C and 430 °C grown samples six equally spaced (period of 60°) peaks are observed, which confirm the six-fold symmetry of the hexagonal crystal structure of InGaN. Similar six equally spaced peaks

are also observed in the case of the 330 °C grown sample, but in addition six more low intensity peaks appear in-between them. These additional peaks suggest that there exists a 30° in-plane rotation with respect to each other, among the grown crystals.

4.1.3.4 PL and Optical Absorption: Optical Properties

To investigate the optical properties for the three samples, room temperature (RT) PL and Optical Absorption measurements are carried out. Figure 4.3(a) shows the intensity normalized PL signals observed for the samples grown at different growth temperatures. The nonlinear dependence of bandgap on the composition of $In_xGa_{1-x}N$ is expressed as $E_g^{In_xGa_{1-x}N} = xE_g^{InN} + (1-x)E_g^{GaN} - bx(1-x)$, where b is the bowing parameter, which defines the deviation from a linear interpolation of bandgap between InN and GaN. For the 530 °C grown sample the PL peak energy is 3.36 eV which is red-shifted with respect to the bandgap of GaN at RT ($\approx$ 3.42 eV)[124] because of the 1% indium incorporation in the lattice. As the other phase containing 14% indium is less abundant compared to 1% indium content phase, we assume that the 14% indium content phase does not contribute significantly to the PL emission. For the 330 °C grown sample, PL peak appears at 2.30 eV which is further red-shifted with respect to the 530 °C grown sample as it contains more amount of indium(23%) and the peak intensity is 25 times lower than that of the 530 °C grown sample. Similar drop of PL intensity with the increase of indium incorporation has been reported earlier.[213,350] However, for 430 °C grown sample with 18% indium, the PL peak is found to be at 1.85 eV, which is even lower than that of the 330 °C grown sample with a small shoulder at 2.38 eV at the high energy side. The PL peak intensity of this sample is found to be 15 times lower than that of the 330 °C grown sample.

The RT optical absorption measurement results are shown in Figure 4.3(b) which are obtained in the transmission mode and plotted by following the relation $\alpha(E) \propto ln(1/T)$ and neglecting optical scattering and reflection losses. Here α, E and T are optical absorption coefficient, energy and transmittance, respectively. Thus, the value of the optical bandgap for the InGaN samples is obtained by plotting α^2 versus E in the high absorption range followed by extrapolating the linear region of the plots to $\alpha^2 = 0$. The optical bandgap values are found to be 2.53 eV, 2.12 eV, and 3.4 eV for the samples grown

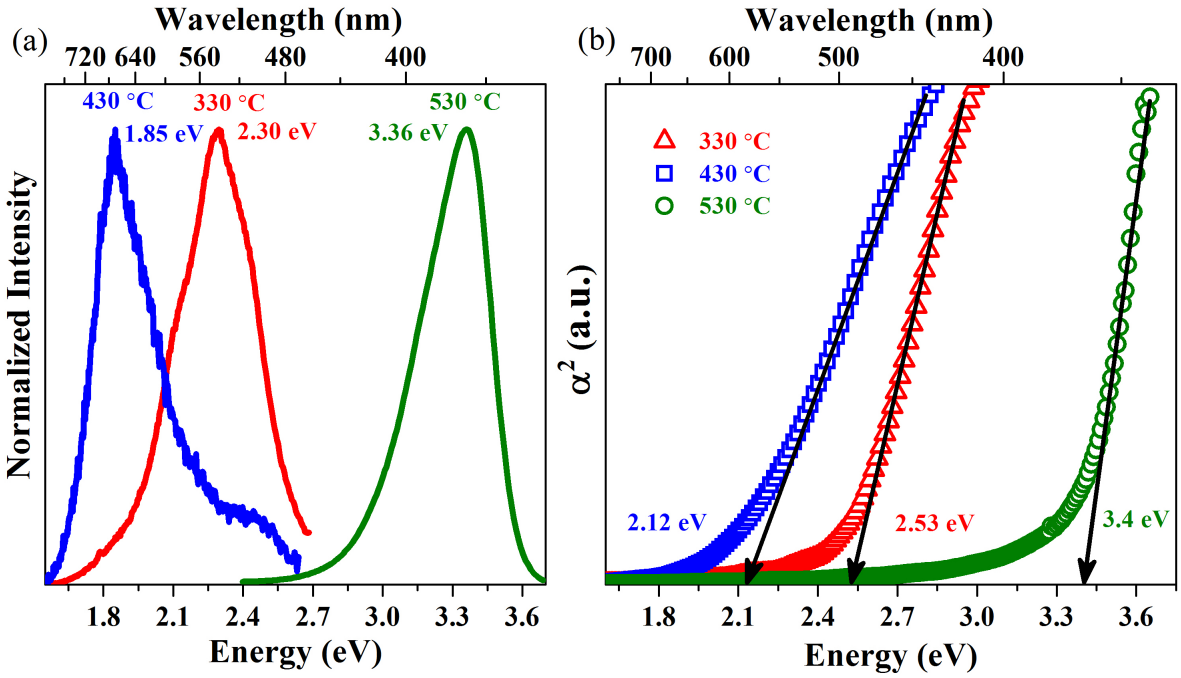

Figure 4.3: (a) shows RT PL emission spectra and (b) shows RT optical absorption spectra of all the samples (Respective growth temperatures, PL peak positions and absorption edges are indicated in the image).

at 330 °C, 430 °C, and 530 °C, respectively. This is again following the same trend of the PL measurements, which does not follow the Vegard's law for the 18% indium content sample. The PL emission at 1.85 eV for the 430 °C grown sample is attributed to the phase containing high indium content of 48%, as observed form HRXRD. This peak is more red-shifted as compared to that for the 330 °C grown sample which contains 23% of indium. On the other hand, the phase containing low indium of 18% is emitting at 2.38 eV and appears as a small shoulder in the PL spectra. It can also be seen that all the samples show positive Stoke's shift (the difference between the absorption band-edge and PL peak position) and it is largest for the 430 °C grown sample. It has been reported[204,237] that the Stoke's shift increases with increasing indium composition as well as with the reduction in emission energy and thus the large shift implies the presence of localized carrier states. The origin of localization in InGaN layers has been attributed to the formation of indium-rich quantum dots within the InGaN matrix having lower indium content. As the indium content increases, the dot size becomes large and the localized state goes deeper causing more red-shift. Therefore, the maximum Stoke's shift indicates strong localization effects and a large degree of compositional fluctuation and/or structural disorder for the 430 °C

grown sample. Thus, it can be understood that the observed red-shifted PL emission is originating from the high indium content phase of the same sample, which explains the PL and absorption data for 430 °C grown sample. In the literature both experimental and theoretical studies have been carried out extensively to determine the value of the bowing parameter.[187,351] However, no consensus has been reached on the magnitude of the bowing parameter which is sufficient to describe the bandgap over the entire composition range.[333,352] By fitting the nonlinear Vegard's law of bandgap to the PL emission values of 2.3, 1.85, and 3.36 eV corresponding to the indium content of 23%, 48%, and 1% for the 330 °C, 430 °C, and 530 °C grown samples, we have calculated the bowing parameter, for our samples, using the bulk InN and GaN bandgaps at RT, to be 0.64 eV[80] and 3.42 eV[124], respectively. The value is found to be 1.54 eV, which is lower and closer to the theoretically estimated value of 1.44 eV.[351]

4.1.4 Inferences

In summary, single crystalline, *c*-oriented and wurtzite InGaN films are grown directly on sapphire(0001) at three different growth temperatures with constant nitrogen and metal fluxes by MBE. Well separated and vertically aligned NRs are obtained at 330 °C and 430 °C, whereas at 530 °C, the initially separated NRs coalesce at the top and form an interconnected random network morphology. With decreasing growth temperature, NR density increases and the average NR diameter decreases. NR growth is initiated by Volmer-Weber growth mode, followed by differential adatom cluster migration along different crystallographic planes due to thermodynamically driven variation in surface sticking coefficients on different surfaces. This results in *m*-plane faceted NR with a preferential growth direction along *c*-axis. Growth temperature dependent indium incorporation in the InGaN lattice shows that at the low growth temperature of 330 °C, higher amount of indium incorporation is achieved without any distinct phase separation. Among the grown crystals, there also exists an in-plane rotation of 30°, as observed from the HRXRD phi-scan. RT PL intensities for 530 °C and 330 °C samples are significantly high. On the other hand, 430 °C grown sample shows distinct phase separation and larger indium composition fluctuation from 18% to 48% which is seen to be relatively of low structural quality and shows least intense PL emission. Large Stoke's shift for 430

°C grown sample has been attributed to the localized states originating from indium rich regions present in the InGaN layer, causing significant phase separation and degradation in sample quality. The PL emissions are found to follow the Vegards law of bandgap with a bowing parameter of ≈ 1.54 eV.

4.2 Effect of Indium Flux

Indium-flux dependent study of the nature of epitaxy, compositional phase-separation and band-edge emission of spontaneously formed *c*-oriented InGaN NRs on *c*-sapphire is performed. At higher indium flux, *m*-faceted thick NRs ($\approx$ 700 nm) form with two in-plane epitaxial orientations, and display compositional phases with indium composition varying from $14 - 63\%$. In these rods, PL emission is seen to originate only from the localized high-indium phase (63%) that is embedded in the low-indium (14%) InGaN matrix. As the indium flux is reduced, NRs of smaller diameter ($\approx$ 60 nm) and a coalesced NR-network are formed, with indium incorporation of 15% and 9%, respectively. These faceted, *c*-aligned thinner NRs are of single compositional phase and epitaxy and display room-temperature PL emission. Optical absorption and emission properties of these nanostructures follow the Vegard's law of bandgaps, and the observed bowing parameter and Stokes's shifts correlate to the observed compositional inhomogeneity and carrier localization.

4.2.1 Introduction

InGaN QWs are extremely important regions of a device structure, because of InGaN's tunability of its direct bandgap from near infrared ($\approx$ 0.64 eV(InN)) to the near UV ($\approx$ 3.4 eV(GaN)) region.[4,36,353–356] With increasing indium content the efficiency of InGaN QWs rapidly drops, especially when the wavelength is longer than 500 nm.[357] Poor crystal quality[358] due to the increased lattice mismatch, large piezoelectric field in an indium rich InGaN QW[359] and compositional phase separation are identified as primary reasons behind this drop in efficiency.[360–366] Poor crystal quality leads to defects that act as nonradiative recombination centers, while the large piezoelectric field causes charge separation between holes and electrons in QWs, reducing the luminescence effi-

ciency.[249] On the other hand, because of its relatively low dissociation energy, InGaN shows strong material decomposition at conventional temperatures required for epitaxial growth.[161,182,329,330] The phase separation in InGaN is a crucial problem for this material and is not yet resolved.[367] However, researchers have observed that phase separation can be a useful process to form stable InGaN QDs by spinodal and binodal decomposition[368] and the variation of the indium concentration in an InGaN QW help to trap carriers at regions with higher indium concentration, thus preventing the diffusion of carriers into dislocation cores.[369] Until recently, MOVPE[370,371] was used to grow nitride based green LDs structures, but now PAMBE is preferred since the films can be grown at lower temperatures.[372] Growth of high quality InGaN structures on *c*-plane GaN in excess of indium flux by PAMBE[373] has been reported. It has been observed that Ga/N ratio[374] and growth temperature[375] determine indium incorporation for InGaN growth using PAMBE, under indium-rich conditions. Currently, growth of nanostructures of InGaN are being intensely investigated[291–295] due to several advantages, such as significantly reduced dislocation density, decreased polarization fields due to small lattice strain and increased light extraction efficiency due to large surface-to-volume ratio.[302]

In the work discussed in this section, we have grown four different InGaN films directly on *c*-sapphire with varying indium flux, while other growth parameters such as growth temperature and gallium and nitrogen fluxes are kept constant, to observe indium incorporation in the lattice, and resulting structural and optical properties.

4.2.2 Experimental Details

The InGaN thin films (samples A−D) are grown by PAMBE, on *c*-sapphire for 180 mins. Chemically pre-cleaned sapphire substrates are thermally degassed inside the preparation chamber at 600 °C for 60 min and further annealed in the growth chamber at 850 °C for 15 min, to get the characteristic RHEED pattern of atomically clean sapphire surface. For all the growths, the nitrogen flow-rate is kept at 4.5 sccm and Radio Frequency (RF) plasma forward power at 375W and the gallium K-cell temperature is held at 1065 °C to maintain a gallium BEP of 4.8×10^{-7} torr. Temperature of the indium K-cell is decreased from 850 °C to 775 °C in steps of 25 °C for the samples A−D, respectively, to reduce the indium flux. All the samples are grown at a growth temperature of 380

°C, and other growth parameters employed are presented in Table 4.1. All the samples are then probed using different complementary characterization techniques, which are RHEED (*in-situ*), FESEM, HRXRD, RT PL Spectroscopy and RT Optical Absorption Spectroscopy (UV-VIS-NIR Spectroscopy in transmission geometry).

Table 4.1: Growth details of the samples

Sample	In K-cell Temp. (°C)	In BEP ($\times 10^{-7}$ Torr)	$x_{Applied}$ (%) (In/In+Ga)	V/III BEP ratio
A	850	5.9	55	23.8
B	825	3.8	44	29.7
C	800	2.3	32	35.9
D	775	1.4	23	41.1

For all samples: Ga BEP = 4.8×10^{-7} Torr and N_2^* BEP = 2.55×10^{-5} Torr

4.2.3 Results and Discussions

4.2.3.1 FESEM: Morphology

Figure 4.4(a-d) show the plan view FESEM images for samples A−D, grown with different indium fluxes, and the top right insets show the respective RHEED pattern. Figure 4.4(a) shows the FESEM image for sample A, which consists of vertically aligned, *m*-plane faceted, thick hexagonal NRs with an average diameter of ≈ 700 nm along with thinner NRs of ≈ 180 nm diameter. It can be seen that the density of thinner NRs, which are isolated, is more than that of the thicker ones and tend to coalesce into each other. The RHEED inset of Figure 4.4(a) shows spotty pattern that is typical of wurtzite structure, signifying the electron transmission through the NRs. These spots are superimposed on a faint streaky pattern that arises due to the electron scattering from the large flat *c*-plane tops of the NRs. As can be seen in Figure 4.4(b), sample B has hexagonal, well separated and vertically aligned NRs with an average diameter of ≈ 270 nm with a narrower diameter distribution than in sample A. The inset shows a sharper spotty RHEED pattern due to electron transmission through the NR structures and weaker streaks due to smaller size of the flat *c*-plane tops than in Figure 4.4(a). For both samples A and B, along with the hexagonal NRs, some triangular 3D structures are also present. Figure 4.4(c) shows the

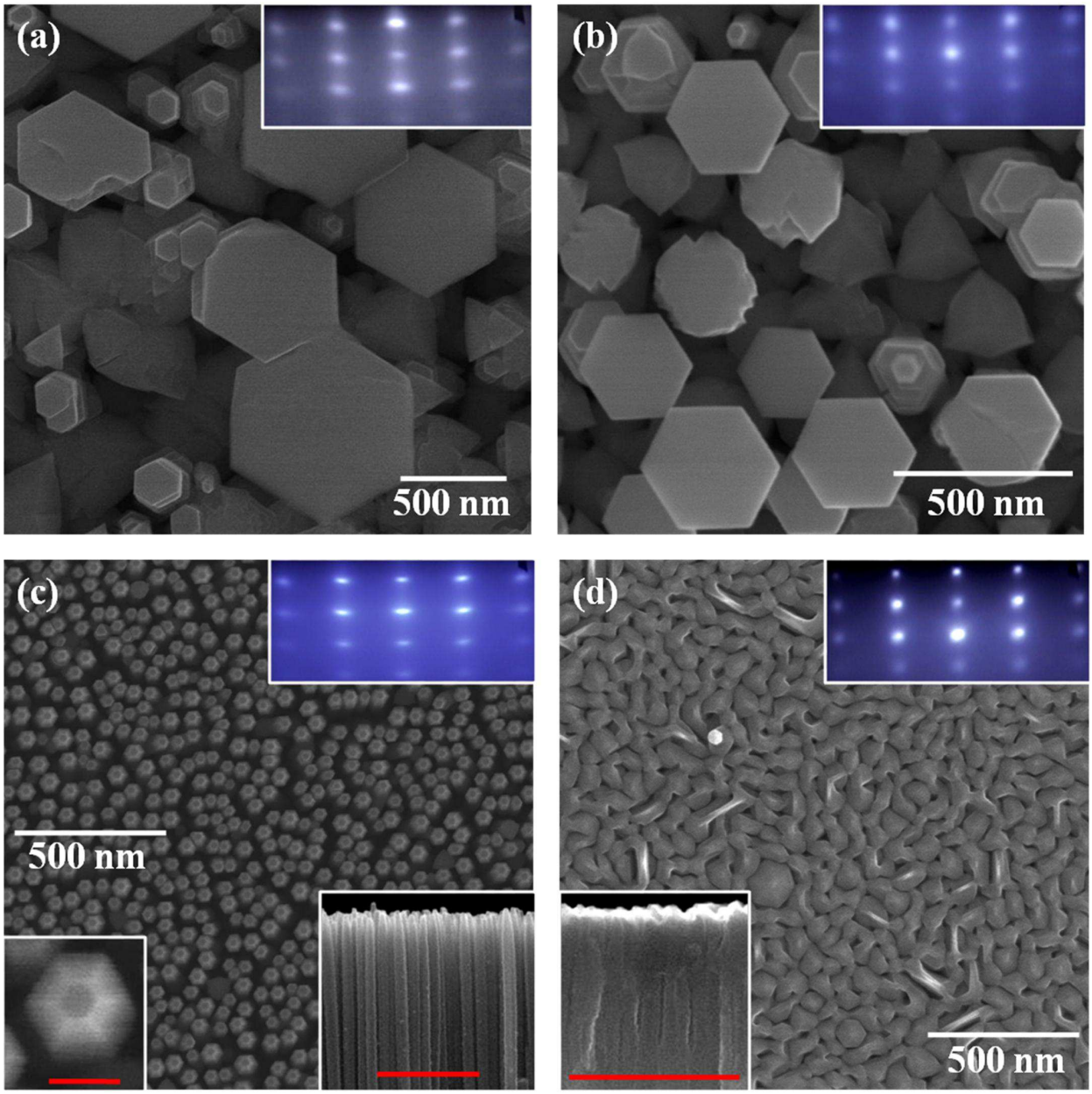

Figure 4.4: (a-d) show the top view FESEM images for samples A-D respectively with their corresponding RHEED pattern taken after growth with e-beam along $< 11\bar{2}0 >$, as top right insets. The bottom left inset of (c) shows zoomed view of the faceted and tapered NR top of sample C and the respective scale bar (red colour) measures 50 nm. The bottom right inset of (c) and bottom left inset of (d) show the top part of the cross-sectional FESEM images of sample C and D, respectively and the respective scale bars (red colour) measures 500 nm.

FESEM image of sample C, which has a very uniform distribution of well separated and vertically aligned thin hexagonal NRs with an average diameter of $\approx$ 60 nm, displaying a sharp spotty and elongated RHEED pattern. It can be seen from the FESEM image of

sample D (Figure 4.4(d)), that it has an interconnected 3D network structure with some sparse hexagonal NRs. Structures similar to sample C and D have also been observed in our earlier study.[376]

4.2.3.2 Growth Mechanism

As we have grown all the films under nitrogen-rich conditions, 3D structures (*c*-oriented hexagonal NRs) are formed. The nitrogen-rich condition (V/III ratio) increases gradually from A-D (see Table 4.1) due to reduction in the indium flux. Under increased V/III ratio, the probability of collision between metal adatoms and nitrogen molecules increases, which enhances the nucleation rate and hinders adatom diffusion on the substrate surface. As a result, the lateral growth of the formed nucleation centers reduces and vertical NR formation is promoted with the metal adatoms diffusing along the *m*-faceted sidewalls of the NRs. Thus, the diameter of the grown NR reduces and the density of the NRs increases with the decrease of indium flux. In our case the diameters of the grown NRs vary from 700 nm to 60 nm for samples A-C with the decrease of indium flux, while the NR diameter distribution narrows. Under elevated indium flux condition, coalescence of smaller NRs to enhance the thickening of other NRs has been reported for InN NW growth[377], which is also evident in our sample A, and is attributed to the enhanced indium adatom migration and the subsequent incorporation on the lateral surfaces (*m*-plane) of the rods. For samples A and B, the NRs have wide flat top c-plane but for sample C, the NRs have smaller flat tops on a truncated hexagonal pyramidal structure, which is shown in the bottom left inset of Figure 4.4(c). During selective area growth of pyramidal GaN, such pyramidal facets have been identified to belong to the $\{10\bar{1}1\}$ family of planes[378], which are N-polar and thus get stabilized under high V/III condition.[379] Since for sample C, the V/III ratio is much higher than those used for samples A and B (see Table 4.1), we also attribute the facets at the NR apex to the $\{10\bar{1}1\}$ family of planes. Thus, it is clear that with increase of V/III ratio, NR density and the formation of $\{10\bar{1}1\}$ facets will be enhanced. With a higher NR density it is more probable that the incoming and desorbing metal atoms will strike a nearby NR[380], and get incorporated on the sidewalls, which increases the lateral dimension at the top of the NRs and consequently leading to their coalescence. Sample D is the direct outcome of these two collective reasons, where the

NRs with faceted tops coalesce into each other, forming a connected network morphology. To clearly visualize the NR assembly we have shown the top part of the cross-sectional FESEM images of sample C and D as bottom right and bottom left inset of Figure 4.4(c) and (d), respectively. Well separated, vertically aligned NRs for sample C and coalesced NRs with voids visible between them for sample D can be observed in cross-sectional FESEM images.

4.2.3.3 HRXRD: Crystal Structure, Indium composition and Epitaxial Relationship

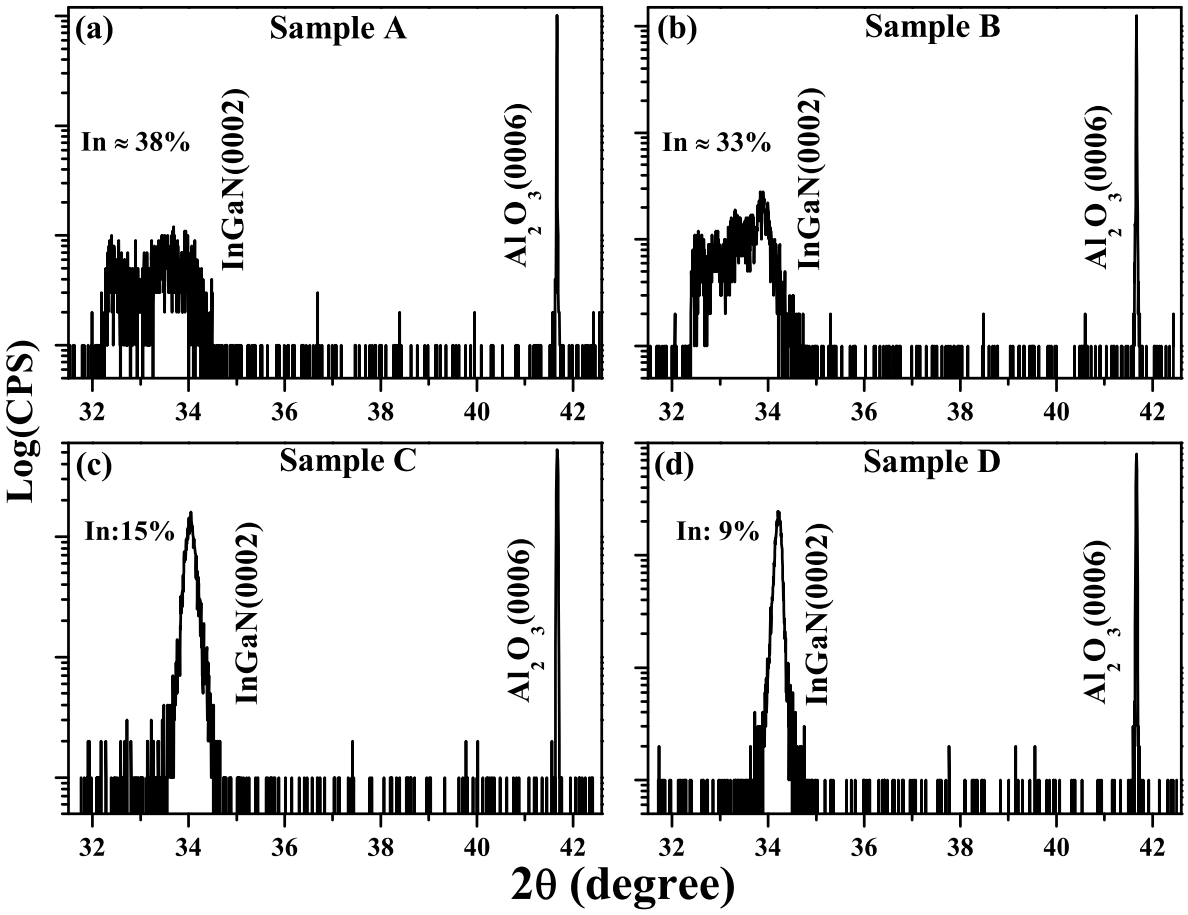

Figure 4.5: (a-d) show symmetric 2θ-ω scans acquired by HRXRD for samples A-D, respectively. Calculated indium compositions are indicated at the top left side.

Figure 4.5 shows the HRXRD results, for all the samples, where the symmetric $2\theta-\omega$ scans are plotted in logarithmic scale. The reflections are acquired on the InGaN(0002) plane with respect to the pre-aligned Al_2O_3(0006) plane. All the InGaN thin films are

seen to possess single crystalline, wurtzite structure with the preferential growth direction along *c*-axis. The pattern in Figure 4.5 displays intense Al_2O_3(0006) substrate peak at 41.68° and *c*-oriented peaks of InGaN(0002) planes in the vicinity of 34° for all the samples, which indicates that the epitaxial relationship between the NRs and substrate is $(0001)_{InGaN}||(0001)_{Sapphire}$. The absence of any other reflection from InN or GaN confirms the absence of those independent phases in our samples. For samples A and B, InGaN(0002) reflection is broad and asymmetric, suggesting the presence of phase separation. However, samples C and D exhibit intense single InGaN(0002) reflections at 34.05° and 34.22°, respectively, displaying the presence of single compositional phases in these two samples. Thus, to estimate the average indium composition of samples A and B, we have deconvoluted the InGaN(0002) peak into constituent peaks and the deconvolution has been shown in Figure 4.6, keeping the FWHM of each of the constituent peaks same as that of the InGaN(0002) peak of sample C. Each of the constituent peaks corresponds to different phases of InGaN in these two samples and their respective indium composition is listed at the top left corner of the plot. For samples A and B, the peak positions of each of the constituent peaks is used to get the *c*-lattice parameters, which is then used to calculated the indium composition by using Vegard's law for lattice parameter ($c^{In_xGa_{1-x}N} = xc_0^{InN} + (1-x)c_0^{GaN}$) where, c_0^{InN} and c_0^{GaN} are the relaxed *c*-lattice parameters for bulk InN[125] and GaN[123], and x is the indium composition of the InGaN alloy, respectively. Considering the integral intensity of each of the constituent peaks (for details see APPENDIX A), samples A and B are estimated to have an average indium composition (x) of 38% and 33%, respectively. Another important thing to notice is that both the samples A and B contain a high indium containing phase ($x \approx 60\%$), which is higher than the applied indium composition of 55% and 44%, respectively (see Table 4.1). Similar observation have been made by C. Tessarek *et. al.*[368], where $In_{0.97}Ga_{0.03}N$ phase has been obtained, though the applied indium composition was 82%, due to the spinodal decomposition of InGaN. Along with this, phases having indium composition lower than the applied value is also formed to minimize the strain in the grown film. Thus, the presence of multiple phases in samples A and B with different indium content can be attributed to spinodal decomposition. Using Vegard's law, the calculated *c*-lattice parameters for sample C and D are 5.2618 and 5.2364 Å, which correspond to indium

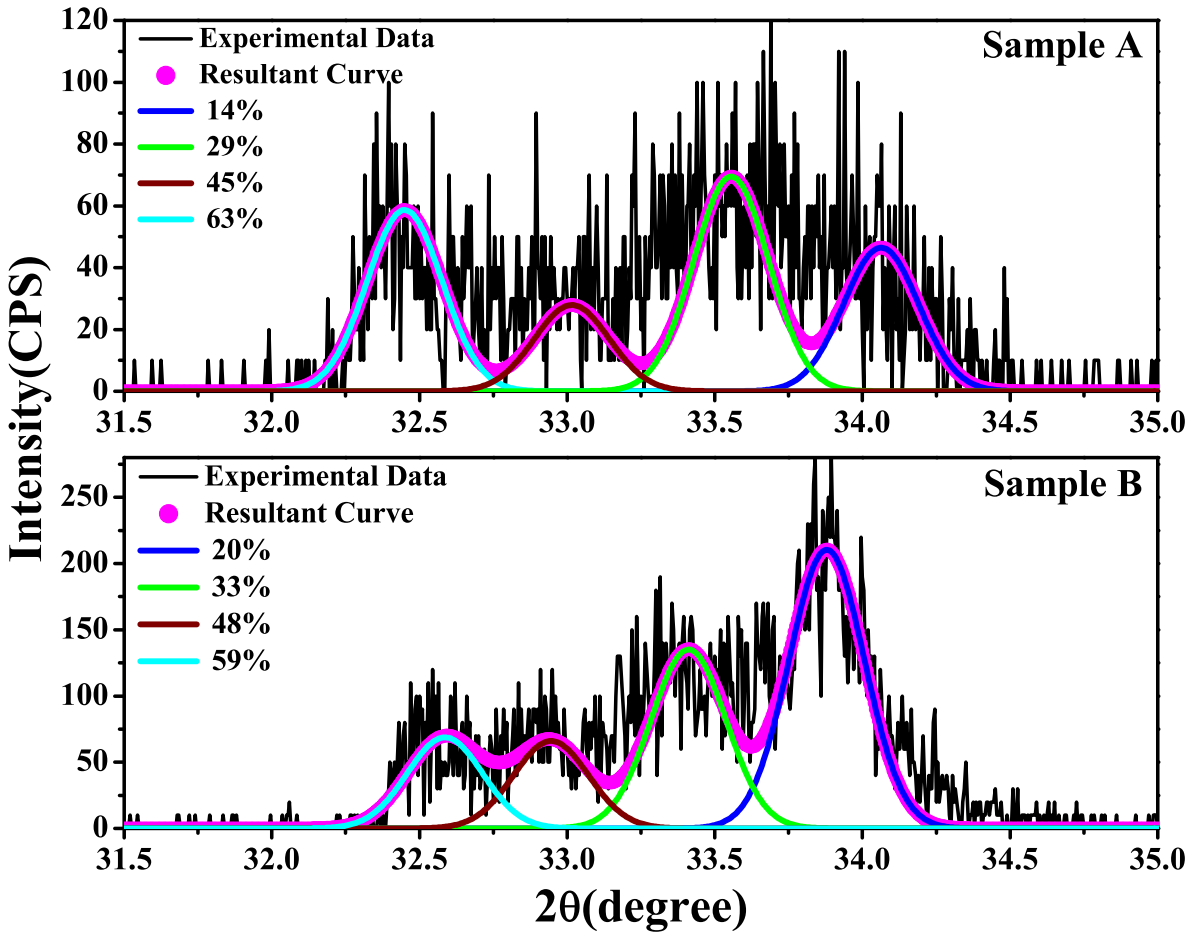

Figure 4.6: shows peak deconvolution of InGaN(0002) peak of the symmetric 2θ-ω HRXRD scans for samples A and B. The indium compositions(x) of the respective InGaN phases corresponding to each constituent peak are written at the top left corner.

compositions(x) of 15% and 9%, respectively. Thus, higher indium flux, while enhancing indium composition, also introduces compositional variations in the grown films. It should also be noted that for indium flux used for sample B and beyond, indium incorporation does not increase significantly and the compositional phase separation continues to occur, but the relative intensity of the low indium containing phase reduces with the increase in indium flux, as can be seen from Figure 4.6.

The HRXRD phi scans of the InGaN($10\bar{1}1$) plane for the four samples are shown in Figure 4.7(a-d). All samples yield six equally spaced (60° apart) peaks, which confirms the hexagonal crystal symmetry of the films and suggests that all the samples are epitaxially oriented along the c-direction. Interestingly, for sample A, additional peaks (marked with red arrows), with the same periodicity of 60° are present, along with the 6

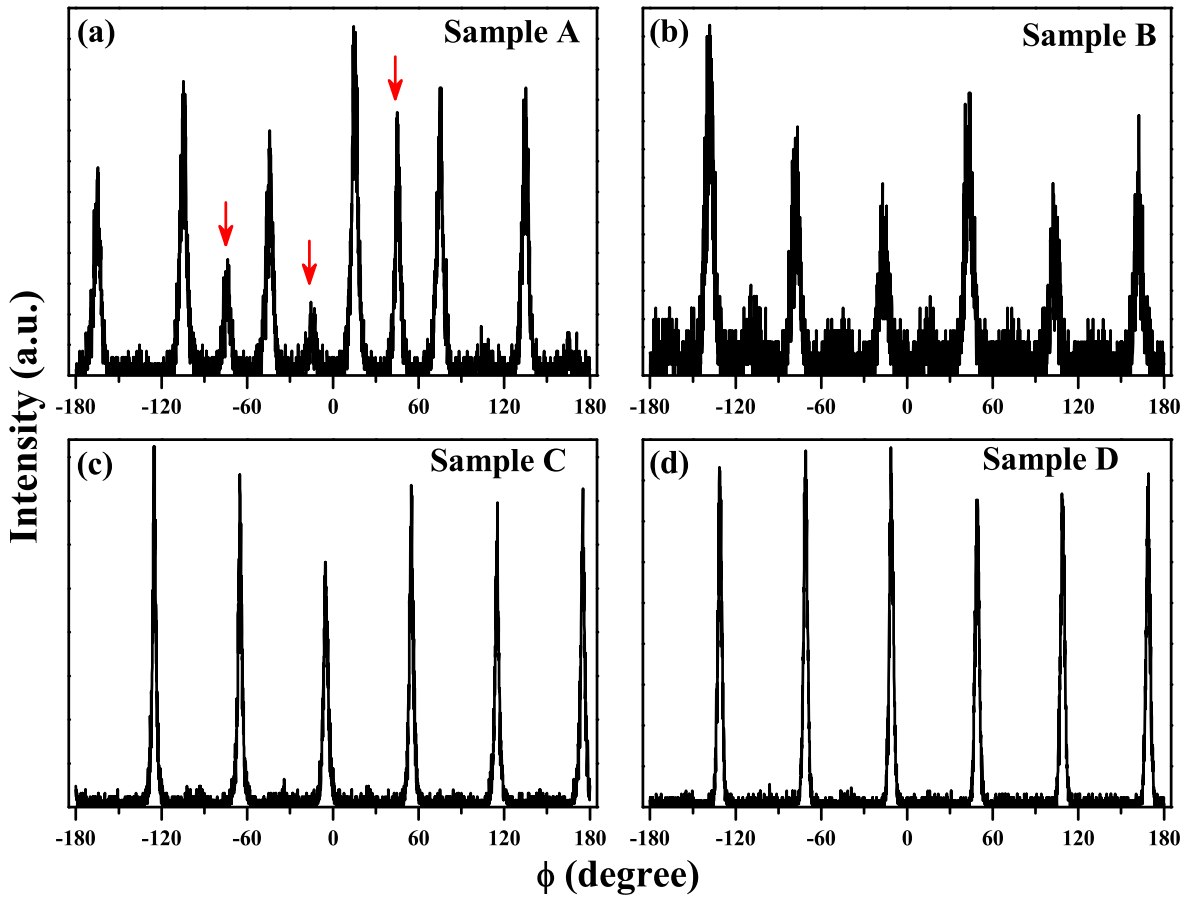

Figure 4.7: (a-d) show phi-scans of the InGaN($10\bar{1}1$) plane acquired by HRXRD for samples A-D, respectively.

main peaks. The intensity of these additional peaks is greatly reduced in sample B and completely absent in samples C and D. Among the grown samples, A and B are indium-rich (InN-like) whereas C and D are gallium-rich (GaN-like). In case of GaN/*c*-sapphire growth, to reduce the lattice mismatch, the favoured in-plane epitaxial relationship is $[10\bar{1}0]_{GaN}||[11\bar{2}0]_{Sapphire}$ and thus GaN crystals grow with an in-plane rotation of 30° with respect to the sapphire substrate. On the other hand, at the InN/*c*-sapphire interface, the lattice mismatch is almost same for both the in-plane epitaxial directions ($[11\bar{2}0]_{InN}||[11\bar{2}0]_{Sapphire}$ and $[10\bar{1}0]_{InN}||[11\bar{2}0]_{Sapphire}$), making the simultaneous growth with both the in-plane orientations equally probable. Thus, the in-plane rotation observed among the grown crystals of samples A and B (which are InN-like), gives rise to additional 60° spaced peaks in phi scan, as shown in Figure 4.7(a and b). However, samples C and D, being more GaN-like, possesses only one in-plane epitaxial relationship with the

substrate and do not show any additional peaks in phi-scan. The phi scan indicates that decreasing indium flux reduces the in-plane rotation among the crystals. Thus, from the HRXRD analysis it is clear that increasing indium flux enhances indium incorporation in the lattice, but also leads to phase-separation and in-plane rotation among the grown crystals.

4.2.3.4 PL and Optical Absorption: Optical Properties

After understanding the morphology and structural phases of the grown films, we have looked at their optical properties. Figure 4.8(a-d) show RT PL and optical absorption spectra for samples A-D. For sample A, the PL spectra consists of one dominant peak at 1.59 eV and two humps at $\approx$ 1.8 eV and at $\approx$ 1.95 eV, resulting in a very broad band-edge emission, due to radiative recombination in the shallow (low-indium-content) and deep (high-indium-content) localization states, respectively, caused by the phase separation in the InGaN alloy[381] as observed by HRXRD shown in Figure 4.5(a). In the case of sample B, though phase separation is observed in HRXRD, only a single PL emission peak is observed at 1.72 eV. Sample C has only one sharp PL peak at 2.67 eV with the narrowest FWHM among the four samples. On the other hand, sample D, which has the lowest indium incorporation, shows a broad PL emission at 2.98 eV. We speculate that in sample D, the coalescence of the NRs introduce grain boundary interface defects which are radiative, causing the PL peak broadening. This needs further studies to understand the emission spectra.

With the increase in indium composition, PL emission energy undergo a red shift and this composition(x) dependence of the bandgap is explained by means of a modified Vegard's law of bandgap, expressed as $E_g^{In_xGa_{1-x}N} = xE_g^{InN} + (1-x)E_g^{GaN} - bx(1-x)$, where E_g^{InN} and E_g^{GaN} are bandgap values of intrinsic InN[15] and GaN[124], and $E_g^{In_xGa_{1-x}N}$ is the value of the emission energy deduced from PL measurements at RT and b is the bowing parameter. Now by fitting the modified Vegard's law to the experimental values (Table 4.2) for our samples, we have obtained the bowing parameter to be $\approx$ 3.24 eV (Figure 4.9) which, is much higher than the theoretically estimated value of 1.44 eV[351], but closer to the value of 3.8 eV obtained by Van de Walle *et. al.*[205] During fitting, the PL emission is assumed to originate from the InGaN phases having the calculated

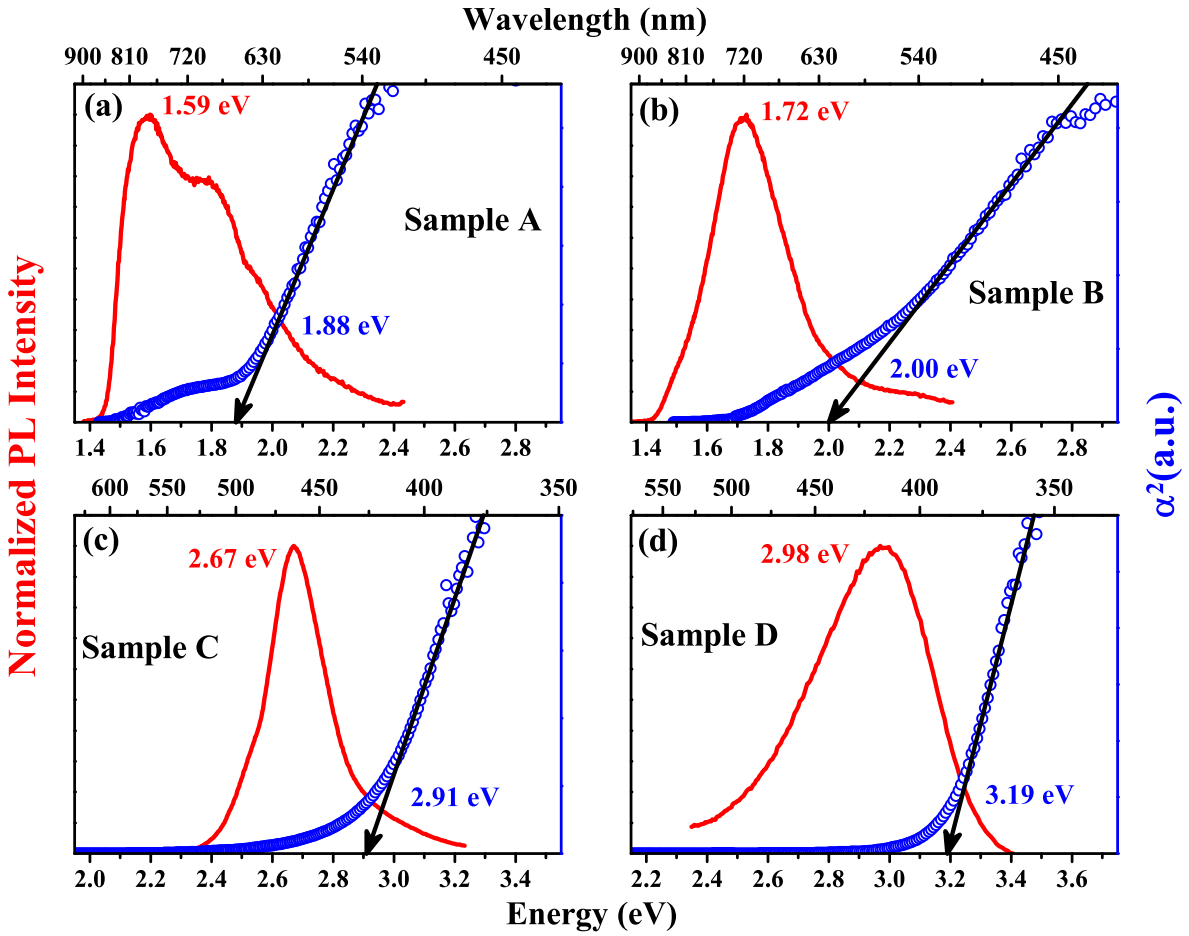

Figure 4.8: (a-d) show PL (red curve) and absorption spectra (open blue circles) for samples A-D, respectively.

average indium compositions, which could be an under-estimate of the actual indium composition responsible for the emission. Particularly, samples A and B, which show phase separation, lead to the estimation of a high value of the bowing parameter. It can also be noted that researchers have not yet arrived at a consensus of any single bowing parameter value which is sufficient to describe the bandgap of InGaN over the entire composition range.[333,352] Formation of QDs, due to phase separation, during growth of InGaN QWs has been reported[382,383] to contain more indium than the surrounding InGaN matrix, which yield two InGaN related PL emissions, where lower energy peak is assigned to the QDs and the higher energy peak to the InGaN matrix. At RT, the relative PL intensity of the QDs is much higher than that of the InGaN matrix[383], due to enhanced carrier transport from the low-indium-content matrix to the high-indium-content QDs. Now, as we have observed 63% and 59% indium content phases in sample

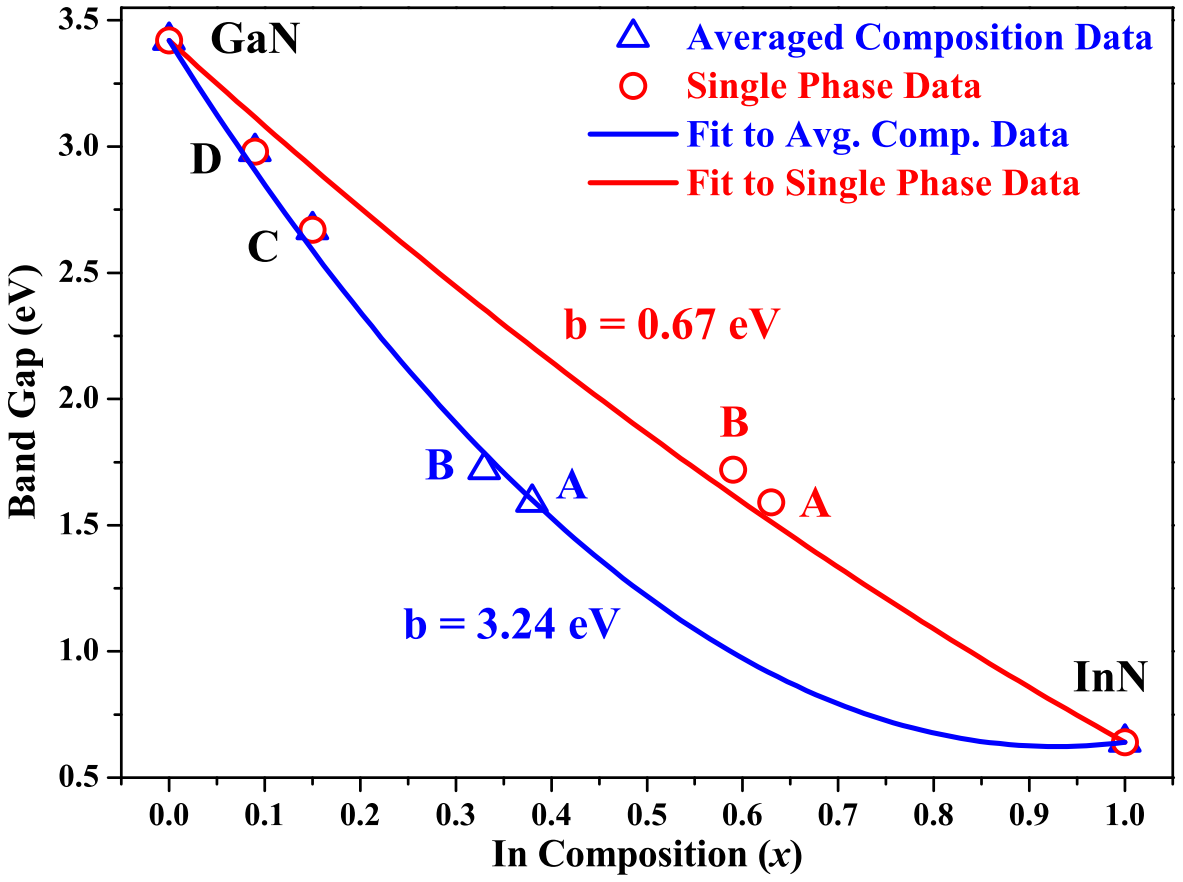

Figure 4.9: shows the fitting of nonlinear Vegrd's law of bandgap to the plot of bandgap values versus the respective indium compositions for all the samples.

A and B, respectively (Figure 4.6), we speculate that for samples A and B, the PL emissions recorded at RT originate from those high-indium-content phases, which have higher luminescence efficiency. On the other-hand, emissions from low-indium-content phase regions, expected in the higher energy regions, are absent for samples A and B, due to low emission efficiency in comparison to that from the high-indium-content phase regions, at RT.[383] In the absence of those high-indium-content phases, low-indium-content phases emit significantly at RT, which is evident from our samples C and D. Hence, if we consider that the 1.59 eV and 1.72 eV emissions, for samples A and B, are originating from the 63% and 59% indium containing InGaN phases, respectively, and re-fit the bandgap vs. composition plot with the modified Vegard's law, we obtain a bowing parameter of 0.67 eV (see Figure 4.9), which is significantly lower than the theoretically estimated value of 1.44 eV[351] and corroborates our assumption. It is well known that "bowing-parameter"

has been extensively used as a measure of the deviation of emission from that for the ideal alloy composition. Taking an average composition value from HRXRD data yields a large bowing parameter of 3.24 eV. However, if we choose the composition of the $In_xGa_{1-x}N$ (x = 0.63 for sample A and 0.59 for sample B), then we get a better bowing parameter value of 0.67 eV, suggesting that the emissions from these phases are dominant. Thus, correct identification of the emitting phases can lead to the lower value of bowing parameter, which is closer to the linear dependence of bandgap on indium composition.

Figure 4.8 also shows the optical absorption measurements done in the transmission mode (optical scattering and reflection losses have been neglected) where α^2 versus E curves are plotted along the alternate y-axis, in the high absorption range by following the relation $\alpha(E) \propto ln(1/T)$, where α, E and T are optical absorption coefficient, energy and transmittance, respectively. The linear regions of the plots have been extrapolated to $\alpha^2 = 0$, to obtain the value of the optical bandgap and they are found to be 1.88 eV, 2.00 eV, 2.91 and 3.19 eV for samples A-D, respectively. Thus, absorption measurements follow the same trend of the PL measurements, with indium incorporation.

Table 4.2: Experimentally obtained parameters of all the samples

Sample	$x_{Average}$ (%) (HRXRD)	E_g^{PL} (eV)	E_g^{Abs} (eV)	Stoke's Shift (eV)
A	38	1.59	1.88	0.29
B	33	1.72	2.00	0.28
C	15	2.67	2.91	0.24
D	9	2.98	3.19	0.21

It can be seen from Table 4.2 that all the samples show a positive Stoke's shift ($E_g^{Abs} - E_g^{PL}$) and it increases with decreasing emission energy, corresponding to increasing levels of indium incorporation. The Urbach tail states[384], that appear near the band-edge of the material due to carrier localization, are responsible for the Stoke's shift. For InGaN systems Stoke's shift increases with increasing indium composition as well as with the reduction in emission energy[204,352] and thus the shift implies the presence of localized carrier states, which can arise from the random distribution of indium atoms.[385] As the indium content increases, the indium-rich regions become larger and the localized state

goes deeper causing more red-shift.[381] It can be seen that, the amount of Stoke's shift is almost equivalent in both the samples A and B. On the other hand, for samples C and D, it is comparatively smaller due to absence of major phase separation in these samples, which is in accordance with our HRXRD observations.

4.2.4 Inferences

Single crystalline, wurtzite InGaN films are grown directly on *c*-sapphire using four different indium fluxes at a low growth temperature of 380 °C with constant nitrogen and gallium flux by MBE, under nitrogen-rich condition. Well separated and vertically aligned thick NRs with flat *c*-plane top are obtained at indium K-cell temperatures of 850 °C and 825 °C, whereas at 800 °C, thin NRs with truncated pyramidal top, consisting of $\{10\bar{1}1\}$ facets are formed. The NR density and uniformity of NR diameter increases with decreasing indium flux. At indium K-cell temperature of 775 °C the initially separated NRs coalesce and form an interconnected network morphology. Nitrogen-rich growth condition initiates of the 3D-growth and the stabilizes of N-polar $\{10\bar{1}1\}$ facets, at lower indium flux. At the lowest indium flux used in our case, NRs coalesce due to larger $\{10\bar{1}1\}$ facet formation and enhancement in the sidewall growth of the closely spaced NRs. HRXRD analysis shows that lower indium flux promotes single InGaN phase formation, whereas higher indium flux causes phase separation. InGaN(0002) peak has been deconvoluted to identify the different InGaN phases present and quantify the average indium composition. Phi scan analysis confirms that high indium flux introduces in-plane rotation among the grown crystals along with phase separation. Only high indium-content phases of the phase-separated samples are observed to be emitting at RT, which is attributed to the formation of high indium-content regions within the surrounding low indium-content InGaN matrix, due to enhanced carrier transport from matrix to these indium-rich regions at RT. Optical absorption measurements and the PL emissions are found to follow the modified Vegard's law of bandgap with a low bowing parameter of ≈ 0.67 eV. The positive Stoke's shift is found to increase with decreasing emission energy, corresponding to increasing levels of indium incorporation, which is attributed to the increasing InGaN phase separation within the films and consequent increase in carrier localization.

4.3 Effect of Gallium and N_2 flux

After observing the effect of growth temperature and indium flux, we have grown InGaN thin films directly on *c*-sapphire with different gallium and N_2 flux, to study their consequent effect on the morphology, structural quality and optical emissions of the grown films, which are discussed in this section.

4.3.1 Experimental Details

All InGaN thin films are grown by PAMBE, on *c*-sapphire for 120 min. Chemically pre-cleaned *c*-sapphire substrates were thermally degassed inside the preparation chamber at 600 °C for 60 min, followed by annealing in the growth chamber at 850 °C for 15 min to obtain the characteristic RHEED pattern of atomically clean *c*-sapphire. Two sets of samples have been studied in this work and all of them are grown at a growth temperature of 330 °C. In the first set of growths, the nitrogen flow-rate is kept at 4.5 sccm, whereas in the second set nitrogen flow-rate is maintained at 8.0 sccm. For both set of growths, the RF plasma forward power is kept at 375W and the indium K-cell temperature is held at 800 °C to maintain a indium BEP of 2.3×10^{-7} torr. In each set, three samples are grown, where the temperature of the gallium K-cell is increased from 950 °C to 1000 °C in steps of 25 °C, to increase the gallium flux-rate, keeping all other

Table 4.3: Growth details of the samples

Sample	Ga K-cell Temperature (°C)	Ga BEP ($\times 10^{-7}$ torr)	N_2 flow-rate (sccm)	$x_{Applied}$ (%) In/(In+Ga)	V/III BEP ratio
A	950	1.0	4.5	70	77.3
B	950	1.0	8.0	70	137.9
C	975	1.6	4.5	59	65.4
D	975	1.6	8.0	59	116.7
E	1000	2.5	4.5	48	53.1
F	1000	2.5	8.0	48	94.8

For all samples: In BEP = 2.3×10^{-7} torr and N_2^* BEP = 2.55×10^{-5} and 4.55×10^{-5} torr for flow-rate of 4.5 sccm and 8.0 sccm, respectively.

growth parameter constant. All the sample notations, along with their growth details are presented in Table 4.3. All the samples are then probed using different complementary characterization techniques, which are FESEM, HRXRD, RT CL Spectroscopy and RT Optical Absorption Spectroscopy (UV-VIS-NIR Spectroscopy in transmission geometry).

4.3.2 Results and Discussions

4.3.2.1 FESEM: Morphology

Figures 4.10(a)-(f) show the plan view FESEM images of all the grown samples A-F, respectively. Figure 4.10(a) shows the FESEM image of sample A which has an uneven, rough and random 3D morphology. A close look of sample A shows some kind of hexagonal borderline around the hillock shapes which could be due to the hexagonal symmetry of the wurtzite crystal of III-nitrides. When sample B is grown at almost twice the V/III ratio than that of sample A (see Table 4.3), vertically aligned, *m*-plane faceted, hexagonal NRs with flat *c*-plane tops are found to form, as can be seen from Figure 4.10(b). It can also be seen from Figure 4.10(b), that the NRs are surrounded by the 3D hillock shapes, which resembles the morphology observed in the case of sample A (Figure 4.10(a)). Sample C, grown at a higher gallium flux-rate, shows rough and 3D morphology (shown in Figure 4.10(c)), which resembles pyramidal shape. It can also be seen that along with the random 3D pyramidal structure, very few vertically aligned, *m*-plane faceted, hexagonal NRs with flat *c*-plane tops are also formed, one of which is visible at the central region of Figure 4.10(c). With the increase of N_2 plasma flow-rate, the density of NRs are found to increase in the case of sample D, shown in 4.10(d). It should be noted here that most of the NRs have C-shape and others are hexagonal in shape, even though all the NRs are vertically aligned, *m*-plane faceted and have flat *c*-plane tops. Along with the NR structure, underlying rough, 3D morphology, similar to the dominant morphology obtained for sample C, can also be observed in sample D. From the top view FESEM image, shown in Figure 4.10(e), of sample E, grown at even higher gallium flux-rate, it can be seen that only vertically aligned, *m*-plane faceted, hexagonal NRs have formed, where most of them have a thin and straight hexagonal protrusion at the top part and rest have *c*-plane flat top. The density of NRs is much higher compared to rest of the samples. Lastly, for sample F, thick vertically aligned, *m*-plane faceted, hexagonal NRs

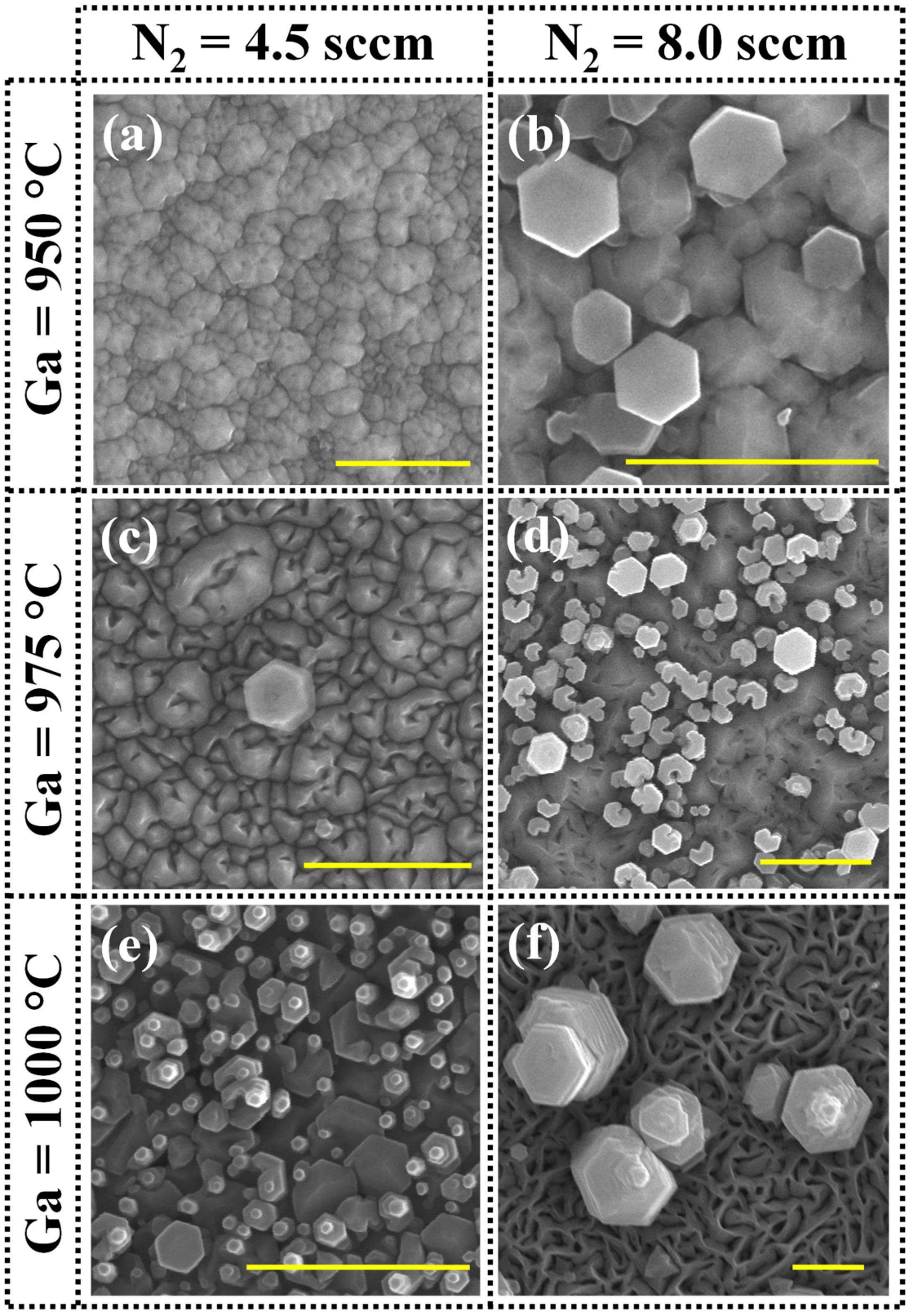

Figure 4.10: (a-f) show the top view FESEM images of all the grown samples A - F, respectively. Respective scale bar in yellow colour measures 500 nm, for all the samples.

with flat *c*-plane tops are found to form in the middle of underlying interconnected 3D random network morphology, as can be seen in Figure 4.10(f). Some kind of steps at the sidewalls of the NRs and hexagonal protrusion at the top, similar to that of sample E, also should be noted for the sample F. Thus, morphology of the InGaN films are greatly influenced by In/(In+Ga) ratio and nitrogen flow-rate.

4.3.2.2 Growth Mechanism

From the FESEM images it can be understood that all the samples have 3D morphology, which is expected as all our sample have been grown under nitrogen-rich condition (see Table 4.3). Comparing samples grown with 4.5 and 8.0 sccm, it can be seen that V/III ratio has increased by 2-fold in the later case and thus the NR formation have become very prominent and NR density comparatively increases with the increase of nitrogen flow-rate. Surprisingly, for sample E and F, though the NR density has reduced in the later sample but the underlying morphology has changed dramatically from pyramidal shape to sharp wall shape due to the increased V/III ratio. On the other hand by comparing sample A, C and E (or, B, D and F), it can be observed that vertical growth has become favourable with the increase of gallium flux-rate. This could be due to the fact that the supply of metal atoms, which helps in vertical growth of the NRs after the supersaturation, is not sufficient for lower gallium flux-rate and thus we have observed only uneven 3D hillock and pyramidal shapes as the dominant morphology for sample A and C. As the gallium flux-rate increases growth along the *c*-direction gets enhanced and prominent NRs are obtained in case of sample E. Similar explanation can be given for sample B, D and F with the exception of sample F, where sharp walls have formed which is the dominant morphology in that case. We believe that all the NRs obtained in this case are formed by following the Frank spiral growth mechanism under low supersaturation condition[386–388], where NR growth is screw-dislocation-driven and an axial screw dislocations provide the self-perpetuating steps to enable 1D crystal growth. This is in contrast to VLS and other catalyst-driven NR growth mechanisms. We believe that underlying rough morphology exposes some screw dislocations at the top surface, which acts as the low supersaturation seed for the consequent NR growth. As the mechanism works at lower supersaturation, we have obtained NR even after increasing gallium flux-rate (or, by reducing V/III ra-

tio). In addition to that, the C-shaped NRs observed in case of sample D, are the initial stages of the screw-dislocation mediated NR growth. Furthermore, hexagonal protrusion observed in case of sample E and F confirms the presence of screw-dislocation at the center of those NRs. Moreover, the steps seen in case of sample F, are formed due to the self-driven perpetual growth of the NRs, as reported earlier[387]. In summary, nitrogen-rich growth condition has facilitated 3D growth for all the samples. With the increase in nitrogen flow-rate NR formation has become favourable. Prominent formation of NRs for higher gallium flux-rate is due to the Frank spiral growth mechanism, which promote NR growth even at lower supersaturation.

4.3.2.3 HRXRD: Crystal Structure and Indium composition

Figure 4.11 shows the HRXRD results, for all the samples, where the symmetric $2\theta-\omega$ scans are plotted in logarithmic scale. The reflections are acquired on the InGaN(0002) plane with respect to the pre-aligned Al_2O_3(0006) plane. All the InGaN thin films are seen to possess a single crystalline, wurtzite structure with a preferential growth direction along the *c*-axis. The pattern in Figure 4.11 displays an intense Al_2O_3(0006) substrate peak at 41.68° and *c*-oriented peaks of InGaN(0002) planes in the vicinity of 32° - 34° region for all the samples, which indicates that the epitaxial relationship between the InGaN films and substrate is $[0001]_{InGaN} \parallel [0001]_{Sapphire}$. The absence of any other reflection from InN or GaN confirms the absence of those independent phases in our samples. All the InGaN samples show intense single InGaN(0002) reflections and the peak positions are located at 32.61°, 32.54°, 33.39°, 33.24°, 33.80° and 33.76°, respectively, for the samples A - F. The peak positions of each of the InGaN(0002) peaks are used to estimate the *c*-lattice parameters, which is then used to calculate the indium composition by using Vegard's law for lattice parameters ($c^{In_xGa_{1-x}N} = xc_0^{InN} + (1-x)c_0^{GaN}$), where, c_0^{InN} and c_0^{GaN} are the relaxed *c*-lattice parameters for bulk InN[125] and GaN[123], and x is the indium composition of the InGaN alloy, respectively. The calculated indium compositions (x) are indicated in the respective plots in Figure 4.11 and are also tabulated in Table 4.4. It should be noticed that there is no major phase separation for any of the samples, even after obtaining an indium composition as high as $\approx 60\%$.

Thus, it can be seen from Figure 4.11(a), (c) and (e) that with increasing gallium flux-

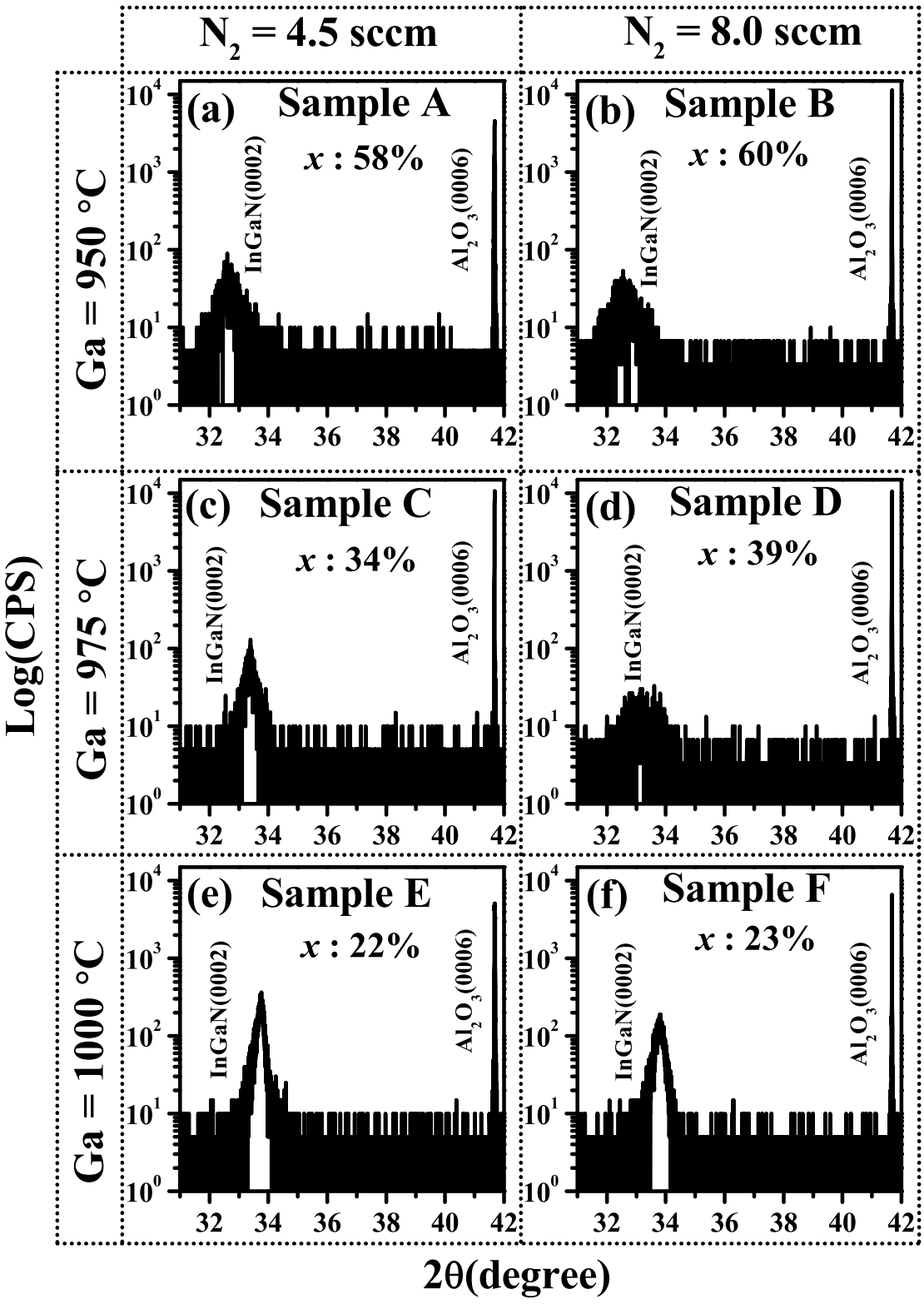

Figure 4.11: (a-f) show symmetric $2\theta-\omega$ scans acquired by HRXRD for all the grown samples A - F, respectively. Calculated indium compositions are indicated in the respective plots.

rate (or, reducing In/(In+Ga) ratio as can be seen from Table 4.3) the indium composition has reduced from 58% to 22% for sample A, C and E, which are grown with 4.5 sccm nitrogen flow-rate. Similar reduction of indium composition can be also observed in case of samples grown with 8.0 sccm nitrogen flow-rate, where the indium composition has dropped from 60% to 23% for samples B, D and F, as can be seen in Figure 4.11(b), (d) and (f). This reduction of indium composition seems to be expected as the applied In/(In+Ga) ratio has changed from 70 to 48 for each set of samples. One important thing should be noticed that for samples A and B the obtained indium composition ($\approx 60\%$) is closer to the applied In/(In+Ga) ratio ($\approx 70\%$), whereas the difference between those two parameters increases with increasing gallium flux-rate. Intermediate difference ($\approx$ 59% and 35%) in case of samples C and D and maximum difference ($\approx$ 48% and 22%) in case of samples E and F have been observed. All the samples are grown at same growth temperature, and thus the desorption rate of incoming metal adatoms, especially indium, remains same and thus, we believe that under higher gallium flux-rate, formation of Ga-N bonds are more favourable than In-N bonds, as it is well known that the In-N bond strength is weaker than Ga-N bond strength, which in turn reduces the indium incorporation in the lattice and increases the difference between the applied and obtained indium composition with increasing gallium flux-rate. Moreover, it can seen that the obtained indium composition for samples grown at higher nitrogen flow-rate (8.0 sccm) is slightly higher than that grown at lower nitrogen flow-rate (4.5 sccm), but at the same time it is clearly visible that the intensity of the InGaN(0002) peak, which is essentially related to the crystal quality of the sample, is slightly lower in case of samples grown at high nitrogen flow-rate. Thus, it can be understood that even though a very high V/III ratio (≥ 100) minimally improves indium incorporation in the lattice, it also nominally degrades the crystal quality of the samples, as compared to the samples grown at lower V/III ratio (≤ 100). Similar drop of InGaN(0002) peak intensity can be observed if samples A, C and D are compared, which is related to the increased incorporation of indium in the lattice. With increasing indium composition, reduction in InGaN(0002) peak intensity has already been reported[213] and is also evident from our present study. Finally, it is clear from the HRXRD study that by employing high V/III ratio we are able to obtain indium composition of $\approx 60\%$ (sample A and B) without any major phase separation, which occurs easily in InGaN with indium

composition > 40% and is considered to be responsible for the well known "Green Gap" in InGaN. Thus, high V/III ratio ($\leq$ 100) suppresses the dissociation of In-N bond due to the presence of excess activated nitrogen on the growth surface and in turn stabilizes the high indium-content InGaN phases efficiently.

4.3.2.4 CL and Optical Absorption: Optical Properties

After understanding the morphology and structural phases of the grown films, we have studied their optical properties. Figures 4.12(a)-(f) show RT CL spectra for all the samples. For sample A, the CL spectra consist of two dominant peaks at 1.72 eV and at 2.18 eV, resulting in a very broad band-edge emission, as shown in Figure 4.12(a). On the other hand for sample B we could not identify any CL peak, as evident from Figure 4.12(b). We believe that in high indium incorporated films the composition fluctuation occurs spontaneously (evident from the broadening of the InGaN(0002) peak in HRXRD) and thus create low-indium-content and high indium-content phases, which are so minute (not large enough to diffract the X-ray beam) in this case that their presence is not clearly recorded by the HRXRD scans. Now, these phases create shallow (low-indium-content) and deep (high-indium-content) localization states within the bandgap and any carrier recombination in those states can give rise to multiple peaks in the CL spectra[381], which we speculate is what is happening in sample A. On the other hand, quenching of PL emission, for high indium composition, has been reported earlier, where phase separation has been claimed to be responsible.[213,350] It has also been reported that, both in low and high-indium content regions of InGaN films, few non-radiative recombination centers exist, which trap the thermally activated carriers and thus emission intensity decreases rapidly with increasing temperature.[338] These non-radiative recombination centers are attributed to structural defects caused by the difference of bond-length between In-N and Ga-N, and the point defects caused by growth under strongly off-stoichiometric conditions. Thus, taking into account very high nitrogen-rich growth condition (V/III ratio $\approx$ 140) as well as higher indium content for sample B, it can be understood that excessive activated nitrogen on the growth surface creates structural defects, which act as non-radiative recombination centers in addition to the defects caused by an increase of the indium content itself, and together they quench the RT CL emission for sample B. For each of the samples C, D, E

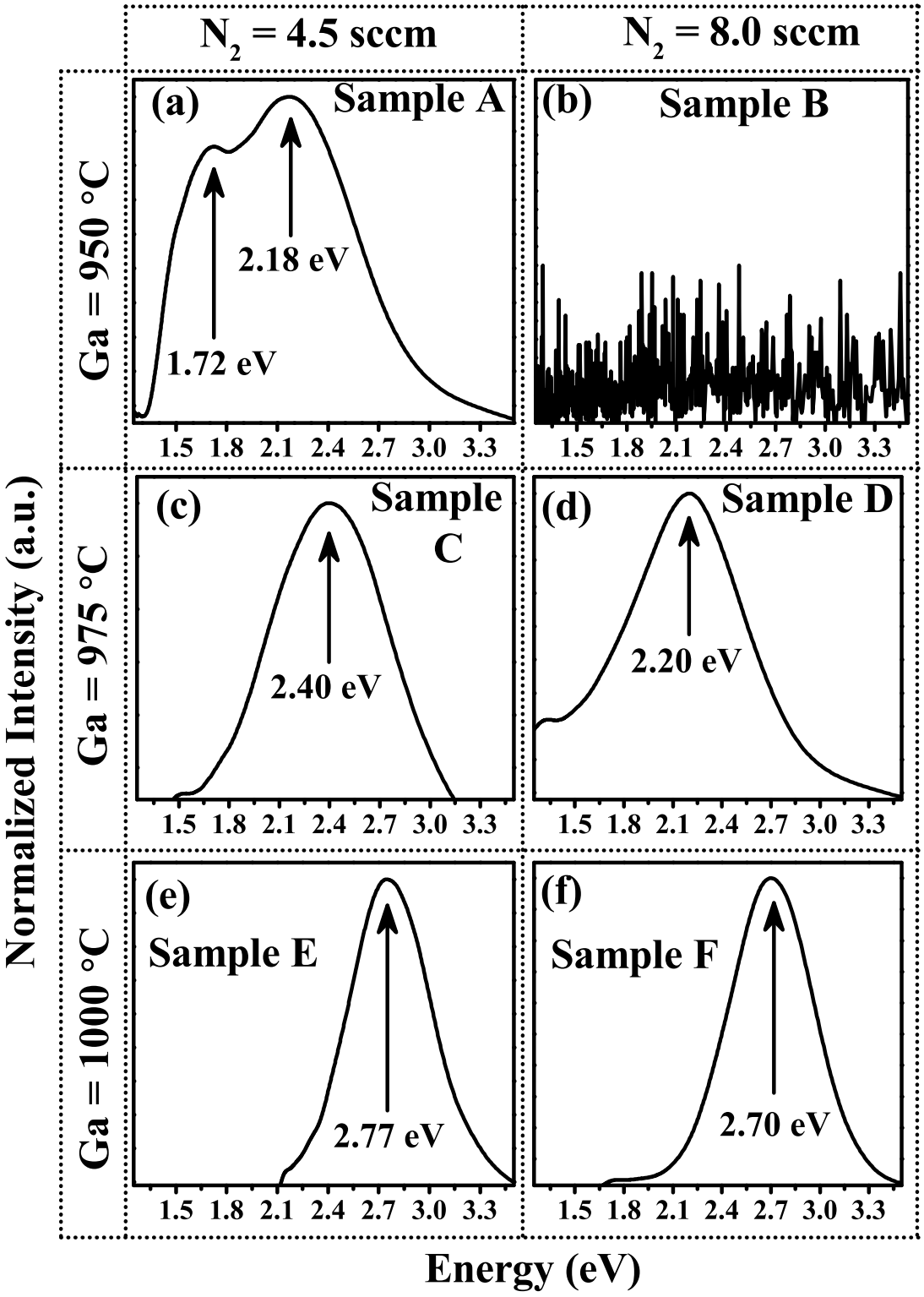

Figure 4.12: (a-f) show room temperature CL spectra for all the grown samples A - F, respectively. CL peak positions are indicated by black arrows and are written in the respective plots. No peak could be identified for sample B.

and F, CL emission peaks have been observed at 2.40 eV, 2.20 eV, 2.77 eV and 2.70 eV, respectively, which indicates that the uniformity of the alloy composition of the InGaN layer has been improved for higher gallium flux-rate. Moreover, samples grown at higher nitrogen flow-rate show red-shifted CL emission with respect to that of the samples grown at lower nitrogen flow-rate, due to the reason that high nitrogen flow-rate stabilizes higher indium incorporated phases in the lattice, as discussed in the HRXRD section.

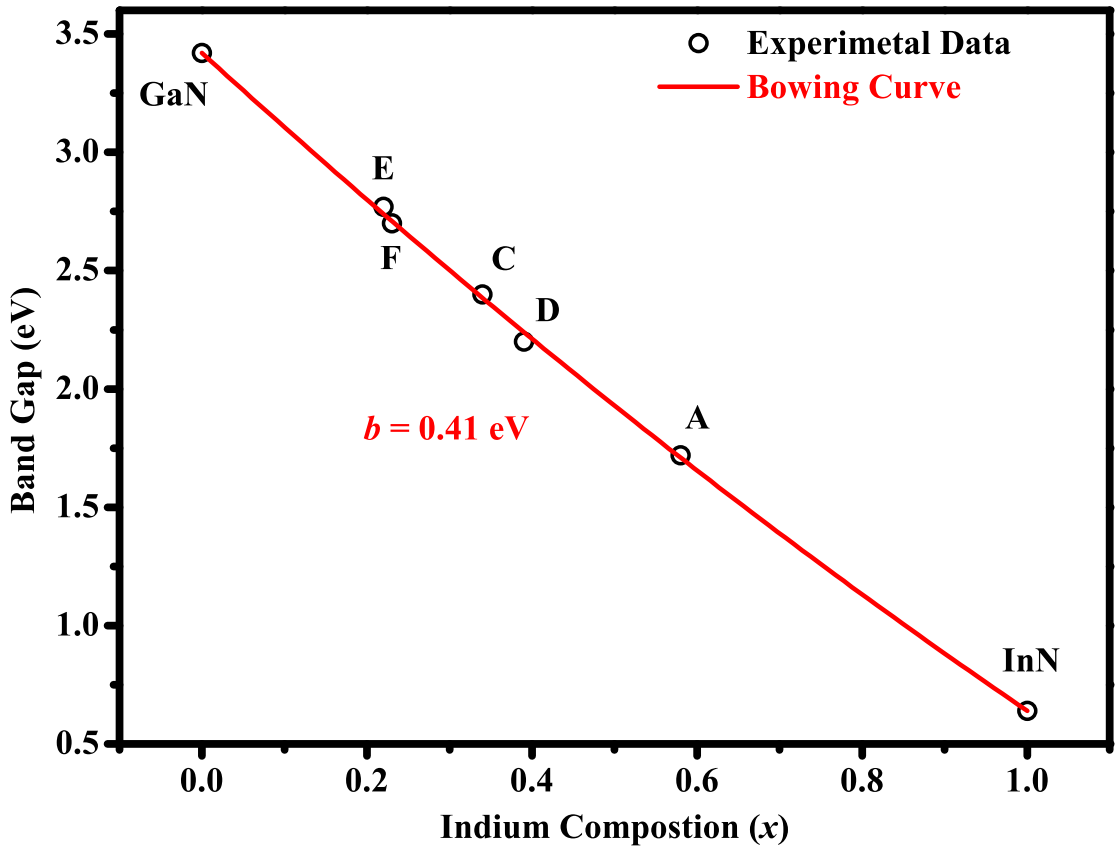

Figure 4.13: shows the fitting of nonlinear Vegrd's law of bandgap to the plot of bandgap values versus the respective indium composition for all the samples.

Now it is evident from the CL study that with increase in indium composition, CL emission energy undergoes a red-shift and this composition(x) dependence of the bandgap is explained using a modified Vegard's law of bandgap, expressed as $E_g^{In_xGa_{1-x}N} = xE_g^{InN} + (1-x)E_g^{GaN} - bx(1-x)$, where E_g^{InN} and E_g^{GaN} are bandgap values of intrinsic InN[15] and GaN[124], and $E_g^{In_xGa_{1-x}N}$ is the value of the emission energy deduced from CL measurements at RT and b is the bowing parameter. Now by fitting the modified Vegard's law to the experimental values (Table 4.4) for our samples, we have obtained the bowing

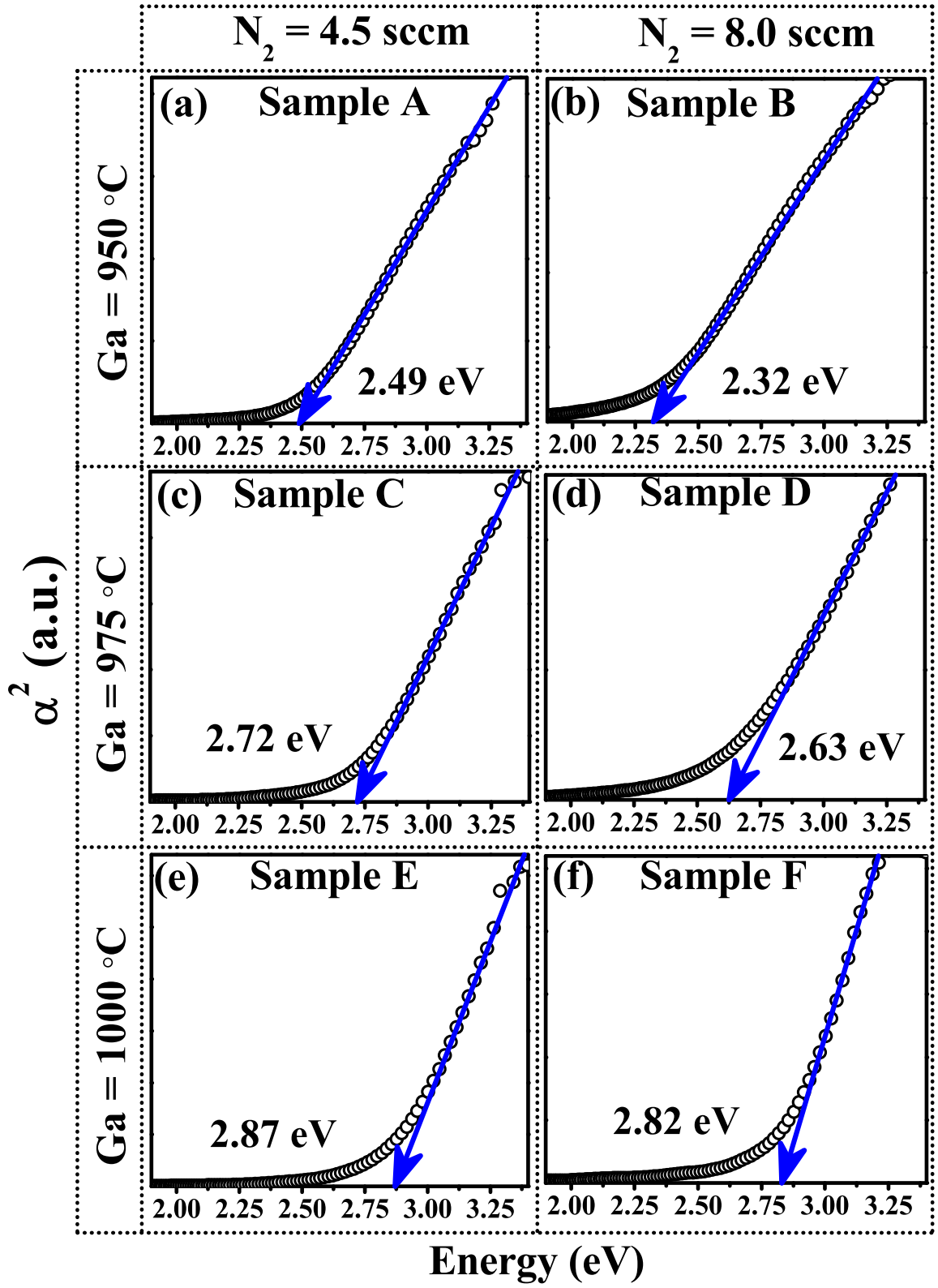

Figure 4.14: (a-f) show room temperature absorption spectra for all the grown samples A - F, respectively. Calculated absorption edge values are indicated in the respective plots.

parameter to be ≈ 0.41 eV (shown in Figure 4.13), which is smaller than the theoretically estimated value of 1.44 eV[351] and closer to the linear dependence of bandgap on indium composition.

The RT optical absorption measurement results are shown in Figure 4.14 which are obtained in the transmission mode and are plotted by following the relation $\alpha(E) \propto ln(1/T)$ and neglecting optical scattering and reflection losses. Here α, E and T are optical absorption coefficient, energy and transmittance, respectively. Thus, the value of the optical bandgap for the InGaN sample is obtained by plotting α^2 versus E in the high absorption range followed by extrapolating the linear region of the plots to $\alpha^2 = 0$. The obtained optical bandgap values are 2.49 eV, 2.32 eV, 2.72 eV, 2.63 eV, 2.87 eV and 2.82 eV, respectively for the samples A - F. Thus, absorption measurements follow similar trend as the CL measurements. It can be seen from Table 4.4 that all the samples show a positive Stoke's shift ($E_g^{Abs} - E_g^{PL}$), which increases with decreasing gallium flux-rate, corresponding to increasing levels of indium incorporation. It is well known that due to carrier localization, Urbach tail states[384] appear near the band-edge of the material, which are responsible for the Stoke's shift. For InGaN systems Stoke's shift increases with increasing indium incorporation[204,352] and thus the shift implies the presence of localized carrier states, which can arise from the random distribution of indium atoms[385] or, due to the formation of indium-rich quantum dots.[237] As the indium content increases, the indium-rich regions become larger and the localized state goes deeper causing more red-shift.[381]

Table 4.4: Experimentally obtained parameters of all the samples

Sample	$x_{Calculated}$ (%) (HRXRD)	E_g^{CL} (eV)	E_g^{Abs} (eV)	Stoke's Shift (eV)
A	58	1.72	2.49	0.77
B	60	–	2.32	–
C	34	2.40	2.72	0.32
D	39	2.20	2.63	0.43
E	22	2.77	2.87	0.10
F	23	2.70	2.82	0.12

4.3.3 Inferences

Single-crystalline, wurtzite InGaN films are grown directly on *c*-sapphire using three different gallium flux-rates at two different nitrogen flow-rates and at a low growth temperature of 330 °C by MBE, under nitrogen-rich conditions. Starting from uneven, rough and random 3D morphology, then C-shaped as well as hexagonal shaped, vertically aligned, *m*-plane faceted NRs with flat *c*-plane tops, and also underlying interconnected 3D random network morphology has been observed depending on different growth conditions. It has been speculated that nitrogen-rich conditions initiates the 3D growth and then NRs are formed by following the Frank spiral growth mechanism under low supersaturation condition, where the growth is screw-dislocation-driven and an axial screw dislocations provide the self-perpetuating steps to enable 1D crystal growth. indium composition is found to vary from $\approx 22\%$ to $\approx 60\%$ with the change of gallium flux-rate, and no major phase separation is observed due to the efficient stabilization of high indium-content InGaN phases under high V/III ratio. Structural defects, created by the excessive activated nitrogen on the growth surface and also by the increase of the indium content, act as the non-radiative recombination centers for the sample B and thus, all the samples, except sample B, are found to emit at room temperature. Optical absorption measurements and the CL emissions are found to follow the modified Vegard's law of bandgap with a very low bowing parameter of ≈ 0.41 eV. The positive Stokes shift is found to increase with decreasing emission energy, corresponding to increasing levels of indium incorporation, which is attributed to the increasing carrier localization with higher indium incorporation.

Chapter 5

Growth of InN and InGaN on *in-situ* modified Si(111) surfaces

This chapter discusses the growth of InN and InGaN nanostructures on different in-situ modified Si(111) surfaces and consequent effects on the morphology, crystal quality, indium incorporation and optical properties of the grown films. The work discussed in this chapter has been published in the following journals: Physica Status Solidi A ***210****, 2409 (2013), Journal of Applied Physics* ***118****, 025301 (2015)*

5.1 Growth of InN on Si(111)

We are able to grow high quality InN films on indium metal induced superstructural phases of Si(111) at comparatively lower growth temperatures than commonly employed in the literature for InN growth. With multi-technique characterization probes, we show that the promising route to obtain better crystallinity and emission properties for films that are grown on the 1×1 surface reconstruction at 200 °C, as compared to those grown on 7×7 reconstruction. These effects are observed in a narrow growth parametric region, and attributed to the better integral match of the 2D unit cells with the substrate reconstruction. Further improvement in the quality of InN films is accomplished by growing InN on the above formed epitaxial layers as intermediate layers which display PL emission even at room temperature. The effect of structural quality, carrier concentration and stoichiometry on band-edge emission and electron mobility of these films, show us the

direction towards obtaining high quality InN films on Si surfaces.

5.1.1 Introduction

InN with its unusually low conduction band-edge and superior electronic properties such as low effective mass and high mobility, highest peak and saturation velocities[389–391], and its exceptional propensity for n-type doping, has attracted great attention. InN films possess high unintentional conductivity, which originates from dislocations, native point defects, unreacted indium, mono-atomic hydrogen, and other guest impurities.[306,392–394] InN still remains as the least studied and understood material among the binary III-nitrides, due to the difficulty in preparation of high quality single crystal material because of its low dissociation temperature and the very high equilibrium vapor pressure of nitrogen.[395] The residual unintentional degenerate n-type doping and the very large surface electron density ($\sim 10^{20}$ cm^{-3})[111] have made it extremely difficult to achieve p-type doping in InN and to accurately determine other fundamental properties such as bandgap and carrier effective mass.[396] The high growth temperature required to crack ammonia precursor, dissociates InN and thus renders CVD processes non-desirable for the growth of InN. The PA-MBE growth has the advantage of employing low growth temperatures because of the high reactivity of the nitrogen (N_2^*) plasma with the elemental indium flux at the substrate surface.

Though lack of a suitable substrate material is a common problem to grow good quality InN, *c*-sapphire and 6H-SiC are the most commonly used substrates for InN growth with lattice mismatch values of 25% and 15%, respectively. But, the high resistivity of these substrates prevents direct electrical connection of InN devices with electronic components. On the other hand, Si(111) is an alternate substrate for InN growth due to its high abundance, low cost, good thermal conductivity, excellent crystal quality, attainability of large sized wafers, cleavability, excellent doping properties and due to the maturity of Silicon technology.[144] In the literature, several surface modifications of the sapphire substrates, such as formation of a thin AlN intermediate layer, growth on GaN epilayers, use of low temperature InN intermediate layer and alternating low and high temperature layers have been employed[304,397] and significantly high mobility was obtained.[145,398] Similar procedures have been pursued for Si as well. For instance, Grandal

et al. reported the improvement of the InN crystal quality when AlN buffer layers were used[399], Wu *et al.* studied the MBE growth of InN using an AlN/ultrathin β-Si_3N_4 as buffer layer on Si and found that β-Si_3N_4 serves as an effective diffusion barrier for Si auto-doping.[93] However, these methods still rely on the use of high growth temperature for the InN films, which itself may result in non stoichiometric films and undesirable effects of thermal expansion mismatches and Si auto-doping.

Recently, we have reported the novel growth scheme of Superlattice Matched Epitaxy, by PAMBE, to grow good quality InN and GaN on Si(111) substrates[305,400] at relatively low growth temperatures by using indium and gallium metal induced Si surface phases as growth templates. Low growth temperatures are not favourable for Si diffusion process, which can avoid unintentional Si doping in the InN films. For InN, we have shown that 0.5 ML indium induced 1×1 surface reconstruction of unit cell size 3.8 Å is the best lattice matched super-structural phase on Si(111) which results in a lower lattice mismatch (8%) with that of InN unit cell of 3.53 Å. Furthering this, in this study InN growth temperature has been optimized on Si (111)-1×1 as well as Si (111)-7×7 surface reconstructions, which are now used as templates to grow superlattice matched epitaxial thin native intermediate layers to form good quality InN films. We report formation of various InN morphological structures of the epitaxial films by varying the growth temperature and superlattice matched native layers.

5.1.2 Experimental Details

The InN thin films are grown by PAMBE and for all the growths indium K-cell temperature is maintained at 800 °C (BEP = 2.3×10^{-7} Torr) and N_2 flow rate of 4.5 sccm with a RF plasma forward power of 375W is used. Si(111) substrates are thermally degassed inside the preparation chamber at 600 °C for 60 min and further cleaned in the growth chamber at 800 °C for 30 min and at 900 °C for 5 min to remove the native oxide. While cooling the substrate down to room temperature (RT), the 1×1 to 7×7 phase transition is observed at ≈ 760 °C. We adsorb about 2ML of indium at RT on Si(111)-7×7 surface and anneal the surface at different temperatures in such a way that the metal desorption results in different surface reconstructions[305,401] by monitoring the evolution of the superstructures using RHEED. All other growth details are provided in

Table 5.1. The thickness of the films is measured by cross sectional FESEM and found to be ≈ 300 nm and surface rms roughness has been obtained using an Bruker Innova Atomic Force Microscopy (AFM) in the contact mode. All the samples are then probed using different complementary characterization techniques, which are RHEED (*in-situ*), FESEM, HRXRD, RT Hall effect measurements and RT PL Spectroscopy. Stoichiometry and composition measurements are performed using XPS with Mg-K_α (1253.6 eV) X-ray source with relative composition detection better than 0.1%. Before performing XPS measurements, InN thin films were sputter cleaned by an optimized low energy (0.5 keV, 2 μA) Ar^+ ions[307,402], to remove physisorbed adventitious carbon and oxygen resulting from atmospheric exposure, without affecting crystalline quality and surface composition of the films.

Table 5.1: Notations for samples prepared by various routes

Sample	Indium induced phase on Si(111)	Growth Temperature(°C)	Superlattice matched intermediate layers
A1	7×7	100	No
A2	7×7	200	No
A3	7×7	300	No
A4	1×1	100	No
A5	1×1	200	No
A6	1×1	300	No
B1	–	350	A5(30 min)
B2	–	350	A6(30 min)

5.1.3 Results and Discussion

5.1.3.1 FESEM: Morphology

Figure 5.1(a – c) show the FESEM plan view images of InN films grown on bare Si(111)-7×7 surface at 100, 200 and 300 °C (samples A1, A2 and A3), while Figure 5.1(d – f) is of InN films A4 - A6 grown on indium metal induced - 1×1 reconstructed Si(111) surface at 100, 200 and 300 °C, respectively. The images show that all the films

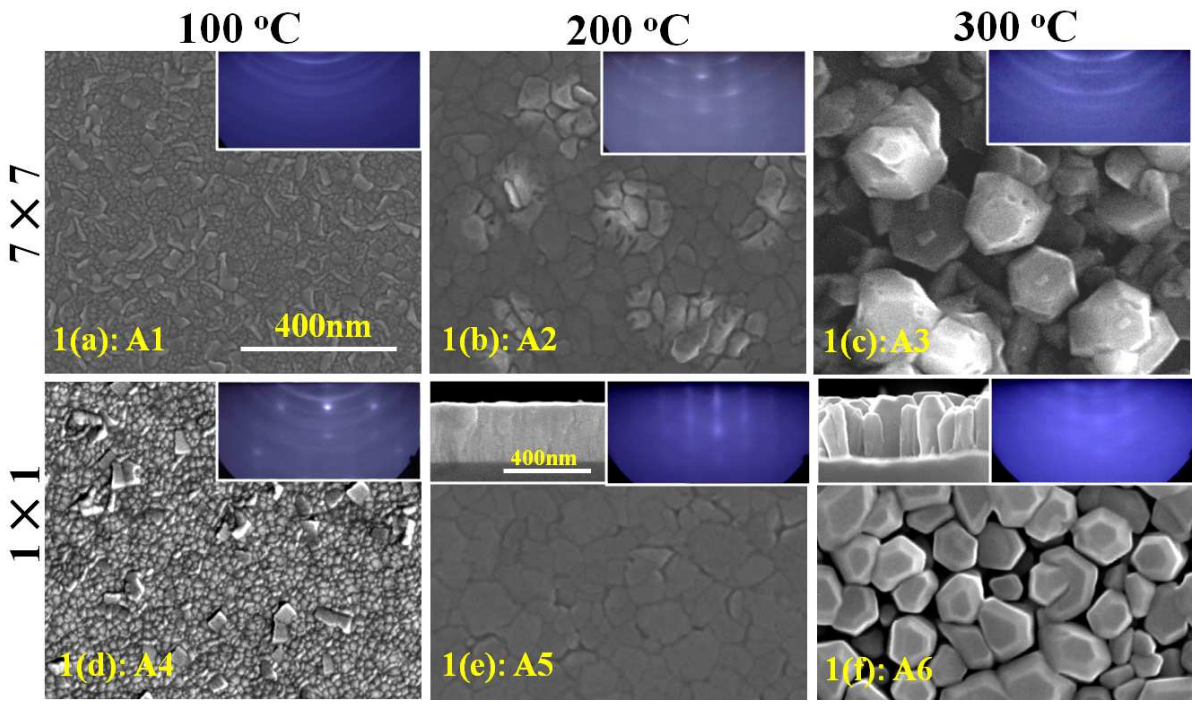

Figure 5.1: (a – f) show the top view FESEM images for all the InN films A1 - A6. Respective growth temperatures and indium induced superstructural phases are mentioned at the top and left side of the image. Scale bar for all the top view images is shown in (a). The top-left insets of (e) and (f) show the FESEM cross sectional view of the films A5 and A6. The top-right insets show respective RHEED pattern taken after growth with e-beam along $< 11\bar{2}0 >$.

have non-continuous granular surface morphology and the surface roughness varies with growth temperature. Samples A2 and A5 grown at 200 °C on Si(111)-7×7 and 1×1 surface reconstructed phases are relatively smoother (see Figure 5.1(b) and (e)) than the films grown at 100 °C and 300 °C on both the phases. RMS values of surface roughness calculated from 5×5 μm^2 scanned area for sample A1 – A6 by AFM are 12.4, 11.0, 32.0, 8.8, 4.7 and 9.2 nm, respectively. These values show that the films grown on Si(111)-7×7 have higher surface roughness than that of the films grown on better lattice-matched Si(111)-1×1 at respective temperatures.[305] Higher surface roughness values (32 and 9.2 nm) for samples A3 and A6 can be due to the enhanced surface diffusion of indium atoms at relatively higher growth temperatures. The corresponding top-right insets of each image show the respective RHEED pattern, taken along $< 11\bar{2}0 >$ direction, consisting of rings or rings with elongated spots for samples A1 – A4, reflecting poor crystal quality and high surface roughness. The faint streaks for sample A5 is due to a fairly smooth crystalline surface. Observation of spots alongside the streaky pattern for sample A6

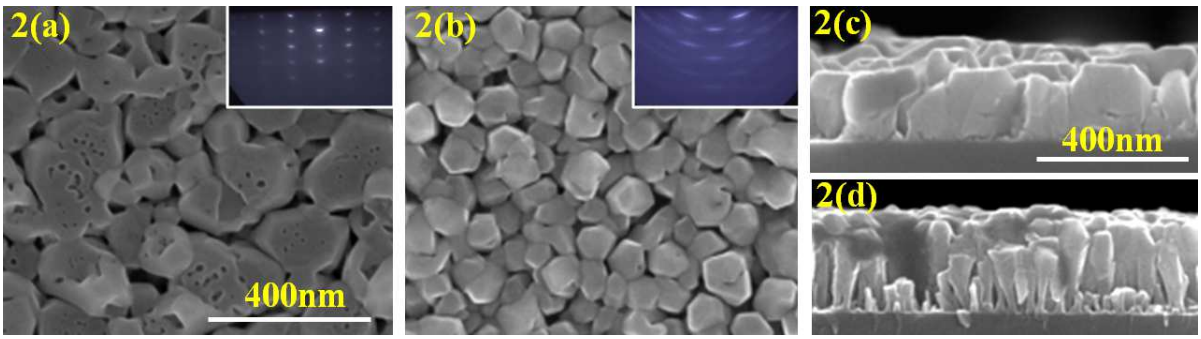

Figure 5.2: (a) and (b) show the top view FESEM images for the samples B1 and B2 respectively. (c) and (d) show the respective FESEM cross sectional view. The top right insets to (a) and (b) show respective RHEED pattern, taken after growth with e-beam along $< 11\bar{2}0 >$.

is due to electron transmission through the crystalline 3D granular structure with flat tops. The Figure 5.1(e) shows less surface rms roughness with closely packed flat top grains which appear to have coalesced owing to less dissociation of InN at this relatively lower growth temperature of 200 °C. The top-left insets to Figure 5.1(e) and (f) show cross-sectional view of samples A5 and A6, respectively. Compact and flat morphology is observed for sample A5, while A6 exhibits 3D columnar growth morphology with faint rings in its RHEED pattern due to the relative azimuthal misorientation of the crystallites.

Among these six samples, A5 and A6 show streaky RHEED pattern and relatively smooth surface morphology and narrower FWHM values in HRXRD ω-scan (discussed later). These films are now used as intermediate layers for growing InN epilayers at 350 °C to get better epitaxial films. As higher temperature is essential for better epitaxy, the second series of growth of InN has been performed at a relatively higher temperature but still 100 °C less than that used in conventional methods of growing InN using MBE. In this set, for further improvement in bulk crystalline quality of InN epilayers, A5 and A6 samples grown for 30 min have been used as low temperature lattice matched epitaxial intermediate layers to grow InN epilayers at 350 °C. Figure 5.2(a) and (b) show FESEM plan view images with their RHEED pattern as insets for the samples B1 and B2 which are grown at 350 °C on top of the low temperature lattice matched epitaxial intermediate layers of thickness $\approx$ 60 nm grown at 200 °C (A5) and 300 °C (A6), respectively. The films consist of isolated granular morphology, whose average grain size for sample B1 and B2 are 200 and 70 nm and AFM rms surface roughness values for these samples

are 5.2 and 8.0 nm, respectively. The spotty RHEED pattern of Figure 5.2(a) is due to transmission of electrons through the 200 nm 3D islands, as evident from Figure 5.2(c). While the RHEED with elongated spots through arcs in Figure 5.2(b) can be due to slight misorientation of nano columns seen in Figure 5.2(d). Thus, the InN film formed on top of 200 °C grown on the lattice matched (1×1) intermediate layer shows better surface crystalline quality than that of the film grown on top of 300 °C grown intermediate layer.

5.1.3.2 HRXRD: Crystal Structure and Quality

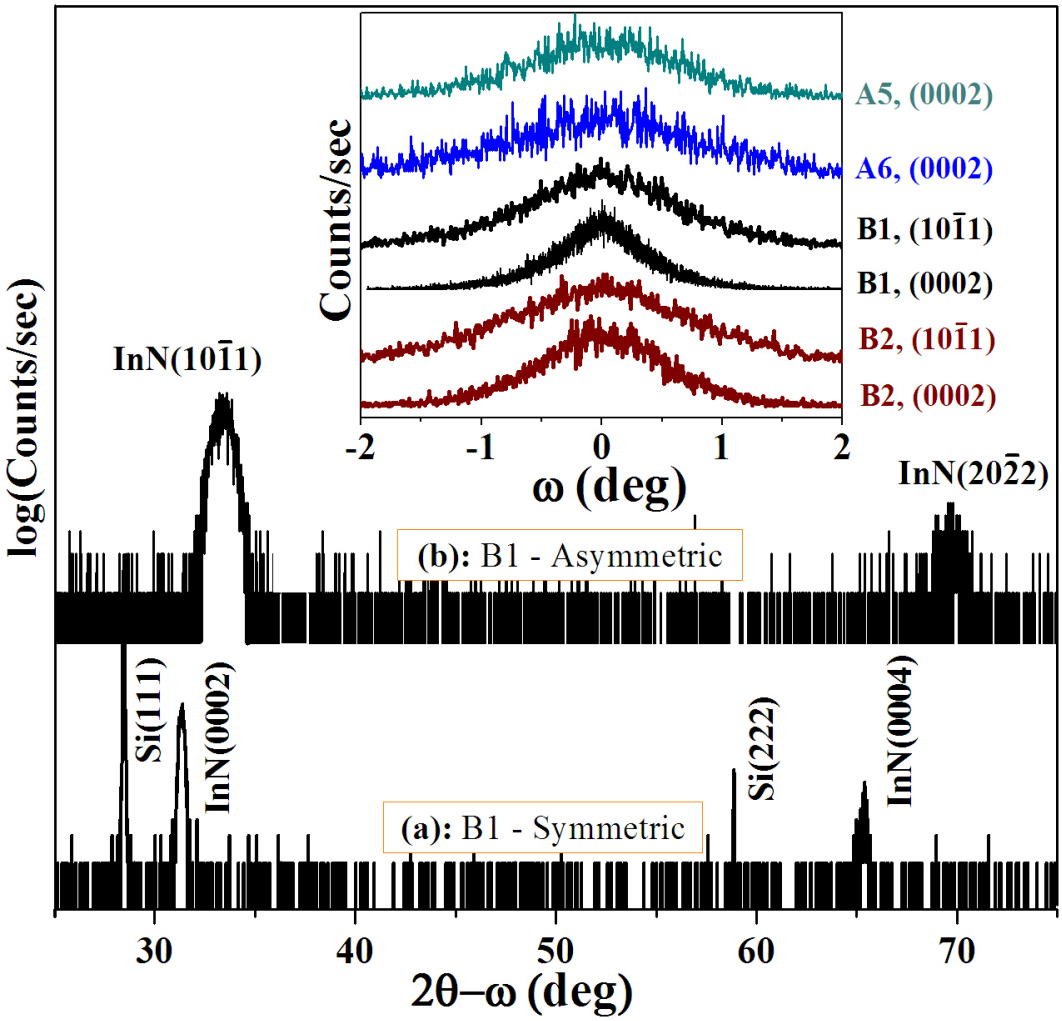

Figure 5.3: (a) and (b) show the HRXRD 2θ-ω scans that are acquired on symmetric and asymmetric reflections for film B1. The inset shows the ω-scans for the InN(0002) reflection of films A5, A6, B1 and B2, and for InN(10$\bar{1}$1) reflection of films B1 and B2, respectively.

To understand the crystal structure and bulk crystalline quality of the InN films HRXRD measurements are carried out and the results are shown in Figure 5.3, which

shows 2θ-ω scans that are acquired on symmetric and asymmetric planes for sample B1, respectively. In symmetric geometry, samples are aligned with reference to the strong Si(111) reflection observed at 28.40°. The film B1 is seen to be single crystalline wurtzite structure, by displaying intense *c*-oriented peaks, InN(0002) at 31.28° and InN(0004) at 65.30° along with substrate peaks viz. Si(111) and Si(222) at 28.40° and 58.80°, respectively, as shown in the Figure 5.3(a). Asymmetric planes are studied in skew-symmetric geometry, where the plane of interest is setup normal to the diffraction plane in such a way that it satisfies Bragg's diffraction condition.[403] Figure 5.3(b) shows 2θ-ω scan for the asymmetric reflection which consists of InN($10\bar{1}1$) and InN($20\bar{2}2$) peaks at 33.4° and 69.79°, respectively. Similar HRXRD patterns are observed (not shown in Figure) for remaining samples (A1 – A6 and B2) which confirm all grown films are single crystalline with wurtzite structure. The inset in the Figure 5.3 shows the ω-scans (rocking curves) around the InN(0002) and InN($10\bar{1}1$) reflections, and the FWHM values are listed in Table 5.2. Comparing the FWHM values for samples A5 (1.35°) and B1 (0.82°), it can be seen that crystalline quality of B1 is better than that of A5. Similar trend has been observed for samples A6 and B2. The high FWHM values of 1.74° and 1.25° for samples A6 and B2 reflects the crystallite tilt, as observed in their FESEM cross sectional view and RHEED studies in Figures 5.1 and 5.2. The rocking curves around InN($10\bar{1}1$) reflection for films B1, B2, A5 and A6 having the FWHM values of 1.55°, 1.88°, 2.10° and 2.36° (for A5 and A6, rocking curves are not shown in the inset), which are higher than the respective InN(0002) rocking curves, indicating the domination of edge dislocations, resulting from twist. Thus mosaicity, resulting from tilt and twist of the grown crystals, is minimum for sample B1, among the grown samples. As described by Lee *et. al*[403], dislocation density is calculated using tilt and twist from InN(*000l*) and extrapolated InN($h0\bar{h}0$) rocking curve broadening values, respectively, and for sample B1 it is found to be $\approx 6\times10^{10}$ cm^{-2}. Hence, the films grown on lattice matched intermediate layers have shown improved crystal quality than the films grown directly on indium induced surface reconstructions Si(111)-7×7 and Si(111)-1×1. Thus, from 2θ-ω and ω-scans, it is observed that the InN film B1 has the best crystalline quality among the films grown.

5.1.3.3 Electron Mobility and Crystal Quality

RT Hall measurements performed on these samples at 0.58T show that they are n-type and the corresponding carrier concentration and mobility values are listed in Table 5.2, which also consists of the respective stoichiometry ratio obtained from XPS and band-edge emission observed by PL, which will be discussed later.

Table 5.2: Different experimentally measured parameters: AFM roughness, rocking curve FWHM, Hall carrier concentration, mobility, XPS % composition ratio and PL band-edge emission for all samples.

Sample	AFM - rms roughness (nm)	Rocking curve InN(0002)/(10$\bar{1}$1) FWHM (°)	Carrier concentration (n) (cm^{-3})	Mobility (μ) (cm^2/V-s)	XPS In / N ratio	PL emission (eV)
A1	12.4	3.21	7.0×10^{21}	11	1.15	–
A2	11.0	2.15	3.0×10^{20}	23	0.91	1.32
A3	32.0	2.73	6.3×10^{20}	13	0.93	2.00[305]
A4	8.8	3.12	3.0×10^{21}	17	1.13	–
A5	4.7	1.35 / 2.10	1.2×10^{20}	50	1.03	1.12
A6	9.2	1.74 / 2.36	6.0×10^{19}	47	1.00	0.74[305]
B1	5.2	0.82 / 1.55	4.2×10^{19}	75	1.00	0.72
B2	8.0	1.25 / 1.88	8.1×10^{19}	57	1.02	0.80

To understand the dependence of electron mobility on structural quality of films, electron mobility and rocking curve FWHM values are plotted as a function of carrier concentration for all samples in Figure 5.4. As expected, it clearly shows that mobility monotonically decreases with increasing bulk carrier concentration. Samples that possess high mobility have good crystalline quality (lower ω-scan FWHM values). Hall measurements also reveal that sample A5 and A6 which have narrower rocking curve FWHM values, have better electrical properties among the first six samples A1 – A6, as listed in Table 5.2. This justifies the choice of the same growth parameters of A5 and A6 to obtain the low temperature lattice matched intermediate layers to form improved thin films. When the lattice matched intermediate layers are employed in the case of samples B1 and B2, grown at 350 °C, the crystalline quality is improved as well as better electri-

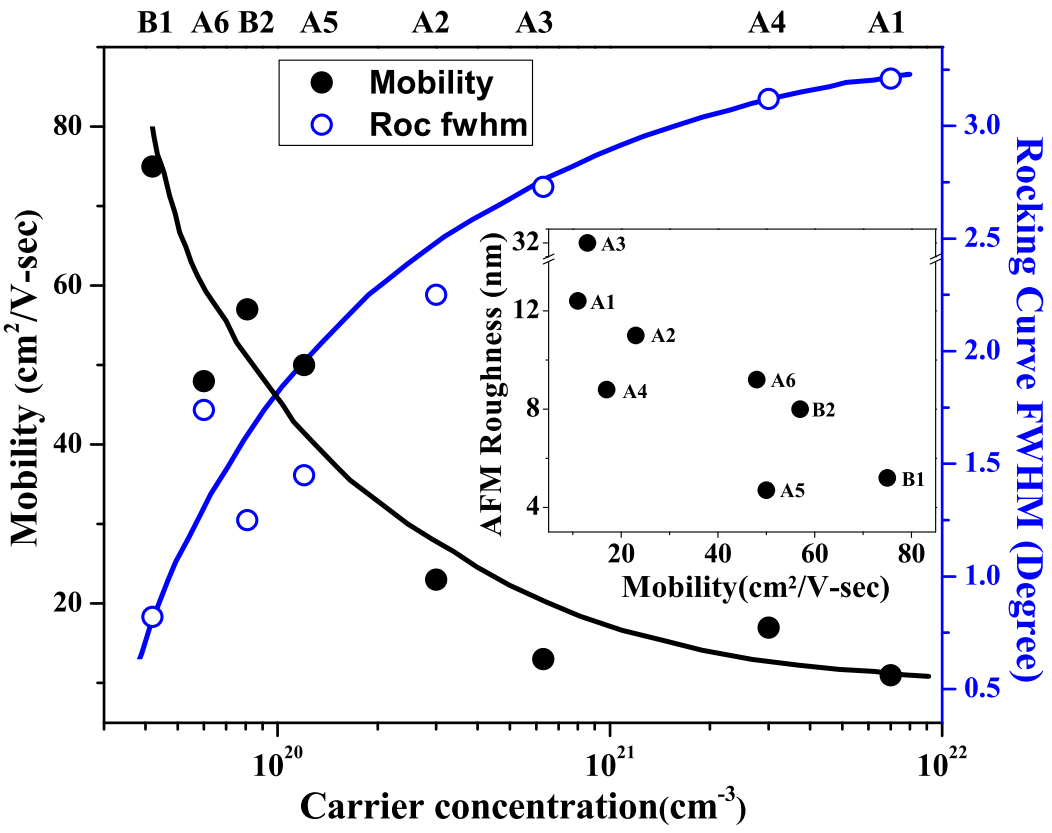

Figure 5.4: shows Hall mobility and HRXRD rocking curve FWHM values plotted as a function of Hall carrier concentration for all the grown samples, solid lines (guide to the eye) show the trend of variation in parameters. Inset shows AFM rms surface roughness versus Hall mobility plot.

cal transport properties are obtained for these samples. Calculated threading dislocation density from HRXRD measurements for sample B1 is $\approx 6\times10^{10}$ cm^{-2}. However, since these films are highly degenerate (10^{19} – 10^{20} cm^{-3}), the effects of dislocations will be minimal on the mobility of electrons, due to their screening by electrons.[404] Inset to Figure 5.4 depicts the plot of AFM surface roughness versus mobility, which reveals that higher the surface roughness, lower is the Hall mobility and samples having AFM roughness > 12 nm show very low mobility. The sample A5 with lower roughness (4.7 nm) is having mobility of 50 cm^2/V-sec which is lower than the mobility of the samples B1 and B2 with higher roughness values. This can be explained by the fact that A5 has relatively broader rocking curve FWHM which reveals relatively poor crystalline quality and hence low mobility among these three samples (A5, B1 and B2). Overall, Figure 5.4 infers that the

mobility of electrons mainly depends on bulk carrier concentration and structural quality rather than surface morphology of the films. Thus, InN film B1 grown on 200 °C lattice matched intermediate layer exhibits minimum carrier concentration and narrow rocking curve FWHM along with a reasonably higher electron mobility of 75 cm^2/V-s.

5.1.3.4 PL: Bandgap and Moss–Burstein shift

The observation of PL for InN films was not reported until 2002[146] and still is rare in literature, due to the poor quality of InN films synthesized. We observe PL emission at RT for most samples, except for A1 and A4 samples. Figure 5.5(a) shows the RT PL spectra obtained for samples A2, A5, B1 and B2 with band-edge emission values of 1.32, 1.12, 0.72 and 0.8 eV, respectively. The PL band-edge emission values of 2.0 and 0.74 eV for samples A3 and A6 are previously reported.[305] The widths of the PL emission peaks are found to increase with increasing Hall carrier concentration. Among the first series of samples (A1 – A6), the lowest band-edge emission is recorded at 0.74 eV for sample A6, whereas sample A5 has the emission peak appearing at a higher value of 1.12 eV though it consists of relatively better structural and morphological characteristics than that of A6. This can be attributed to the higher carrier concentration that raises the Fermi level high into the conduction band. All these bandgap values are higher than the lowest reported value ($\approx$ 0.64 eV), which can be attributed to the strong band-filling effects (Moss-Burstein shift) caused by high carrier concentrations.[405] Samples (A1 and A4) grown at 100 °C do not show any PL emission because of its poor morphology and structural quality, which was evident from the ring like RHEED pattern, high values of AFM rms surface roughness and wider rocking curve FWHM values. Among the samples grown with lattice matched intermediate layers, sample B1 emits at the lower values of 0.72 eV than that of sample A5. On the other hand, sample B2 has an increased bandgap (0.80 eV) relative to sample A6 due to its higher unintentionally doped carrier concentration. However, it is clear that improvement in structural quality of InN films can be achieved by using intermediate super lattice matched epitaxial thin InN layers grown on indium induced 1×1 superstructural phase of Si(111).

As the accumulation of surface charge, present due to excess indium adatoms on grown InN surfaces, causes ambiguity in measuring the electrical properties and optical

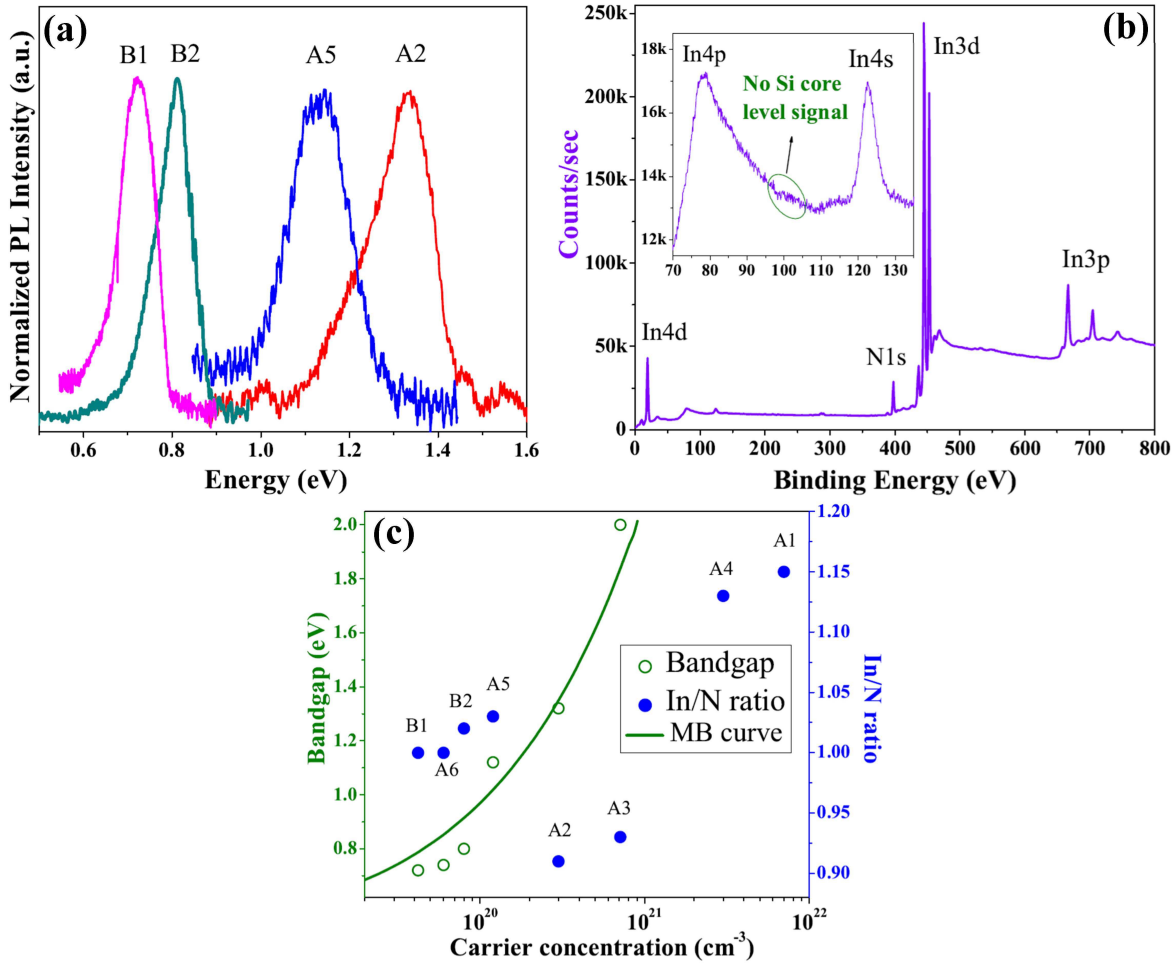

Figure 5.5: (a) shows PL spectra obtained for samples A2, A5, B2 and B1. (b) and respective inset show the survey scan and high resolution Si core level collected on sample B1, after treating with low and high energy Ar^+ ions, respectively. (c) shows PL band-edge emission values and XPS indium to nitrogen ratio plotted as a function of Hall carrier concentration and solid line indicates the theoretical Moss–Burstein curve.

properties of InN thin films[406], their dependence on stoichiometry also becomes important. As a measure of stoichiometry, the indium to nitrogen ratio is calculated from XPS survey scans. The scans are acquired on the films treated by low energy Ar^+ ions, ensuring removal of surface contaminants but no preferential sputtering of the nitrogen and thus no III–V bond breaking of InN films.[307,402] Figure 5.5(b) shows the survey scan for the film B1, where O*1s* and C*1s* core level peaks almost vanish, which indicates the removal of adventitious carbon and oxygen. Inset shows the high resolution core level performed for Si*2p* signal that is obtained close to the interface of sample B1 upon treatment with high energy (2 keV, 11 μA) Ar^+ ions. The absence of Si signal in bulk of the films confirms that

there is no significant diffusion of Si atoms into the overgrown InN film from substrate. Thus, high carrier concentration could be due to crystalline quality, donor like native point defects and stoichiometry of the formed films.

Figure 5.5(c) shows indium to nitrogen ratio and the bandgap values obtained from PL, plotted as a function of carrier concentration. The solid line shows the theoretically calculated Moss-Burstein curve using **k.p** theory by considering conduction band non-parabolicity, and normalization effects (electron–electron and electron–impurity interaction) using InN bandgap value of 0.63 eV.[304,390] The bandgap values obtained for these samples, represented by open circles in Figure 5.5(c), follow the trend of the MB curve. It can be seen that samples showing low bandgap are having nearly stoichiometric indium to nitrogen ratio, whereas samples with non-stoichiometric composition either show very high bandgap values, or absence of PL emission, as compared to the stoichiometric samples. As the indium tetragonal phase related peaks are not observed in HRXRD measurements for any of the samples, presence of indium metal crystallites in the bulk of the film can be excluded, and thus the observed IR emission is solely arising from InN.[407] This indicates that band filling effect alone does not determine PL emission, but stoichiometry also plays a deterministic role. It is evident from Figure 5.5(c) that InN film grown on top of 200 °C lattice matched intermediate layer (sample B1) has stoichiometric composition and has the lowest bandgap of 0.72 eV, among all the grown samples.

5.1.4 Inferences

The careful experiments are directed towards obtaining improved crystal quality of InN/Si(111) with low bandgap grown on native epitaxial intermediate layers. They are grown at relatively low temperatures compared to usual growth temperatures that are adopted in MBE systems for InN growth, so that there is a reduction in thermal expansion misfit effects and reduced Si diffusion in the film causing unintentional auto doping. This work demonstrates the optimization of growth temperature (of 200 °C) for single step growth of InN on indium metal induced superstructural 7×7 and 1×1 phases of Si(111). The results reveal that better crystalline quality of InN is achieved on the indium induced Si(111)-1×1 superstructural phase due to the smallest lattice mismatch of 8%

between the InN unit cell and 1×1 surface reconstruction, as compared to other observed superlattices. HRXRD measurements show that all the films grown in this study are *c*-oriented with wurtzite crystal structure and better crystalline quality is achieved for the film grown at 200 °C on 1×1 reconstruction. Further improvement in the crystal quality, confirmed by relatively narrower rocking curve FWHM widths, has been accomplished for the two step grown films B1 and B2, in which superlattice matched epitaxial thin InN layers, grown on indium induced 1×1 surface reconstruction, are used as intermediate layers. The obtained mobility values for the samples are found to be influenced by bulk structural quality and carrier concentration. Stoichiometric and good crystalline films that yield lower band-edge emission. On the other hand, higher bandgap values result due to the high degeneracy and non stoichiometry of the films. Absence of PL emission for samples A1 and A4 is due to poor crystal quality and high indium to nitrogen ratio. PL band-edge emissions are found to be varying in accordance with the band filling effects depicted by theoretical MB curve. Thus, our experiments not only demonstrate a method to form better quality InN at a reduced temperature and the dependence of optical and electrical properties on stoichiometry and structural quality of the grown films, but also show that lattice matched epitaxial native intermediate layers can act as hetero-buffers to attain good quality InN films. More studies are underway to achieve higher mobility and lower carrier concentration by optimizing growth parameters at relatively low growth temperatures to arrest the dissociation of InN and prevent Si out diffusion into the over grown InN layers by sheer kinetic control.

5.2 Growth of InGaN on Si(111)

We address the issue of obtaining high quality InGaN NRs without any phase separation on Si(111) substrate. Role of pre-nitridation of the Si(111) substrate and growth temperature, on the morphology, structural and optical properties of InGaN films grown by PAMBE, has been studied. Growth on bare Si(111) has resulted in columnar structure with poor epitaxy. The nitrogen rich growth environment and surface nitridation results in the formation of vertically well-aligned single crystalline NRs that are coalesced and isolated at 400 °C and 500 °C, respectively. Indium incorporation is also seen to be

enhanced to ≈ 28% at 400 °C. The orientation, phase separations and optical properties characterized by RHEED, FESEM, HRXRD, XPS and PL are corroborated to understand the underlying mechanism. The study optimizes conditions to grow high quality catalyst-free well-aligned InGaN rods on nitrided Si surface, showing stable PL emission at RT.

5.2.1 Introduction

The ternary alloy InGaN, is an important semiconducting material because of the tunability of its direct bandgap from near infrared to near UV.[356] Thus, InGaN can absorb and emit basic visible (red, blue, and green) wavelengths, whose combination can be used to create low-energy consuming high-brightness white light sources and for whole-spectrum multijunction tandem solar cells with excellent irradiance resistance.[80,84,408] However, fabricating highly efficient InGaN green wavelength emitters requires active regions with higher indium incorporation (>40%), which is difficult to achieve due to composition fluctuation and phase separation.[367] Thus, the role of composition, strain, ordering, and phase separation on the optical and structural properties of InGaN films and nanostructures is a crucial problem that demands more attention.[182,409]

The high resistivity of the most commonly used substrates for InGaN growth, such as *c*-sapphire and 6H−SiC, prevent direct electrical connection of overgrown InGaN devices with electrical components. Thus, Si(111) is being explored as an alternate substrate for InGaN growth due to its excellent doping properties, high abundance, low cost, good thermal conductivity, excellent crystal quality, availability of large sized wafers, ease of cleavability, and also for the integration of III-nitrides with the mature Silicon technology.[144] Researchers have tried to grow flat InGaN films on Si(111)[410,411] and high-quality $In_{0.4}Ga_{0.6}N$ film on GaN/AlN/Si(111) templates using MOCVD, with negligible phase separation.[412] Thick InGaN films (≈ 1μm) grown on AlN/Si(111) substrates by MOVPE showed the presence of GaN-rich InGaN and metallic indium phases by HRXRD.[413]

Most recent attempts involve the formation of InGaN nanostructures either directly or by using AlN or GaN buffer layers on Si(111).[296–301] These nanostructures exhibit significantly reduced defect density and high light extraction efficiency due to their large surface-to-volume ratio, and their reduced strain distribution that leads to a weaker piezo-

electric polarization field. However, the use of any buffer layers introduces an energy barrier, that electrically isolates the InGaN layer from the Si substrate, making advanced device design difficult. Recently, $In_xGa_{1-x}N$ NWs have been grown by halide chemical vapour deposition where the entire compositional range from $x = 0$ to 1 has been realized,[356] while using hydride vapor phase epitaxy indium composition only upto 10% has been achieved.[414] In the case of MBE grown InGaN nanostructures, researchers have obtained films with indium composition ranging from 2% to close to 25%, that show PL emission at RT and possessing good structural quality.[297–300] Using MBE, synthesis of well-aligned, good quality, single-phase InGaN nanostructures on Si substrates with high indium incorporation, that yields intense PL emission at RT, is still a challenging task.

The aim of this work is to compare the growth of InGaN films directly on Si(111) with that on surface modified (nitrided) Si(111) substrates, in terms of morphological, structural and optical properties, in order to obtain InGaN NRs with high indium incorporation having good structural and optical quality.

5.2.2 Experimental Details

The InGaN thin films (samples A−C) are grown by PAMBE on Si(111) substrate for 120 min. Si(111) substrates are thermally degassed inside the preparation chamber at 600 °C for 60 min and further cleaned in the growth chamber at 800 °C for 30 min and at 900 °C for 5 min to remove the native oxide. This results in the 1×1 surface reconstruction and has been observed by *in-situ* RHEED. While cooling the substrate, the transition from 1×1 to 7×7 reconstruction is observed at ≈ 760 °C by RHEED, confirming the atomic cleanness of the Si(111) surface. For all the InGaN growths, gallium and indium K-cell temperatures are set at 1000 °C (gallium BEP = 4.8×10^{-7} Torr) and 800 °C (indium BEP = 2.3×10^{-7} Torr), respectively, and the nitrogen flux is maintained at 4.5 sccm with a RF plasma forward power of 375W. The samples A and B are grown at 400 °C growth temperature, while sample C is grown at 500 °C. For samples B and C, prior to the InGaN growth, Si(111) substrate surface is pre-nitrided by exposing the substrate to nitrogen plasma at 800 °C for 10 mins to form a crystalline Silicon Nitride layer, which is confirmed by a diffuse streaky RHEED pattern. The thickness of the films are measured to be ≈ 1.8 μm, 1.0 μm and 1.3 μm for the samples A, B and C, respectively, using cross sectional

FESEM. All the samples are then probed using different complementary characterization techniques, which are RHEED (*in-situ*), FESEM, HRXRD, RT PL Spectroscopy and XPS (with Mg-K_α (1253.6 eV) X-ray source).

5.2.3 Results and Discussions

5.2.3.1 FESEM: Morphology

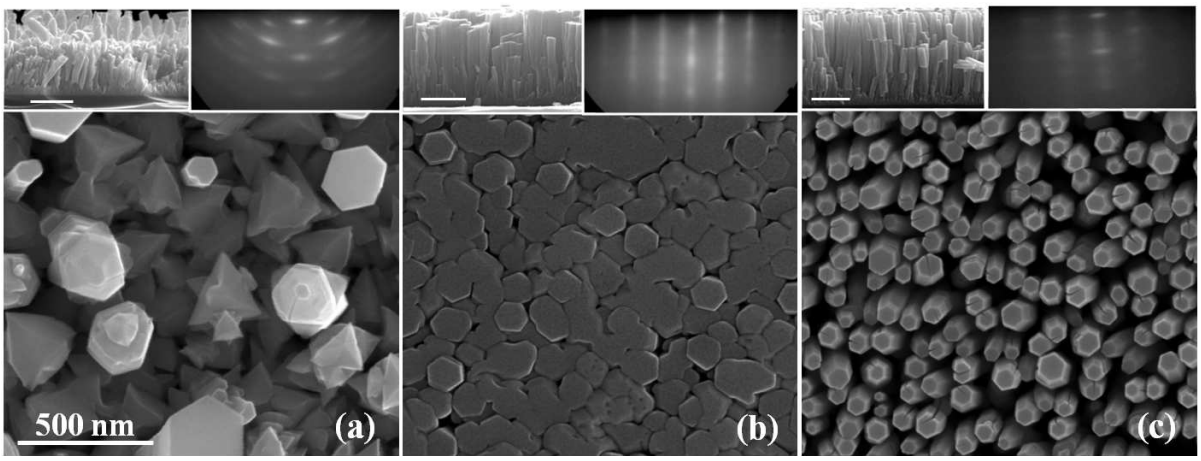

Figure 5.6: (a−c) show the top view FESEM images for samples A−C, respectively, with their corresponding cross-sectional FESEM image and RHEED pattern (taken after growth with e-beam along<11$\bar{2}$0>) as top left and right insets, respectively.

Figure 5.6(a−c) show the plan view FESEM image, with their right and left insets above showing the respective cross sectional FESEM image and RHEED pattern for samples A−C. Figure 5.6(a) shows the FESEM image for sample A grown on bare Si(111), without an intermediate nitride layer, at a growth temperature of 400 °C. It consists of triangular 3D NRs of $\approx$ 1.0μm length and $\approx$ 250 nm diameter with a few longer ($\approx$ 1.8 μm) hexagonally faceted rods among them. The variation in the lengths of the triangular islands and hexagonal rods can be seen in its corresponding inset showing the cross sectional FESEM image. The RHEED inset in Figure 5.6(a) shows spots due to the 3D features superimposed on a discontinuous ring-pattern that reflects tilt among the NRs and/or the poor crystallinity of the film. From Figure 5.6(b) it can be seen that sample B, grown on nitrided Si(111) at the same growth temperature used for sample A (400 °C), has closely packed *c*-oriented NRs, with density $\approx 6\times10^9$ cm^{-2} and an average diameter of $\approx$ 120 nm. It is also observed by the corresponding FESEM cross sectional

inset, that the individual NRs now coalesce into each other in the upper regions. The right inset to Figure 5.6(b) shows the streaky RHEED pattern formed due to electron reflection from the coalesced *c*-flat tops of the densely packed NRs. Thus, the quality of films, grown at 400 °C (samples A and B), is better when grown on pre-nitrided Si(111) surface. Figure 5.6(c) shows FESEM image of sample C, grown on the pre-nitrided Si(111) at a growth temperature of 500 °C, where hexagonal NRs with flat-tops are uniformly positioned and are well separated. The rods have an uniform length ($\approx$ 1.3 μm) with an average diameter of $\approx$ 75 nm and density $\approx 8\times10^9$ cm^{-2}. The right inset shows the streaky RHEED pattern with dots superimposed on them, due to simultaneous diffraction from the flat top *c*-plane and electron transmission through the crystalline 3D rods. It can also be seen that for InGaN growth on nitrided Si(111) (samples B and C), with increasing growth temperature (500 °C), the NRs appears separated and retain their *c*-plane tops, though the NR density remains similar. NRs grown on pre-nitrided Si(111) at 400 °C are thicker ($\approx$ 120 nm) and shorter ($\approx 1.0\mu$m) whereas, for sample C formed at 500 °C, NRs are comparatively thinner and longer. Thus, the film grown on nitrided Si(111) at 400 °C shows better surface crystallinity than other films with a morphology of coalesced NRs, while that grown at 500 °C yields *c*-oriented hexagonally faceted isolated NRs.

5.2.3.2 HRXRD: Crystal Structure and Indium composition

To understand the crystalline quality of the three InGaN films and their indium composition, HRXRD measurements are performed and the results are shown in Figure 5.7. The $2\theta-\omega$ scans, (intensity in logarithmic y-scale), are acquired on the InGaN(0002) plane with respect to the pre-aligned Si(111) plane. All the InGaN thin films are seen to possess wurtzite structure with preferential growth direction along *c*-axis. The pattern in Figure 5.7 displays intense Si(111) substrate peak at 28.44° and *c*-oriented peaks of InGaN(0002) planes in the region of $33° < 2\theta < 35°$, for all the samples. Sample A exhibits a low intensity peak at $\approx 32.78°$[415], characteristic of a crystalline tetragonal In(101) reflection, along with the InGaN($10\bar{1}1$) peak at 36.03°. Thus, sample A grown directly (without nitridation) on Si(111) substrate results in crystalline NRs that are tilted relative to each other. They also have remnant unreacted crystalline indium and as a result shows poor epitaxial relationship with the underlying substrate. The tilt

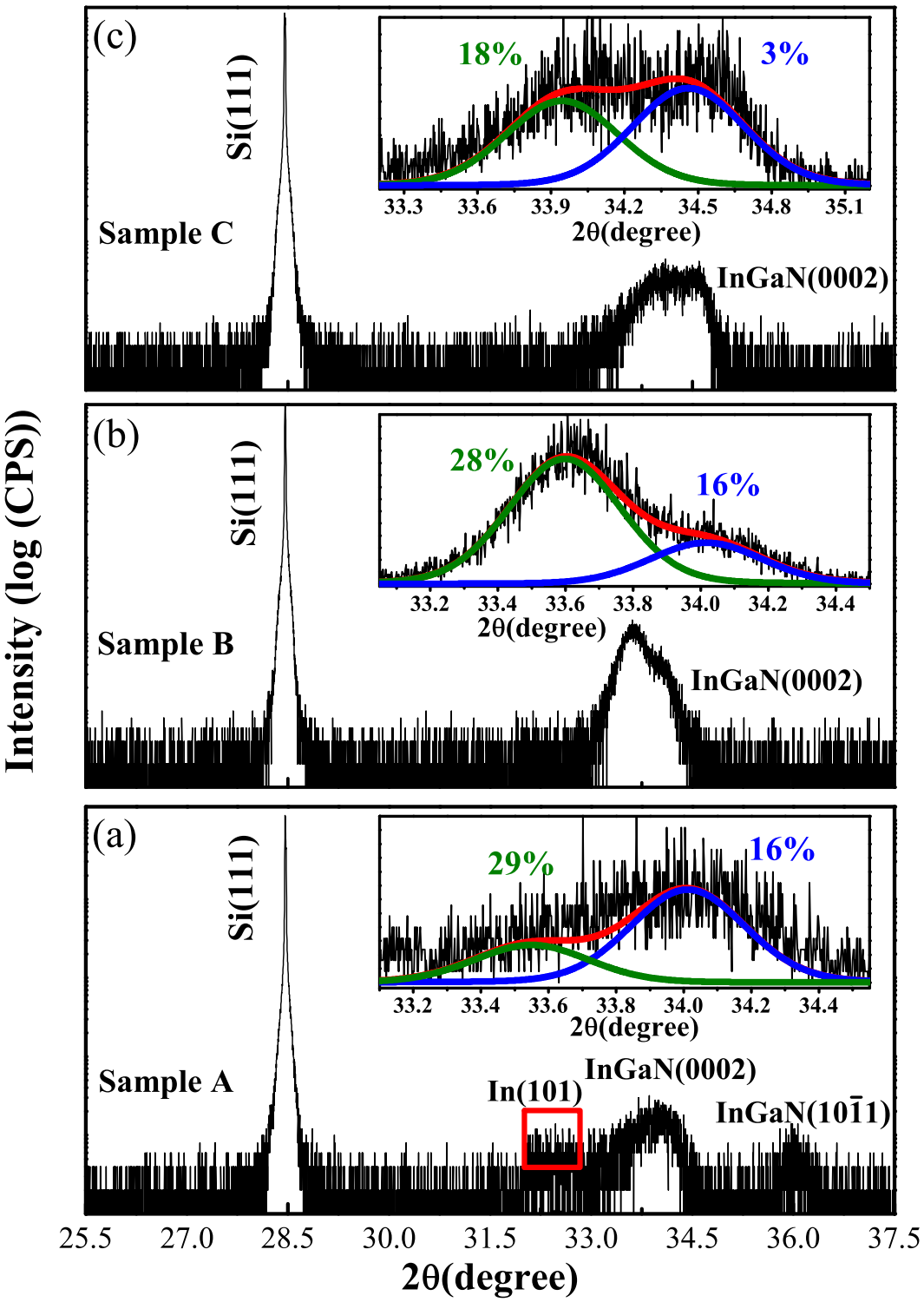

Figure 5.7: (a−c) show symmetric $2\theta - \omega$ scans acquired by HRXRD for samples A−C, respectively. Peak deconvolution of InGaN(0002) peak is shown as an inset to the respective $2\theta - \omega$ scans. The percentages written indicate the indium composition of the respective InGaN phases.

among the NRs is evident from the FESEM cross-sectional image as well as the RHEED pattern. On the other hand, samples B and C are single crystalline in nature and the absence of metallic indium confirms that all the indium present is incorporated in the crystal structure of InGaN. The broad and asymmetric InGaN(0002) peak in all the HRXRD pattern is a signature of multi-phase formation.[182,329] We have deconvoluted the InGaN(0002) peak to identify the possible constituent phases, as shown in the respective insets of the $2\theta - \omega$ scans in Figure 5.7 . As can be seen in Figure 5.7, InGaN(0002) peak for all the samples consists of two features. From the 2θ value of each constituent peak position, the respective c-lattice parameters have been calculated. From this, the indium composition (x) is estimated using Vegard's law ($c^{In_xGa_{1-x}N} = xc_0^{InN} + (1-x)c_0^{GaN}$) where c_0^{InN} and c_0^{GaN} are the relaxed c-lattice parameters for InN and GaN.[123,125] The corresponding indium composition percentages (x) are shown next to each peak in Figure 5.7 inset. It can be seen that samples A and B have the same constituent InGaN phases with $\approx$ 29% and 16% indium. For sample A, 16% indium phase is twice more abundant than the 29% indium phase, and on the other hand for sample B, 28% indium phase is thrice more abundant than the 16% indium phase. This shows that pre-nitridation of the Si surface increases the amount of indium incorporation in the lattice and improves the crystalline quality as well. In case of sample C, the prevailing phases have 18% and 3% indium, of almost same abundance. The lower indium content of the constituent phases in sample C has been attributed to the higher growth temperature, and the consequent increase of the desorption of indium atoms before their incorporation in the lattice.

5.2.3.3 PL: Optical Properties

Figure 5.8(a–c) shows RT PL band-edge emission spectra for the three samples. Using the phase separation information from the HRXRD data, we have analyzed the PL data in order to correlate the emission values with the constituent phases. In case of sample A (Figure 5.8(a)) two Gaussian peaks are fitted to the experimental PL data, which represent two emissions at 2.42 eV and 2.80 eV corresponding to the two phases of sample A, which have indium composition of 29% and 16%, respectively. On the other hand for sample B, the band-edge emission peak, which is the narrowest among the three samples, is fitted by a single peak at 2.44 eV emitted from the InGaN phase having

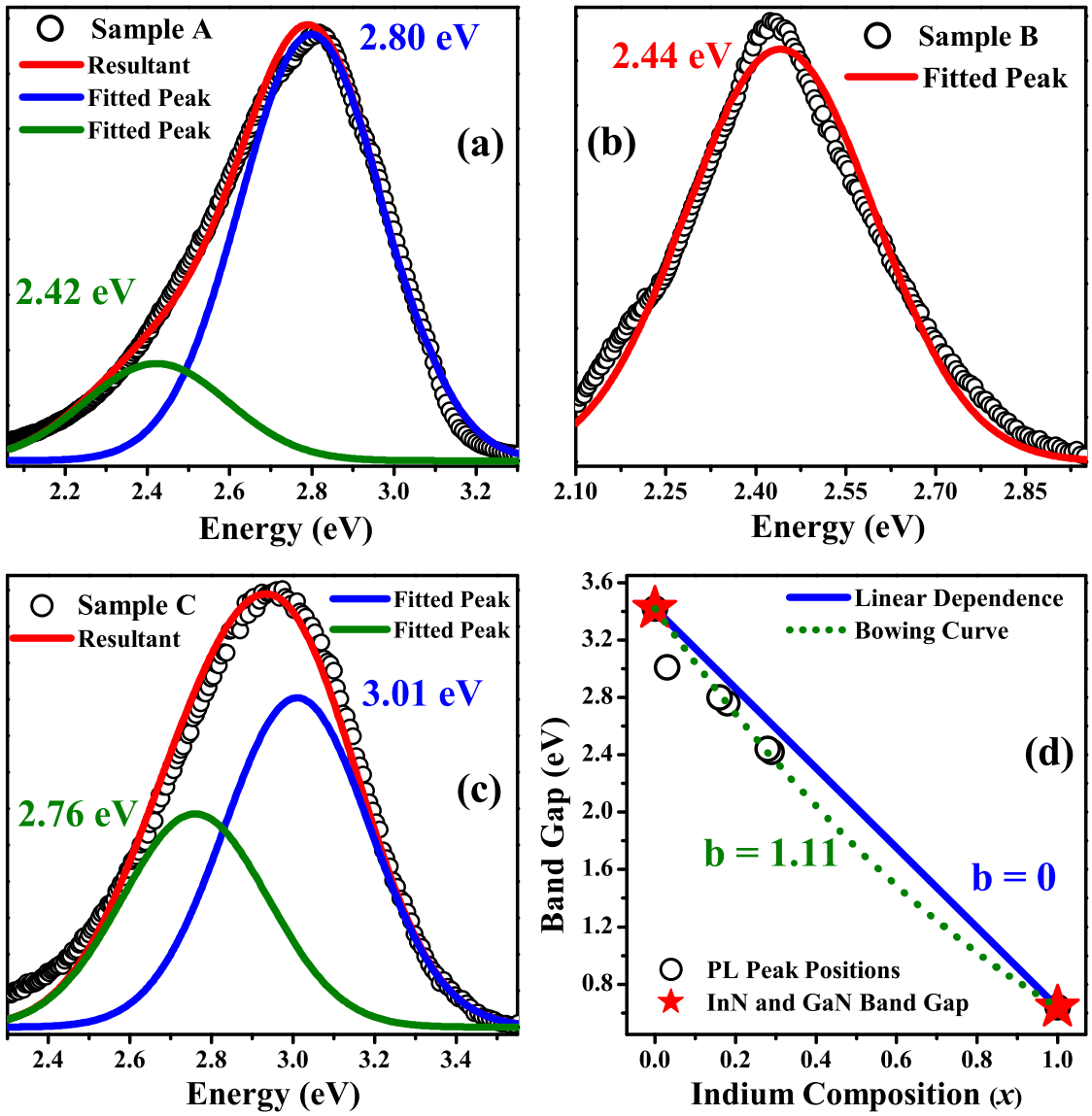

Figure 5.8: (a−c) shows RT PL emission spectra and the respective deconvolution for samples A−C, respectively and (d) shows indium composition versus bandgap plot for different phases of all samples and also the fitting of nonlinear Vegard's law of bandgap to that plot.

28% indium. The other phase (with 16% indium) is relatively of low intensity (as seen by HRXRD) and thus, we speculate that the phase hardly contributes to the RT PL emission. Besides, according to our speculation, the 2.42 eV emission is due to the 29% indium containing phase of sample A, and thus we infer that the 2.44 eV emission is solely from the 28% indium containing phase of sample B. However, PL data of sample C exhibits two peaks at 2.76 eV and 3.01 eV, which can be attributed to the InGaN phases with

18% and 3% indium, respectively. It can also be observed that by increasing the indium composition, the PL emission undergoes a red shift due to decrease in its bandgap. The composition (x) dependence of the bandgap is explained by means of a modified Vegard's law which includes an extra quadratic term associated with the nonlinear dependence of bandgap, quantified by a bowing parameter b, in addition to the linear interpolation. This is empirically expressed as $E_g^{In_xGa_{1-x}N} = xE_g^{InN} + (1-x)E_g^{GaN} - bx(1-x)$, where E_g^{InN} and E_g^{GaN} are the bandgap values of intrinsic InN and GaN[15,124] and $E_g^{In_xGa_{1-x}N}$ is the value of the emission energy deduced from the PL data analysis. Figure 5.8(d) shows the band bowing plot where bandgap (PL emission) values of the different InGaN phases deviate from linearity (solid line) with varying indium composition. Instead, it follows a nonlinear curve which is fitted with the modified Vegard's law (dotted line), yielding a bowing parameter b of $\approx$ 1.11 eV, which is lower than the theoretically estimated value of 1.44 eV.[351]

5.2.3.4 XPS: Presence of unreacted metallic Indium

Further, XPS analysis of N1s and $In3d_{5/2}$ core-levels is carried out to estimate the percentage of indium composition and unreacted indium on the surface of samples A−C. Figure 5.9 shows the deconvoluted N1s and $In3d_{5/2}$ core-level spectra, using Shirley base line correction and fitting Voigt line shapes with 10% Lorentzian component. The deconvolution of N1s core-level yields two chemical states at $\approx$ 395.8 eV and $\approx$ 396.9 eV assigned to the N−In[393] and N−Ga[416] bonding, while $In3d_{5/2}$ consists of In−In and In−N components at $\approx$ 442.7 and 443.8 eV, respectively.[307] The integrated intensity of the deconvoluted peaks of N−In and N−Ga in N1s core-level is used to calculate indium atomic percentage composition by using the relation $\frac{I_{N-In}}{I_{N-In}+I_{N-Ga}} \times 100$. The values are found to be 17, 30 and 10 % for samples A, B and C, respectively, which match closely with the composition obtained from the constituent peaks in HRXRD analysis. The deconvoluted $In3d_{5/2}$ peaks show that unreacted excess indium is $\approx$ 13%, 3% and 5% in samples A, B and C, respectively. Thus, presence of 13% unreacted indium in sample A corroborates with the presence of low intensity In(101) peak in HRXRD and implies that the nitridation of Si surface improves the incorporation of indium in the InGaN lattice.

From the above results, it is clear that growth in nitrogen rich condition yields NR

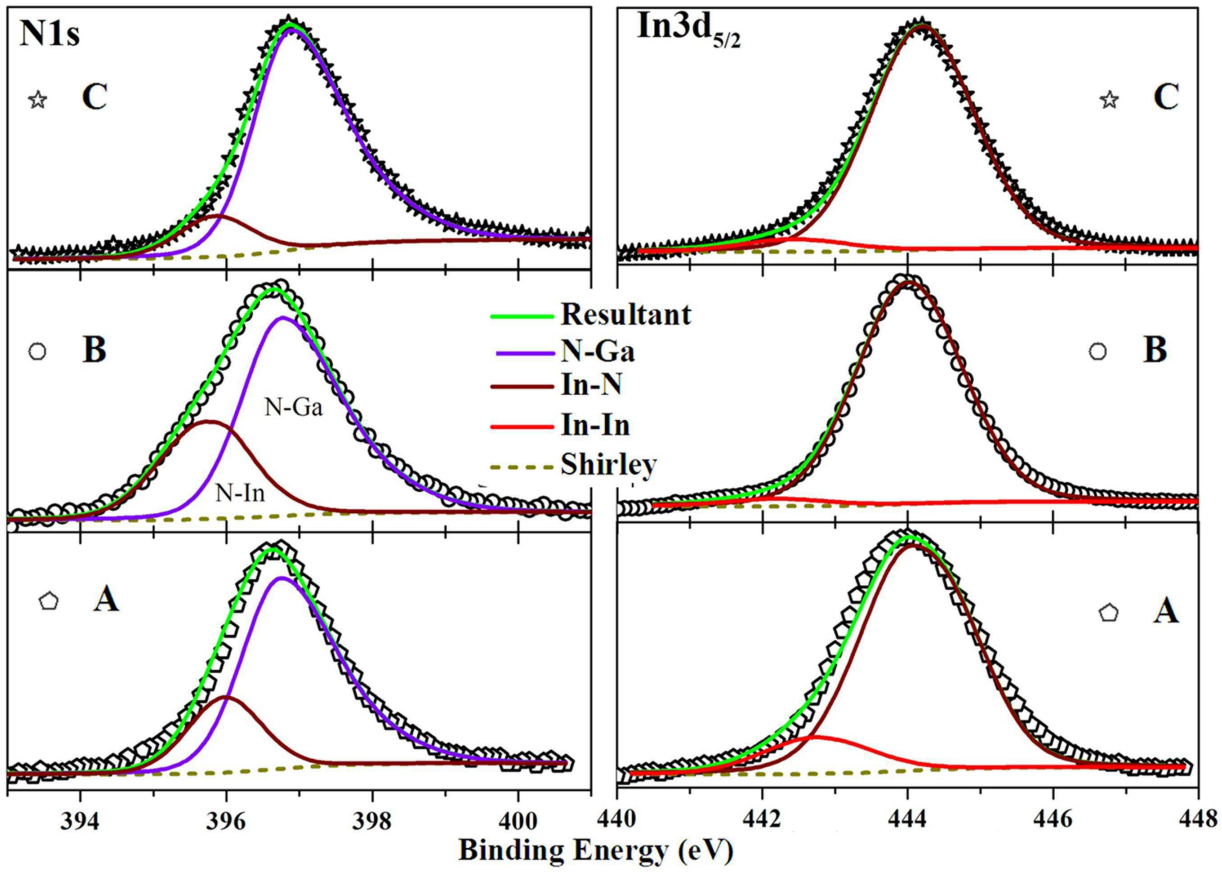

Figure 5.9: (a) and (b) show N1s and In3d XPS core level peak deconvolution for all the samples.

formation on Si(111) surface, but the composition, uniformity and orientation of rods vary with growth temperature and surface nitridation. On bare Si(111) surface, as also seen earlier,[417] the presence of unintentional and non-uniform amorphous Si_xN_y layer results in the non-uniform tilt and shapes of rods, and some indium metal segregates and does not get incorporated in the crystal lattice. However, for rods formed at the same temperature on intentionally nitrided surface, the rods are oriented and no indium metal segregates. The formation of $\beta-Si_3N_4$ upon nitridation, saturates the Si dangling bonds and yield a strain-free N-terminated surface that is more favourable for InGaN formation. In the literature, the formation of $\beta-Si_3N_4$ is predicted to form a high density of surface steps,[418] which enhances InGaN nucleation sites and indium incorporation.[419] When the rods are formed at 500 °C on the nitrided Si(111) surface, due to significant indium metal desorption and high surface diffusion of metal atoms along the sidewalls of the NRs[348,349], we observe thinner, and longer faceted NRs of almost the same density

as the 400 °C-nitrided substrate case, however, with lesser indium-incorporation. Thus, we clearly identify that 400 °C is the optimal growth temperature to grow high quality InGaN NRs on pre-nitrided Si(111) with ≈ 28% indium incorporation, having minimal phase separation and indium segregation with prominent PL emission at RT.

5.2.4 Inferences

Single crystalline, *c*-oriented and wurtzite InGaN films are grown directly on Si(111) as well as on nitrided Si(111) substrate, at two different growth temperatures under nitrogen rich conditions. For the InGaN film grown directly on Si(111), a mixture of triangular 3D islands and hexagonal rods is obtained, which have remnant unreacted crystalline indium. Due to the presence of strain free N-terminated $\beta-Si_3N_4$ on the nitrided Si(111) surface, vertically well-aligned, hexagonal NRs are obtained. Lower growth temperature (400 °C) on nitrided surface result in wide, coalesced NR formation with ≈ 28% indium incorporation, which results in the observation of PL emission at 2.44 eV at RT with minimal phase separation. We also show that increasing the growth temperature of the nitrided surface to 500 °C can yield high quality InGaN NRs with RT PL emission close to 2.96 eV. PL emission is found to follow the Vegards law of bandgap with a low bowing parameter of 1.11 eV. Thus, high quality well-aligned InGaN NRs with minimal phase separation and high indium content can be formed by surface nitridation of Si. Further, experiments are necessary to enhance indium incorporation by a systematic control of the growth kinetics, to obtain high quality InGaN NRs emitting across the visible spectral range.

Chapter 6

Growth of InN and InGaN nanostructures on GaN Nanowall Network template grown on *c*-Sapphire

This chapter presents the growth of InN and InGaN nanostructures on GaN Nanowall Network (NWN) template grown on c-sapphire and describes the effects on the morphology, crystal quality, indium incorporation within the lattice and optical properties of the grown films. The work discussed in this chapter has been published in the following journals: Journal of Applied Physics ***119****, 205701 (2016), IEEE Conference Proceedings, 1-5 (2014)*

6.1 Growth of InN on GaN Nanowall Network

A kinetically controlled two-step growth process for the formation of an array of dislocation free high mobility InN NRs on GaN NWN by PAMBE is presented here. The epitaxial GaN NWN is formed on *c*-sapphire under nitrogen rich conditions, and then changing the source from gallium to indium at appropriate growth temperature yields the nucleation of a self assembled spontaneous *m*-plane side faceted InN NRs. By HRTEM, the NRs are shown to be dislocation-free and have a very low bandgap value of 0.65 eV. Hall measurements are carried out on a single InN NR along with J-V

measurements that yield unprecedented mobility value as high as ≈ 4453 cm^2/V-s and low carrier concentration of ≈ 1.1×10^{17} cm^{-3}, for comparable InN NR diameters in the literature.

6.1.1 Introduction

The outstanding properties of InN such as narrowest bandgap, the smallest effective mass and the highest electron mobility among group III–nitride semiconductors[5,15,307,420,421] with wurtzite non-centro symmetric crystal structure provide the great potential of using it to fabricate efficient electronic, optoelectronic,[422,423] and piezotronic devices,[424] while enabling scaling down device dimensions. In recent years, the formation of high quality InN nano-columnar structures is pursued since they possess reduced dislocation density and large surface-to-volume ratio. The absence of misfit induced strain and the ability to tune their size dependent properties make nanostructures more promising and attractive to study. Although much progress has been made in the preparation of InN 2D films, synthesis of high quality InN nanostructures remains difficult because of the low dissociation temperature of InN and the lack of suitable substrates. Growth of III-V NRs is generally achieved through catalyst assisted routes such as catalytic metal induced VLS mechanism or self-catalytic vapor-solid (V-S) method (also called droplet epitaxy), where metal droplets enable the material to solidify below the frozen liquid-solid interface.[425,426] However, use of native metal droplets results in strain, absence of epitaxy and the remanence of an unnecessary non-native metal causes deep defect levels which can degrade the optical and electrical properties.[427,428] Researchers have also extensively used SAG method where complex lithographic techniques are used to pattern a dielectric mask on a substrate where they form epitaxial NRs defined by the pattern.[429–431] Since lithographic and VLS processes are complex, time consuming and difficult to control doping and crystalline quality, catalyst free methods are sought to obtain self-assembled nano-columnar arrays.

The theoretically estimated value of mobility[404,420] for InN is ≈ 14000 cm^2/V-s, whereas experimentally reported mobility values are only in the range of 500 - 3000 cm^2/V-s[397,398,404,432–434], limited by the inevitable presence of defects such as charge centers and dislocations. The dislocation density for InN layers is in the range of 10^9-10^{11} cm^{-2}

and thus attaining low electron concentration ($< 10^{15}$ cm^{-3}) and high mobility (14000 cm^2/V-s) has remained elusive. Miller *et al.* have shown that the calculated mobility of > 4000 cm^2/V-s can be achieved with the dislocation density value of $< 10^7$ cm^{-2} for concentration $\approx 10^{17}$ cm^{-3}, reiterating the dominant deleterious role of dislocations at low carrier concentrations.[435] In order to reduce dislocations in the InN epilayers, several efforts have been made in the literature, for instance, Dimakis *et al.* reported the growth of InN film with thickness of 10 μm and found the reduction of dislocations from interface to surface.[436] Kamimura *et al.*[421] and Wang *et al.*[434] have made an attempt to lower the dislocation density of InN epilayers by employing ELOG on a sapphire substrate by MBE. On the other hand, the reduction of dislocation density is also pursued by growing III-nitride materials as nanostructures.[422] Group III-nitride nano-rods/wires have been grown directly on Si substrates[437] but unintentional formation of Silicon Nitride (Si_xN_y), particularly in the case of nitrogen plasma assisted MBE growth, yields a non-ohmic contact that restricts the carrier flow, thereby consuming more power.

For the convenience of the reader and for the sake of clarity and continuity of the discussion in this chapter, we discuss some of the remarkable properties of GaN NWN here. In the past, we have reported[344,417,438] the spontaneous formation of high quality self assembled GaN nanostructures on sapphire and Silicon substrates under nitrogen rich conditions, by sheer kinetic control without involving lithography, catalysts, buffer layers, or any surface pretreatment, using PA-MBE growth. In this highly nitrogen- rich condition, the Ga adatoms diffuse over short distances before they get nitrided, promoting 3D nucleation at the steps of edge dislocations, and the strain relaxes to form a hexagonal GaN NWN, surrounding a void region which consists of open screw dislocations.[344] Figure 6.1 shows the top view FESEM image of a typical GaN NWN grown on *c*-sapphire. The NWN structure also shows very high emission with almost no defect related emission present, which shows that the GaN NWN is stoichiometric and of high structural quality, despite the presence of a large void density.[344] It has also been observed that once the nanowalls attain the *r*-plane configuration, which has a low sticking coefficient for Ga adatoms, further vertical growth of the nanowall stops. Along with the complete suppression of yellow luminescence at RT, transport and optical properties of GaN NWN suggests 1D confinement of carriers at the top edges of these connected nanowalls, which

results in a blue shift of the band edge luminescence, a reduction of the exciton-phonon coupling, and an enhancement of the exciton binding energy.[439] More interestingly, the electron mobility through the network is found to be significantly higher than that is typically observed for GaN epitaxial films, which is attributed to the transport of electrons through the edge states formed at the top edges of the nanowalls and to a 2D quantum confinement of electrons in the central vertical plane of the walls.[440] All these properties are highly desirable for the enhancement of the luminescence efficiency of the material. The PL intensity of the NWN structure is observed to be a hundred times more than nanostructures consisting of tubes, as well as flat films, due to its least stress and minimal defect band as observed from XRD and XPS studies.[441] Compared to a standard epilayer, the NWN samples display a higher binding energy for different hybridization levels appearing near the top of valence band, arising due to the reduction of defects in the NWN films.[442] The depth distribution of the transport properties as well as the temperature

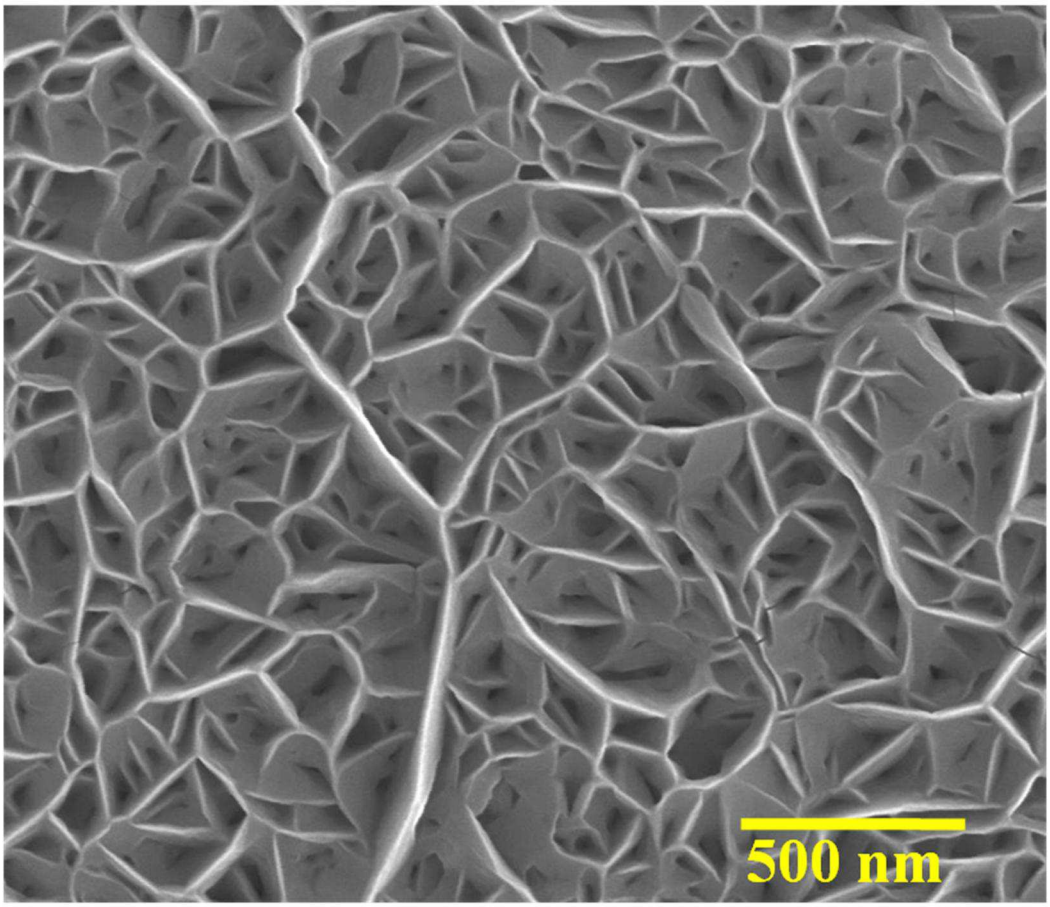

Figure 6.1: shows the top view FESEM image of a typical GaN NWN grown on *c*-sapphire.

dependence of the low field magneto-conductance for *c*-axis oriented GaN NWN samples show evidence of weak localization effect in the sample.[443] Same study supports the high mobility of NWN compared to bulk GaN and also reveals that the high electron mobility region extends down to several hundreds of nanometer below the tip of the walls. As the GaN NWN possesses a large surface and high conductivity, uncapped silver nanoparticles are vapor deposited on GaN NWN to study the band-edge plasmon-coupling. Surface enhanced Raman spectroscopy studies performed with a rhodamine 6G analyte on that configuration clearly show enhancement of the Raman signal, with a very large enhancement factor of 2.8×10^{7} and a very low limit of detection of 10^{-10}M is observed.[444] This is attributed to the surface plasmon resonance owing to the high surface electron concentration on the GaN NWN in addition to that of the Ag nanoparticles. All these outstanding properties of GaN NWN has motivated us to use that morphology as a template to grow InN and InGaN on top of that.

In this work, we have utilized the cavities of GaN NWN to grow high quality dislocation free InN NRs in a single-growth catalyst-free process by PAMBE. We have then characterized the morphological, structural, optical and electrical properties using complementary techniques. The use of GaN NWN, which is highly conducting[344,438,439] (unintentional doping $\sim 10^{20}$ cm^{-3}), as intermediate layer can be advantageous on the insulating sapphire substrate to provide the bottom contact to the InN NRs. We have also shown that these grown rods possess the highest mobility values which are among the best reported values for comparable InN NR diameters in the literature.

6.1.2 Experimental Details

The GaN NWN template and the InN NRs are grown by PAMBE on *c*-sapphire. Chemically pre-cleaned *c*-sapphire substrates were thermally degassed inside the preparation chamber at 600 °C for 60 min, followed by annealing in the growth chamber at 850 °C for 15 min to obtain the characteristic RHEED pattern of atomically clean *c*-sapphire. For GaN NWN growth, gallium K-cell temperature is set to 1000 °C (BEP = 4.8×10^{-5} Torr) and the nitrogen flow rate is kept at 4.5 sccm, with RF plasma forward power of 375W while the growth temperature is maintained at 630 °C and GaN NWN is grown for 30 min. Further details of the GaN NWN are reported elsewhere.[438] After this, gallium

K-cell and N_2 plasma source shutters are closed while the growth temperature is ramped down to the InN growth temperature of 450 °C. On top of the pre-formed GaN NWN, InN is grown for 3 hours at 450 °C with the same RF plasma conditions employed for GaN NWN growth and indium K-cell temperature is kept at 750 °C (BEP = 8.2×10^{-8} Torr). The average height of the InN NRs are found to be ≈ 700 nm from FESEM study. TEM studies are carried out using FEI Tecnai T20 with electron beam energy of 200 keV. The sample is then probed using different complementary characterization techniques, which are FESEM, HRXRD, Low temperature (77 K) CL, RT Optical Absorption and RT Hall effect measurements.

6.1.3 Results and Discussions

6.1.3.1 FESEM: Morphology

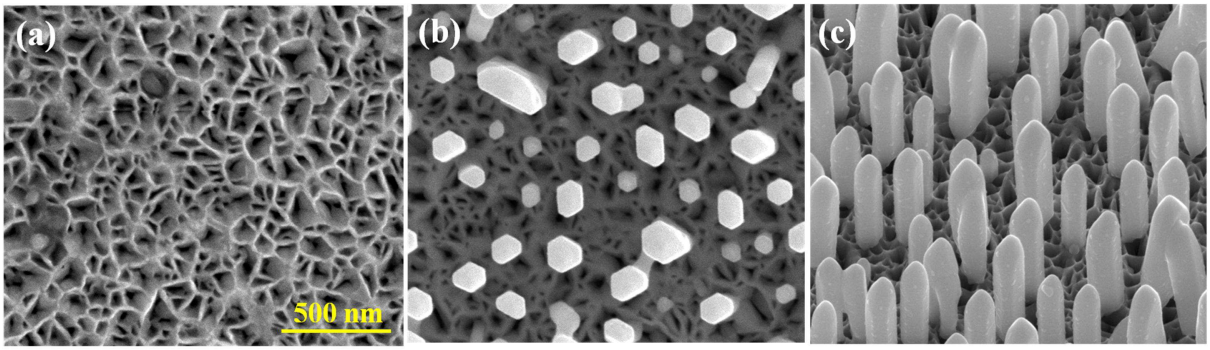

Figure 6.2: (a) and (b) show the top views of FESEM images of bare GaN NWN and overgrown InN, respectively, while (c) is the tilted view of InN NRs.

Figure 6.2(a) shows the top view FESEM image for GaN NWN template grown for 30 min on bare sapphire at 630 °C. Figure 6.2(b) and (c) are the top and tilted views of the FESEM images obtained after growing InN NRs at 450 °C on the GaN NWN template. Figure 6.2(a) shows the hexagonal network of the GaN nanowalls, whereas, Figure 6.2(b) clearly shows the NRs formed inside the cavities of the GaN NWN are hexagonally faceted. All the rods are vertically aligned and well separated with heights of most of these NRs being ≈ 700 nm, while a few are in the range of 100 – 750 nm. This vertical growth of the InN NRs is attributed to the low sticking coefficient of indium atoms on the GaN NWN at 450 °C that funnel into the cavities encouraging super-saturation inside them[344] and nucleating the InN nanocolumns. Figure 6.2(c) shows the tilted view

of the vertically aligned NRs that stem from the closed cavities of the network. All the NRs, irrespective of the heights, have identical orientation (except very few tilted NRs) and a tapered-top morphology with similar aspect ratios. The average diameter of the NR is $\approx$ 120 nm and density is $\approx 1.2\times10^{8}$ cm^{-2}.

6.1.3.2 HRXRD: Crystal Structure and Epitaxial Relationship

To understand the crystalline structure and quality of the InN NRs, HRXRD measurements are performed and the results are shown in Figure 6.3. The 2θ-ω scans, in logarithmic scale, are acquired on the symmetric and asymmetric planes for InN NRs, respectively. Asymmetric planes are studied in skew-symmetric geometry, where the plane of interest is setup normal to the diffraction plane, satisfying the Bragg's condition, using

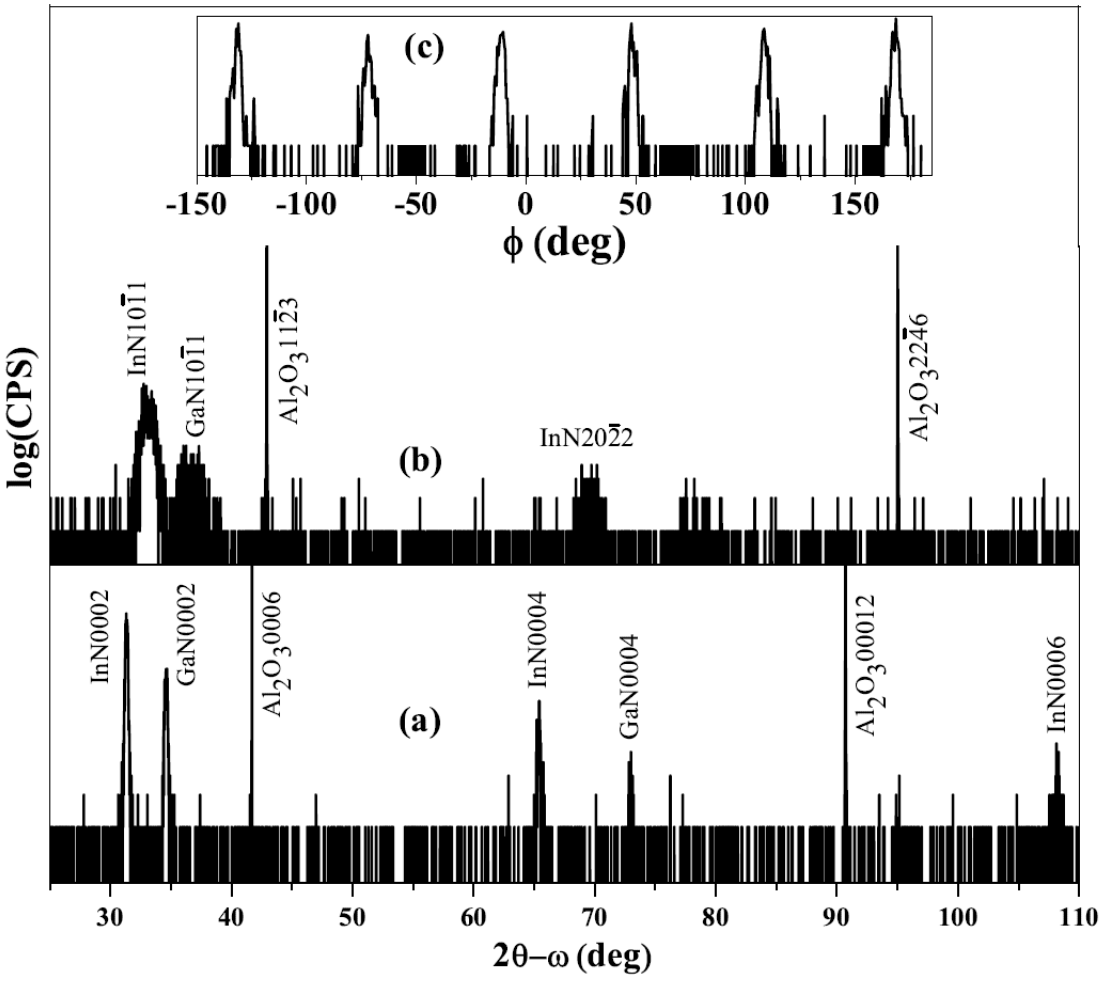

Figure 6.3: (a) and (b) show symmetric and asymmetric 2θ-ω scans acquired by HRXRD on InN(0002) and InN(10$\bar{1}$1) planes, respectively. The inset (c) shows the phi scan acquired on InN(10$\bar{1}$1) plane.

the pivotal ability of the HRXRD instrument. InN NRs are seen to possess single crystalline wurtzite structure with the preferential growth direction along *c*-axis. The pattern in Figure 6.3(a) displays intense *c*-oriented peaks: InN(0002) at 31.28°, InN(0004) at 65.30° and InN(0006) at 108.30° along with the GaN(0002) peak at 34.58° and the Al_2O_3 substrate (0006) and (000 12) peaks at 41.68° and 90.80°, respectively. Figure 6.3(b) shows 2θ-ω scan for the asymmetric reflection which consists of InN($10\bar{1}1$) and InN($20\bar{2}2$) peaks at 33.13° and 69.57° along with GaN($10\bar{1}1$) peak at 36.81° and the substrate peaks viz. Al_2O_3($11\bar{2}3$) and Al_2O_3($22\bar{4}6$) at 42.89° and 95.11°, respectively. Absence of any peak related to metallic indium confirms that there is no excess unreacted crystalline indium on the surface, bulk or at the tip of the NRs. Figures 6.3(a) and (b) give the epitaxial relationship of InN with respect to the GaN NWN and *c*-sapphire, as InN[0001] ||GaN[0001] ||Al_2O_3[0001] and InN[$10\bar{1}0$] ||GaN[$10\bar{1}0$] ||Al_2O_3[$11\bar{2}0$], revealing that *c*-oriented InN and GaN unit cells are azimuthally rotated by 30° with respect to the sapphire substrate, to minimize the lattice mismatch between GaN template and *c*-sapphire. Figure 6.3(c) is the phi-scan that is obtained from asymmetric plane InN($10\bar{1}1$) for the InN NRs, exhibiting six equally spaced peaks characteristic of the six fold symmetry of wurtzite InN. Absence of any other random peak in the phi-scan suggests that the NRs predominantly grow along the *c*-direction. From symmetric and asymmetric scans, the calculated high precision lattice parameters (c, a) for the InN NRs (5.7058, 3.5372Å) are very close to the unstrained values[125] revealing that the InN NRs are relaxed.

6.1.3.3 TEM: Dislocation-free Crystal Structure

Figure 6.4 (a) and (b) show bright field and dark field TEM images of a typical InN NR where Burgers Vector (**g**) is setup along [$11\bar{2}0$] and [0002], respectively. It is evident from Figure 6.4(a) and 6.4(b) that the NR has an uniform diameter of ≈ 150 nm throughout the rod length of ≈ 750 nm and a tapering at the apex with a small *c*-plane terrace. Figure 6.4(c) and (d) show the SAED pattern for bright field image in Figure 6.4(a), taken along the <$11\bar{2}0$> and <$10\bar{1}0$> zone axis, indicate good crystalline wurtzite InN NRs that grow along the [0002] direction. The top *c*-plane plateau is bound by *m*-planes ($10\bar{1}0$) as the six side walls, and the apex of the InN NRs has truncated pyramidal *s*-plane ($10\bar{1}1$) facets with an inclination angle of ≈ 62° with respect to the top *c*-plane.

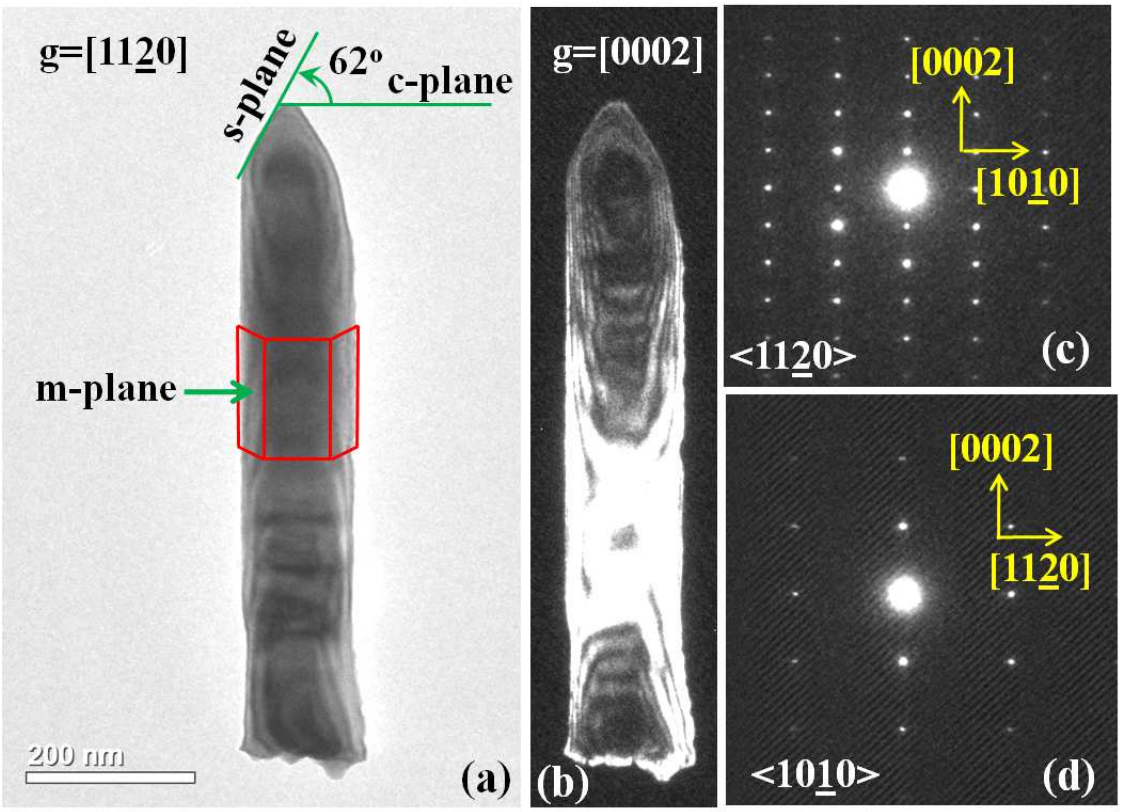

Figure 6.4: (a) is the bright field and (b) the dark field TEM images of an InN NR along [11$\bar{2}$0] and [0002], respectively. (c) and (d) show the SAED pattern acquired on InN NR along zone axis <11$\bar{2}$0> and <10$\bar{1}$0>. All facets are marked according to SAED pattern.

Figure 6.4(a) show some stacking faults but the absence of any dislocation lines in InN NRs is notable. Figure 6.4(b) exhibits fringes and contours in dark field image, which are attributed to the slight bend and thickness variation at edges of NR, respectively.[445] The lattice-parameter values calculated from HRXRD and SAED yield the relaxed values, suggesting that the InN NRs are strain free. Thus, the InN NRs that form inside the GaN NW cavities are single crystalline *c*-oriented and found to be dislocation and strain free.

After observing the various stages of growth and analyzing the structural properties by different techniques, we try to understand the possible mechanism involved in the InN NR growth. The impinged III and V group atoms on to the GaN NWN bound by *r*-planes have a low sticking coefficient[446] and are funneled into the cavities. Contrary to the dislocation mediated NR formation in GaN[438] the InN NRs appear to adopt the vapor-solid (V-S)[340] or the droplet epitaxy[447] route. At this temperature the adatoms do not spend much time in smaller cavities, and thus leads to super-saturation only in

larger cavities where they nucleate and get nitrided by the N_2* plasma into m-faceted hexagonal NRs. The InN NRs with non polar m-plane side facets grow spontaneously along the c-direction, due to the low diffusion barrier (E_{diff}) of indium adatoms along m-plane ($E_{diff}^{||c-axis} = 0.06eV$) than along the c-plane ($E_{diff}^{\perp c-axis} = 1.30eV$) as reported by Aliano *et al.*,[448] which results in higher sticking coefficient of indium atoms on c-plane than that on the m-plane. Thus, indium adatoms having low sticking coefficient on the m-plane InN NR side-walls and r-plane GaN facets creep along those planes and nucleate on the c-terraces, promoting the 1D growth of dislocation free InN NR[380]. This catalyst free and self induced growth results in dislocation free c-oriented InN NRs having m-planes as side walls and s-plane facets at the apex.

6.1.3.4 CL and Optical Absorption: Bandgap

The high quality of the spontaneously formed self assembled isolated InN NRs in the GaN NWN matrix prompted us to look at the resulting optical properties, by optical absorption and CL measurements on the ensemble of NRs. The optical absorption measurements done in the transmission mode (optical scattering and reflection losses have been neglected) where αE^2 versus E curve is plotted along the alternate y-axis, in the high absorption range by following the relation $\alpha(E) \propto ln(1/T)$, where α, E and T are optical absorption coefficient, energy and transmittance, respectively. The linear regions of the plots have been extrapolated to $\alpha E^2 = 0$, to obtain the value of the optical bandgap.

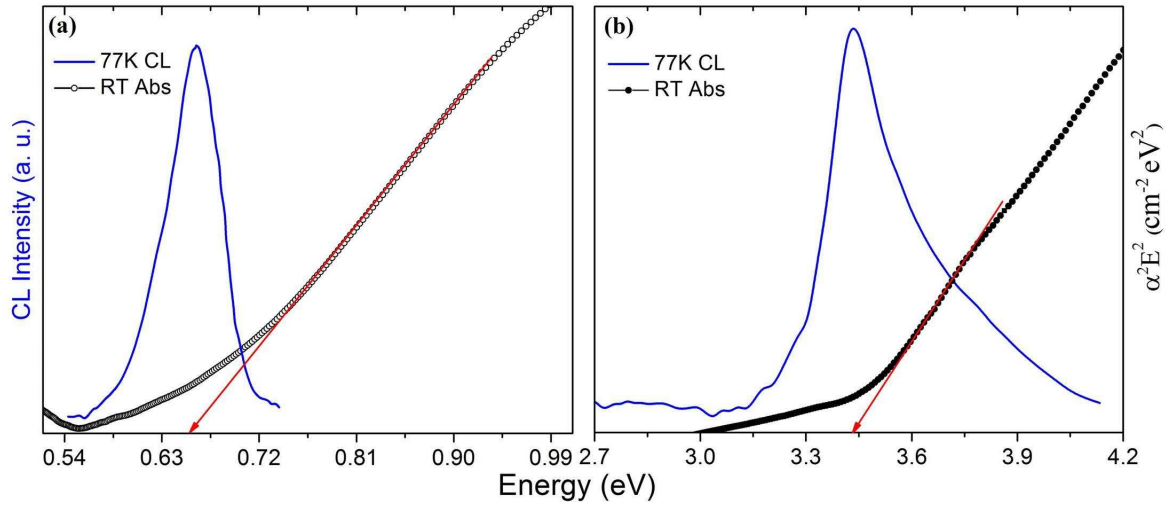

Figure 6.5: (a) and (b) show CL emission and optical absorption spectra acquired on InN NRs and GaN NWN.

Figure 6.5(a and b) show CL (normal y-axis) and optical absorption (alternate y-axis) measurements for InN NRs and GaN NWN, where the CL band-edge emission is obtained at liquid nitrogen temperature (77 K). The emission peaks (absorption edges) that occur at 0.65 (0.66±0.05) and 3.44 (3.45±0.05) eV, correspond to the InN NRs and the GaN NWN template.

6.1.3.5 Electrical Measurements: High Mobility

In order to measure the electron mobility and carrier concentration of InN NRs, Hall measurements are carried out on a single NR. Using masking technique, four isolated In(20 nm)/Ag(20 nm) pads having separation of ≈ 20 μm are deposited on the sapphire substrate by e-beam evaporation. The InN NRs are deposited on sapphire substrate in middle of the four In/Ag pads by drop casting. The Platinum (Pt) connecting wires are deposited in FESEM environment having high vacuum conditions, followed by annealing at 200 °C for 60 mins in UHV conditions (5×10^{-10} Torr). Figure 6.6(a) shows the FESEM image of the NR after depositing Pt connecting wires. The respective inset is the schematic representation of the contacts where Pt wires electrically connect the NR and In/Ag pads. The Hall measurements are performed within the ohmic region of the contacts by assuming rectangular bar geometry using Van der Pauw method, which can be used for any arbitrary disc shape to measure resistivity and Hall voltage.[328] The Hall carrier concentration and mobility are found to be ≈ 3.1×10^{17} cm^{-3} and ≈ 4263 cm^2/V-s at RT.

Further confirmation of measured mobility and carrier concentration is achieved by employing Space Charge Limited Current (SCLC) formalism to J-V characteristics that are performed on InN NR across the contacts B and D. Figure 6.6(b) shows log-log plot of J-V characteristics, where increasing forward bias switches ohmic region J∼V to SCLC region J∼V$^{\beta+2}$, where $\beta \approx 2.1$, due to the space charge limited currents,[449] associated with charged traps like unavoidable native point defects,[306] which initiates at the voltage value of $V_c \approx 0.74$V. Further increasing bias leads to the saturation of the charged traps and thus SCLC jumps to J∼V^2 region at $V_s \geq 1.95$V, which consequently result in non-linear J-V characteristics. Inset shows J-V characteristics in linear scale along with the fitted curves which depicts the dependence of J on forward bias V, $V^{4.1}$ and V^2. The SCLC for nano-wires/rods[450] can be described by the following modified Mott and

Gurney expression.[451]

$$J_{SCLC}^{NR} = \left(\frac{R}{L}\right)^{-2} \frac{\epsilon\mu\xi}{L^3} V^2 \tag{6.1}$$

where J is current density, R is radius, L is length of NR, ϵ is static dielectric constant, μ is electron mobility, $\xi = \xi_0(V/V_c)^\beta$ and V_c is cross over voltage, ξ_0 is constant.[449] When $V = V_s$, $\xi \longrightarrow 1$ and $\xi_0 \sim (V_c/V_s)^\beta$. The mobility thus extracted from SCLC region in J-V characteristics using Eq. 6.1 is $\approx$ 4453 cm^2/V-s. For the NR geometry, the expression[450,452] for the carrier concentration is $n = \epsilon V_c/eR^2$, which yields a value of $\approx 1.1\times10^{17}$cm^{-3} for InN NR. We have fitted the negative bias side (not shown) of I-V curve for clarification and found same mobility and carrier concentration values as the right side. The reason in obtaining similar values is due to the same Pt metal electrical contacts that are used at both the ends of NR. The carrier concentration (mobility) obtained from SCLC model is lower (higher) than that of the value obtained from Hall measurements, which could be due to the consideration of rectangular bar geometry and the non-negligible large contacts in comparison to the rod dimensions. Thus, mobility and carrier concentration values are measured directly on a single dislocation free InN NR using Hall measurements, which are also confirmed by employing SCLC analysis to the J-V characteristics.

Recently, it has been shown that the highest mobility is in the range of 8000-12000

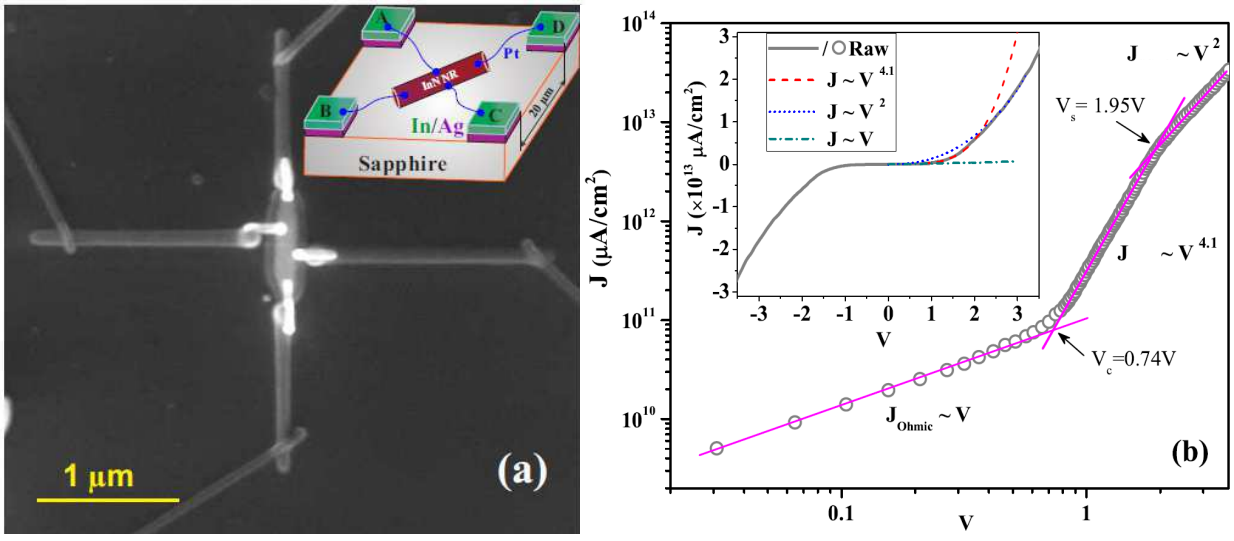

Figure 6.6: (a) shows the InN NR having four Pt contacts and the respective inset shows the schematic representation of the InN NR with four metal contacts Pt/In/Ag. (b) and respective inset show non-linear J-V characteristics in logarithmic and linear scale. Inset also describes the dependence of J on V, V^2 and V$^{4.1}$ in the forward bias region.

cm^2/V-s for intrinsic InN NWs with carrier concentration in the range of 10^{13} to $10^{15}cm^{-3}$ from I-V measurements where the mobility reduces drastically with decreasing radius of NWs. However, obtained mobility values for NR of $\approx$ 150 nm diameter in this study is less than the highest mobility value reported on InN NRs with larger diameter up to $\approx$ 2 μm.[453] The possible reason for reduction of mobility in InN NR with less diameter is significant scattering due to surface charge accumulation at near surface of NR.[454] This scattering can be suppressed by increasing NR diameter which enhances bulk electrical conduction. The obtained high electron mobility and low carrier concentration values agree well with earlier Monte Carlo simulations[420] performed by Polyakov *et al.* for InN material and also dislocation density dependent mobility calculations by Miller *et al.*, where it has been shown that when the dislocation density reaches $\leq 10^7$ cm^{-2}, electron mobility of InN attains $\approx$ 4000 cm^2/V-s.[435] The mobility of the dislocation free InN NR is higher than that of state-of-the-art InN epilayers ($\approx$ 3000 cm^2/V-s)[404] having the dislocation density in the range of 10^9 to 10^{10} cm^{-2}. Thus, this study clearly shows the method to obtain reasonably high mobility and low carrier concentration for dislocation free InN NRs having diameter of $\approx$ 150 nm.

6.1.4 Inferences

In summary, spontaneous self-assembled vertically aligned InN NRs are formed on GaN NWN template deposited on *c*-sapphire by a two step MBE growth process. This method enables the growth of dislocation free high quality InN NRs exhibiting good structural, optical and electrical properties. The HRXRD and TEM studies reveal that InN NRs posses relaxed wurtzite crystal structure grown along *c*-orientation and are dislocation and strain free. The low temperature CL studies show a sharp and low band-edge emission at 0.65eV for InN NRs. Electrical characterization on a single NR yields a carrier concentration as low as $\approx 1.1\times10^{17}$ cm^{-3} and electron mobility is as high as $\approx$ 4453 cm^2/V-s, which are among the best reported values so far for a dislocation free InN NR having diameter of $\approx$ 150 nm. Thus, the present work reports a simple method to fabricate a single NR device to obtain low carrier concentration and high mobility. Experiments to kinetically control the GaN NWN cavity and InN NR size and position distribution are underway. The use of the highly conducting GaN NWN as the intermediate layer enables

making good bottom contacts to the InN NRs, which will be useful for device fabrication and will be explored shortly.

6.2 Growth of InGaN on GaN Nanowall Network

It is clear by now that GaN NWN structure has lot of potential as a candidate material to be used in future optoelectronic devices because of its inherent outstanding properties. All the fascinating material properties observed in the case of GaN are either enhanced or modified in a better way or completely new material properties emerges because of the unique NWN structure. Now, it will be great, if we can get similar exceptional properties in other material system. For instance, GaN has bandgap in the UV region and if we can make InGaN NWN with varying bandgap then we can span the whole visible spectrum and tune the properties accordingly. This being the motivation of the following work and also after noticing the potential of GaN NWN template to grow defect free, high crystalline InN NRs, we have attempted the growth of InGaN on the same template. We aimed to observe the effect of the NWN template on the indium composition, morphology, structural and optical properties of the InGaN film.

6.2.1 Experimental Details

InGaN thin film is grown by PAMBE on GaN NWN grown on *c*-sapphire substrate. Chemically pre-cleaned *c*-sapphire substrates were thermally degassed inside the preparation chamber at 600 °C for 60 min, followed by annealing in the growth chamber at 850 °C for 15 min to obtain the characteristic RHEED pattern of atomically clean *c*-sapphire. GaN NWN template is grown at a growth temperature of 630 °C for 30 min and gallium K-cell temperature is set at 1080 °C, to maintain a gallium BEP of 4.8×10^{-7} Torr and the nitrogen flow rate is kept at 4.5 sccm with a plasma forward power of 375W. For InGaN growth, indium and gallium K-cell temperatures are maintained at 800 °C (indium BEP = 2.3×10^{-7} Torr) and 1080 °C (gallium BEP = 4.8×10^{-7} Torr) and the nitrogen flow rate is maintained at 4.5 sccm with a plasma forward power of 375W. InGaN is grown at a growth temperature of 380 °C for 3 hours. All the samples are then probed using different complementary characterization techniques, which are FESEM, HRXRD and RT

CL Spectroscopy.

6.2.2 Results and Discussions

6.2.2.1 FESEM: Morphology

Figure 6.7(a) and (b) show the top and tilted view FESEM images of the InGaN sample grown on a 30 min grown GaN NWN network, respectively. The morphology of the 30 min grown GaN NWN is similar to that, which is shown in Figure 6.2(a). It can be seen from Figure 6.7 that the InGaN sample has the morphology of interconnected nanowall network, mimicking the morphology of the underlying GaN NWN template (see Figure 6.1 and 6.2(a)). It can also be seen that InGaN nanowalls are also surrounding a void at the center and the walls have wedge shape. As the growth has been done under nitrogen-rich condition, the surface diffusion of incoming adatoms gets reduced in lateral direction and the adatoms gets nitrided easily due to lack of mobility which helps in further nucleation and eventually initiate vertical growth. Thus, 3D morphology for the grown sample is expected. Moreover, the sidewalls has been reported to be r-planes and the void has been proposed to be a screw-dislocation[438] which opens up to facilitate the growth of the unique NWN morphology. As the V/III ratio, used in both the cases of

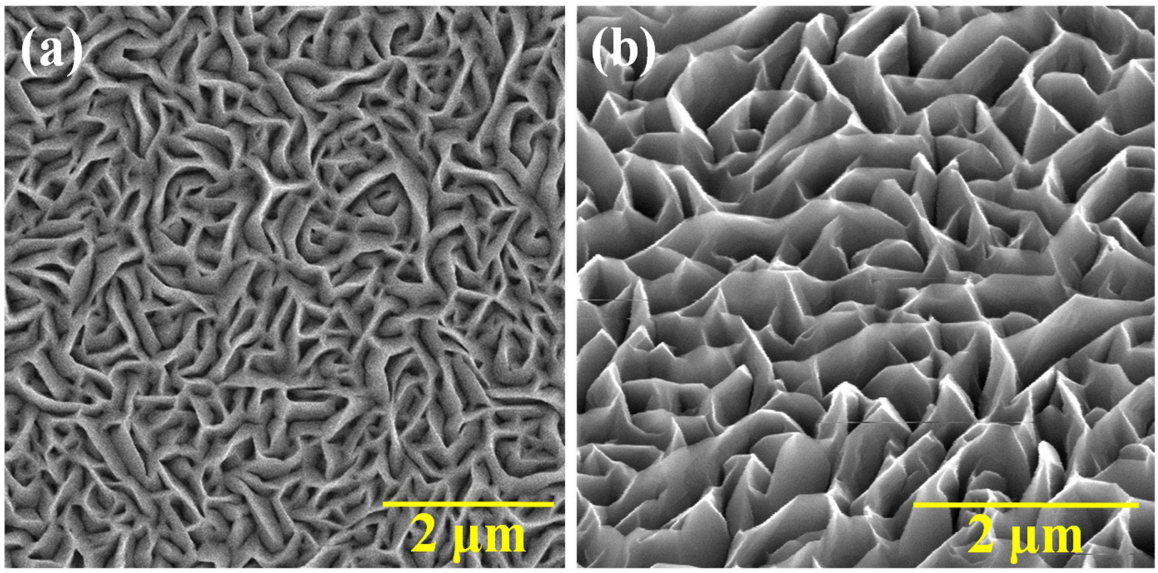

Figure 6.7: (a) and (b) show the top and tilted view FESEM images of the grown InGaN sample, respectively.

GaN template and overgrown InGaN growths, are comparable or similar in nature, the overgrown InGaN morphology follows the underlying template morphology and uniformly covers the exposed surface of GaN NWN template and continues to grow in the same manner throughout the growth. So we have successfully optimized the growth parameter in such a way that the overgrown InGaN film follows the underlying GaN morphology and emerges as a NWN.

6.2.2.2 HRXRD: Crystal Structure, Indium composition and Epitaxial Relationship

To understand the structural quality, HRXRD measurements are performed on the InGaN sample and the result is shown in Figure 6.8, where the symmetric $2\theta - \omega$ scan is plotted in logarithmic scale. The reflections are acquired on the InGaN(0002) plane

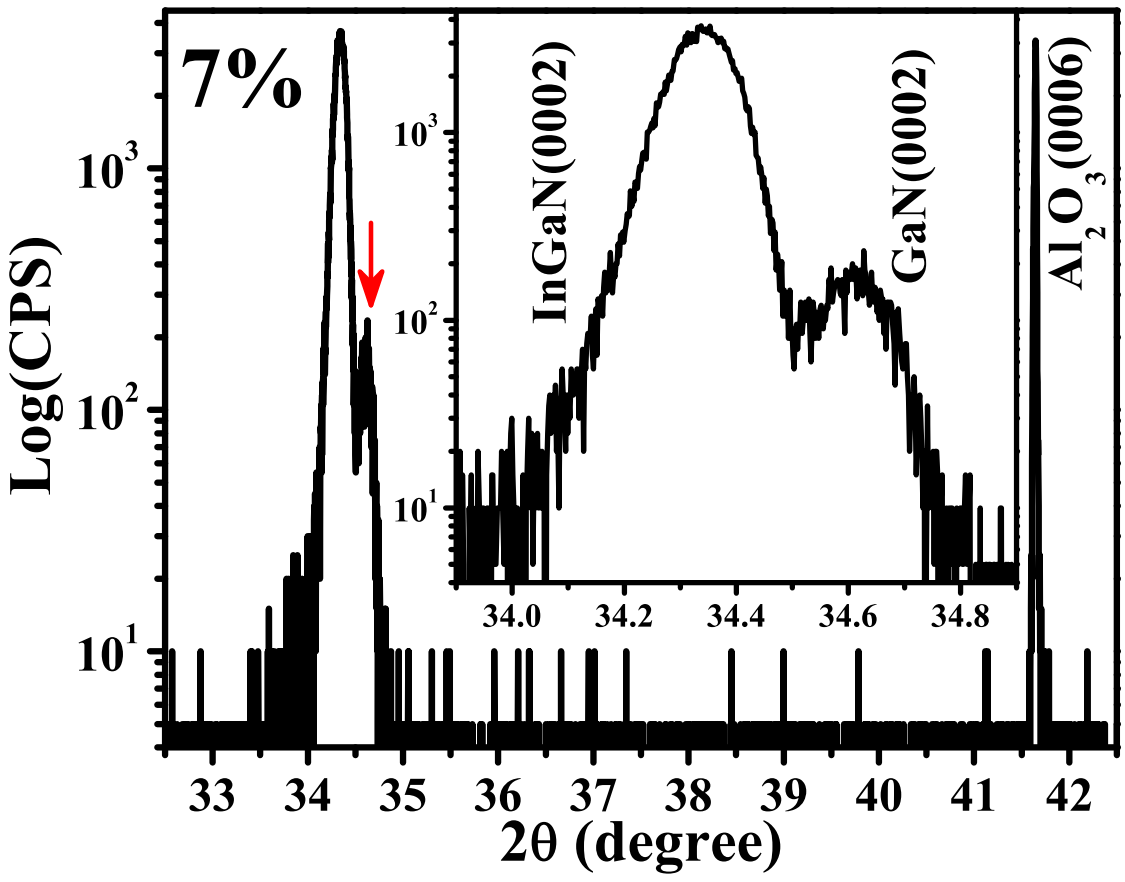

Figure 6.8: shows symmetric $2\theta - \omega$ scans acquired by HRXRD for the InGaN sample. Inset shows zoomed view of the respective symmetric (0002) peak. Calculated indium composition is indicated at the top left side.

with respect to the pre-aligned Al_2O_3(0006) plane. The pattern in Figure 6.8 displays an intense Al_2O_3(0006) substrate peak at 41.68°. It is clearly visible that the InGaN thin film is single crystalline having a wurtzite structure with a preferential growth direction along the *c*-axis. From Fig 6.8 it can be seen that the *c*-oriented peak of III-N(0002) plane has a prominent shoulder (shown by red arrow) and thus for clarity the zoomed view of the III-N(0002) peak has been plotted in the inset of Fig 6.8, where the two peak positions are found to be 34.31° and 34.61°, respectively, and it has been clearly identified that the shoulder peak situated at 34.61° is originating from the GaN(0002) planes of the underlying NWN template, and the high intense peak situated at 34.31° correspond to InGaN(0002) plane. The calculated *c*-lattice parameter from the 2θ value is then used to calculate the indium composition by using Vegard's law for lattice parameter ($c^{In_xGa_{1-x}N} = xc_0^{InN} + (1-x)c_0^{GaN}$) where c_0^{InN} and c_0^{GaN} are the relaxed *c*-lattice parameters for bulk InN[125] and GaN[123], and x is the indium composition of the InGaN alloy, respectively, and the obtained indium composition is found to be 7%. From all these observation it can also be understood that the epitaxial relationship between the grown films and substrate is $(0001)_{InGaN} \parallel (0001)_{GaN} \parallel (0001)_{Sapphire}$. The samples exhibit intense single InGaN(0002) reflection, displaying the presence of single compositional phase in the sample. The absence of any other reflection from InN confirms the absence of that independent phase in our samples.

6.2.2.3 CL: Optical Properties

Thus, we have obtained a very interesting NWN morphology of InGaN, which grows with a morphology similar to the underlying GaN NWN and it has very good crystal quality and is epitaxial with the underlying GaN NWN template. Now, it is known that tuning of bandgap in InGaN is the main attraction of this material system and thus to investigate the optical properties of the InGaN sample, RT CL is carried out and the obtained spectra is shown in Figure 6.9. As can be seen in Figure 6.9, the sample shows CL peak at 3.02 eV, which is red-shifted with respect to the GaN bandgap of 3.42 eV and confirms the incorporation of indium atoms into the lattice and stabilization of the 7% indium content phase in the grown sample. Thus, the overgrown NWN morphology is indeed InGaN NWN having 7% of indium incorporation and emitting at 3.02 eV at RT.

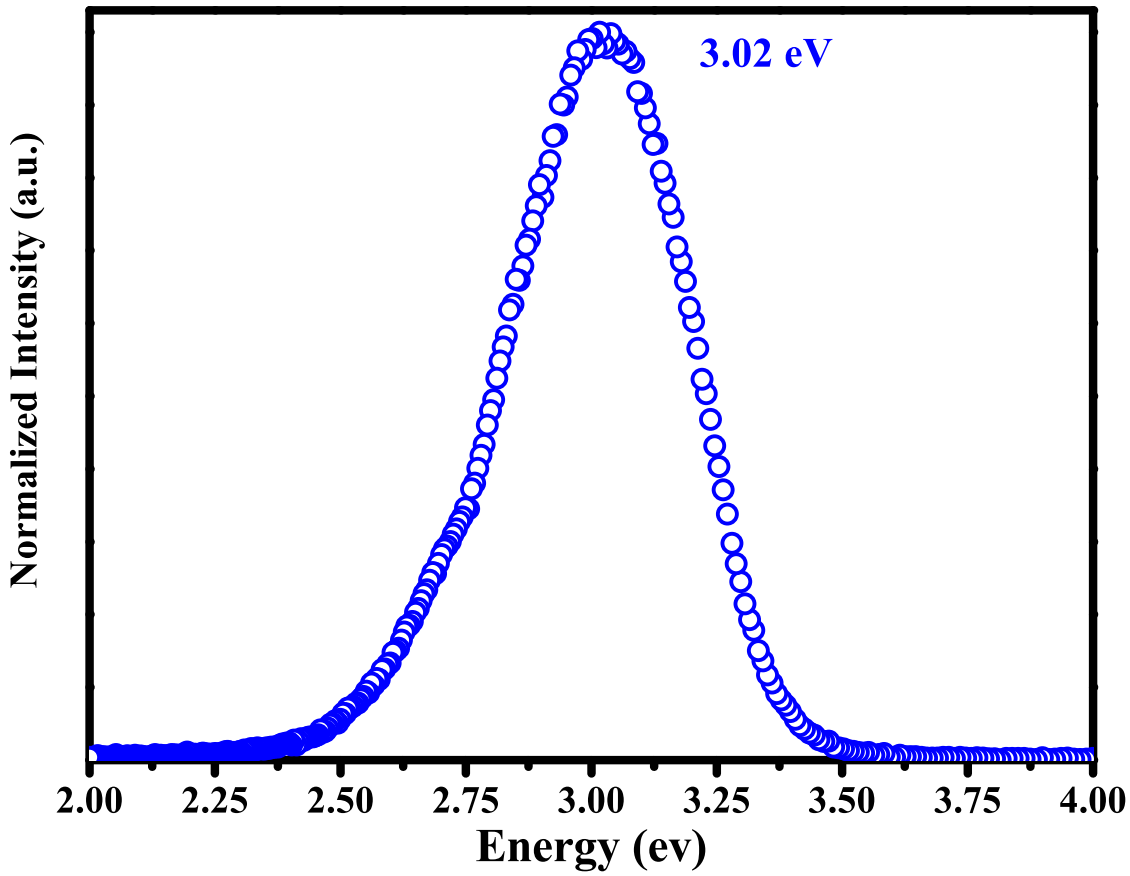

Figure 6.9: shows RT CL spectra for the InGaN sample. CL peak position is indicated in the image.

This once again shows the capability of GaN NWN, which can be used as an underlying template to grow structurally and optically good quality InGaN NWN.

6.2.3 Inferences

Single crystalline, *c*-oriented, wurtzite InGaN NWN is grown on 30 min grown GaN NWN template, which is grown on *c*-sapphire, where the overgrown InGaN film morphology resembles that of the underlying GaN template, which is attributed to the similar type of V/III ratio used for both the growths of GaN and InGaN. HRXRD study shows that indium incorporation is $\approx 7\%$ in the InGaN NWN film and the epitaxial relationship between the grown films and substrate is $(0001)_{InGaN} \parallel (0001)_{GaN} \parallel (0001)_{Sapphire}$. CL study confirms that the 7% indium content phase is stable in the sample, which emits at 3.02 eV at RT. In summary, by optimizing the growth parameters, GaN NWN can be utilized as an useful template to grow InGaN NWN, having good structural and optical

properties. Further, experiments are necessary to enhance indium incorporation by a systematic control of the growth kinetics, to obtain high quality InGaN NWN emitting across the visible spectral range.

Chapter 7

Conclusions

This chapter summarizes the contents of the present thesis and draws conclusions from the observed results. Overall, the thesis is a systematic approach to understand the growth of $In_xGa_{1-x}N$ with different morphology to understand the role of growth templates as well as to obtain different indium compositions without phase separation. This chapter also lists the highlights of this work and provides suggestions for the future direction for research, as an outcome of the present work.

7.1 Issues Related to InGaN Growth and Material Properties

The nitride semiconductor alloys due to their tunable bandgap from IR to deep UV and their chemically robustness under high electrical current and temperature, make it a great material for the fabrication of high power, high temperature and high frequency electronic and optoelectronic devices. Among the ternary compounds of Group-III nitride materials, $In_xGa_{1-x}N$ is considered as the indispensable material for the fabrication of light emitters which can be tuned to be active in the entire visible, IR and in the near-UV spectral regions. However, due to the huge miscibility gap, the large difference in bond-length, vapour pressure and formation enthalpy between InN and GaN, the $In_xGa_{1-x}N$ material system suffer problems such as phase-separation, low indium incorporation and indium surface segregation. Moreover, several technical limitations arise causing difficulty in growing high-quality $In_xGa_{1-x}N$ alloys, particularly with high indium molar fraction,

due to the large difference between growth temperatures of InN and GaN. The inaccuracy and uncertainties in determining the indium composition, and the presence of multiple phases within the same structure, exists for the $In_xGa_{1-x}N$ material system. Therefore, the fundamental mechanism underlying related to the different phases of $In_xGa_{1-x}N$ materials has not been well developed. Some of the physical and chemical properties such as the bandgap, lattice parameters, elastic constants, effective electron mass, etc., are still estimated based on the two binary compounds, GaN and InN.

A severe drop of efficiency of $In_xGa_{1-x}N$ LEDs, especially green emitters (emitting wavelength $\approx$ 530 nm and therefore having more than 40% indium content), on increasing injection current through the LEDs, is a long-standing problem for this particular alloy system and popularly known as the "Green Gap". The bandgap of $In_xGa_{1-x}N$ with indium composition is found to vary nonlinearly and we estimate the "bowing parameter" to reflect the nonlinearity in the linear Vegard's law of bandgap. However, the value of bowing parameter applicable for the whole composition range of indium is formation dependent and the reported values ranges from 1.0 eV to 6.0 eV, in the literature, and the origin of luminescence is also observed to be ambiguous for $In_xGa_{1-x}N$ material system. Multiple peaks in PL spectra and nonlinear dependence of PL peak position with temperature, are observed, which do not follow Varshni's equation of bandgap, and also display the linear increase of Stoke's shift with the decrease of bandgap. All these phenomena have been explained in terms of the presence of high indium content $In_xGa_{1-x}N$ quantum dot like structure within the $In_xGa_{1-x}N$ matrix having lower indium composition. These complicate the emission properties in the material, which directly affect the fabrication of high-performance and reliable optoelectronic devices with the desired optical properties.

Of late, the growth of low-dimensional structures have been observed to offer some inherent advantages e.g. reduced defect density, higher light extraction efficiency due to large surface-to-volume ratio, weaker piezoelectric polarization field due to reduced strain distribution, etc. These advantages of nanostructures have motivated us to address the existing issues of $In_xGa_{1-x}N$ by growing their nanostructures. In order to understand how different growth parameters (e.g. Growth Temperature, indium and gallium flux-rate, nitrogen Flow-rate etc.) affect the morphology, structure and optical properties of the $In_xGa_{1-x}N$ material system, we have performed systematic experiments by varying the

growth parameters on *c*-sapphire substrate. The grown films are probed by using several complementary characterization tools to understand the various reasons for the variation of indium composition, epitaxial relationships and bandgap. We have also studied the $In_xGa_{1-x}N$ growth on two other important substrates viz. Si(111) and GaN Nanowall Network template grown on *c*-sapphire, to understand the dependence of structural and optical properties on the epitaxy and morphology of the films.

7.2 Summary and Conclusions

In chapter 4 growth of InGaN nanostructures on *c*-sapphire has been carried out using different growth parameters e.g. growth temperature, metal (indium and gallium) and nitrogen fluxes and their effects on the morphology, crystal quality, indium incorporation within the lattice and optical properties of the grown films have been discussed. Single crystalline, wurtzite InGaN films are grown directly on *c*-sapphire at 330 °C, 430 °C, and 530 °C, with constant nitrogen and metal fluxes by MBE. Well separated and vertically aligned NRs are obtained at substrate temperature of 330 °C and 430 °C, whereas at 530 °C, the initially separated NRs coalesce at the top and form a morphology with an interconnected random network. At the lower growth temperature of 330 °C, higher amount of indium incorporation is achieved without any distinct compositional phase separation, but some among the grown crystals have an in-plane rotation of 30°, as observed from the HRXRD phi-scan. This is explained to be possible since, at the InN/*c*-sapphire interface, the lattice mismatch is almost same ($\approx 26\%$) for both the in-plane epitaxial directions ($[11\bar{2}0]_{InN}||[11\bar{2}0]_{Sapphire}$ and $[10\bar{1}0]_{InN}||[11\bar{2}0]_{Sapphire}$), making the simultaneous growth with both the in-plane orientations equally probable. The sample grown at 430 °C shows distinct phase separation and larger indium composition fluctuation from 18% to 48% with a relatively low structural quality and shows least intense PL emission and largest Stoke's shift. This under-performance has been attributed to the localized states originating from indium composition fluctuation in the InGaN layer. The PL emissions are found to follow the nonlinear Vegard's law of bandgap with a bowing parameter of ≈ 1.54 eV, which is a reasonable value for good films. Most importantly, the sample grown at 330 °C, which is much lower than the growth temperature conventionally used for InGaN

growth, contains 23% indium, has good structural as well as optical quality.

Next, to study the effect of indium flux, single crystalline, wurtzite InGaN films are grown directly on *c*-sapphire using four different indium fluxes at a low growth temperature of 380 °C, with constant nitrogen and gallium flux by MBE, under a nitrogen-rich condition. Well separated and vertically aligned thick NRs of average diameter of 700-300 nm, with flat *c*-plane top are obtained at indium K-cell temperatures of 850 °C and 825 °C, whereas at 800 °C, thin NRs with average diameter of 60 nm, with truncated pyramidal top, consisting of $\{10\bar{1}1\}$ facets are formed. At indium K-cell temperature of 775 °C the initially separated NRs coalesce and form an interconnected network morphology, due to larger $\{10\bar{1}1\}$ facet formation and enhancement in the sidewall growth of the closely spaced NRs. HRXRD analysis shows that lower indium flux promotes single InGaN phase formation, whereas higher indium flux causes phase separation. InGaN(0002) peak has been deconvoluted to identify the different InGaN phases present and quantify the average indium composition. Phi scan analysis confirms that high indium flux introduces in-plane rotation among the grown crystals along with phase separation, since, at the InN/*c*-sapphire interface, the lattice mismatch is almost same ($\approx 26\%$) for both the in-plane epitaxial directions ($[11\bar{2}0]_{InN}||[11\bar{2}0]_{Sapphire}$ and $[10\bar{1}0]_{InN}||[11\bar{2}0]_{Sapphire}$), making the simultaneous growth with both the in-plane orientations equally probable. Only high indium-content phases of the phase-separated samples are observed to be emitting at RT, which is attributed to the formation of high indium-content ($\approx 60\%$) regions within the surrounding low indium-content ($\approx 20\%$) InGaN matrix, due to enhanced carrier transport from matrix to these indium-rich regions at RT. Optical absorption measurements and the PL emissions are found to follow the nonlinear Vegard's law of bandgap with a low bowing parameter of ≈ 0.67 eV. The positive Stoke's shift observed in all the samples, is found to increase with decreasing emission energy and is attributed to the increasing InGaN phase separation within the films and consequent increase in carrier localization.

After varying the substrate temperature and indium flux, the influence of gallium and nitrogen flux rates on growth of InGaN is studied. Single crystalline, wurtzite InGaN films are grown directly on *c*-sapphire using three different gallium flux-rates (1.0×10^{-7} torr, 1.6×10^{-7} torr, 2.5×10^{-7} torr) at two different nitrogen flow-rates (4.5 and 8.0 sccm) and at a low growth temperature of 330 °C by MBE, under nitrogen-rich conditions. Start-

ing from uneven, rough and random 3D morphology, then C-shaped and also hexagonal shaped, vertically aligned, *m*-plane faceted NRs with flat *c*-plane tops. An underlying interconnected 3D random network morphology is also been observed depending on different growth conditions. indium composition is found to change from $\approx 22\%$ to $\approx 60\%$ with the change of gallium flux-rate, and no major phase separation is observed due to the presence of high V/III ratio, which stabilizes the high indium-content InGaN phases efficiently. All the samples, except the one grown under extremely off-stoichiometric growth condition, are found to emit at room temperature, which is a very encouraging result. Structural defects are observed to be created by the excessive activated nitrogen on the growth surface during extremely off-stoichiometric growth conditions and also by the increase of the indium content. Together they act as the non-radiative recombination centers that quench the CL emission completely. Optical absorption measurements and the CL emissions are found to follow the nonlinear Vegard's law of bandgaps with a very low bowing parameter of ≈ 0.41 eV, suggesting a very high quality of films with least phase separation. The positive Stoke's shift observed in all the samples, is found to increase with decreasing emission energy and is attributed to the increasing carrier localization with higher indium incorporation.

Chapter 5 presents the studies of growth of InN and InGaN nanostructures on different *in-situ* modified Si(111) surfaces. The consequent effects on the morphology, crystal quality, indium incorporation and optical properties of the grown films have been discussed. The chapter assumes significance since there is intense technological effort to grow InGaN based optoelectronic devices on Silicon substrates, to integrate them with conventional electronics.

The experiments are directed towards obtaining improved crystal quality of InN grown on native epitaxial intermediate layers at relatively low temperatures (100-300°C) to reduce thermal expansion misfit effects and to prevent Si auto doping. The novel approach of Superstructural Matching Epitaxy, identified by our group has been employed here. Better crystalline quality of InN is achieved on the indium induced Si(111)-1×1 superstructural phase due to the smallest lattice mismatch of 8% between the InN unit cell and 1×1 surface reconstruction, as compared to other observed superlattices. HRXRD measurements show that all the films grown in this study are *c*-oriented with wurtzite

crystal structure and better crystalline quality is achieved for the film grown at 200 °C on 1×1 reconstruction. Further improvement in the crystal quality, confirmed by relatively narrower rocking curve FWHM widths, has been accomplished by the two step grown films, in which superlattice matched atomically epitaxial thin InN layers, grown on indium induced 1×1 surface reconstruction, are used as intermediate layers. Electron Mobility values obtained for the samples are found to be influenced by bulk structural quality and carrier concentration. Stoichiometric and good crystalline films show lower band-edge emission. PL band-edge emissions are found to be varying in accordance with the band filling effects depicted by theoretical Moss-Burstein curve. Overall, these experiments show that lattice matched epitaxial native intermediate layers are a better alternative to the current practice of using thick hetero-buffers to attain good quality InN films.

Single crystalline, wurtzite InGaN films are grown directly on Si(111) as well as on nitrided Si(111) substrate, at two different growth temperatures (400 and 500 °C) under nitrogen rich conditions. For the InGaN film grown directly on Si(111), a mixture of triangular 3D islands and hexagonal rods (average diameter ≈ 250 nm) are obtained, which have remnant unreacted crystalline indium. Due to the presence of strain free N-terminated $\beta-Si_3N_4$ on the nitrided Si(111) surface, vertically well-aligned, hexagonal NRs of average diameter ≈ 120 nm are obtained. Lower growth temperature (400 °C) on nitrided surface result in wide, coalesced NRs with ≈ 28% indium incorporation, which results in RT PL emission at 2.44 eV and minimal phase separation, whereas, at higher growth temperature (500 °C) high quality InGaN NRs with RT PL emission close to 2.96 eV are formed. PL emission is found to follow the nonlinear Vegard's law of bandgap with a moderately good bowing parameter of ≈ 1.11 eV. Overall, it has been found that high quality well-aligned InGaN NRs with minimal phase separation and high indium content can be formed by surface nitridation of Si.

The next chapter (Chapter 6) is the novel apporach of growth of InN and InGaN nanostructures on GaN Nanowall Network template grown on *c*-sapphire. In this chapter growth of InN and InGaN nanostructures on GaN Nanowall Network (NWN) template grown on *c*-sapphire has been presented and their effects on the morphology, crystal quality, indium incorporation within the lattice and optical properties of the grown films have been discussed.

In the recent past, spontaneous formation of high quality self assembled GaN NWN on sapphire, under nitrogen rich conditions, by sheer kinetic control without involving lithography, catalysts, buffer layers, or any surface pretreatment, using PA-MBE growth, has been achieved. Highly nitrogen- rich condition and consequent limited surface diffusion of Ga adatoms, promotes 3D nucleation at the steps of edge dislocations, and thus the relaxed hexagonal GaN NWN forms surrounding a void region which consists of open screw dislocations. The NWN structure shows very high emission with almost no defect related emission present. More interestingly, the electron mobility through the network is found to be significantly higher than that is typically observed for GaN epitaxial films, which is attributed to the transport of electrons through the edge states formed at the top edges of the nanowalls and to a 2D quantum confinement of electrons in the central vertical plane of the walls.

Spontaneous self-assembled vertically aligned InN NRs are formed on GaN NWN template deposited on *c*-sapphire by a two step MBE growth process. This method enables the growth of dislocation free high quality InN NRs with average height of $\approx$ 700 nm and average diameter of $\approx$ 120 nm, having good structural, optical and electrical properties. The HRXRD and TEM studies reveal that InN NRs possesses relaxed wurtzite crystal structure and are dislocation and strain free. The low temperature CL studies show a sharp and low band-edge emission at 0.65eV for InN NRs, which is among the best values reported in the literature. Electrical characterization on a single NR yields a carrier concentration as low as $\approx 1.1\times10^{17}$ cm^{-3} and electron mobility as high as $\approx$ 4453 cm^2/V-sec, which are among the best reported values so far for a dislocation free InN NR having diameter of $\approx$ 150 nm to the best of our knowledge. Thus, the present work reports a simple method to fabricate a dislocation free InN NRs having low carrier concentration and high mobility. These defect free InN NRs that are highly stable and defect and strain free with such large mobility and low carrier concentration, is a promising material for terahertz emission and detection.

Single crystalline, *c*-oriented, wurtzite InGaN NWN is grown on 30 min grown GaN NWN template, which is grown on *c*-sapphire, where the overgrown InGaN film morphology resembles that of the underlying GaN template, which is attributed to the similar type of V/III ratio used for both the growths of GaN and InGaN. HRXRD study shows

that indium incorporation is ≈ 7% in the InGaN NWN film and the epitaxial relationship between the grown films and substrate is $(0001)_{InGaN} \parallel (0001)_{GaN} \parallel (0001)_{Sapphire}$. CL study confirms that the 7% indium content phase is stable in the sample, which emits at 3.02 eV at RT. In summary, by optimizing the growth parameters, GaN NWN can be utilized as an useful template to grow InGaN NWN, having good structural and optical properties. Further, experiments are necessary to enhance the quantity of indium incorporation by a systematic control of the growth kinetics, to obtain high quality InGaN NWN emitting across the visible spectral range.

7.3 Highlights of The Present Work

The most important and significant observations made in the present work have been listed below:

- Low growth temperature, low gallium flux and high V/III ratio is found to be suitable for forming $In_xGa_{1-x}N$ on *c*-sapphire with suppression of phase separation and increased indium incorporation. [**Publication**: Materials Research Express **1**, 035019 (2014), Journal of Physics D: Applied Physics **49**, 355304 (2016)]

- Under high V/III BEP ratio, $In_xGa_{1-x}N$ phase with ≈ 60% indium content has been achieved, for which room temperature CL emission has been observed.

- *in-situ* Surface modification of Si(111) substrate has been utilized to grow good quality InN on the indium induced Si(111)-1×1 superstructural phase, at lower temperature than conventionally used in MBE, due to the smallest lattice mismatch of 8% between the InN unit cell and 1×1 surface reconstruction, as compared to other observed superlattices. [**Publication**: Physica Status Solidi A **210**, 2409 (2013)]

- Surface nitridation of Si(111) surface is found to increase indium incorporation in $In_xGa_{1-x}N$ films upto 30%. [**Publication**: Journal of Applied Physics **118**, 025301 (2015)]

- Very high mobility and dislocation free InN nanorods have been grown on a GaN Nanowall Network template, that show very high electron mobility (≈ 4453 cm^2/V-

sec) and low carrier concentration ($\approx 1.1\times10^{17}$ cm^{-3}), which can be a very appropriate material for terahertz emission and detection. [**Publication**: Journal of Applied Physics **119**, 205701 (2016), IEEE Conference Proceedings, 1-5 (2014)]

- Spontaneous growth of $In_xGa_{1-x}N$ Nanowall Network has been demonstrated on GaN Nanowall Network, which shows $\approx$ 7% indium incorporation in the InGaN NWN film and the epitaxial relationship between the grown films and substrate is $(0001)_{InGaN} \parallel (0001)_{GaN} \parallel (0001)_{Sapphire}$ and the 7% indium content phase is stable in the sample, which emits at 3.02 eV at RT.

7.4 Future Directions

The work has addressed the influence of growth kinetics and suitable template use for growing high quality InGaN films. However, the studies yield some interesting results that may be taken forward intensely to arrive at a better scientific understanding or technological progress.

We have obtained InGaN nanostructures with indium composition upto $\approx$ 60 %, which means emission is in green colour. So, growth of InGaN with higher than 60% indium content should be attempted to span whole visible spectrum.

We have grown all our samples mostly on *c*-sapphire and also on Si(111). So, growth of InGaN on different other polar and nonpolar planes of sapphire (*e.g. m, r, a*) as well as Silicon (*e.g.* (100), (110), (5 5 12) etc.) can be carried out to understand the dependence of the morphology, structural and optical properties of InGaN on those substrates.

The particular morphology of Nanowall Network shows several outstanding properties, as already mentioned in the present thesis and thus, it is very interesting to employ it as a template to grow InGaN films and nanostructures. We are able to grow InGaN Nanowall Network, which itself is a significant success, but with only one composition ($\approx$ 7%). So, growth of InGaN Nanowall Network of different other indium compositions can be conducted to obtain same morphology with different bandgap and then other material properties can also be studied. The defect and strain free properties of these nanostructures with large surface area and nanosized cavities can be of great interest and value.

We have demonstrated the growth of InGaN having different indium composition and variation of bandgap with indium composition in the current work. However, the bandgap of InGaN is limited in a small region of solar spectrum and thus, it will be interesting to grow InAlGaN and InAlN, in order to span whole UV to IR spectrum covering most of the solar spectrum. Forming nanostructures with varying indium content along their depth can give broad absorption/emission properties which will be useful for a large wavelength range absorption and white light emission for high brightness LEDs and wide-spectrum solar cells.

Finally, doping of InGaN should be attempted as it is eventually necessary to fabricate any device structures using InGaN. Though these films are unintentionally n-doped, obtaining significant p-doping in these materials to over-compensate the n-type carriers and give significant p-carrier concentration will be and essential step to make devices in the future with much superior properties. Overall the thesis has brought out new observations that can be intensely pursued to obtain materials for enhanced performance in optoelectronic devices.

APPENDIX A

Average Indium composition (x) calculation

A. For Sample A:

Peak No.	Peak Position (degree)	c-lattice parameter (nm)	Indium Composition (x)	Area of the Peak (A)	Peak Area* In Composition (A*x)
Peak 1	32.45	0.55138	0.63	18.72	11.79
Peak 2	33.02	0.54218	0.45	8.91	4.01
Peak 3	33.56	0.53371	0.29	22.18	6.43
Peak 4	34.06	0.52599	0.14	14.84	2.08

Sum of A = 18.72+8.91+22.18+14.84 = **64.65**

Sum of (A*x) = 11.79+4.01+6.43+2.08 = **24.31**

Average x = Sum of (A*x) / Sum of A = 24.31/64.65 = **0.38**

B. For Sample B:

Peak No.	Peak Position (degree)	c-lattice parameter (nm)	Indium Composition (x)	Area of the Peak (A)	Peak Area* In Composition (A*x)
Peak 1	32.59	0.54914	0.59	21.96	12.96
Peak 2	32.94	0.54331	0.48	21.07	10.11
Peak 3	33.41	0.53595	0.33	43.14	14.24
Peak 4	33.87	0.52876	0.20	67.20	13.44

Sum of A = 21.96+21.07+43.14+67.20 = **153.37**

Sum of (A*x) = 12.96+10.11+14.24+13.44 = **50.75**

Average x = Sum of (A*x) / Sum of A = 50.75/153.37 = **0.33**

Bibliography

[1] H. Morkoç, *Handbook of Nitride Semiconductors and Devices, Materials Properties, Physics and Growth* (John Wiley & Sons, 2009).

[2] B. Gil, *Group III Nitride Semiconductor Compounds: Physics and Applications* (Clarendon Press, 1998).

[3] O. Ambacher, J. Phys. D. Appl. Phys. **31**, 2653 (1998).

[4] F. A. Ponce and D. P. Bour, Nature **386**, 351 (1997).

[5] J. Wu, J. Appl. Phys. **106**, 011101 (2009).

[6] F. K. Yam and Z. Hassan, Superlattices Microstruct. **43**, 1 (2008).

[7] S. Nakamura, Science **281**, 956 (1998).

[8] K. S. A. Butcher and T. L. Tansley, Superlattices Microstruct. **38**, 1 (2005).

[9] H. Morkoc, Mater. Sci. Eng. B **43**, 137 (1997).

[10] Y. Nanishi, Y. Saito, and T. Yamaguchi, Jpn. J. Appl. Phys. **42**, 2549 (2003).

[11] A. G. Bhuiyan, A. Hashimoto, and A. Yamamoto, J. Appl. Phys. **94**, 2779 (2003).

[12] X. Wang and A. Yoshikawa, Prog. Cryst. Growth Charact. Mater. **48/49**, 42 (2004).

[13] A. Khan, K. Balakrishnan, and T. Katona, Nat. Photonics **2**, 77 (2008).

[14] S. Strite and H. Morkoç, J. Vac. Sci. Technol. B **10**, 1237 (1992).

[15] J. Wu, W. Walukiewicz, W. Shan, K. M. Yu, J. W. Ager III, S. X. Li, E. E. Haller, H. Lu, and W. J. Schaff, J. Appl. Phys. **94**, 4457 (2003).

[16] M. Feneberg, R. A. R. Leute, B. Neuschl, K. Thonke, and M. Bickermann, Phys. Rev. B **82**, 075208 (2010).

[17] S. C. Jain, M. Willander, J. Narayan, and R. V. Overstraeten, J. Appl. Phys. **87**, 965 (2000).

[18] V. R. Juza and H. Hahn, Zeitschrift für Anorg. und Allg. Chemie **239**, 282 (1938).

[19] H. P. Maruska and J. J. Tietjen, Appl. Phys. Lett. **15**, 327 (1969).

[20] J. I. Pankove, E. A. Miller, and J. E. Berkeyheiser, RCA Rev. **32**, 383 (1971).

[21] H. Amano, I. Akasaki, T. Kozawa, K. Hiramatsu, N. Sawaki, K. Ikeda, and Y. Ishii, J. Lumin. **40-41**, 121 (1988).

[22] S. Nakamura, T. Mukai, and M. Senoh, Jpn. J. Appl. Phys. **30**, L1998 (1991).

[23] S. Nakamura, M. Senoh, and T. Mukai, Jpn. J. Appl. Phys. **32**, L8 (1993).

[24] S. Nakamura, M. Senoh, N. Iwasa, and S.-i. Nagahama, Jpn. J. Appl. Phys. **34**, L797 (1995).

[25] S. Nakamura, Diam. Relat. Mater. **5**, 496 (1996).

[26] M. A. Khan, J. M. V. Hove, J. N. Kuznia, and D. T. Olson, Appl. Phys. Lett. **58**, 2408 (1991).

[27] M. A. Khan, A. Bhattarai, J. N. Kuznia, and D. T. Olson, Appl. Phys. Lett. **63**, 1214 (1993).

[28] J. Kuzmik, IEEE Electron Device Lett. **22**, 510 (2001).

[29] A. J. Sierakowski and L. F. Eastman, J. Appl. Phys. **86**, 3398 (1999).

[30] Y. H. Kwon, G. H. Gainer, S. Bidnyk, Y. H. Cho, J. J. Song, M. Hansen, and S. P. DenBaars, Appl. Phys. Lett. **75**, 2545 (1999).

[31] Y. Narukawa, Y. Kawakami, M. Funato, S. Fujita, S. Fujita, and S. Nakamura, Appl. Phys. Lett. **70**, 981 (1997).

[32] W. Xie, D. C. Grillo, R. L. Gunshor, M. Kobayashi, H. Jeon, J. Ding, A. V. Nurmikko, G. C. Hua, and N. Otsuka, Appl. Phys. Lett. **60**, 1999 (1992).

[33] K. Koga and T. Yamaguchi, Prog. Cryst. Growth Charact. Mater. **23**, 127 (1992).

[34] H. Amano, M. Kito, K. Hiramatsu, and I. Akasaki, Jpn. J. Appl. Phys. **28**, L2112 (1989).

[35] S. Nakamura, T. Mukai, and M. Senoh, Jpn. J. Appl. Phys. **32**, L16 (1993).

[36] S. Nakamura, T. Mukai, and M. Senoh, Appl. Phys. Lett. **64**, 1687 (1994).

[37] S. Nakamura, J. Vac. Sci. Technol. A **13**, 705 (1995).

[38] J. Zhang, C. Xiong, J. Liu, Z. Quan, L. Wang, and F. Jiang, Appl. Phys. A **114**, 1049 (2014).

[39] K. Lekhal, B. Damilano, H. T. Ngo, D. Rosales, P. De Mierry, S. Hussain, P. Vennéguès, and B. Gil, Appl. Phys. Lett. **106**, 142101 (2015).

[40] K. Shojiki, T. Tanikawa, J.-h. Choi, S. Kuboya, T. Hanada, R. Katayama, and T. Matsuoka, Appl. Phys. Express **8**, 061005 (2015).

[41] J.-I. Hwang, R. Hashimoto, S. Saito, and S. Nunoue, Appl. Phys. Express **7**, 071003 (2014).

[42] P. de Mierry, L. Kappei, F. Tendille, P. Vennegues, M. Leroux, and J. Zuniga-Perez, Phys. Status Solidi B **253**, 105 (2016).

[43] J. Bai, B. Xu, F. G. Guzman, K. Xing, Y. Gong, Y. Hou, and T. Wang, Appl. Phys. Lett. **107**, 261103 (2015).

[44] S. N. Mohammad, A. A. Salvador, and H. Morkoc, Proc. IEEE **83**, 1306 (1995).

[45] M. A. Littlejohn, J. R. Hauser, and T. H. Glisson, Appl. Phys. Lett. **26**, 625 (1975).

[46] V. W. L. Chin, T. L. Tansley, and T. Osotchan, J. Appl. Phys. **75**, 7365 (1994).

[47] B. E. Foutz, L. F. Eastman, U. V. Bhapkar, and M. S. Shur, Appl. Phys. Lett. **70**, 2849 (1997).

[48] B. Gelmont, K. Kim, and M. Shur, J. Appl. Phys. **74**, 1818 (1993).

[49] D. L. Rode and D. K. Gaskill, Appl. Phys. Lett. **66**, 1972 (1995).

[50] R. Gaska, J. W. Yang, A. Osinsky, Q. Chen, M. A. Khan, A. O. Orlov, G. L. Snider, and M. S. Shur, Appl. Phys. Lett. **72**, 707 (1998).

[51] C. F. Lin, H. C. Cheng, J. A. Huang, M. S. Feng, J. D. Guo, and G. C. Chi, Appl. Phys. Lett. **70**, 2583 (1997).

[52] E. Sichel and J. Pankove, J. Phys. Chem. Solids **38**, 330 (1977).

[53] Y.-F. Wu, B. P. Keller, S. Keller, N. X. Nguyen, M. Le, C. Nguyen, T. J. Jenkins, L. T. Kehias, S. P. Denbaars, and U. K. Mishra, IEEE Electron Device Lett. **18**, 438 (1997).

[54] Z. Fan, S. N. Mohammad, Ö. Aktas, A. E. Botchkarev, A. Salvador, and H. Morkoç, Appl. Phys. Lett. **69**, 1229 (1996).

[55] M. Khan, Q. Chen, M. Shur, B. Dermott, J. Higgins, J. Burm, W. Schaff, and L. Eastman, Electron. Lett. **32**, 357 (1996).

[56] Q. Z. Liu, L. S. Yu, S. S. Lau, J. M. Redwing, N. R. Perkins, and T. F. Kuech, Appl. Phys. Lett. **70**, 1275 (1997).

[57] Y.-F. Wu, B. P. Keller, S. Keller, D. Kapolnek, P. Kozodoy, S. P. Denbaars, and U. K. Mishra, Appl. Phys. Lett. **69**, 1438 (1996).

[58] R. Gaska, A. Osinsky, J. W. Yang, and M. S. Shur, IEEE Electron Device Lett. **19**, 89 (1998).

[59] E. T. Yu, G. J. Sullivan, P. M. Asbeck, C. D. Wang, D. Qiao, and S. S. Lau, Appl. Phys. Lett. **71**, 2794 (1997).

[60] R. Dingle, K. L. Shaklee, R. F. Leheny, and R. B. Zetterstrom, Appl. Phys. Lett. **19**, 5 (1971).

[61] S. Nakamura, M. Senoh, S.-i. Nagahama, N. Iwasa, T. Yamada, T. Matsushita, Y. Sugimoto, and H. Kiyoku, Appl. Phys. Lett. **69**, 1477 (1996).

[62] S. Nakamura, M. Senoh, S.-i. Nagahama, N. Iwasa, T. Yamada, T. Matsushita, Y. Sugimoto, and H. Kiyoku, Appl. Phys. Lett. **69**, 3034 (1996).

[63] S. Nakamura, M. Senoh, S.-i. Nagahama, N. Iwasa, T. Yamada, T. Matsushita, H. Kiyoku, Y. Sugimoto, T. Kozaki, H. Umemoto, et al., Jpn. J. Appl. Phys. **36**, L1568 (1997).

[64] S. Nakamura, M. Senoh, S.-i. Nagahama, N. Iwasa, T. Yamada, T. Matsushita, H. Kiyoku, Y. Sugimoto, T. Kozaki, H. Umemoto, et al., Appl. Phys. Lett. **72**, 2014 (1998).

[65] M. Razeghi and A. Rogalski, J. Appl. Phys. **79**, 7433 (1996).

[66] M. A. Khan, J. N. Kuznia, D. T. Olson, J. M. V. Hove, M. Blasingame, and L. F. Reitz, Appl. Phys. Lett. **60**, 2917 (1992).

[67] M. A. Khan, M. Shatalov, H. P. Maruska, H. M. Wang, and E. Kuokstis, Jpn. J. Appl. Phys. **44**, 7191 (2005).

[68] J. M. V. Hove, R. Hickman, J. J. Klaassen, P. P. Chow, and P. P. Ruden, Appl. Phys. Lett. **70**, 2282 (1997).

[69] Q. Chen, J. W. Yang, A. Osinsky, S. Gangopadhyay, B. Lim, M. Z. Anwar, M. A. Khan, D. Kuksenkov, and H. Temkin, Appl. Phys. Lett. **70**, 2277 (1997).

[70] G. Y. Xu, A. Salvador, W. Kim, Z. Fan, C. Lu, H. Tang, H. Morkoç, G. Smith, M. Estes, B. Goldenberg, et al., Appl. Phys. Lett. **71**, 2154 (1997).

[71] X. Zhang, P. Kung, D. Walker, J. Piotrowski, A. Rogalski, A. Saxler, and M. Razeghi, Appl. Phys. Lett. **67**, 2028 (1995).

[72] C. Campbell, *Surface Acoustic Wave Devices and Their Signal Processing Applications* (Elsevier, 2012).

[73] N. F. Foster and G. A. Rozgonyi, Appl. Phys. Lett. **8**, 221 (1966).

[74] H. Okano, Y. Takahashi, T. Tanaka, K. Shibata, and S. Nakano, Jpn. J. Appl. Phys. **31**, 3446 (1992).

[75] M. T. Duffy, C. C. Wang, G. D. O'clock, S. H. McFarlane, and P. J. Zanzucchi, J. Electron. Mater. **2**, 359 (1973).

[76] A. Kazimirov, G. Scherb, J. Zegenhagen, T.-L. Lee, M. J. Bedzyk, M. K. Kelly, H. Angerer, and O. Ambacher, J. Appl. Phys. **84**, 1703 (1998).

[77] J. K. Liu, K. M. Lakin, and K. L. Wang, J. Appl. Phys. **46**, 3703 (1975).

[78] C. Deger, E. Born, H. Angerer, O. Ambacher, M. Stutzmann, J. Hornsteiner, E. Riha, and G. Fischerauer, Appl. Phys. Lett. **72**, 2400 (1998).

[79] T. Aubert, O. Elmazria, B. Assouar, L. Bouvot, and M. Oudich, Appl. Phys. Lett. **96**, 203503 (2010).

[80] J. Wu, W. Walukiewicz, K. M. Yu, W. Shan, J. W. Ager III, E. E. Haller, H. Lu, W. J. Schaff, W. K. Metzger, and S. Kurtz, J. Appl. Phys. **94**, 6477 (2003).

[81] A. D. Vos, *Endoreversible Thermodynamics of Solar Energy Conversion* (Oxford University Press, 1992).

[82] H. Hamzaoui, A. S. Bouazzi, and B. Rezig, Sol. Energy Mater. Sol. Cells **87**, 595 (2005).

[83] S. R. Kurtz, P. Faine, and J. M. Olson, J. Appl. Phys. **68**, 1890 (1990).

[84] L. Hsu and W. Walukiewicz, J. Appl. Phys. **104**, 024507 (2008).

[85] N. H. Rafat and S. E. D. Habib, Sol. Energy Mater. Sol. Cells **55**, 341 (1998).

[86] N. Miller, R. E. Jones, K. M. Yu, J. W. Ager, Z. Liliental-Weber, E. E. Haller, W. Walukiewicz, T. L. Williamson, and M. A. Hoffbauer, Phys. Status Solidi C **5**, 1866 (2008).

[87] S. Gwo, C. L. Wu, C. H. Shen, W. H. Chang, T. M. Hsu, J. S. Wang, and J. T. Hsu, Appl. Phys. Lett. **84**, 3765 (2004).

[88] C.-L. Hsiao, L.-W. Tu, M. Chen, Z.-W. Jiang, N.-W. Fan, Y.-J. Tu, and K.-R. Wang, Jpn. J. Appl. Phys. **44**, L1076 (2005).

[89] J. Grandal and M. A. Sánchez-García, J. Cryst. Growth **278**, 373 (2005).

[90] B. Maleyre, S. Ruffenach, O. Briot, B. Gil, and A. Van der Lee, Superlattices Microstruct. **36**, 517 (2004).

[91] T. Yodo, Y. Kitayama, K. Miyaki, H. Yona, and Y. Harada, Jpn. J. Appl. Phys. **43**, L139 (2004).

[92] T. Yamaguchi, Y. Saito, C. Morioka, K. Yorozu, T. Araki, A. Suzuki, and Y. Nanishi, Phys. Status Solidi B **240**, 429 (2003).

[93] C. L. Wu, C. H. Shen, H. W. Lin, H. M. Lee, and S. Gwo, Appl. Phys. Lett. **87**, 241916 (2005).

[94] M. A. Sánchez-Garcia, J. Grandal, E. Calleja, S. Lazic, J. M. Calleja, and A. Trampert, Phys. Status Solidi B **243**, 1490 (2006).

[95] C. H. Shen, H. Y. Chen, H. W. Lin, S. Gwo, A. A. Klochikhin, and V. Y. Davydov, Appl. Phys. Lett. **88**, 253104 (2006).

[96] C. C. Huang, R. W. Chuang, S. J. Chang, J. C. Lin, Y. C. Cheng, and W. J. Lin, J. Electron. Mater. **37**, 1054 (2008).

[97] M. Jamil, R. A. Arif, Y.-K. Ee, H. Tong, J. B. Higgins, and N. Tansu, Phys. Status Solidi A **205**, 1619 (2008).

[98] Z.-Y. Li, S.-M. Lan, W.-Y. Uen, Y.-R. Chen, M.-C. Chen, Y.-H. Huang, C.-T. Ku, S.-M. Liao, T.-M. Yang, S.-C. Wang, et al., J. Vac. Sci. Technol. A **26**, 587 (2008).

[99] C. Yang, X. Wang, H. Xiao, J. Ran, C. Wang, G. Hu, X. Wang, X. Zhang, J. Li, and J. Li, Phys. Status Solidi A **204**, 4288 (2007).

[100] X. Chen, K. D. Matthews, D. Hao, W. J. Schaff, and L. F. Eastman, Phys. Status Solidi A **205**, 1103 (2008).

[101] C. J. Neufeld, N. G. Toledo, S. C. Cruz, M. Iza, S. P. DenBaars, and U. K. Mishra, Appl. Phys. Lett. **93**, 143502 (2008).

[102] O. Jani, I. Ferguson, C. Honsberg, and S. Kurtz, Appl. Phys. Lett. **91**, 132117 (2007).

[103] C. A. M. Fabien and W. A. Doolittle, Sol. Energy Mater. Sol. Cells **130**, 354 (2014).

[104] R. Dahal, B. N. Pantha, J. Li, J. Y. Lin, and H. X. Jiang, Appl. Phys. Lett. **104**, 143901 (2014).

[105] J. Bai, C. C. Yang, M. Athanasiou, and T. Wang, Appl. Phys. Lett. **104**, 051129 (2014).

[106] N. G. Young, E. E. Perl, R. M. Farrell, M. Iza, S. Keller, J. E. Bowers, S. Nakamura, S. P. Denbaars, and J. S. Speck, Appl. Phys. Lett. **104**, 163902 (2014).

[107] M. F. Cansizoglu, S. M. Hamad, D. P. Norman, F. Keles, E. Badraddin, T. Karabacak, and H.-W. Seo, Appl. Phys. Express **8**, 042302 (2015).

[108] L. Sang, M. Liao, Y. Koide, and M. Sumiya, J. Appl. Phys. **117**, 105706 (2015).

[109] K. Wang, D. Imai, K. Kusakabe, and A. Yoshikawa, Appl. Phys. Lett. **108**, 042108 (2016).

[110] H. Lu, W. J. Schaff, L. F. Eastman, and C. E. Stutz, Appl. Phys. Lett. **82**, 1736 (2003).

[111] I. Mahboob, T. D. Veal, C. F. McConville, H. Lu, and W. J. Schaff, Phys. Rev. Lett. **92**, 036804 (2004).

[112] I. Mahboob, T. D. Veal, L. F. J. Piper, C. F. McConville, H. Lu, W. J. Schaff, J. Furthmüller, and F. Bechstedt, Phys. Rev. B **69**, 201307 (2004).

[113] K. A. Rickert, A. B. Ellis, F. J. Himpsel, H. Lu, W. Schaff, J. M. Redwing, F. Dwikusuma, and T. F. Kuech, Appl. Phys. Lett. **82**, 3254 (2003).

[114] R. E. Jones, K. M. Yu, S. X. Li, W. Walukiewicz, J. W. Ager, E. E. Haller, H. Lu, and W. J. Schaff, Phys. Rev. Lett. **96**, 125505 (2006).

[115] H. Lu, W. J. Schaff, and L. F. Eastman, J. Appl. Phys. **96**, 3577 (2004).

[116] O. Kryliouk, H. J. Park, H. T. Wang, B. S. Kang, T. J. Anderson, F. Ren, and S. J. Pearton, J. Vac. Sci. Technol. B **23**, 1891 (2005).

[117] C.-F. Chen, C.-L. Wu, and S. Gwo, Appl. Phys. Lett. **89**, 252109 (2006).

[118] Y.-S. Lu, C.-C. Huang, J. A. Yeh, C.-F. Chen, and S. Gwo, Appl. Phys. Lett. **91**, 202109 (2007).

[119] Y.-S. Lu, C.-L. Ho, J. A. Yeh, H.-W. Lin, and S. Gwo, Appl. Phys. Lett. **92**, 212102 (2008).

[120] R. D. Shannon and C. T. Prewitt, Acta Crystallogr. B **25**, 925 (1969).

[121] M. Tanaka, S. Nakahata, K. Sogabe, H. Nakata, and M. Tobioka, Jpn. J. Appl. Phys. **36**, L1062 (1997).

[122] J. Li, K. B. Nam, M. L. Nakarmi, J. Y. Lin, H. X. Jiang, P. Carrier, and S. H. Wei, Appl. Phys. Lett. **83**, 5163 (2003).

[123] V. Darakchieva, B. Monemar, and A. Usui, Appl. Phys. Lett. **91**, 031911 (2007).

[124] W. Shan, T. J. Schmidt, X. H. Yang, S. J. Hwang, J. J. Song, and B. Goldenberg, Appl. Phys. Lett. **66**, 985 (1995).

[125] M. F. Wu, S. Q. Zhou, A. Vantomme, Y. Huang, H. Wang, and H. Yang, J. Vac. Sci. Technol. A **24**, 275 (2006).

[126] C. J. Sun, P. Kung, A. Saxler, H. Ohsato, E. Bigan, M. Razeghi, and D. K. Gaskill, J. Appl. Phys. **76**, 236 (1994).

[127] T. Sasaki and S. Zembutsu, J. Appl. Phys. **61**, 2533 (1987).

[128] R. E. Ewing and P. E. Greene, J. Electrochem. Soc. **111**, 917 (1964).

[129] F. A. Ponce, D. P. Bour, W. T. Young, M. Saunders, and J. W. Steeds, Appl. Phys. Lett. **69**, 337 (1996).

[130] A. R. Smith, R. M. Feenstra, D. W. Greve, J. Neugebauer, and J. E. Northrup, Phys. Rev. Lett. **79**, 3934 (1997).

[131] T. George, E. Jacobsohn, W. T. Pike, P. ChangChien, M. A. Khan, J. W. Yang, and S. Mahajan, Appl. Phys. Lett. **68**, 337 (1996).

[132] A. Kuramata, K. Horino, K. Domen, K. Shinohara, and T. Tanahashi, Appl. Phys. Lett. **67**, 2521 (1995).

[133] C. J. Sun, J. W. Yang, Q. Chen, M. A. Khan, T. George, P. ChangChien, and S. Mahajan, Appl. Phys. Lett. **68**, 1129 (1996).

[134] G. Popovici, W. Kim, A. Botchkarev, H. Tang, H. Morkoç, and J. Solomon, Appl. Phys. Lett. **71**, 3385 (1997).

[135] N. P. Kobayashi, J. T. Kobayashi, P. D. Dapkus, W.-J. Choi, A. E. Bond, X. Zhang, and D. H. Rich, Appl. Phys. Lett. **71**, 3569 (1997).

[136] W. Li and W. Ni, Appl. Phys. Lett. **68**, 2705 (1996).

[137] P. Kung, A. Saxler, X. Zhang, D. Walker, R. Lavado, and M. Razeghi, Appl. Phys. Lett. **69**, 2116 (1996).

[138] F. Hamdani, M. Yeadon, D. J. Smith, H. Tang, W. Kim, A. Salvador, A. E. Botchkarev, J. M. Gibson, A. Y. Polyakov, M. Skowronski, et al., J. Appl. Phys. **83**, 983 (1998).

[139] S. Kaiser, H. Preis, W. Gebhardt, O. Ambacher, H. Angerer, M. Stutzmann, A. Rosenauer, and D. Gerthsen, Jpn. J. Appl. Phys. **37**, 84 (1998).

[140] M. K. Kelly, O. Ambacher, R. Dimitrov, R. Handschuh, and M. Stutzmann, Phys. Status Solidi A **159**, R3 (1997).

[141] W. Paszkowicz, R. Černý, and S. Krukowski, Powder Diffr. **18**, 114 (2003).

[142] L. Liu and J. H. Edgar, Mater. Sci. Eng. R **37**, 61 (2002).

[143] K. Dovidenko, S. Oktyabrsky, J. Narayan, and M. Razeghi, J. Appl. Phys. **79**, 2439 (1996).

[144] J. Grandal, M. A. Sánchez-García, F. Calle, and E. Calleja, Phys. Status Solidi C **2**, 2289 (2005).

[145] J. Wu, W. Walukiewicz, K. M. Yu, J. W. Ager III, E. E. Haller, H. Lu, W. J. Schaff, Y. Saito, and Y. Nanishi, Appl. Phys. Lett. **80**, 3967 (2002).

[146] V. Y. Davydov, A. A. Klochikhin, R. P. Seisyan, V. V. Emtsev, S. V. Ivanov, F. Bechstedt, J. Furthmüller, H. Harima, A. V. Mudryi, J. Aderhold, et al., Phys. Status Solidi B **229**, R1 (2002).

[147] T. Matsuoka, H. Okamoto, M. Nakao, H. Harima, and E. Kurimoto, Appl. Phys. Lett. **81**, 1246 (2002).

[148] Y. Saito, H. Harima, E. Kurimoto, T. Yamaguchi, N. Teraguchi, A. Suzuki, T. Araki, and Y. Nanishi, Phys. Status Solidi B **234**, 796 (2002).

[149] B. Arnaudov, T. Paskova, P. P. Paskov, B. Magnusson, E. Valcheva, B. Monemar, H. Lu, W. Schaff, H. Amano, and I. Akasaki, Phys. Rev. B **69**, 115216 (2004).

[150] W. Walukiewicz, S. X. Li, J. Wu, K. M. Yu, J. W. Ager III, E. E. Haller, H. Lu, and W. J. Schaff, J. Cryst. Growth **269**, 119 (2004).

[151] B. Monemar, P. P. Paskov, and A. Kasic, Superlattices Microstruct. **38**, 38 (2005).

[152] K. S. A. Butcher, M. Wintrebert-Fouquet, P. P. T. Chen, T. L. Tansley, H. Dou, S. K. Shrestha, H. Timmers, M. Kuball, K. E. Prince, and J. E. Bradby, J. Appl. Phys. **95**, 6124 (2004).

[153] Q. X. Guo, T. Tanaka, M. Nishio, H. Ogawa, X. D. Pu, and W. Z. Shen, Appl. Phys. Lett. **86**, 231913 (2005).

[154] P. Specht, J. C. Ho, X. Xu, R. Armitage, E. R. Weber, R. Erni, and C. Kisielowski, Solid State Commun. **135**, 340 (2005).

[155] S. J. Pearton, J. C. Zolper, R. J. Shul, and F. Ren, J. Appl. Phys. **86**, 1 (1999).

[156] S. J. Pearton, F. Ren, A. P. Zhang, and K. P. Lee, Mater. Sci. Eng. R **30**, 55 (2000).

[157] S. N. Mohammad and H. Morkoç, Prog. Quantum Electron. **20**, 361 (1996).

[158] R. F. Davis, A. M. Roskowski, E. A. Preble, J. S. Speck, B. Heying, J. A. Freitas Jr., E. R. Glaser, and W. E. Carlos, Proc. IEEE **90**, 993 (2002).

[159] M. A. Reshchikov and H. Morkoc, J. Appl. Phys. **97**, 061301 (2005).

[160] T. Matsuoka, Superlattices Microstruct. **37**, 19 (2005).

[161] I. Ho and G. B. Stringfellow, Appl. Phys. Lett. **69**, 2701 (1996).

[162] T. Nagatomo, T. Kuboyama, H. Minamino, and O. Omoto, Jpn. J. Appl. Phys. **28**, L1334 (1989).

[163] N. Yoshimoto, T. Matsuoka, T. Sasaki, and A. Katsui, Appl. Phys. Lett. **59**, 2251 (1991).

[164] E. L. Piner, F. G. McIntosh, J. C. Roberts, M. E. Aumer, V. A. Joshkin, S. M. Bedair, and N. A. El-Masry, MRS Internet J. Nitride Semicond. Res. **1**, 43 (1996).

[165] W. V. der Stricht, I. Moerman, P. Demeester, L. Considine, E. J. Thrush, and J. A. Crawley, MRS Internet J. Nitride Semicond. Res. **2**, 16 (1997).

[166] R. A. Oliver, M. J. Kappers, C. J. Humphreys, and G. A. D. Briggs, J. Cryst. Growth **272**, 393 (2004).

[167] S. Keller, B. P. Keller, D. Kapolnek, A. C. Abare, H. Masui, L. A. Coldren, U. K. Mishra, and S. P. Den Baars, Appl. Phys. Lett. **68**, 3147 (1996).

[168] S. Keller, B. Keller, D. Kapolnek, U. Mishra, S. DenBaars, I. Shmagin, R. Kolbas, and S. Krishnankutty, J. Cryst. Growth **170**, 349 (1997).

[169] T. Matsuoka, N. Yoshimoto, T. Sasaki, and A. Katsui, J. Electron. Mater. **21**, 157 (1992).

[170] F. Nakamura, S. Hashimoto, M. Hara, Synji, Imanaga, M. Ikeda, and H. Kawai, J. Cryst. Growth **195**, 280 (1998).

[171] S.-N. Lee, T. Sakong, W. Lee, H. Paek, M. Seon, I.-H. Lee, O. Nam, and Y. Park, J. Cryst. Growth **250**, 256 (2003).

[172] D.-J. Kim, Y.-T. Moon, K.-M. Song, I.-H. Lee, and S.-J. Park, J. Electron. Mater. **30**, 99 (2001).

[173] H. Chen, R. M. Feenstra, J. E. Northrup, J. Neugebauer, and D. W. Greve, MRS Internet J. Nitride Semicond. Res. **6**, 11 (2001).

[174] K. Kushi, H. Sasamoto, D. Sugihara, S. Nakamura, A. Kikuchi, and K. Kishino, Mater. Sci. Eng. B **59**, 65 (1999).

[175] T. Bottcher, S. Einfeldt, V. Kirchner, S. Figge, H. Heinke, D. Hommel, H. Selke, and P. L. Ryder, Appl. Phys. Lett. **73**, 3232 (1998).

[176] J. Wu, W. Walukiewicz, K. M. Yu, J. W. Ager III, E. E. Haller, H. Lu, and W. J. Schaff, Phys. Status Solidi B **240**, 412 (2003).

[177] S. Yoshida, J. Appl. Phys. **81**, 7966 (1997).

[178] N. Grandjean and J. Massies, Appl. Phys. Lett. **72**, 1078 (1998).

[179] N. Grandjean and J. Massies, Appl. Phys. Lett. **71**, 1816 (1997).

[180] A. V. Blant, T. S. Cheng, C. T. Foxon, J. C. Bussey, S. V. Novikov, and V. V. Tret'yakov, MRS Proc. **449**, 465 (1996).

[181] R. Singh and T. Moustakas, MRS Proc. **395**, 163 (1995).

[182] D. Doppalapudi, S. N. Basu, K. F. Ludwig Jr., and T. D. Moustakas, J. Appl. Phys. **84**, 1389 (1998).

[183] T. Saito and Y. Arakawa, Phys. Rev. B **60**, 1701 (1999).

[184] M. Ferhat and F. Bechstedt, Phys. Rev. B **65**, 075213 (2002).

[185] P. Ruterana and F. Deniel, Mater. Sci. Eng. B **59**, 186 (1999).

[186] F. B. Naranjo, S. Fernandez, M. A. Sánchez-García, F. Calle, E. Calleja, A. Trampert, and K. H. Ploog, Mater. Sci. Eng. B **93**, 131 (2002).

[187] M. Kurouchi, T. Araki, H. Naoi, T. Yamaguchi, A. Suzuki, and Y. Nanishi, Phys. Status Solidi B **241**, 2843 (2004).

[188] X. Shen, T. Ide, M. Shimizu, and H. Okumura, J. Cryst. Growth **237-239**, 1148 (2002).

[189] Y. Okamoto, K. Takahashi, H. Nakamura, Y. Okada, and M. Kawabe, Phys. Status Solidi A **180**, 59 (2000).

[190] S. Chichibu, T. Azuhata, T. Sota, and S. Nakamura, Appl. Phys. Lett. **69**, 4188 (1996).

[191] H. Sakai, T. Koide, H. Suzuki, M. Yamaguchi, S. Yamasaki, M. Koike, H. Amano, and I. Akasaki, Jpn. J. Appl. Phys. **34**, L1429 (1995).

[192] P. Laukkanen, S. Lehkonen, P. Uusimaa, M. Pessa, A. Seppälä, T. Ahlgren, and E. Rauhala, J. Cryst. Growth **230**, 503 (2001).

[193] S. Nakamura, Mater. Sci. Eng. B **43**, 258 (1997).

[194] S. Nakamura, Microelectronics J. **25**, 651 (1994).

[195] S. Keller, U. K. Mishra, S. P. Denbaars, and W. Seifert, Jpn. J. Appl. Phys. **37**, L431 (1998).

[196] J. Heffernan, M. Kauer, S. E. Hooper, V. Bousquet, and K. Johnson, Phys. Status Solidi A **201**, 2688 (2004).

[197] X. Q. Shen, T. Ide, M. Shimizu, S. Hara, and H. Okumura, Jpn. J. Appl. Phys. **39**, L1270 (2000).

[198] X. Q. Shen, T. Ide, S. H. Cho, M. Shimizu, S. Hara, H. Okumura, S. Sonoda, and S. Shimizu, J. Cryst. Growth **218**, 155 (2000).

[199] X. Q. Shen, T. Ide, M. Shimizu, F. Sasaki, and H. Okumura, Phys. Status Solidi B **228**, 99 (2001).

[200] X. Q. Shen, T. Ide, S. H. Cho, M. Shimizu, S. Hara, H. Okumura, S. Sonoda, and S. Shimizu, Jpn. J. Appl. Phys. **39**, L16 (2000).

[201] E. S. Hellman, MRS Internet J. Nitride Semicond. Res. **3**, 11 (1998).

[202] M. Stutzmann, O. Ambacher, M. Eickhoff, U. Karrer, A. L. Pimenta, R. Neuberger, J. Schalwig, R. Dimitrov, P. J. Schuck, and R. D. Grober, Phys. Status Solidi B **228**, 505 (2001).

[203] P. Prystawko, M. Leszczyński, A. Śliwiński, H. Teisseyre, T. Suski, M. Boćkowski, S. Porowski, J. Domagała, C. Kirchner, A. Pelzmann, et al., J. Cryst. Growth **198-199**, 1061 (1999).

[204] R. W. Martin, P. G. Middleton, K. P. O'Donnell, and W. Van der Stricht, Appl. Phys. Lett. **74**, 263 (1999).

[205] C. G. Van De Walle, M. D. McCluskey, C. P. Master, L. T. Romano, and N. M. Johnson, Mater. Sci. Eng. B **59**, 274 (1999).

[206] I. Akasaki and H. Amano, Jpn. J. Appl. Phys. **36**, 5393 (1997).

[207] J. W. Matthews and A. E. Blakeslee, J. Cryst. Growth **27**, 118 (1974).

[208] A. Fischer, H. Kuhne, and H. Richter, Phys. Rev. Lett. **73**, 2712 (1994).

[209] K. P. O'Donnell, J. F. W. Mosselmans, R. W. Martin, S. Pereira, and M. E. White, J. Phys. Condens. Matter **13**, 6977 (2001).

[210] S. Pereira, M. R. Correia, T. Monteiro, E. Pereira, E. Alves, A. D. Sequeira, and N. Franco, Appl. Phys. Lett. **78**, 2137 (2001).

[211] S. Pereira, M. R. Correia, T. Monteiro, E. Pereira, M. Soares, and E. Alves, J. Cryst. Growth **230**, 448 (2001).

[212] M. E. Vickers, M. J. Kappers, T. M. Smeeton, E. J. Thrush, J. S. Barnard, and C. J. Humphreys, J. Appl. Phys. **94**, 1565 (2003).

[213] H.-C. Lin, C.-K. Shu, J. Ou, Y.-C. Pan, W.-K. Chen, W.-H. Chen, and M.-C. Lee, J. Cryst. Growth **189-190**, 57 (1998).

[214] W. V. der Stricht, I. Moerman, P. Demeester, J. Crawley, and E. Thrush, J. Cryst. Growth **170**, 344 (1997).

[215] S. Bedair, F. McIntosh, J. Roberts, E. Piner, K. Boutros, and N. El-Masry, J. Cryst. Growth **178**, 32 (1997).

[216] N. Grandjean and J. Massies, Mater. Sci. Eng. B **59**, 39 (1999).

[217] A. Sohmer, J. Off, H. Bolay, V. Härle, V. Syganow, J. S. Im, V. Wagner, F. Adler, A. Hangleiter, A. Dörnen, et al., MRS Internet J. Nitride Semicond. Res. **2**, 14 (1997).

[218] Y.-L. Lai, C.-P. Liu, and Z.-Q. Chen, Thin Solid Films **498**, 128 (2006).

[219] R. W. Martin, P. R. Edwards, R. Pecharroman-Gallego, C. Liu, C. J. Deatcher, I. M. Watson, and K. P. O'Donnell, J. Phys. D. Appl. Phys. **35**, 604 (2002).

[220] N. Grandjean, B. Damilano, and J. Massies, J. Phys. Condens. Matter **13**, 6945 (2001).

[221] B. Damilano, N. Grandjean, C. Pernot, and J. Massies, Jpn. J. Appl. Phys. **40**, L918 (2001).

[222] S. F. Chichibu, A. C. Abare, M. P. Mack, M. S. Minsky, T. Deguchi, D. Cohen, P. Kozodoy, S. B. Fleischer, S. Keller, J. S. Speck, et al., Mater. Sci. Eng. B **59**, 298 (1999).

[223] P. Lefebvre, T. Taliercio, S. Kalliakos, A. Morel, X. B. Zhang, M. Gallart, T. Bretagnon, B. Gil, N. Grandjean, B. Damilano, et al., Phys. Status Solidi B **228**, 65 (2001).

[224] J. Wagner, A. Ramakrishnan, D. Behr, M. Maier, N. Herres, M. Kunzer, H. Obloh, and K.-H. Bachem, MRS Internet J. Nitride Semicond. Res. **4S1**, G2.8 (1999).

[225] C. Wetzel, T. Takeuchi, S. Yamaguchi, H. Katoh, H. Amano, and I. Akasaki, Appl. Phys. Lett. **73**, 1994 (1998).

[226] M. D. McCluskey, C. G. V. de Walle, C. P. Master, L. T. Romano, and N. M. Johnson, Appl. Phys. Lett. **72**, 2725 (1998).

[227] T. Takeuchi, H. Takeuchi, S. Sota, H. Sakai, H. Amano, and I. Akasaki, Jpn. J. Appl. Phys. **36**, L177 (1997).

[228] C. A. Parker, J. C. Roberts, S. M. Bedair, M. J. Reed, S. X. Liu, N. A. El-Masry, and L. H. Robins, Appl. Phys. Lett. **75**, 2566 (1999).

[229] Y.-K. Kuo, W.-W. Lin, and J. Lin, Jpn. J. Appl. Phys. **40**, 3157 (2001).

[230] W. Shan, B. D. Little, J. J. Song, Z. C. Feng, M. Schurman, and R. A. Stall, Appl. Phys. Lett. **69**, 3315 (1996).

[231] J. Wagner, A. Ramakrishnan, D. Behr, H. Obloh, M. Kunzer, and K.-H. Bachem, Appl. Phys. Lett. **73**, 1715 (1998).

[232] S. Chichibu, T. Azuhata, T. Sota, and S. Nakamura, Appl. Phys. Lett. **70**, 2822 (1997).

[233] S. Srinivasan, R. Liu, F. Bertram, F. A. Ponce, S. Tanaka, H. Omiya, and Y. Nakagawa, Phys. Status Solidi B **228**, 41 (2001).

[234] M. Schuster, P. O. Gervais, B. Jobst, W. Hosler, R. Averbeck, H. Riechert, A. Iberl, and R. Stommer, J. Phys. D. Appl. Phys. **32**, A56 (1999).

[235] T. L. Tansley and C. P. Foley, J. Appl. Phys. **59**, 3241 (1986).

[236] J. R. Jinschek, R. Erni, N. F. Gardner, A. Y. Kim, and C. Kisielowski, Solid State Commun. **137**, 230 (2006).

[237] K. P. O'Donnell, R. W. Martin, and P. G. Middleton, Phys. Rev. Lett. **82**, 237 (1999).

[238] C. Kisielowski, Z. Liliental-Weber, and S. Nakamura, Jpn. J. Appl. Phys. **36**, 6932 (1997).

[239] P. G. Eliseev, P. Perlin, J. Lee, and M. Osiński, Appl. Phys. Lett. **71**, 569 (1997).

[240] Y. Narukawa, Y. Kawakami, S. Fujita, S. Fujita, and S. Nakamura, Phys. Rev. B **55**, R1938 (1997).

[241] P. Perlin, C. Kisielowski, V. Iota, B. A. Weinstein, L. Mattos, N. A. Shapiro, J. Kruger, E. R. Weber, and J. Yang, Appl. Phys. Lett. **73**, 2778 (1998).

[242] A. Hangleiter, J. S. Im, H. Kollmer, S. Heppel, J. Off, and F. Scholz, MRS Internet J. Nitride Semicond. Res. **3**, 15 (1998).

[243] T. Takeuchi, S. Sota, M. Katsuragawa, M. Komori, H. Takeuchi, H. Amano, and I. Akasaki, Jpn. J. Appl. Phys. **36**, L382 (1997).

[244] Y. Kawakami, K. Omae, A. Kaneta, K. Okamoto, Y. Narukawa, T. Mukai, and S. Fujita, J. Phys. Condens. Matter **13**, 6993 (2001).

[245] H. J. Chang, C. H. Chen, Y. F. Chen, T. Y. Lin, L. C. Chen, K. H. Chen, and Z. H. Lan, Appl. Phys. Lett. **86**, 021911 (2005).

[246] M. Rao, D. Kim, and S. Mahajan, Appl. Phys. Lett. **85**, 1961 (2004).

[247] Z. Jing and Z. Guo-Yi, Chinese Phys. Lett. **19**, 707 (2002).

[248] A. Satake, Y. Masumoto, T. Miyajima, T. Asatsuma, F. Nakamura, and M. Ikeda, Phys. Rev. B **57**, R2041 (1998).

[249] F. Bernardini, V. Fiorentini, and D. Vanderbilt, Phys. Rev. B **56**, R10024 (1997).

[250] M. Leroux, N. Grandjean, M. Laügt, J. Massies, B. Gil, P. Lefebvre, and P. Bigenwald, Phys. Rev. B **58**, R13371 (1998).

[251] J. Seo Im, H. Kollmer, J. Off, A. Sohmer, F. Scholz, and A. Hangleiter, Phys. Rev. B **57**, R9435 (1998).

[252] B. Damilano, N. Grandjean, J. Massies, L. Siozade, and J. Leymarie, Appl. Phys. Lett. **77**, 1268 (2000).

[253] N. A. Shapiro, P. Perlin, C. Kisielowski, L. S. Mattos, J. W. Yang, and E. R. Weber, MRS Internet J. Nitride Semicond. Res. **5**, 1 (2000).

[254] T. J. Ochalski, B. Gil, P. Bigenwald, M. Bugajski, A. Wojcik, P. Lefebvre, T. Taliercio, N. Grandjean, and J. Massies, Phys. Status Solidi B **228**, 111 (2001).

[255] B. Monemar, J. P. Bergman, J. Dalfors, G. Pozina, B. Sernelius, P. Holtz, H. Amano, and I. Akasaki, MRS Internet J. Nitride Semicond. Res. **4**, 16 (1999).

[256] B. Monemar, Mater. Sci. Eng. B **59**, 122 (1999).

[257] S. De, A. Layek, A. Raja, A. Kadir, M. R. Gokhale, A. Bhattacharya, S. Dhar, and A. Chowdhury, Adv. Funct. Mater. **21**, 3828 (2011).

[258] X. Li, D. G. Zhao, J. Yang, D. S. Jiang, Z. S. Liu, P. Chen, J. J. Zhu, W. Liu, X. G. He, X. J. Li, et al., Superlattices Microstruct. **97**, 186 (2016).

[259] A. Thiaville and J. Miltat, Science **284**, 1939 (1999).

[260] A. P. Alivisatos, P. F. Barbara, A. W. Castleman, J. Chang, D. A. Dixon, M. L. Klein, G. L. McLendon, J. S. Miller, M. A. Ratner, P. J. Rossky, et al., Adv. Mater. **10**, 1297 (1998).

[261] P. G. A. Ozin, Adv. Mater. **4**, 612 (1992).

[262] K. Ziemelis, Nature **406**, 1021 (2000).

[263] C. A. Ross, Annu. Rev. Mater. Res. **31**, 203 (2001).

[264] M. G. Bawendi, M. L. Steigerwald, and L. E. Brus, Annu. Rev. Phys. Chem. **41**, 477 (1990).

[265] A. P. Alivisatos, Science **271**, 933 (1996).

[266] C. B. Murray, C. R. Kagan, and M. G. Bawendi, Annu. Rev. Mater. Sci. **30**, 545 (2000).

[267] J. M. KRANS, J. M. V. RUITENBEEK, V. V. FISUN, I. K. YANSON, and L. J. D. JONGH, Nature **375**, 767 (1995).

[268] B. L. Al'tshuler and P. A. Lee, Phys. Today **41**, 36 (1988).

[269] K. K. Likharev, IBM J. Res. Dev. **32**, 144 (1988).

[270] G. Markovich, C. P. Collier, S. E. Henrichs, F. Remacle, R. D. Levine, and J. R. Heath, Acc. Chem. Res. **32**, 415 (1999).

[271] P. Alivisatos, Pure Appl. Chem. **72**, 3 (2009).

[272] A. Zunger, MRS Bull. **23**, 15 (1998).

[273] M. Nirmal and L. Brus, Acc. Chem. Res. **32**, 407 (1999).

[274] V. I. Klimov, A. A. Mikhailovsky, S. Xu, A. Malko, J. A. Hollingsworth, C. A. Leatherdale, H.-J. Eisler, and M. G. Bawendi, Science **290**, 314 (2000).

[275] D. L. Klein, R. Roth, A. K. L. Lim, A. P. Alivisatos, and P. L. McEuen, Nature **389**, 699 (1997).

[276] H. Pettersson, L. Baath, N. Carlsson, W. Seifert, and L. Samuelson, Appl. Phys. Lett. **79**, 78 (2001).

[277] A. N. Shipway, E. Katz, and I. Willner, ChemPhysChem **1**, 18 (2000).

[278] J. Phillips, J. Appl. Phys. **91**, 4590 (2002).

[279] S. Coe, W.-K. Woo, M. Bawendi, and V. Bulović, Nature **420**, 800 (2002).

[280] Z. L. Wang, Adv. Mater. **12**, 1295 (2000).

[281] J. Hu, T. W. Odom, and C. M. Lieber, Acc. Chem. Res. **32**, 435 (1999).

[282] C. Thelander, P. Agarwal, S. Brongersma, J. Eymery, L. F. Feiner, A. Forchel, M. Scheffler, W. Riess, B. J. Ohlsson, U. Gosele, et al., Mater. Today **9**, 28 (2006).

[283] Y. Li, F. Qian, J. Xiang, and C. M. Lieber, Mater. Today **9**, 18 (2006).

[284] R. Agarwal and C. M. Lieber, Appl. Phys. A Mater. Sci. Process. **85**, 209 (2006).

[285] T. Stoica, R. J. Meijers, R. Calarco, T. Richter, E. Sutler, and H. Lüth, Nano Lett. **6**, 1541 (2006).

[286] T. Richter, C. Blömers, H. Lüth, R. Calarco, M. Indlekofer, M. Marso, and T. Schäpers, Nano Lett. **8**, 2834 (2008).

[287] E. Calleja, J. Ristić, S. Fernández-Garrido, L. Cerutti, M. A. Sanchez-Garcia, J. Grandal, A. Trampert, U. Jahn, G. Sanchez, A. Griol, et al., Phys. Status Solidi B **244**, 2816 (2007).

[288] C. Denker, J. Malindretos, F. Werner, F. Limbach, H. Schuhmann, T. Niermann, M. Seibt, and A. Rizzi, Phys. Status Solidi C **5**, 1706 (2008).

[289] E. Calleja, J. Grandal, M. A. Sánchez-García, M. Niebelschütz, V. Cimalla, and O. Ambacher, Appl. Phys. Lett. **90**, 262110 (2007).

[290] K. R. Wang, S. J. Lin, L. W. Tu, M. Chen, Q. Y. Chen, T. H. Chen, M. L. Chen, H. W. Seo, N. H. Tai, S. C. Chang, et al., Appl. Phys. Lett. **92**, 123105 (2008).

[291] Q. Wang, J. Bai, Y. P. Gong, and T. Wang, J. Phys. D. Appl. Phys. **44**, 395102 (2011).

[292] J. Bai, Q. Wang, and T. Wang, J. Appl. Phys. **111**, 113103 (2012).

[293] Y. Kawakami, S. Suzuki, A. Kaneta, M. Funato, A. Kikuchi, and K. Kishino, Appl. Phys. Lett. **89**, 163124 (2006).

[294] Y. Kawakami, A. Kaneta, L. Su, Y. Zhu, K. Okamoto, M. Funato, A. Kikuchi, and K. Kishino, J. Appl. Phys. **107**, 023522 (2010).

[295] B. Jiang, C. Zhang, X. Wang, F. Xue, M. J. Park, J. S. Kwak, and M. Xiao, Opt. Express **20**, 13478 (2012).

[296] C. H. Chiu, T. C. Lu, H. W. Huang, C. F. Lai, C. C. Kao, J. T. Chu, C. C. Yu, H. C. Kuo, S. C. Wang, C. F. Lin, et al., Nanotechnology **18**, 445201 (2007).

[297] A. P. Vajpeyi, A. O. Ajagunna, K. Tsagaraki, M. Androulidaki, and A. Georgakilas, Nanotechnology **20**, 325605 (2009).

[298] T. Kehagias, Phys. E **42**, 2197 (2010).

[299] T. Tabata, J. Paek, Y. Honda, M. Yamaguchi, and H. Amano, Phys. Status Solidi C **9**, 646 (2012).

[300] K. Wu, T. Han, K. Shen, B. Liu, T. Peng, Y. Pan, H. Sun, and C. Liu, J. Nanosci. Nanotechnol. **10**, 8139 (2010).

[301] Y. H. Kim, J. Y. Lee, S.-H. Lee, J.-E. Oh, H. S. Lee, and Y. Huh, Chem. Phys. Lett. **412**, 454 (2005).

[302] D. Zubia and S. D. Hersee, J. Appl. Phys. **85**, 6492 (1999).

[303] J. Kuyyalil, M. Tangi, and S. M. Shivaprasad, J. Appl. Phys. **109**, 093513 (2011).

[304] J. Kuyyalil, M. Tangi, and S. M. Shivaprasad, J. Appl. Phys. **112**, 083521 (2012).

[305] J. Kuyyalil, M. Tangi, and S. M. Shivaprasad, Mater. Res. Bull. **48**, 256 (2013).

[306] M. Tangi, J. Kuyyalil, and S. M. Shivaprasad, J. Appl. Phys. **112**, 073510 (2012).

[307] M. Tangi, J. Kuyyalil, and S. M. Shivaprasad, J. Appl. Phys. **114**, 153501 (2013).

[308] F. Mao, J. Yang, W. Austin, and J. Heck, Vacuum **37**, 335 (1987).

[309] W. Braun, *Applied RHEED: Reflection High-Energy Electron Diffraction During Crystal Growth* (Springer Science & Business Media, 1999).

[310] A. Ichimiya and P. I. Cohen, *Reflection High-Energy Electron Diffraction* (Cambridge University Press, 2004).

[311] G.-C. Wang and T.-M. Lu, *RHEED Transmission Mode and Pole Figures: Thin Film and Nanostructure Texture Analysis* (Springer Science & Business Media, 2013).

[312] L. Reimer, *Scanning Electron Microscopy: Physics of Image Formation and Microanalysis* (Springer Science & Business Media, 1998).

[313] B. D. Cullity and S. R. Stock, *Elements of X-ray Diffraction* (Prentice Hall, 2001).

[314] D. Bowen and B. K. Tanner, *High Resolution X-Ray Diffractometry And Topography* (CRC Press, 2005).

[315] U. Pietsch, V. Holy, and T. Baumbach, *High-Resolution X-Ray Scattering: From Thin Films to Lateral Nanostructures* (Springer Science & Business Media, 2013).

[316] O. Stenzel, *The Physics of Thin Film Optical Spectra: An Introduction* (Springer International Publishing, 2015).

[317] J. Tauc, R. Grigorovici, and A. Vancu, Phys. Status Solidi B **15**, 627 (1966).

[318] J. Tauc, Mater. Res. Bull. **3**, 37 (1968).

[319] S. Perkowitz, *Optical Characterization of Semiconductors: Infrared, Raman, and Photoluminescence Spectroscopy* (Elsevier, 2012).

[320] C. S. Kumar, *UV-VIS and Photoluminescence Spectroscopy for Nanomaterials Characterization* (Springer Science & Business Media, 2013).

[321] L. Ozawa, *Cathodoluminescence and Photoluminescence: Theories and Practical Applications* (CRC Press, 2007).

[322] D. Briggs and M. P. Seah, *Practical Surface Analysis, Auger and X-ray Photoelectron Spectroscopy* (Wiley, 1990).

[323] P. Woodruff, *Modern Techniques of Surface Science* (Cambridge University Press, 2016).

[324] M. Prutton, *Introduction to surface physics* (Clarendon Press, 1994).

[325] S. Hüfner, *Photoelectron Spectroscopy: Principles and Applications* (Springer Science & Business Media, 2013).

[326] J. F. Watts and J. Wolstenholme, *An Introduction to Surface Analysis by XPS and AES* (Wiley, 2003).

[327] C. Chien, *The Hall Effect and Its Applications* (Springer US, 2013).

[328] L. J. van der Pauw, Philips Res. Reports **13**, 1 (1958).

[329] A. Wakahara, T. Tokuda, X.-Z. Dang, S. Noda, and A. Sasaki, Appl. Phys. Lett. **71**, 906 (1997).

[330] M. D. McCluskey, L. T. Romano, B. S. Krusor, D. P. Bour, N. M. Johnson, and S. Brennan, Appl. Phys. Lett. **72**, 1730 (1998).

[331] H. C. Yang, P. F. Kuo, T. Y. Lin, Y. F. Chen, K. H. Chen, L. C. Chen, and J.-I. Chyi, Appl. Phys. Lett. **76**, 3712 (2000).

[332] W. Shan, W. Walukiewicz, E. E. Haller, B. D. Little, J. J. Song, M. D. McCluskey, N. M. Johnson, Z. C. Feng, M. Schurman, and R. A. Stall, J. Appl. Phys. **84**, 4452 (1998).

[333] J. Wu, W. Walukiewicz, K. M. Yu, J. W. Ager III, E. E. Haller, H. Lu, and W. J. Schaff, Appl. Phys. Lett. **80**, 4741 (2002).

[334] F. B. Naranjo, M. A. Sanchez-Garca, F. Calle, E. Calleja, B. Jenichen, and K. H. Ploog, Appl. Phys. Lett. **80**, 231 (2002).

[335] P. Waltereit, O. Brandt, K. H. Ploog, M. A. Tagliente, and L. Tapfer, Phys. Status Solidi B **228**, 49 (2001).

[336] M. Hori, K. Kano, T. Yamaguchi, Y. Satio, T. Araki, Y. Nanishi, N. Teraguchi, and A. Suzuki, Phys. Status Solidi B **234**, 750 (2002).

[337] H. Komaki, T. Nakamura, R. Katayama, K. Onabe, M. Ozeki, and T. Ikari, J. Cryst. Growth **301**, 473 (2007).

[338] H. Komaki, R. Katayama, K. Onabe, M. Ozeki, and T. Ikari, J. Cryst. Growth **305**, 12 (2007).

[339] H. Naoi, M. Kurouchi, S. Takado, D. Muto, T. Araki, and Y. Nanishi, Phys. Status Solidi A **202**, 2642 (2005).

[340] R. S. Wagner and W. C. Ellis, Appl. Phys. Lett. **4**, 89 (1964).

[341] Y. K. Mishra, S. Kaps, A. Schuchardt, I. Paulowicz, X. Jin, D. Gedamu, S. Freitag, M. Claus, S. Wille, A. Kovalev, et al., Part. Part. Syst. Charact. **30**, 775 (2013).

[342] T. Reimer, I. Paulowicz, R. Röder, S. Kaps, O. Lupan, S. Chemnitz, W. Benecke, C. Ronning, R. Adelung, and Y. K. Mishra, ACS Appl. Mater. Interfaces **6**, 7806 (2014).

[343] K. Ostrikov, E. C. Neyts, and M. Meyyappan, Adv. Phys. **62**, 113 (2013).

[344] M. Kesaria, S. Shetty, and S. M. Shivaprasad, Cryst. Growth Des. **11**, 4900 (2011).

[345] K. Bertness, A. Roshko, N. Sanford, J. Barker, and A. Davydov, J. Cryst. Growth **287**, 522 (2006).

[346] J. Ristić, E. Calleja, S. Fernández-Garrido, L. Cerutti, A. Trampert, U. Jahn, and K. H. Ploog, J. Cryst. Growth **310**, 4035 (2008).

[347] C. Y. Nam, D. Tham, and J. E. Fischer, Appl. Phys. Lett. **85**, 5676 (2004).

[348] T. Stoica, R. Meijers, R. Calarco, T. Richter, and H. Lüth, J. Cryst. Growth **290**, 241 (2006).

[349] R. K. Debnath, R. Meijers, T. Richter, T. Stoica, R. Calarco, and H. Luth, Appl. Phys. Lett. **90**, 123117 (2007).

[350] C.-C. Hong, H. Ahn, C.-Y. Wu, and S. Gwo, Opt. Express **17**, 17227 (2009).

[351] C. Caetano, L. K. Teles, M. Marques, A. Dal Pino, and L. G. Ferreira, Phys. Rev. B **74**, 045215 (2006).

[352] M. D. McCluskey, C. G. Van de Walle, L. T. Romano, B. S. Krusor, and N. M. Johnson, J. Appl. Phys. **93**, 4340 (2003).

[353] E. D. Le Boulbar, P. R. Edwards, S. H. Vajargah, I. Griffiths, I. Gîrgel, P.-M. Coulon, D. Cherns, R. W. Martin, C. J. Humphreys, C. R. Bowen, et al., Cryst. Growth Des. **16**, 1907 (2016).

[354] Y. Hou, J. Bai, R. Smith, and T. Wang, Nanotechnology **27**, 205205 (2016).

[355] S. Nozaki, S. Yoshida, K. Yamanaka, O. Imafuji, S. Takigawa, T. Katayama, and T. Tanaka, Jpn. J. Appl. Phys. **55**, 04EH05 (2016).

[356] T. Kuykendall, P. Ulrich, S. Aloni, and P. Yang, Nat. Mater. **6**, 951 (2007).

[357] D. Fuhrmann, C. Netzel, U. Rossow, A. Hangleiter, G. Ade, and P. Hinze, Appl. Phys. Lett. **88**, 071105 (2006).

[358] J. C. Brooksby, J. Mei, and F. A. Ponce, Appl. Phys. Lett. **90**, 231901 (2007).

[359] Y.-L. Lai, C.-P. Liu, Y.-H. Lin, R.-M. Lin, D.-Y. Lyu, Z.-X. Peng, and T.-Y. Lin, Appl. Phys. Lett. **89**, 151906 (2006).

[360] P. Ren, N. Zhang, B. Xue, Z. Liu, J. Wang, and J. Li, J. Phys. D. Appl. Phys. **49**, 175101 (2016).

[361] S.-C. Tsai, H.-C. Fang, Y.-L. Lai, C.-H. Lu, and C.-P. Liu, J. Alloys Compd. **669**, 156 (2016).

[362] Z. Lin, H. Wang, Y. Lin, M. Yang, W. Wang, and G. Li, J. Phys. D. Appl. Phys. **49**, 115112 (2016).

[363] W. Liu, D. Zhao, D. Jiang, P. Chen, Z. Liu, J. Zhu, X. Li, F. Liang, J. Liu, L. Zhang, et al., J. Phys. D. Appl. Phys. **49**, 145104 (2016).

[364] C.-L. Tsai, J. Lumin. **174**, 36 (2016).

[365] Ž. Gačević, N. Vukmirović, N. García-Lepetit, A. Torres-Pardo, M. Müller, S. Metzner, S. Albert, A. Bengoechea-Encabo, F. Bertram, P. Veit, et al., Phys. Rev. B **93**, 125436 (2016).

[366] X. Zhang, H. Lourenço-Martins, S. Meuret, M. Kociak, B. Haas, J.-L. Rouvière, P.-H. Jouneau, C. Bougerol, T. Auzelle, D. Jalabert, et al., Nanotechnology **27**, 195704 (2016).

[367] J. M. Phillips, M. E. Coltrin, M. H. Crawford, A. J. Fischer, M. R. Krames, R. Mueller-Mach, G. O. Mueller, Y. Ohno, L. E. Rohwer, J. A. Simmons, et al., Laser Photonics Rev. **1**, 307 (2007).

[368] C. Tessarek, S. Figge, T. Aschenbrenner, S. Bley, A. Rosenauer, M. Seyfried, J. Kalden, K. Sebald, J. Gutowski, and D. Hommel, Phys. Rev. B **83**, 115316 (2011).

[369] R. A. Oliver, S. E. Bennett, T. Zhu, D. J. Beesley, M. J. Kappers, D. W. Saxey, A. Cerezo, and C. J. Humphreys, J. Phys. D. Appl. Phys. **43**, 354003 (2010).

[370] T. Miyoshi, S. Masui, T. Okada, T. Yanamoto, T. Kozaki, S.-i. Nagahama, and T. Mukai, Appl. Phys. Express **2**, 062201 (2009).

[371] Y. Yoshizumi, M. Adachi, Y. Enya, T. Kyono, S. Tokuyama, T. Sumitomo, K. Akita, T. Ikegami, M. Ueno, K. Katayama, et al., Appl. Phys. Express **2**, 092101 (2009).

[372] C. Skierbiszewski, M. Siekacz, P. Perlin, A. Feduniewicz-Żmuda, G. Cywiński, I. Grzegory, M. Leszczyński, Z. Wasilewski, and S. Porowski, J. Cryst. Growth **305**, 346 (2007).

[373] C. Skierbiszewski, Z. Wasilewski, I. Grzegory, and S. Porowski, J. Cryst. Growth **311**, 1632 (2009).

[374] M. Siekacz, A. Feduniewicz-Żmuda, G. Cywiński, M. Kryśko, I. Grzegory, S. Krukowski, K. Waldrip, W. Jantsch, Z. Wasilewski, S. Porowski, et al., J. Cryst. Growth **310**, 3983 (2008).

[375] R. Averbeck and H. Riechert, Phys. Status Solidi A **176**, 301 (1999).

[376] A. De, K. K. Nagaraja, M. Tangi, and S. M. Shivaprasad, Mater. Res. Express **1**, 035019 (2014).

[377] Y.-L. Chang, F. Li, and Z. Mi, J. Vac. Sci. Technol. B **28**, C3B7 (2010).

[378] W. Yang, S. A. McPherson, Z. Mao, S. McKernan, and C. B. Carter, J. Cryst. Growth **204**, 270 (1999).

[379] K. Hiramatsu, K. Nishiyama, A. Motogaito, H. Miyake, Y. Iyechika, and T. Maeda, Phys. Status Solidi A **176**, 535 (1999).

[380] K. Bertness, A. Roshko, L. Mansfield, T. Harvey, and N. Sanford, J. Cryst. Growth **310**, 3154 (2008).

[381] M. Ebaid, J.-H. Kang, Y.-S. Yoo, S.-H. Lim, Y.-H. Cho, and S.-W. Ryu, Sci. Rep. **5**, 17003 (2015).

[382] Q. Wang, C. Zhu, Y. Zhou, X. Wang, B. Liu, X. Wang, Y. Lv, Z. Feng, X. Xu, and Z. Ji, Superlattices Microstruct. **88**, 323 (2015).

[383] Y.-L. Lai, C.-P. Liu, Y.-H. Lin, T.-H. Hsueh, R.-M. Lin, D.-Y. Lyu, Z.-X. Peng, and T.-Y. Lin, Nanotechnology **17**, 3734 (2006).

[384] F. Urbach, Phys. Rev. **92**, 1324 (1953).

[385] D. Watson-Parris, M. J. Godfrey, P. Dawson, R. A. Oliver, M. J. Galtrey, M. J. Kappers, and C. J. Humphreys, Phys. Rev. B **83**, 115321 (2011).

[386] B. W. Jacobs, M. A. Crimp, K. McElroy, and V. M. Ayres, Nano Lett. **8**, 4353 (2008).

[387] S. Jin, M. J. Bierman, and S. A. Morin, J. Phys. Chem. Lett. **1**, 1472 (2010).

[388] D. Cherns, L. Meshi, I. Griffiths, S. Khongphetsak, S. V. Novikov, N. R. S. Farley, R. P. Campion, and C. T. Foxon, Appl. Phys. Lett. **93**, 111911 (2008).

[389] J. Grandal, J. Pereiro, A. Bengoechea-Encabo, S. Fernandez-Garrido, M. A. Sanchez-Garcia, E. Munoz, E. Calleja, E. Luna, and A. Trampert, Appl. Phys. Lett. **98**, 061901 (2011).

[390] J. Wu, W. Walukiewicz, K. M. Yu, J. W. Ager III, E. E. Haller, H. Lu, and W. J. Schaff, Phys. Rev. B **66**, 201403 (2002).

[391] B. E. Foutz, S. K. O'Leary, M. S. Shur, and L. F. Eastman, J. Appl. Phys. **85**, 7727 (1999).

[392] L. F. J. Piper, T. D. Veal, C. F. McConville, H. Lu, and W. J. Schaff, Appl. Phys. Lett. **88**, 252109 (2006).

[393] K. S. A. Butcher, A. J. Fernandes, P. P.-T. Chen, M. Wintrebert-Fouquet, H. Timmers, S. K. Shrestha, H. Hirshy, R. M. Perks, and B. F. Usher, J. Appl. Phys. **101**, 123702 (2007).

[394] G. Pettinari, F. Masia, M. Capizzi, A. Polimeni, M. Losurdo, G. Bruno, T. H. Kim, S. Choi, A. Brown, V. Lebedev, et al., Phys. Rev. B **77**, 125207 (2008).

[395] J. B. MacChesney, P. M. Bridenbaugh, and P. B. O'Connor, Mater. Res. Bull. **5**, 783 (1970).

[396] B. R. Nag, Phys. Status Solidi B **237**, R1 (2003).

[397] C. L. Wu, C. H. Shen, H. Y. Chen, S. J. Tsai, H. W. Lin, H. M. Lee, S. Gwo, T. F. Chuang, H. S. Chang, and T. M. Hsu, J. Cryst. Growth **288**, 247 (2006).

[398] H. Lu, W. J. Schaff, J. Hwang, H. Wu, W. Yeo, A. Pharkya, and L. F. Eastman, Appl. Phys. Lett. **77**, 2548 (2000).

[399] J. Grandal, M. A. Sánchez-García, E. Calleja, E. Luna, and A. Trampert, Appl. Phys. Lett. **91**, 021902 (2007).

[400] P. Kumar, J. Kuyyalil, and S. M. Shivaprasad, Appl. Phys. Lett. **97**, 221913 (2010).

[401] K. Jithesh, Govind, U. V. Waghmare, and S. M. Shivaprasad, Appl. Surf. Sci. **256**, 348 (2009).

[402] S. J. Pearton, C. R. Abernathy, F. Ren, and J. R. Lothian, J. Appl. Phys. **76**, 1210 (1994).

[403] S. R. Lee, A. M. West, A. A. Allerman, K. E. Waldrip, D. M. Follstaedt, P. P. Provencio, D. D. Koleske, and C. R. Abernathy, Appl. Phys. Lett. **86**, 241904 (2005).

[404] X. Wang, S. Liu, N. Ma, L. Feng, G. Chen, F. Xu, N. Tang, S. Huang, K. J. Chen, S. Zhou, et al., Appl. Phys. Express **5**, 015502 (2012).

[405] V. M. Naik, R. Naik, D. B. Haddad, J. S. Thakur, G. W. Auner, H. Lu, and W. J. Schaff, Appl. Phys. Lett. **86**, 201913 (2005).

[406] T. D. Veal, P. D. C. King, P. H. Jefferson, L. F. J. Piper, C. F. McConville, H. Lu, W. J. Schaff, P. A. Anderson, S. M. Durbin, D. Muto, et al., Phys. Rev. B **76**, 075313 (2007).

[407] T. V. Shubina, S. V. Ivanov, V. N. Jmerik, D. D. Solnyshkov, V. A. Vekshin, P. S. Kop'ev, A. Vasson, J. Leymarie, A. Kavokin, H. Amano, et al., Phys. Rev. Lett. **92**, 117407 (2004).

[408] W. W. Chow, H. Amano, T. Takeuchi, and J. Han, Appl. Phys. Lett. **75**, 244 (1999).

[409] S. Mahajan, Scr. Mater. **75**, 1 (2014).

[410] A. Yamamoto, A. Mihara, D. Hironaga, K. Sugita, A. G. Bhuiyan, A. Hashimoto, N. Shigekawa, and N. Watanabe, Phys. Status Solidi C **10**, 437 (2013).

[411] A. G. Bhuiyan, A. Mihara, T. Esaki, K. Sugita, A. Hashimoto, A. Yamamoto, N. Watanabe, H. Yokoyama, and N. Shigekawa, Phys. Status Solidi C **9**, 670 (2012).

[412] B.-T. Tran, E.-Y. Chang, K.-L. Lin, Y.-Y. Wong, K. C. Sahoo, H.-Y. Lin, M.-C. Huang, H.-Q. Nguyen, C.-T. Lee, and H.-D. Trinh, Appl. Phys. Express **4**, 115501 (2011).

[413] A. Yamamoto, M. T. Hasan, A. Mihara, N. Narita, N. Shigekawa, and M. Kuzuhara, Appl. Phys. Express **7**, 035502 (2014).

[414] H.-M. Kim, W. Lee, T. Kang, K. Chung, C. Yoon, and C. Kim, Chem. Phys. Lett. **380**, 181 (2003).

[415] M. Horie, K. Sugita, A. Hashimoto, and A. Yamamoto, Sol. Energy Mater. Sol. Cells **93**, 1013 (2009).

[416] J. Hedman and N. Martensson, Phys. Scr. **22**, 176 (1980).

[417] P. Kumar, M. Tuteja, M. Kesaria, U. V. Waghmare, and S. M. Shivaprasad, Appl. Phys. Lett. **101**, 131605 (2012).

[418] Y. E. Romanyuk, D. Kreier, Y. Cui, K. M. Yu, J. W. Ager III, and S. R. Leone, Thin Solid Films **517**, 6512 (2009).

[419] S. V. Ivanov, V. N. Jmerik, T. V. Shubina, S. B. Listoshin, A. M. Mizerov, A. A. Sitnikova, M.-H. Kim, M. Koike, B.-J. Kim, and P. S. Kop'ev, J. Cryst. Growth **301**, 465 (2007).

[420] V. M. Polyakov and F. Schwierz, Appl. Phys. Lett. **88**, 032101 (2006).

[421] J. Kamimura, K. Kishino, and A. Kikuchi, Appl. Phys. Lett. **97**, 141913 (2010).

[422] S. Li and A. Waag, J. Appl. Phys. **111**, 071101 (2012).

[423] K. Tomioka, M. Yoshimura, and T. Fukui, Nature **488**, 189 (2012).

[424] N. J. Ku, J. H. Huang, C. H. Wang, H. C. Fang, and C. P. Liu, Nano Lett. **12**, 562 (2012).

[425] F. Qian, Y. Li, S. Gradec, D. Wang, C. J. Barrelet, and C. M. Lieber, Nano Lett. **4**, 1975 (2004).

[426] S. K. Lim, M. J. Tambe, M. M. Brewster, and S. Gradečak, Nano Lett. **8**, 1386 (2008).

[427] Z. X. Yan and A. G. Milnes, J. Electrochem. Soc. **129**, 1353 (1982).

[428] S. H. Oh, K. Van Benthem, S. I. Molina, A. Y. Borisevich, W. Luo, P. Werner, N. D. Zakharov, D. Kumar, S. T. Pantelides, and S. J. Pennycook, Nano Lett. **8**, 1016 (2008).

[429] J. Noborisaka, J. Motohisa, and T. Fukui, Appl. Phys. Lett. **86**, 213102 (2005).

[430] J. Park, P. A. Grudowski, C. J. Eiting, and R. D. Dupuis, Appl. Phys. Lett. **73**, 333 (1998).

[431] K. Tomioka, K. Ikejiri, T. Tanaka, J. Motohisa, S. Hara, K. Hiruma, and T. Fukui, J. Mater. Res. **26**, 2127 (2011).

[432] D. C. Look, H. Lu, W. J. Schaff, J. Jasinski, and Z. Liliental-Weber, Appl. Phys. Lett. **80**, 258 (2002).

[433] A. A. Klochikhin, V. Y. Davydov, V. V. Emtsev, A. V. Sakharov, V. A. Kapitonov, B. A. Andreev, H. Lu, and W. J. Schaff, Phys. Rev. B **71**, 195207 (2005).

[434] K. Wang, T. Araki, M. Takeuchi, E. Yoon, and Y. Nanishi, Appl. Phys. Lett. **104**, 032108 (2014).

[435] N. Miller, E. E. Haller, G. Koblmuller, C. Gallinat, J. S. Speck, W. J. Schaff, M. E. Hawkridge, K. M. Yu, and J. W. Ager III, Phys. Rev. B **84**, 075315 (2011).

[436] E. Dimakis, J. Z. Domagala, A. Delimitis, P. Komninou, A. Adikimenakis, E. Iliopoulos, and A. Georgakilas, Superlattices Microstruct. **40**, 246 (2006).

[437] S. Zhao, H. P. T. Nguyen, M. G. Kibria, and Z. Mi, Prog. Quantum Electron. **44**, 14 (2015).

[438] M. Kesaria and S. M. Shivaprasad, Appl. Phys. Lett. **99**, 143105 (2011).

[439] H. P. Bhasker, S. Dhar, A. Sain, M. Kesaria, and S. M. Shivaprasad, Appl. Phys. Lett. **101**, 132109 (2012).

[440] H. P. Bhasker, V. Thakur, S. M. Shivaprasad, and S. Dhar, Solid State Commun. **220**, 72 (2015).

[441] V. Thakur, M. Kesaria, and S. M. Shivaprasad, Solid State Commun. **171**, 8 (2013).

[442] V. Thakur and S. M. Shivaprasad, Appl. Surf. Sci. **327**, 389 (2015).

[443] H. P. Bhasker, V. Thakur, S. M. Shivaprasad, and S. Dhar, J. Phys. D. Appl. Phys. **48**, 255302 (2015).

[444] S. Sharvani, K. Upadhayaya, G. Kumari, C. Narayana, and S. M. Shivaprasad, Nanotechnology **26**, 465701 (2015).

[445] B. Fultz and J. M. Howe, *Transmission Electron Microscopy and Diffractometry of Materials* (Springer, Berlin, Heidelberg, New York, 2008), 3rd ed.

[446] V. Darakchieva, M. Y. Xie, N. Franco, F. Giuliani, B. Nunes, E. Alves, C. L. Hsiao, L. C. Chen, T. Yamaguchi, Y. Takagi, et al., J. Appl. Phys. **108**, 073529 (2010).

[447] B. J. Ohlsson, M. T. Bjork, M. H. Magnusson, K. Deppert, L. Samuelson, and L. R. Wallenberg, Appl. Phys. Lett. **79**, 3335 (2001).

[448] A. Aliano, A. Catellani, and G. Cicero, Appl. Phys. Lett. **99**, 193106 (2011).

[449] A. Rose, Phys. Rev. **97**, 1538 (1955).

[450] A. A. Talin, F. Léonard, B. S. Swartzentruber, X. Wang, and S. D. Hersee, Phys. Rev. Lett. **101**, 076802 (2008).

[451] N. F. Mott and R. W. Gurney, *Electronic Processes in Ionice Crystals* (Oxford University Press, New York, 1940).

[452] A. A. Talin, B. S. Swartzentruber, F. Leonard, X. Wang, and S. D. Hersee, J. Vac. Sci. Technol. B **27**, 2040 (2009).

[453] S. Zhao, O. Salehzadeh, S. Alagha, K. L. Kavanagh, S. P. Watkins, and Z. Mi, Appl. Phys. Lett. **102**, 073102 (2013).

[454] S. Zhao, S. Fathololoumi, K. H. Bevan, D. P. Liu, M. G. Kibria, Q. Li, G. T. Wang, H. Guo, and Z. Mi, Nano Lett. **12**, 2877 (2012).

List of Publications

1. Malleswararao Tangi, **Arpan De**, and S. M. Shivaprasad, *Lowering of growth temperature of epitaxial InN by superlattice matched intermediate layers*: **Physica Status Solidi A** 210, 2409 (2013)

2. **Arpan De**, K. K. Nagaraja, Malleswararao Tangi and S. M. Shivaprasad, *Spontaneous growth of $In_xGa_{1-x}N$ nanostructures directly on c-plane sapphire by plasma assisted molecular beam epitaxy*: **Materials Research Express** 1, 035019 (2014)

3. **Arpan De**, Malleswararao Tangi, and S. M. Shivaprasad, *Pre-nitridation induced In incorporation in $In_xGa_{1-x}N$ nanorods on Si(111) grown by molecular beam epitaxy*: **Journal of Applied Physics** 118, 025301 (2015)

4. **Arpan De** and S. M. Shivaprasad, *Epitaxy, phase separation and band-edge emission of spontaneously formed InGaN nanorods*: **Journal of Physics D: Applied Physics** 49, 355304 (2016)

5. Malleswararao Tangi, **Arpan De**, Jay Ghatak, and S. M. Shivaprasad, *Electron mobility of self-assembled and dislocation free InN nanorods grown on GaN nano wall network template*: **Journal of Applied Physics** 119, 205701 (2016)

6. Malleswararao Tangi, **Arpan De** and S. M. Shivaprasad, *Growth of high quality InN films and nano-rods grown on GaN nano wall network*: **IEEE Conference Proceedings**, 1-5 (2014)

7. **Arpan De** and S. M. Shivaprasad, *Effect of Gallium and Nitrogen flux on the structural and optical properties of InGaN nanostructures grown on c-Sapphire by MBE*: **under preparation**

8. **Arpan De** and S. M. Shivaprasad, *Growth of InGaN nanowall network on GaN nanowall network template using MBE*: **under preparation**